Alma Mater Studiorum – Università di Bologna

DOTTORATO DI RICERCA IN

CHIMICA

Ciclo XXVIII

Settore Concorsuale di afferenza: 03/C2, 09/D1

Settore Scientifico disciplinare: CHIM/05

DESIGN AND DEVELOPMENT OF BIOMINERALIZED NANOSTRUCTURED DEVICES FROM NATURAL SOURCES FOR BIOMEDICAL APPLICATIONS

Presentata da: Elisa Savini

Coordinatore Dottorato

Prof. Aldo Roda

Relatore

Prof.ssa Maria Letizia Focarete

Correlatore

Dott.ssa Monica Sandri

Esame finale anno 2016

Abstract

The using of petroleum-based plastics is nowadays a growing problem: they are currently produced from fossil fuels, a finite resource, consumed and discarded as non-degradable wastes, worsening the environment. The aim of this work was to produce newly conceived bio-based and bio-inspired solutions towards the treatment of dental diseases and air filtration in artificial ventilation. To this aim, natural polymer derived from renewable materials of food industry were used.

Following concepts of bio-mimicking and hierarchical organization, scaffolds chemically and morphologically mimicking different components of the tooth, in specific the dentin and the whole periodontium (cementum, periodontal ligament and alveolar bone), were developed. Biomineralization processes performed on appropriate polymeric matrixes were setup to synthesize hybrid materials with the same chemico-physical properties of the natural mineralized tissues (dentin, cementum and alveolar bone). Self-assembling pH-dependent process and tape-casting were applied to type I collagen to develop the thin layer mimicking the not mineralized periodontal ligament. Structural and morphological features reproducing those of the natural tissues were achieved through chemical cross-linking treatments and freeze-casting or electrospinning processes. *In vitro* investigations performed on the developed 3D scaffolds indicate good cell viability, adhesion and proliferation.

Employing biomimetic principles and natural renewable materials, also a core-shell Heat and Moisture Exchange (HME) air filter, was developed. The shell part was obtained by applying the freeze-drying process on a chemically cross-linked hydrogel developed by blending suitable ratios of gelatin and chitosan. The core part of the filter was instead reached by mixing the FeHA powder, endowed with high hyperthermic properties, with an alginate matrix.

With this approach an air filter suitable for tracheostomised patient was successfully developed, having antibacterial and heat and moisture exchange properties, able to absorb the moisture from exhaled air of the patient and to release it into the inhaled air.

AIM OF THE WORK

Nature has always been inspiration for human advancements, since the solutions presented by nature are examples of highly effective and power-efficient mechanisms and materials with the additional advantage of being non-polluting. In particular the bio-based polymers are receiving high interest from researchers all over the world, because advanced materials from renewable resources are becoming more and more in demand. Two are the main motivations of this focusing: (i) the deteriorating environmental conditions, caused by advancements in technology, population expansion, etc. and (ii) the availability of fossil and not renewable resource which, according to the experts, will decrease drastically between one and three generations.

Within this context the European project "SMILEY" (Smart nano-structured devices hierarchically assembled by bio-mineralization processes) was conceived. The aim of this project is to point out that nature-inspired ideas may provide innovative and non-conventional processes that could be used in the design of medical devices, not only to be implanted, but also to be used *ex vivo*. Starting from abundant and environmentally safe raw materials and through phenomena inspired by nature like bio-mineralization, self-assembly and self-organization it's possible to generate elementary micro-sized building blocks, which are properly directed to be organized in macroscopic complex materials for application in EHS (Environment, Health, Safety) and Biomedical fields. In particular the present research activity is focused on the development of new class of devices fully made by environmental friendly materials designed to provide new solutions towards the local cure of teeth and the treatment of the air from artificial ventilation before it reaches the user.

Oral diseases are common results of a variety of causes like lifestyle (i.e. dietary habits, use of tobacco), trauma, genetic disorders and aging. These disorders, quite apart from

the socio-economic impact (traditional treatments of oral diseases have economic burden of 5-10% of the whole healthcare expenses in developed countries), can lead to physical and mental suffering that markedly lower the individual's quality of life. Given the progressive raise in the mean age of the active population, it is reasonable to assume that tooth lost and impaired oral function are expected to increase, while there is the need instead to quickly regain full activity and retain chewing capacity even at advanced ages. Progresses in these fields driven by advanced and innovative clinical treatments are main goals of modern medicine as they will significantly extend the quality-of-life years population, also ensuring patient's faster recovery with minimally invasive solutions and improved functionality of the diseased tissues.

The artificial ventilation bypassing the upper airways is very common in critically ill patients and in long-term care, in order to facilitate ventilation of the lungs, and to prevent the possibility of airway collapse or obstruction. As critical care advances and intensive care unit mortality declines, the number of survivors of critical illness is increasing. These survivors frequently experience long-lasting complications of critical care, beginning precisely from breathing. Respiratory system hypothermia, disruption of the airway epithelium and hospital-acquired infection are some of the inconveniences that a bankrupt artificial ventilation can cause to patients. In order to meet the increasing needs of healthcare the continuous improvement of the medical devices must be the subject of mainstream academic and commercial research and development activity.

The implanting devices developed in this Ph.D. project consist in bioresorbable scaffold mimicking dentin for the repair and regeneration of defects left by normal and deep caries and a chemically and morphologically graded scaffold for the regeneration of the whole periodontium apparatus (alveolar bone, periodontal ligament, cementum).
The highlight of the first scaffold resides in the high biomimicry with the target tissue, and this will enable it to direct the differentiation of the cells recruited from the bloodstream, reaching strong regenerative effects.

The second device was designed, instead, for the stabilization of titanium dental implants; in fact it could increase the resilience of implants up to the performances of normal tooth. Restoration of the periodontal ligament at the bone-cement interface will strongly reduce the peri-implantitis incidence impacting either on mechanical or biological factors.

The third device developed in this Ph.D. project is a completely biodegradable air filter capable of moisture exchange, during the alternate breathing cycle, from the exhaled air to the inhaled air. At the same time the device, under a magnetic field is capable to heat the air directed to the patient thanks to its hyperthermic power.

INTRODUCTION

2.1 Biologically inspired approach for materials development

Biomimetics is a relatively recent multidisciplinary study embracing the use of nature as a model for innovative materials, structures and strategies. The first biological inspired process was brought to public attention by Otto H. Schmitt in 1957, who produced a physical device mimicking explicitly the electrical action of a nerve. He coined the term "Biophysics" which is the base of "Biomimetics"[1], increasingly used in emerging technology interchangeably with "Biomimesis", "Biomimicry" and "Biological inspired design"[2]. Biologically inspired approaches have been particularly attractive in several fields; in over 3.8 billion years of evolution, in fact, nature has introduced solutions maximizing functionality with reduced energy and materials and with no impact on environment, exactly the targets faced by the actual technological challenges. For these reasons researchers have been interested for years in trying to copy biological useful characteristics, including self-assembling and structural hierarchical organization, multifunctionality and environmental adaptability. In the past fifty years there was an increasing number of bioinspired technologies such as bone-like materials based on wood, tough ceramics based on mother-of-pearl, self-cleaning structures based on flowers, underwater glues based on mussel adhesive, drag reduction based on dermal riblet on shark skin, flight mechanisms based on insect flight, etc.[3,4,5,6,7,8].

In particular the last decade developments concerning nature-based materials and nature-inspired processes with potential biomedical applicability are achieving particular prominence thanks to their low impact on environment and exclusive high biocompatibility[9,10,11,12].

2.2 Bio-based polymers and cross-linkers

The exploitation of biomimesis using polymers from natural sources for end-user applications represents a formidable challenge for industries worldwide in order to enhance their innovation potential. Bio-based polymers can be produced from renewable biogenic resources and are efficiently biodegraded, so represents eco-sustainable and, in most cases, inexpensive feedstock with exclusive features which often cannot be obtained in laboratory.

A definition of bio-based products was provided in 2002 by the US Congress in the Farm Security and Rural Investment Act which defined them as commercial or industrial products that is composed, in whole or in significant part, of biological products or renewable domestic agricultural materials (including plant, animal, and marine materials) or forestry materials[13]. Native bio-based materials could also be modified by physical, chemical or enzymatic methods to impart conformational changes or activation of functional groups and meet specific industrial applications.

Bio-polymers could be originated from several resources included microorganisms fermentation (like polyhydroxyalkanoate, bacterial cellulose, etc.), synthesis from bio-derived monomers (i.e. polylactic acid) or extract from plant and animals (Fig. 2.1).

Regarding the polymers from biomass the three major groups of plant-based polymers are proteins, oils and polysaccharides[14]. The amino acid polymers derive mainly from oilseeds (i.e. soybeans) and grains (i.e. wheat and corn) and are usually produced as by-products of processing. They are commonly used as major ingredients for feed and pharmaceuticals[15,16,17]. Plant oil which are mostly produced and used are soy oil, corn oil and flax oil; they are composed by triglycerides and contain several fatty acids with differ in chain length, distribution and composition, which results in differences in physical and chemical property of the oil. Adhesives and resins can be derived from bio-oils using synthetic techniques similar to those used with petroleum-based polymers[18,19].

Starch and cellulose are the main naturally occurring polymers in the carbohydrate family and they can be obtained from various sources with environmentally safe processes. The major resources for starch are corn, wheat, sorghum and potato and vegetal fibers, include wood and crop residues such as straw and milling by-products are the main sources of cellulose. These polysaccharides have been used in the food and nonfood industries, as well as in the paper production[20,21,22]. Also alginate, a polysaccharide polymer made from brown algae is widely used in food and nutraceutical industries[23].

Protein and polysaccharide polymers could be also made from animal sources. Collagen is the most abundant protein polymer in mammals, and gelatin is its hydrolyzed derivative. They are extracted from animal tissues, such as equine tendon and porcine skin. They have a massive application both in food and biomedical fields[24,25]. In the family of polysaccharide polymers made from animals chitin and chitosan, its deacetilated compound, are and they find their major use is in feed and biomedical the fields[26].

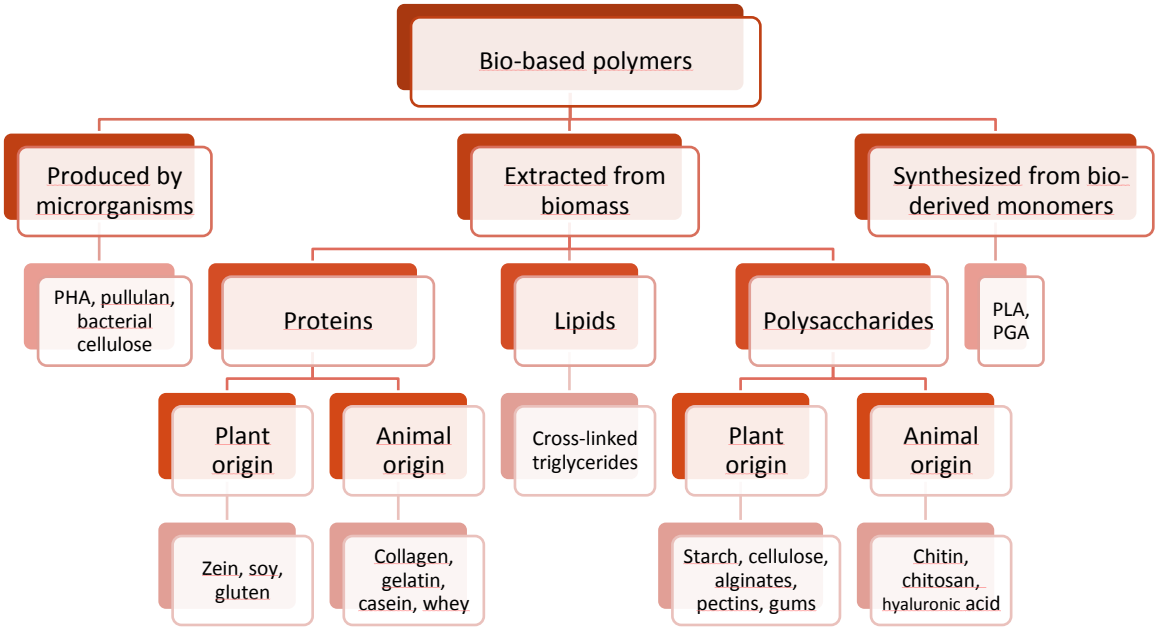

Figure 2.1. *Reassume of possibly sources of main natural polymers.*

The biggest challenge in the use of natural polymers in devices development lies in their frequent poor mechanical properties. For this reason is well-known the introduction of molecules that will act as cross linking agents to improve mechanical properties[27, 28,29].

Some of the main bio-based polymers, which are used in this PhD thesis, and their cross-linking agents are subsequently more thoroughly treated.

2.2.1 Collagen

Collagen is the most abundant protein in animals and is the major component of the extracellular matrix and connective tissues, like tendons, ligament, and forms the matrix of bone and teeth[30]. A single collagen molecule (also known as tropocollagen) consists of three polypeptide chains, which contains a predominant sequence of amino acids, Gly-X-Y, where X and Y position are frequently occupied by proline and hydroxyproline respectively (primary structure). Thanks to the rigidity of their structure, these amino acids locally affect the configuration of the chains which is wrapped in left-handed helix (secondary structure), made steady by inter-chain hydrogen bonds. The three chains are then wrapped in a right-handed triple helix (tertiary structure), stabilized by intra-and intermolecular interactions as well as the water of hydration. The quaternary structure is characterized by the repetition of the structural triple helix unit, packed to form a collagen microfibrilla (Fig. 2.2). This particular three-dimensional structure, makes the collagen not soluble in water. The amino acids present in the amino acid sequences of collagen contain amino (-NH2), carboxyl (-COOH) and hydroxyl (-OH) groups which, together with the peptide bond of the main chain, represent the possible sites of chemical interaction of collagen molecule. By the amino acid composition of the collagen protein depends its isoelectric point (pI) that is the value of pH where a particular molecule or surface carries no net electrical charge; for the collagen, this pH value is equal to 5.5[31].

So far, 28 types of collagen have been identified, but the type I is largely the most abundant and exhibits identical amino acid composition in two of the three polypeptide

chains. Type I collagen is the most used in the development of materials for regenerative medicine, due to its good physico-chemical stability and processability, high safety and biocompatibility profile[32,33].

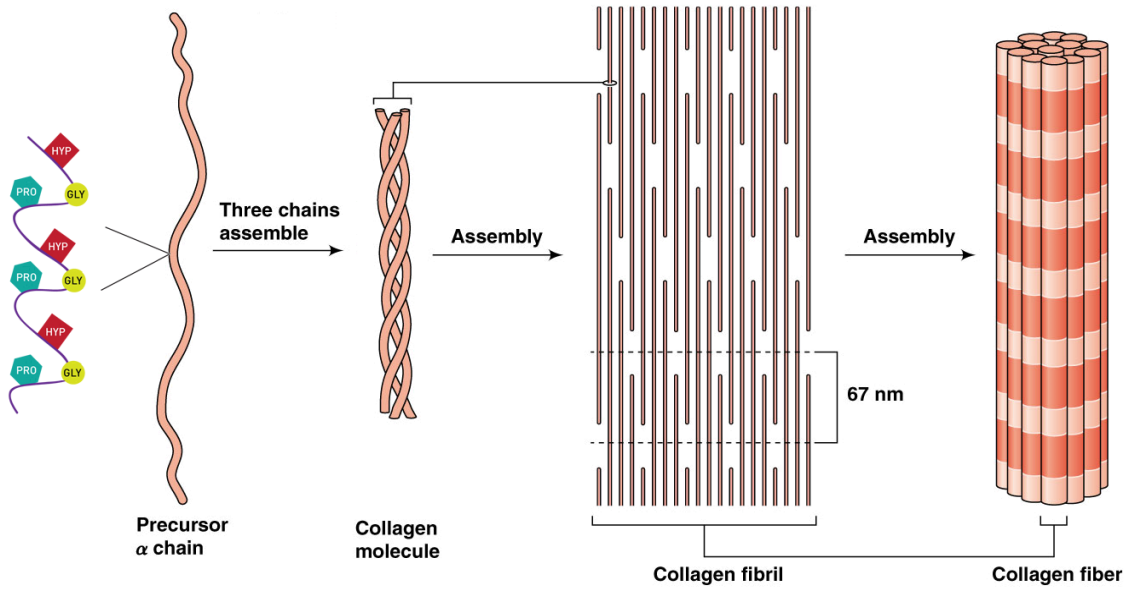

***Figure 2.2** Assembling and final structure of collagen fiber[34].*

2.2.2 Gelatin

Gelatin derives from thermal, physical or chemical degradation of collagen. It is an edible biodegradable and biocompatible polymer[35] and it is divided into two main types: Type A, which is derived from collagen of pig skin by acid pre-treatment, and Type B, which is derived from collagen of beef hides or bones by an alkaline process; gelatin Type A was used for the experiments described in this Ph.D. thesis. Amino acid composition of gelatine is variable, depending on the raw material and process used, but mostly it's composed by glycine, proline and lysine (Fig. 2.3).

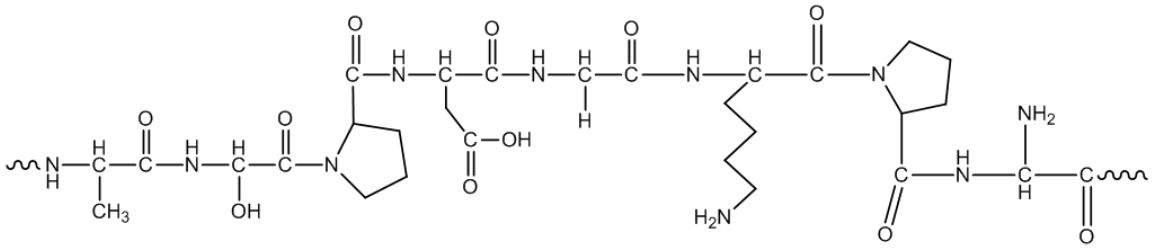

***Figure 2.3** A general structure of gelatin[36].*

Gelatin naturally forms physical gels in hydrogen-bond friendly solvents above a concentration larger than the chain overlap concentration (~2 % w/w). The gelatin sol undergoes a first order thermo-reversible gelation transition at temperatures lower than 30°C, during which gelatin molecules undergo an association-mediated conformational transition from random coil to triple helix. The aggregation is stabilized through intermolecular hydrogen bonding[37], during which, three dimensional interconnected network connecting large fractions of the gelatin chains is formed[38].

2.2.3 Chitosan

Chitosan is a biocompatible and bioerodible cationic polymer made by partial deacetylation of chitin, the structural element of exoskeleton of crustaceans. It is composed so, of randomly distributed β-(1-4)-linked D-glucosamine (deacetylated unit) and N-acetyl-D-glucosamine (acetylated unit) (Fig. 2.4).

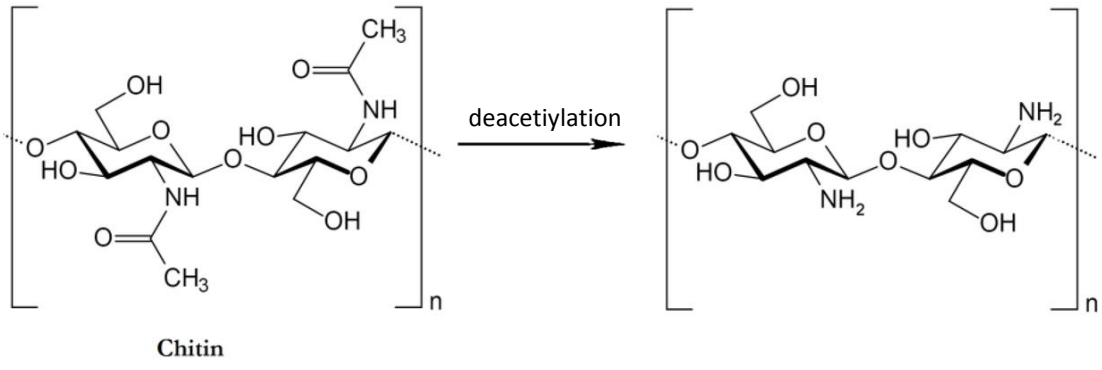

***Figure 2.4** Structure of chitosan from the deacetylation of chitin.*

Chitosan has a broad agricultural, and industrial uses as well as biomedical applications thanks to its pH-sensitive structure, due by amine groups that become deprotonated above the pH range of 6.2 –7.0, and antimicrobial activity[39]. Naturally insoluble in water, chitosan can be dissolved in aqueous solutions with a pH below 6.2, such as acetic acid, and the amino- and hydroxyl groups on chitosan chains allow for relatively easy cross-linking.

2.2.4 Alginate

Alginate is a natural polysaccharide mainly isolated from brown sea algae[40] and is biodegradable under normal physiological conditions. It is an unbranched binary copolymer and consists of alternating residue of (1-4)-linked β-D-mannuronate (M) and its C-5 epimer α-L-guluronate (G), covalently linked together in different sequences or homopolymeric blocks. (Fig. 2.5). Different formulations have been tested showing good ability in supporting cells proliferation, because it's able to provide micro-environments similar to those presented by the extracellular matrix, and slow degradation rate in physiological conditions[41,42].

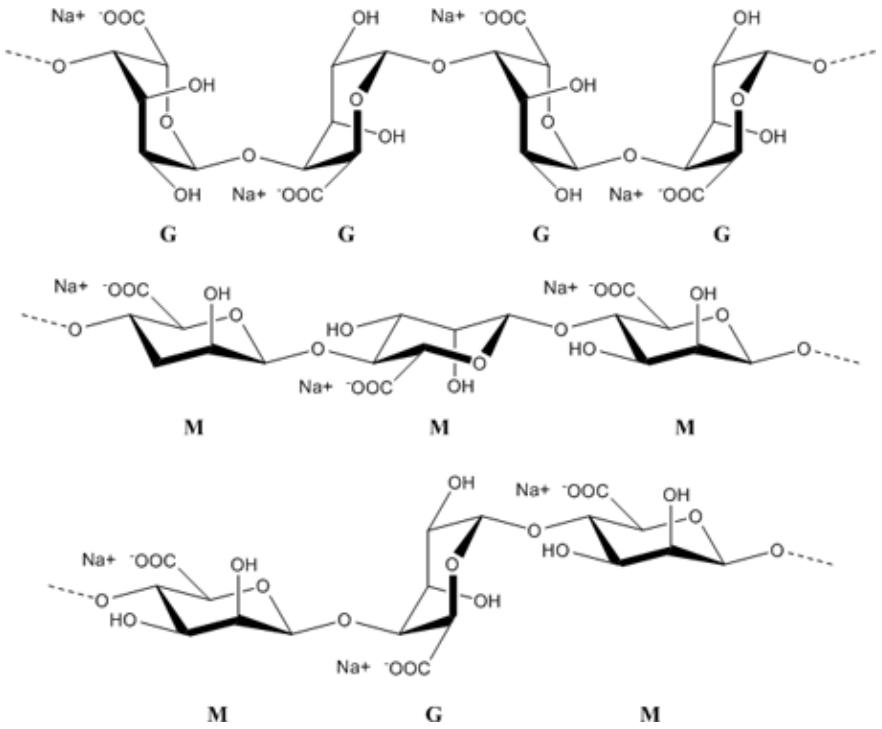

Figure 2.2 *Structure of alginate with with homopolymeric blocks β-D-mannuronate (M) and L-guluronate (G). Ring conformations in the alginate chain: M: $^4C_1$ and G: $^1C_4$.*

It is an anionic polymer, and as many ionic polysaccharides, alginate has the ability to bind divalent cations and forms sable ionically cross-linked gels. The most common alginate cross-linking is a calcium-mediated interaction, where two pairs of two consecutive G units, each pair belonging to different polymer chains, are packed with the calcium ions located between them (Fig. 2.6). The polymer chain adopts a characteristic zigzag shape called, for this reason, "Egg-box" model[43].

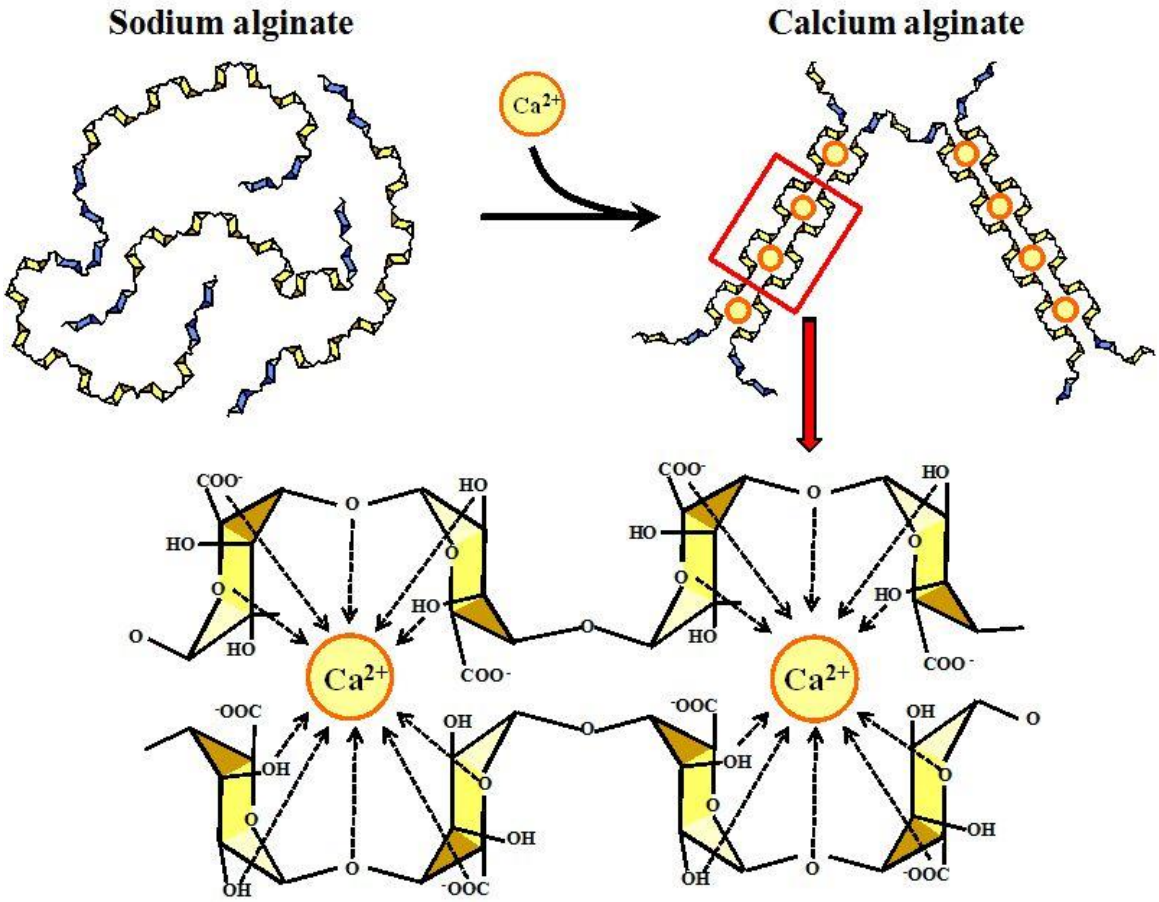

Figure 2.6 *Gelation of homopolymeric blocks of α-L-guluronic acid junction with calcium ions: the "Egg-box" model[44] (blue rings: M, yellow rings: G).*

2.2.5 Cellulose Acetate

Cellulose acetate (CA) is a modified natural polymer produced through esterification of cellulose (Fig. 2.7). It is a thermoplastic material generally recognized as a biodegradable polymer within the scientific community[45]. Different raw materials such as cotton, recycled paper, wood cellulose, and sugarcane are being used in producing the cellulose ester biopolymers and this makes it an inexpensive material.

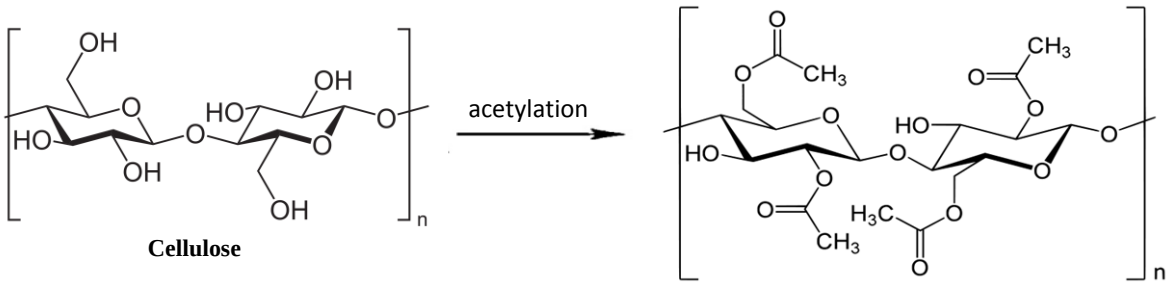

***Figure 2.7** Structure of cellulose acetate from the acetylation of cellulose*

Among the cellulose derivatives, cellulose acetate is widely used in industry out of its high modulus and resistance in the form of films and electrospun membranes[46,47].

2.2.6 Cross-linking agents

Natural polymers commonly have low functional properties, due to the extraction processes which often are highly aggressive and deleterious for the material structure. To address this disadvantage chemical, thermal or photo-induced cross-linking processes was implemented in order to achieve new strong intermolecular bonds, closer molecule packing, and reduced polymer mobility. Therefore, cross-linking has been explored as a viable method to modulate thermal resiliency and mechanical strength, as well as decrease solubility in high humidity condition and physiological environment.

2.2.6.1 Genipin

Genipin is a natural water soluble cross-linking agent extracted from gardenia fruit (*Gardenia Jasminoides Ellis*). Many studies have reported on genepin's much lower level of cytotoxicity compared to glutaraldehyde or other cross-linkers[48].

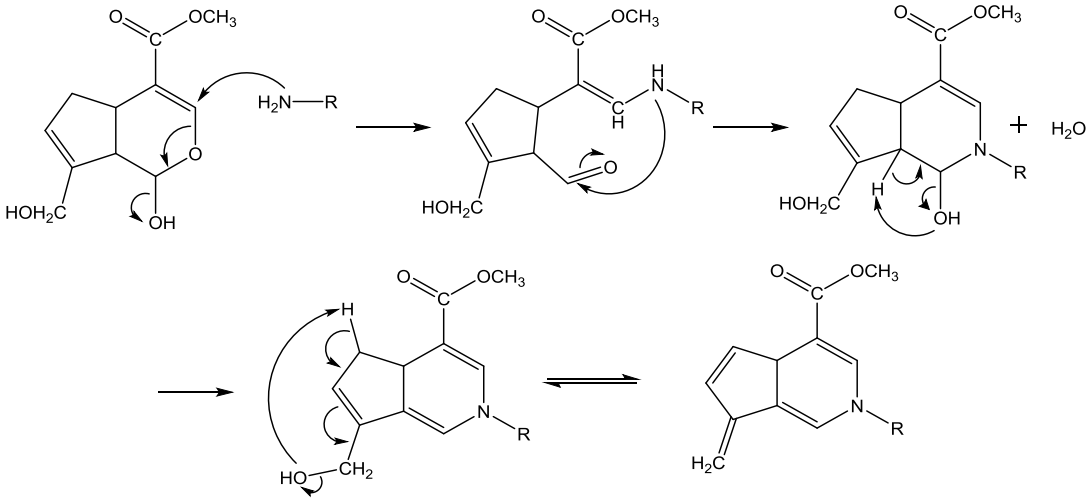

1)

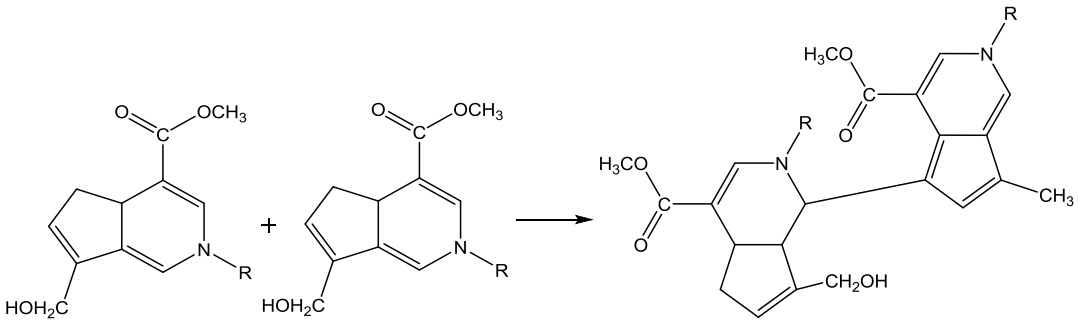

2)

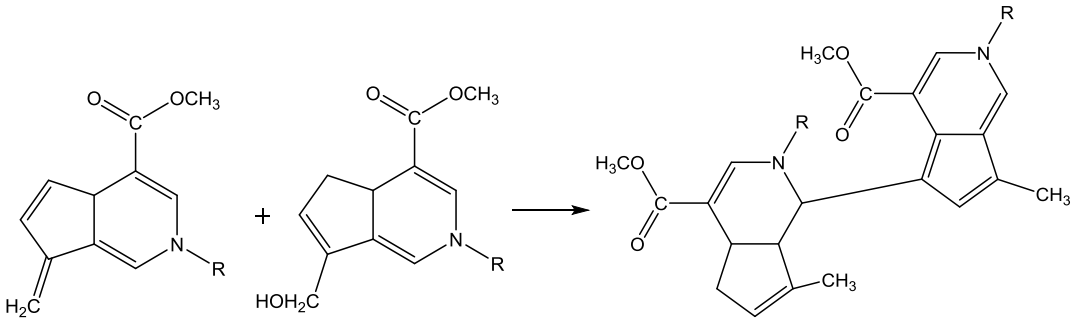

3)

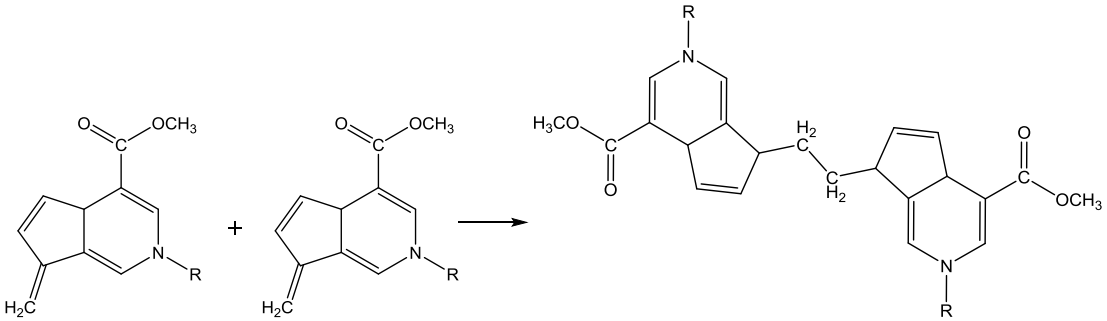

Figure 2.8 *Presumable reaction mechanism involving genipin and a generic primary amine group (R–NH$_2$)[49] and the three possible formation of a cross-linker genipin dimer-bridge[50].*

Genipin has been reported to bind spontaneously with biological tissues and biopolymers[51] containing amino groups, like collagen, gelatin, chitosan, etc. Genipin itself has no color, but forms blue particles by spontaneous reaction with amino acids and protein[52]. The cross-linking mechanism of genipin and two generic primary amino groups, at pH greater or equal to 5.5, are schematically explained in Fig. 2.8.

Among other naturally occurring biocompatible cross-linkers, genipin has established its captivating potential in the field of biomedical application[51,52,53].

2.2.6.1 1,4-Butanediol diglycidyl ether

1,4-Butanediol diglycidyl ether (BDDGE) is a diepoxy cross-linking agent used to stabilize polymers with free amine or carboxylic acid groups. BDDGE has a significantly lower toxicity than other ether-bond crosslinking agents and is biodegradable[56], so it is wieldy used to increase longevity and final properties of biomaterials[57].

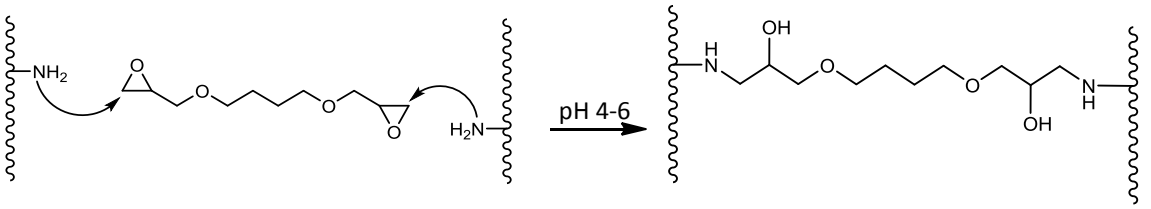

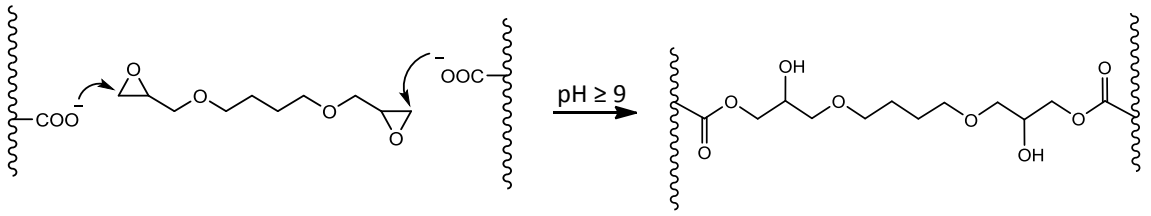

Figure 2.9 *Reaction mechanism involving BDDGE and primary amine or carboxylic acid groups in different pH conditions.*

Its cross-linking ability is attributed to the reactivity of the epoxide groups at the two ends of the molecule: in basic conditions, the epoxide groups preferentially react with alcohol or carboxylic acids, while in quite acid condition (pH 4÷6) it can react with primary amino groups (Fig. 2.9).

2.3 Biomaterials for regenerative medicine

Regenerative medicine is the process of creating living, functional tissues to repair or replace tissue or organ function lost due to age, disease, damage, or congenital defects by stimulating previously irreparable organs to heal themselves[58]. It is a critical frontier in biomedical and clinical because it applies the principles of engineering and life sciences to enhance the comprehension of the fundamental biological mechanisms underlying the structure function relationships in physiologic and pathologic tissues and to accomplish alternative strategies for developing substitutes which are able to restore, maintain, or improve tissue and organ function[59].

In the last few years the biomedical research area is going towards materials science aiming applications of materials to health care, the so-called biomaterials. In the first Consensus Conference of the European Society for Biomaterials (ESB) in 1987, a biomaterial was defined by Williams as “a nonviable material used in a medical device, intended to interact with biological systems”[60]. However, in 2009, a more recent definition has been published : “A biomaterial is a substance that has been engineered to take a form which, alone or as part of a complex system, is used to direct, by control of inter-

actions with components of living systems, the course of any therapeutic or diagnostic procedure, in human or veterinary medicine[61]. This change in definition is indicative of how the field of biomaterials has evolved. The first generation of biomaterial, in fact, was developed in 1960s to achieve suitable chemico-physical properties to mimic those of the replaced tissue with a minimal toxic response[62]: a possibly non-toxic and inert material. The second generation of biomaterials, born in 1980s, was instead bioactive components that could elicit a controlled action by the biological tissue[63]. During this second generation of biomaterials there was also the development of resorbable materials; in this way the implantation, after a controlled chemical breakdown, would be replaced by regenerating tissues. Finally the third-generation of biomaterials are being designed to stimulate highly precise reactions at the molecular level and so direct cell proliferation and differentiation thereby stimulating regeneration of living tissues[64].

According to the new concept of biomaterial it is clear that in order to replicate proper function and organization of native tissues, it's fundamental the detailed understanding and mimicking of tissue properties up to the nanoscale. Below, the features of biological tissues concerned in this PhD. project were analyzed.

2.3.1 Biological tissues

All biological tissues are composed of cells surrounded by the ExtraCellular Matrix (ECM), mainly composed by collagen. Cells are tissue building blocks and compose the great variety of mammalian organs. Cells do not grow efficiently in suspension, so they need to be attached to a substratum[65] with proper chemical and structural properties: them survival is deeply influenced by the support where they are engrafted and physicochemical properties of the environment. The ECM, in fact, is composed by soluble and physically bound signals as well as signals arising from cell-cell interactions. These signaling can induces complex intracellular signaling cascades that converge to regulate gene expression, and direct tissue formation, homeostasis and regeneration[66].

2.3.1.1 Structure of teeth

The completed permanent human dentition consists of 32 teeth and it is completed at about 14 to 15 years of age, except for the third molars, which are completed at 18 to 25 years of age. Teeth are complex organs that has long held the attention of the engineering which seeks materials with which replace the chewing apparatus vacations caused by physiological basis, like caries and aging, or trauma. Those are bioceramic composites, composed by hard and soft tissues.

Each tooth is divided in crown, the upper and exposed part, and root, the lower part inserted into the alveolar bone; the crown and root join at the cervical line. The crown is covered with enamel, while the root portion is covered with cementum and attached to the alveolar bone within which it sits thanks to periodontal ligament. The main bulk of the tooth is composed of dentin, which it encloses in its interior the pulp chamber, is in the crown portion, and the pulp canal, in the root, which normally contain the pulp tissue (Fig. 2.10)[67].

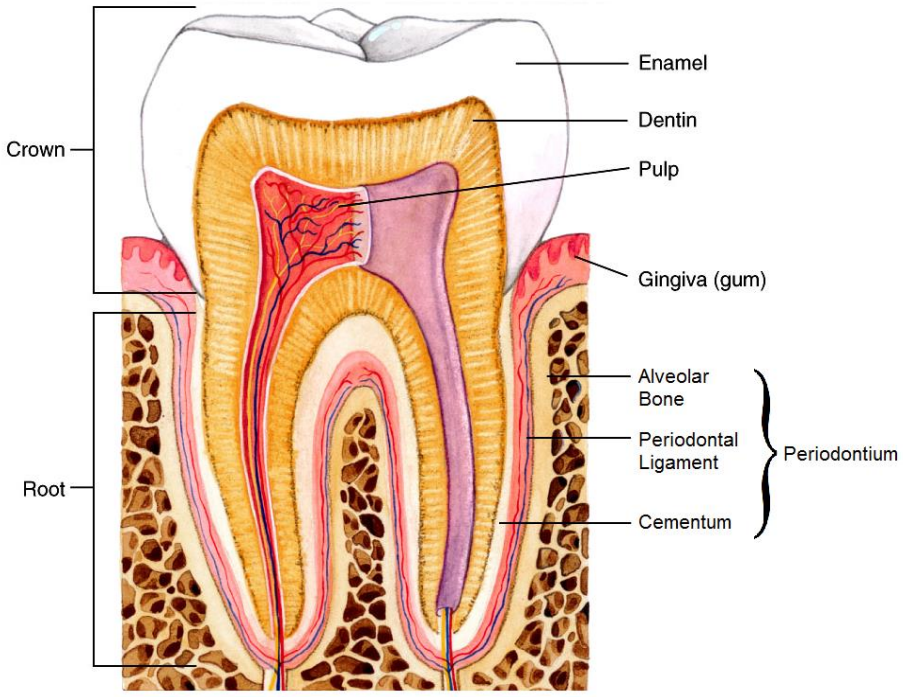

Figure 2.10 *Schematic tooth structure.*

More specifically, enamel, the outer layer of the tooth, is composed of more than 96% by inorganic elements, in the form of plural-substituted hydroxyapatite, and it is the hardest tissue in the body. The cells responsible for its formation are lost as the tooth emerges and this renders enamel is a non-vital and insensitive tissue. This means that when destroyed, for example by caries (Fig. 2.12), the enamel cannot be naturally replaced or regenerated[68]. Because of its high density and high mineral content, enamel is strong enough to withstand the stress of biting, chewing and grinding. However, that same trait makes enamel brittle and susceptible to cracking and chipping.

Dentin builds the second layer. This component is similar to bone tissue, but results a brittle tissue. It is an avascular area composed by apatite (about 70% weight) and organic components, mainly fibrillar collagen[69]. It is the core of the tooth and extends almost the entire length of it, with the particular morphology represented by closely packed tubules traversing its entire thickness (Fig. 2.11). Because of this structure, dentin is adapted for dissipating pressures or forces which otherwise would induce enamel fissures and detachment of the fragmented enamel from the outer dentin-enamel junction. Within these tubules reside the cytoplasmic extensions of cells from dentin/pulp junction that form and maintain the dentin, the odontoblasts. For this reason this tooth portion is sensitive and capable of repair[68].

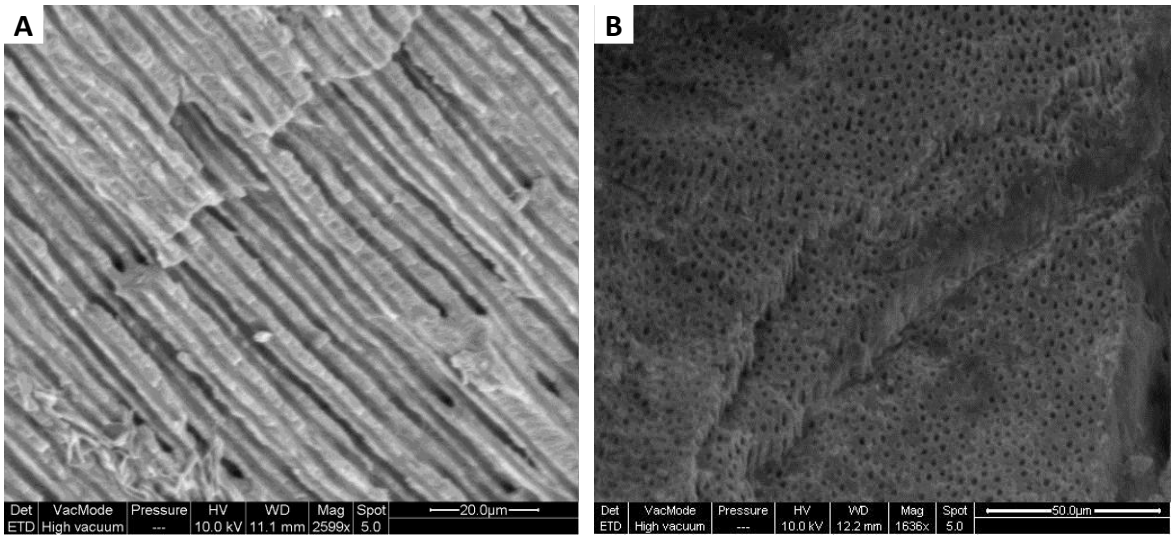

Figure 2.11 *SEM images of longitudinal (A) and transversal section (B) of dentin from a human molar.*

Dental pulp, the inner tooth layer, is a connective tissue organ containing cells, tiny blood vessels and nerves located in the deep central area within the tooth structure. Its primary function is to form the dentin and furnishes the blood and nerve supply to the tooth. The pulp canal extends almost the whole length of the tooth and communicates with the body's general nutritional and nervous systems through the holes at the end of the roots.

Cementum is a mineralized connective tissue, similar in structure to bone except that it is more dense and avascular; it consists of about 45-50% of apatite and the remaining organic matrix is largely collagen[69]. Cementum covers the entire root surface and forms the interface between the root dentin and the periodontal ligament; for its intermediary position it functionally belongs to the periodontium, the specialized dental supporting apparatus. The cementum provides the anchorage of the principal collagen fibers of the periodontal ligament to the root surface. It has also a crucial role in adaptative and reparative functions, maintaining occlusal relationship and to protect the integrity of the root surface. The cementum thickness varies by the type of tooth and with age, but is in the range of 100-300 µm[70]. It has a complex architecture described as a twisted ply-

wood structure with an alternating lamellar pattern, so that it may be represented as a woven fabric with wide radial and narrower circumferential collagen fibers.

The periodontal ligament is a non-mineralized connective tissue situated between the tooth and the alveolar bone. Its principal function is to connect the tooth to the jaw, which it must do in such a way that the tooth will withstand the considerable forces of mastication, allowing some degree of movement of the tooth within its bone cavity. The periodontal ligament has also the function to minimizing the trauma of teeth of being pushed together and preventing the tooth to from being pushed into the bone. This requirement is met by the masses of collagen fiber bundles that span the distance between the bone and the tooth and by ground substance between them. At one extremity the fibers of the periodontal ligament are embedded in bone and at the other extremity the collagen fiber bundles are embedded in cementum. Besides the collagen, the periodontal ligaments contains small blood, lymph vessels and nerves. Periodontal natural disease can establish itself when the gums detach from the teeth as a result of an inflammatory response to plaque, disease responsible for loss of periodontal tissue, pocket formation, and loosening and loss of teeth (Fig. 2.12).

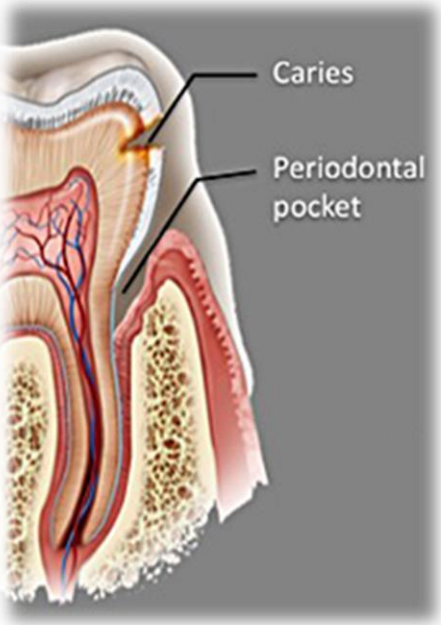

Figure 2.12 *Tooth structure in natural diseases[71].*

The final component of the periodontal apparatus is the alveolar bone, which lines the sockets in which the roots of teeth are held. Alveolar bone is thin and compact, with many small openings through with blood vessels and nerves pass. The composition is close to the one of other bones, that is a 70% wt. of apatitic matter and collagen-based organic matrix as well as water and cells. Further away from the tooth, in alveolar bone increases trabecular morphology. Unlike the tooth, the alveolar bone is a very active tissue, constantly in flux, undergoing tissue growth and resorption. Living cells are hosted inside the matrix and they can be classified into osteoblasts (and pre-osteoblasts), responsible of the production of the bone organic matrix and the regulation of the deposition of the mineral part, osteocytes, positioned in the inner part of the bone, which can be transformed again in osteoblasts when a new formation of matrix is needed, and osteoclasts, which are big cells able to dissolve the mineral part of the bone.

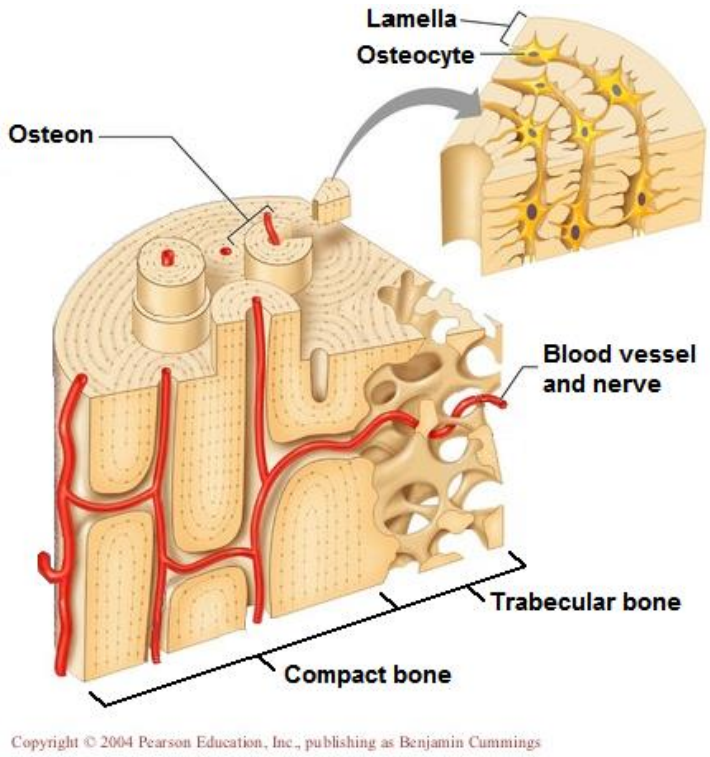

Figure 2.13 *Schematic drawing of the bone structure*

In alveolar bone there are two different types of bone tissue: compact (or cortical) and trabecula (or cancellous) bone; the compact one is dense and harder, while the trabecular one is a sponge-like tissue, but they are identical in their chemical composition. The tridimensional structure of the compact bone is made of canals, called osteons and each one consists of concentric layers, or lamellae, that surround a central canal which contain blood vessels and nerves. Trabecular bone is less dense of cortical one, it has higher surface area and is high vascularized. This structure gives the bone good mechanical properties with low density at the same time (Fig. 2.13).

2.3.1.2 Hydroxyapatite

Apatites constitute a large class of materials with many applications both in biomedical and environmental field, with general formula $[M'_2][M''_3](XO_4)_3Z$, where M represents a bivalent cation; XO_4 represents a trivalent oxyanion and Z represents a monovalent anion[72]. Among all the apatites, calcium hydroxyapatite (HA) is the most relevant in biological systems, as it is the major component of bones and teeth; its formula is defined as: $Ca_5(PO_4)_3(OH)$[73]. In a stoichiometry HA calcium, phosphate and hydroxyl ion are present in the following weight percentage: Ca^{2+} = 39.84%; PO_4^{3-} = 56.77%; OH^- = 3.39% so the ratio Ca/P correspond to 1.667. The apatite prototype structure was first determined by Naray-Szabo in 1930[74] and was confirmed to adopt $P6_3/m$ symmetry (Fig. 2.14)

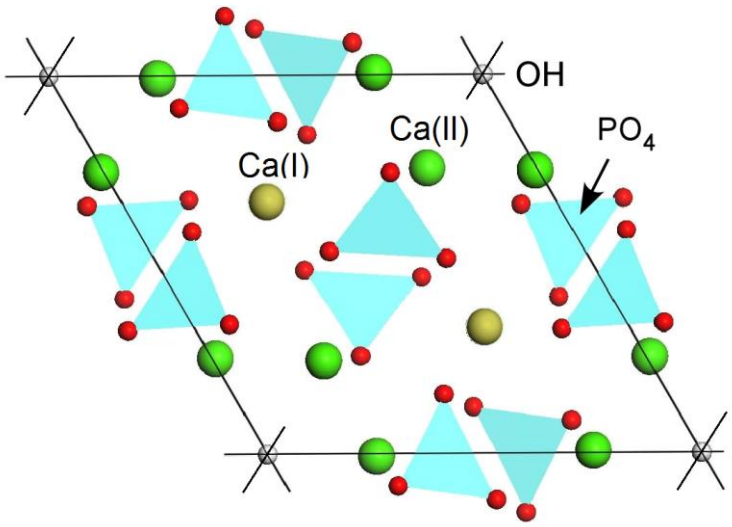

Figure 2.14 *Crystal structure of Hydroxyapatite*[75].

The calcium ions, occupy two crystallographically different symmetry sites, 4f and 6h, respectively for Ca(I) and Ca(II). The Ca(I) ions are located in columns along the three-fold axes and each is coordinated to nine O atoms. The Ca(II) ions are seven-coordinated, with six O atoms and one OH^- ion.

The above-described HA has been used as a model for the apatite present in the human hard tissues for many years, but many differences in composition and in other properties make the biological apatites different from stoichiometric calcium hydroxyapatite. The biological HA could be defined as a calcium-deficient, multi-substituted hydroxyapatite: the Ca/P ranges varies from 1.54 to 1.73 (compared to 1.67 for pure HA) and its lattice is very tolerant of substitutions, vacancies and solid solutions. For example Ca can be replaced by by Sr, Ba, Pb, Na or vacancies[76] and PO_4 by HPO_4, AsO_4, VO_4, SiO_4 or CO_3. Owing to this ability, biological apatites are capable of variable composition and therefore to be heterogeneous even within each category and even within each calcified tissue (enamel, dentine, bone). Based on observations from in vitro systems some of these foreign ions affect crystallinity, morphology, lattice parameters of the biological apatites, and as a consequence, impart stability or instability to the tissues involved[77].

In particular the presence of carbonate and magnesium ions in the biological apatites strongly contributes to the reduction of HA crystallinity and makes HA more soluble and

bioresorbable in physiological fluids. Thanks to its very poor crystallinity degree, biological apatite is not a stable material, as it is involved in the complex bone metabolism and thus subject to a continuous structural remodeling. An HA crystallinity increasing, due for example for aging, reflects in solubility decreases and a progressive decrease of the capacity of biologic HA to remodel itself.

The higher is the carbonate content the higher is the metabolic activity of the tissue: for example, enamel, which is a nearly inert tissue, contains very few carbonate, compared to bone and dentin. Carbonate ions are either adsorbed on the surface or incorporated into the HA structure, into two different crystallographic sites, hydroxyl (A-type carbonation) or phosphate (B-type carbonation). B-type carbonation is related to a higher affinity of apatite for osteoblast cells, compared to A-type carbonation, as it does not alter the surface polarity of HA. This reflects in a higher cellular adhesion and an increase production of collage[78].

It has been verified also that in calcified tissues the amount of magnesium associated with the apatite phase is higher (about 5% at.) at the first stages of the bone remodeling process and decreases with increasing calcification and with the ageing of individual. The presence of magnesium increases the nucleation kinetic of HA contemporary retarding that of its crystallization[79].

2.3.1.3 Hard tissues mineralization

The natural formation of hard tissue takes place through different events; the first is the synthesis inside osteoblast and the extrusion into the extracellular space of collagen. Here, the collagen microfibrils, start to assemble into fibres; during this self-assembling, a quarter-staggered arrangement of parallel molecules of tropocollagen is established, leaving a regular array gaps within each periodic unit. These areas are known as hole

zones (40 nm in length and 5 nm in width) and as reported[80] are the preferential sites for the nucleation of the mineral phase (Fig. 2.15).

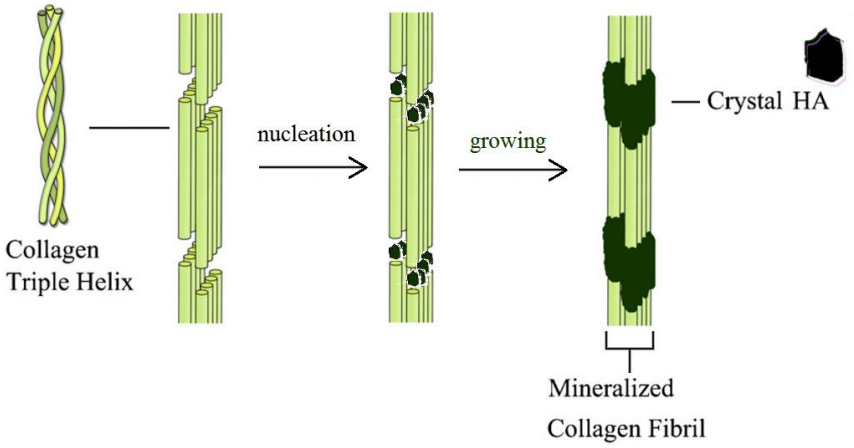

Figure 2.15 *Schematic illustration of nucleation of bone mineral crystals during self-assembling of collagen fibrils[81].*

The nucleation of mineral nanocrystals takes place in specific loci, highly charged from carboxylate groups that can bind Ca^{2+} ions. Following the chemical binding of calcium, the supersaturation of physiological fluids in phosphate ions, and optionally other minor species, provokes the precipitation and nucleation of the HA phase as nano-sized, plate-shaped particles, which are initially confined to the hole zones, and progressively extend along the collagen fibrils. The organic template transfers several information to the mineral phase at the molecular level: the chemical interaction of hydroxyapatite with collagen prevents the crystallization of the mineral phase; the size and shape of the nuclei are constrained by the activation of structural and morphological control mechanisms during the bio-mineralization process; the growth of nuclei is limited to very thin lamellae, which are spatially confined and have a specific crystal orientation. Crystal growth is limited to very few unit cells of the apatite lattice, with values ranging from 30-50 nm long, 15-30 nm wide, and 2-10 nm thick. The apatite platelets develop along the long axis of collagen, so that the apatite crystals grow preferentially along the c axis of the hexagonal apatite lattice. The mineralized fibrils with a self-organization process

pair up to constitute fibers and then lamellae, organized through different hierarchical levels up to the macroscopic bone.

2.3.2 Scaffold development for tissue replace and regeneration

Most approaches currently pursued within the framework of replacing lost or damaged tissues by initiating the natural regenerative process rely greatly on the ability to synthesize or otherwise generate novel biomaterials, to fabricate or assemble biomaterials into appropriate three-dimensional (3D) forms, and to tailor physical, chemical, structural and biological properties to achieve desired clinical efficacy. In a regeneration strategy, biomaterials promote new tissue formation by providing porosity and appropriate surface to foster and direct cellular attachment, migration, proliferation, desired differentiation. The scaffold 3D architecture refers to the way in which a bulk material is distributed in space from the macro, micro to nano scales (corresponding to tissue, cellular and molecular scales in a specific tissue, respectively). Consequently, such porous architectures plays a pivotal role for regenerating cells to form new tissues, for vascularization as well as the pathways for mass transport via diffusion and/or convection. While interconnected macroporosity of a biomaterial is important to provide sufficient space for cellular activity[82], interactions between cells and biomaterials occur at the interface, i.e. the entire internal pore walls of the scaffold. The surface morphology or topography directly and significantly affects cell-scaffold interactions and ultimately tissue formation and function[83].

The regeneration of hard tissue is very complex process that is known to be regulated by multiple factors and requires a scaffold chemically and morphologically similar to bone in order to facilitate the attachment of osteoblasts and the formation of blood vessels that mediate the transport of osteogenic precursors, of secretory molecules that act as activators for osteoblasts, exchange the fluids and transporters of nutrients and oxygen (Fig. 2.16).

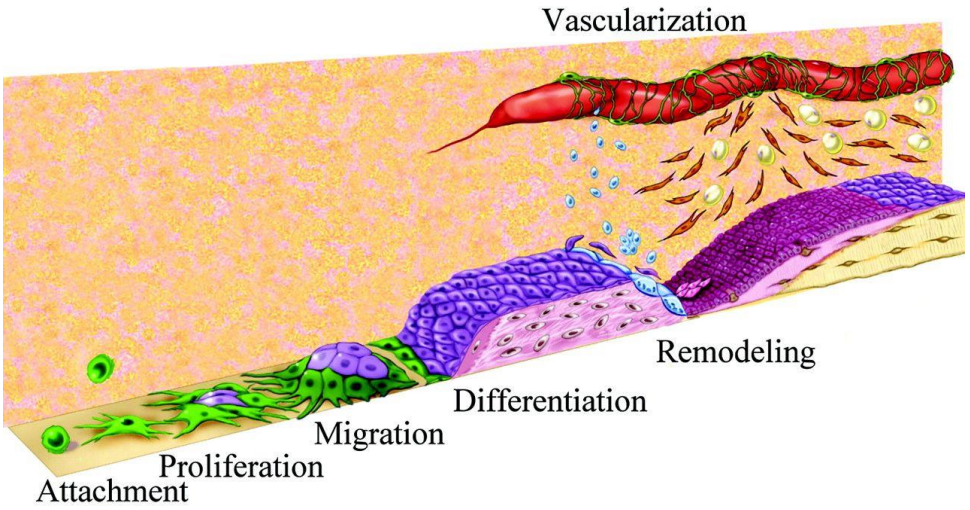

***Figure 2.16** Schematic illustration of cellular integration and growing on a new support*[84].

Although there are various therapeutic strategies for promoting the regeneration of hard tissues, the use of biomaterials alone or associated with osteo-progenitor cells and/or growth factors is considered the safer and the less invasive. The use of auto-grafts comes with some disadvantages such as the limited quantity available and its use also requires additional surgical procedures, and therefore, longer surgical time and possible complications of the wound of the donor site such as bleeding, pain and infection among others. Allografts and xenografts have the potential of transferring pathogens and to avoid the biological risk, these materials are subjected to exhaustive procedures which can reduce their structural integrity leading to graft fracture and have dramatic effects primarily on their osteogenic and osteoinductive[85].

A wide range of biomaterials and synthetic bone substitutes are currently used as scaffolds, including collagen, hydroxyapatite (HA), β-tricalcium phosphate (β-TCP) and calcium-phosphate cements, and glass ceramics, and the research into this field is ongoing[86]. The use of biomaterials as scaffolds for bone regeneration requires that scaffold is able to exchange chemical and biochemical signals with the surrounding physiological environment, in order to address the activity of progenitor cells towards selective differentiation. Physical signals, imparted by the scaffold morphology and structure, determine also the cell conductivity and colonization of the inner part of the scaffold. Therefore,

the design and development of three-dimensional mineralized scaffolds reproducing the structure and the hierarchically organized morphology of hard tissues is still a challenge, due to limitations in the current manufacturing technologies. In this view, the new trends in materials science research are looking at the peerless characteristics and properties of natural structures as new sources of inspiration to obtain innovative and smart biomorphic devices[12].

2.3.2.1 Biominealization

Bio-inspired crystallization of inorganic phases on natural template (also called bio-mineralization), self-assembly and self-organization are an ensemble of concomitant phenomena, inspired by natural bone formation, that will be properly directed to generate artificial elementary nano-sized building blocks organized in macroscopic porous devices. It is so possible exploit the ability of such a cascade of processes to form complex hybrid nano-composites starting from natural polymers using “green” conditions, that is operate under ambient conditions in aqueous solution, whose characteristics and organization are mediated by the activation of control mechanisms and structural confinement conferring defined functionalities to the final devices[87]. Due to the close reproduction at a laboratory scale of the conditions naturally occurring in the formation of the natural tissues, Tampieri et al.[88] realized bio-hybrid composites through a “biologically inspired” through a direct nucleation of biomimetic HA on self-assembling collagen fibers or other natural polymeric matrix[89]. The crystals formed are very much like bone mineral crystals: they are multi-substituted and with a low crystallinity degree.

2.3.2.1 Magnetism in biomedical applications

Magnetic materials can be classified in paramagnetic, which become magnetized upon exposure to a magnetic field without showing permanent magnetization once the field is turned off, and ferromagnetic, which underwire can retain their own magnetic field

even when the magnetic field previously applied is switches off. The materials classified as “superparamagnetic” are ferromagnetic nanoparticles (at a size of < 20 nm) where each particle is constituted by a single magnetic domain, non-magnetic on a macroscopic scale and behave like common materials in the absence of an exterior magnetic field. However, each particle could be considered a single magnetic domain, providing a magnetic field at a nano-scale. In a simple approximation, the total magnetic moment of the nanoparticle can be regarded as one giant magnetic moment, composed of all the individual magnetic moments of the atoms which form the nanoparticle. Very often, ferromagnetic nanoparticles show a certain preference for the direction, along which their magnetization aligns to: these nanoparticles are said to have an anisotropy in these directions. Nanoparticles with an uniaxial anisotropy can quickly and randomly flip the direction of their magnetization. If the average time between flips results much smaller than the measurement time, the measurement actually observes a fluctuating state with different unresolved magnetization spin directions. As long as there is no external field applied, a time-averaged net moment of zero is measured, but as soon as an external field is applied, the nanoparticles react similar to a paramagnet with the one exception that their magnetic susceptibility is much larger. This situation is called the superparamagnetic state of a system[90].

Of late the introduction of magnetism in the field of biology and biomaterials has been found useful in sophisticated bio-medical applications such as cell separation[91], drug delivery[92], diagnostic and contrast agent[93] and magnetic intracellular hyperthermia treatment of cancer[94]. The peculiarity of the magnetic materials is to allow an ON-OFF mechanism through the application of the electromagnetic field.

Magnetic materials have also recently attracted a big interest in the field of regenerative medicine, because recent findings show that the local application of weak magnetic fields may stimulate cells to reproduction and differentiate[95]. In adding, regarding the bone tissue regeneration, it has been demonstrated that magnetic nanoparticles have the effect of osteoinduction even without external magnetic force[96]. In vitro test show

that if magnetic scaffolds are subjected to static magnetic field application, their performance in cell proliferation is even improved respect to the not-magnetic control[97].

Iron-doped hydroxyapatite. Among the magnetic materials usually used in the biomedical field, magnetic nanoparticles (MNPs) have drawn great interest owing to their unique magnetic properties, including the fact that they become superparamagnetic at diameters of < 20 nm[98]. A point worth noting is that uncoated magnetite nanoparticles are significantly cytotoxic[99], and are believed to induce redox cycling and catalytic chemistry via the Fenton[100], the most prevalent source of reactive oxygen species (ROS) in bbiological system. In adding coated iron oxide MNPs could accumulate in the brain, liver, spleen and lungs, demonstrating their ability to cross the blood–brain-barrier[101]. For these reasons the use of biomimetic nanostructured apatite-based matrices MNPs will be rapidly magnetized to saturation and respond to the exterior magnetic field, however ensuring their biocompatibility[102], because the metabolism of iron-substituted hydroxyapatite leads to the release only of ions ferric, one of the most essential elements in the human metabolism.

Naturally, the concentration of iron within hard tissue is low, indicating that iron can be present within the body without entering in the apatite structure. Exposure of teeth to externally applied solutions containing iron leads, however, to easier incorporation of iron. It was investigated the local geometry of Fe^{2+} and Fe^{3+} in Fe-doped hydroxyapatite[103] and it was find that the Ca(II) site is energetically favoured over Ca(I) sites for Fe^{2+} substitution and that sixfold coordination is most stable. However for non-stoichiometric Fe^{3+} substitution, the fourfold case is most stable at the Ca(I) site.

2.4 Bio-based materials as air filters for mechanical ventilation

The increase in life expectancy and the advancement of medical technology have led in the last 50 years an exponential increase in cases of patients who need a mechanical

ventilation. A valuation made by the America Association for the Surgery of Trauma estimated 2.7 episodes of hospitalizations involving mechanical ventilation per 1000 population per year and, within these, acute respiratory tract injury were estimated at 86,2/100.000 person years, with an estimated national costs of 27 billion representing 12% of all hospital costs[104].

Mechanical ventilation, in fact, is one of the most common interventions in the intensive care unit and anesthesia treatments. In adding, mechanical ventilation is necessary in general when there are signs that the patient cannot maintain an airway or adequate oxygenation, e.g. who have acute respiratory failure, compromised lung function, difficulty in breathing, or failure to protect their airway. Although lifesaving, mechanical ventilation can be associated with life threatening complications, including air leaks, pneumonia and respiratory tract injury.

Below physiological principles of respiratory apparatus and the main features of mechanical ventilation were treated, emphasizing the features to be improving.

2.4.1 The breath process

The two phases of the ventilation, the inspiration and the expiration, take place thanks to the negative and subsequent positive pressure which goes to establish in the rib cage. With the rib cage expansion and the diaphragm contraction, the pressure in the chest cavity decreases, the lungs expand and this, in turn, causes the inhalation of the air. The air flux enter from nasal or oral cavity, it passes through larynx, trachea and reach bronchi in the lungs where the body is supplied with oxygen.

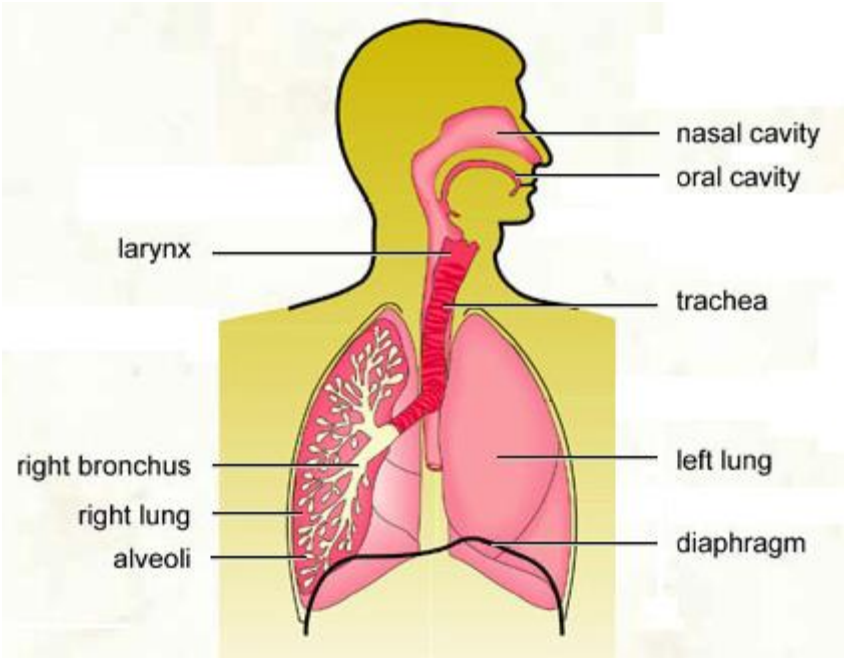

Figure 2.17 *Schematic illustration of the respiratory apparatus.*

Thanks to the antlers of alveoli and the rest breathing, there is the diffusion between the gaseous external environment and the blood. The next passage of air is out of the lungs to expel carbon dioxide, thanks to the diaphragm relaxation, and the contraction of the rib cage (Fig. 2.17).

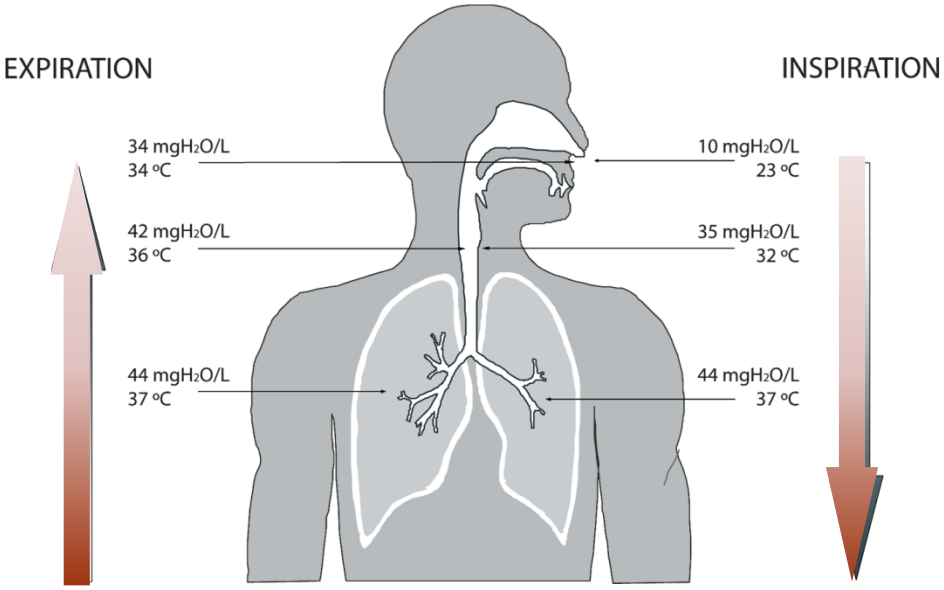

***Figure 2.18** Temperature and absolute humidity (AH) during inspiration and expiration of a normal person in rest at room environment (23°C, 10mgH_2O/L, 40% of relative humidity)[105].*

During normal nasal inspiration (Fig. 2.18), air at different ambient conditions is warmed and simultaneously moistened, firstly from the mucosal respiratory epithelium, causing the mucosa cooling, and then along the whole respiratory tract. When inhaled reach the body temperature, 37 °C, its capacity to hold water increases and when it reaches the complete saturation it contain about 44 mgH_2O/L of water vapor[106]. During the expiration, the air which comes from the alveolar environment is at the same temperature and moisture conditions but when goes along the previously cooled epithelium, it is cooled down warming the mucosa and the water vapor is partially released by condensation[107].

2.4.2 Mechanical ventilation

During the mechanical ventilation, an artificially assisted breathing was induced when disease of the heart or lungs leads to failure to maintain adequate blood oxygen levels (hypoxia) or increased blood carbon dioxide levels (hypercapnia). There are two main executive modes for the ventilation; the negative pressure ventilation exploits the features of most mammals natural breath, namely by negative pressure. During the negative pressure ventilation the patient must be insert into the commonly called “iron lung”, a chamber sealed, except for the head and neck which remain free, and where the air pressure into the chamber is cyclically decreased and increased, inducing an expansion and a compression of lungs and so the breath. This is an inherently uncomfortable process and it has been almost entirely superseded by positive pressure ventilators, which work by pushing the air from tanks directly into the patient airway. This last methodology could be divided in “noninvasive” ventilation, when the ventilation is delivered through a face mask, or "invasive" when there is the need of instrument penetrating through the mouth or the skin, such as an endotracheal or tracheostomy tube. This type of treatment has unfortunately not only beneficial but it can lead to various kinds of

complications, one of all is the risk of infection and in particular the risk of contracting pneumonia associated to mechanical ventilator.

In particular the tracheal intubation by-passes the natural filter provided by the upper respiratory tract, which physiologically warms and humidifies inspired gases and shuts out bacteria. Consequently the trachea/bronchial mucosa is subjected to an unconditionated air, to a too dry and cold, which may lead to hyperactivity of the mucous, derangement of the bronchial epithelium, mucociliary clearance mechanisms and lung mechanics, setting the stage for intercurrent pulmonary infections and other disorders like coughing and dyspnea[108].

2.4.2.1 Heat and Moisture Exchanger

In order to reduce the unfavorable effects of inspiring unconditioned air, Heat and Moisture Exchangers (HMEs), also known as "artificial noses", have been developed; they are intended to accumulating a portion of the patient's exhaled heat and moisture and returning them to the patient into the inspired gas. During expiration, air coming from the lungs is warm and humid; passing through the HME the air undergoes a release of heating due to the relatively cold device and the water condensate on the internal surfaces of HME. Water cached from the filter is evaporated to the cold and dry air that following is to be inspired, coupled with heat withdrawal (Fig. 2.19).

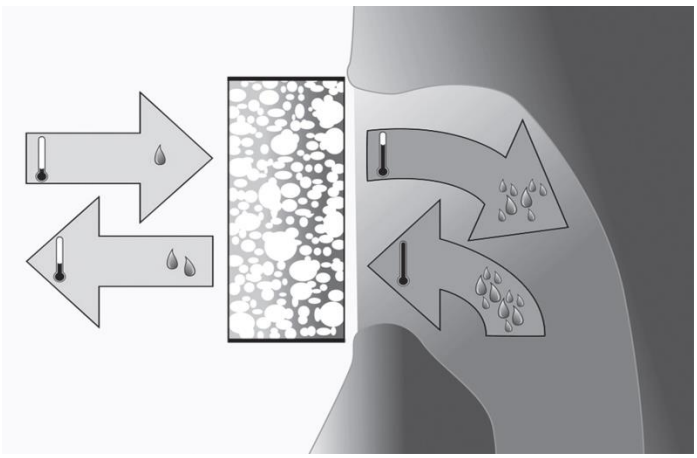

***Figure 2.19** Schematic illustration of the principles of a passive HME device at the environment/patient interface[109].*

The International Standard for biomedical humidifiers stated that the minimum amount of moisture necessary for patients whose upper airways are bypassed is 33 mgH_2O/L expressed in absolute humidity, AH (75% expressed relative humidity, RH) at 30 °C[110]. This value principally concerns laryngectomized/tracheotomized patients and using for long-term in intensive care units. During anaesthesia, in fact, the time duration of the bypass of the upper airway is shorter, so lower levels of humidity could be tolerated without causing dysfunction. For 10 h of mechanical ventilation it has been proposed that a minimum level of 20 mgH_2O/L (RH: 45%)[111] is sufficient to prevent damage to tracheo-bronchial epithelia. However the using of Heat and Moisture Exchange devices is growing also during anesthesia treatments, since anaesthetic gases reach a maximum relative humidity of 40% at a temperature of 24.8 °C[112].

The first HME filter was patented in 1954[113] after the introduction of the technique of tracheostomy and positive-pressure artificial ventilation, when a good humidifier turned out to be essential and hot waters humidifiers are proved to bring high cost and increased work load[114]. Nowadays HME filters were employed as the sole method of humidification in patients receiving mechanical ventilation[115], and many different HMEs are commercially available, which vary in shape, size and type of basic material. The devices currently on the adopt a technology of almost 20 years ago; they consist mainly of

polyurethane foam (hydrophobic HMEs) or very chip but not performing materials, such as cellulose sheets (hydrophilic HMEs)[116]. In order to increase heat and water retaining capacity, these materials are often impregnated with hygroscopic chemicals, such as magnesium or lithium chloride[117] and actually there are no cost effectively HME filters that exploit hyperthermia properties inside the filters for increment the heating.

2.4.2.2 Antibacterial effect in HME filters

Nosocomial bacterial pneumonia continues to complicate the course of 7 to 41% of patients receiving continuous mechanical ventilation[118]. Most have serious underlying disease, increased oropharyngeal colonization with hospital flora, and numerous reasons for elevated body temperature or leukocytosis[119]. These effects are caused by a sum of causes, including the bypassing of the natural bacterial barriers and the hospital-acquired infection due to transmission of infection between patients[120]. Anesthetic equipment is also characterized by the risk of cross-contamination, due to frequent patient changes at the anesthesia workstation[121].

During mechanical ventilation both inspired and expired gases pass through the same apparatus, consequently this is a suitable site at which applying a block of microbial contamination. For this reason the latest generation HMEs also provide a barrier from bacterial or viral infection, thus providing considerable advantages over traditional heater-warmers[122]. Often, however, these barriers are namely sieves which stop the passage of bacteria, but does not oppose the engraftment and colonization and, in the most case, cause an increasing of the pressure drop of the system which is set at 5 mbar[123].

2.5 Porous scaffolds fabrication technologies

Depending on the desired properties and the used material, many techniques have been developed aimed to producing porous scaffolds for several applications. Nowadays the techniques varies from cheap and simple processes which gives relatively poor control over microstructure, to elaborate processes which give excellent control over microstructure, but often at the cost of time and expense.

Solvent casting is one of the most simple technique and it is often used in combination with other common methods, for example, with particulate leaching. In this methods solid particle are embedding into the principal material solution, in order to form pores in the bulk of material upon removal. When the solvent evaporates, the material solidifies around the particles which are leached out of the material using distilled water, an organic solvent or through degradation (Fig.2.20).

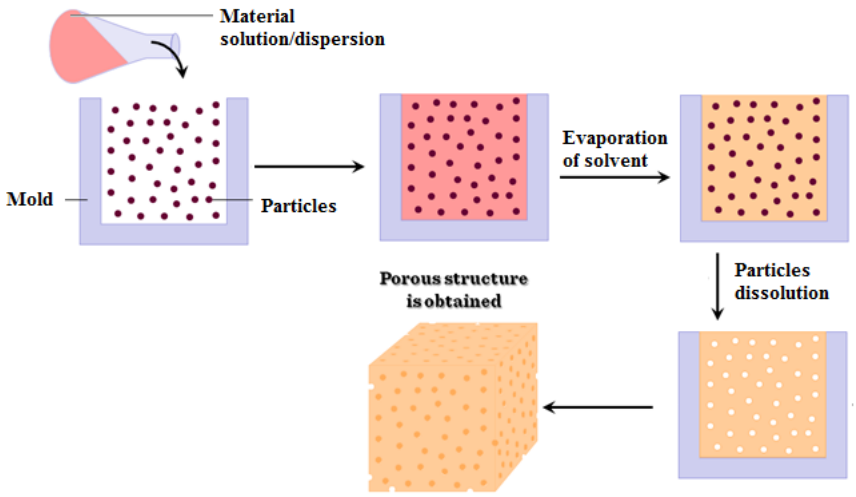

Figure 2.20 *Schematic illustration of the solvent casting and particulate leaching technique*[124].

Rapid prototyping, especially three-dimensional printing (3D printing) is widely used in the production of large and complex 3D porous matrices; it is a computer aided technique using a deposition layer by layer of the material with the desired geometry (Fig. 2.22).

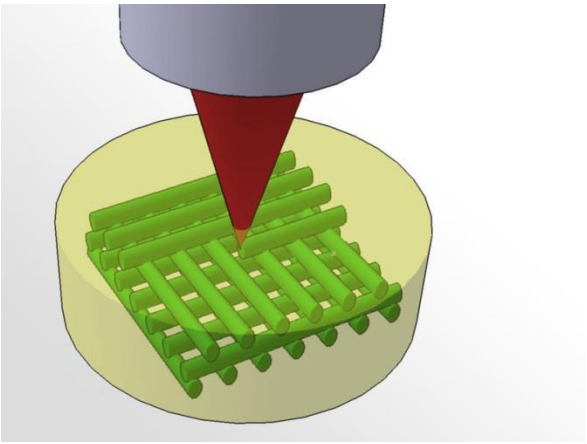

Figure 2.22 *Schematic illustration of the three-dimensional printing.*

Gas-foaming with carbon dioxide as foaming agent has been often used to form three-dimensional (3-D) scaffolds. In this technology the nucleation and growth of gas bubbles directly into the material matrix is induced and thanks to the increasing viscosity of the material, bubbles remain trapped into the structure (Fig.2.21).

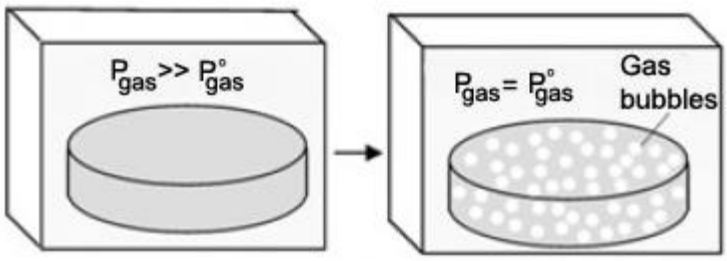

Figure 2.21 *Schematic illustration of the gas-foaming technique*[125].

Peptide-self-assembling exploits the natural behavior of some peptides to assemble in α-helixes or β-sheets thanks by non-covalent bonds and interactions. It is a reversible and pH-dependent process, controlled by peptide type and concentration. This technique alleviate problems inevitably associated with materials handling and solvent using (Fig.2.23).

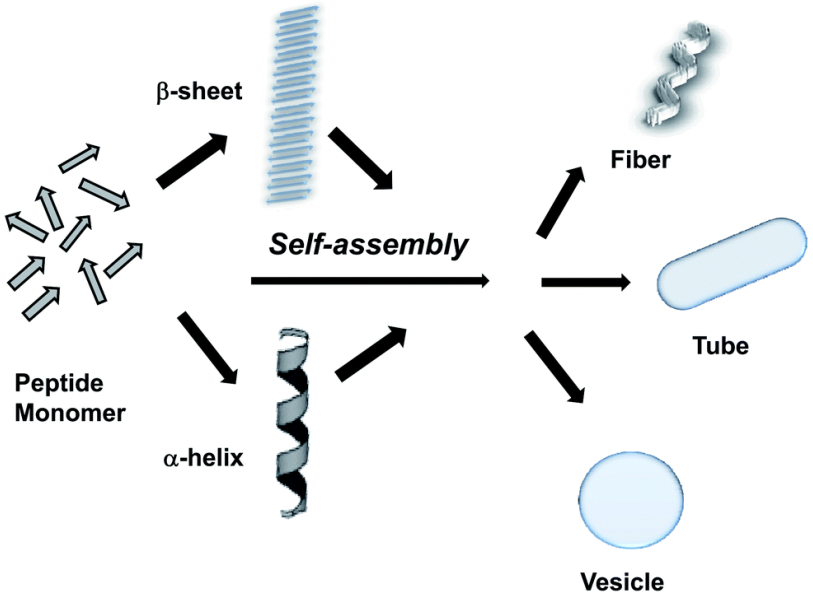

Figure 2.23 *Schematic illustration of the possibly peptide self-assembling*[126].

Electrospinning is a versatile technology used to produce highly porous nonwoven mats of micro-nanometric fibers. The machinery is composed by a metallic capillary, ejecting the material solution, and a metallic collector, among which an high voltage is applied. When the electrostatic force overcomes the cohesive force of the solution, an accelerated and stretched flux of material emerges from the needle directed to the collector. Before the deposition the electrostatic repulsions cause a convective motion of the material which leads to dry continuous solid fibers formation. Fiber diameter and morphology of sheets can be controlled varying features of the solution and the spinning variables (Fig. 2.24).

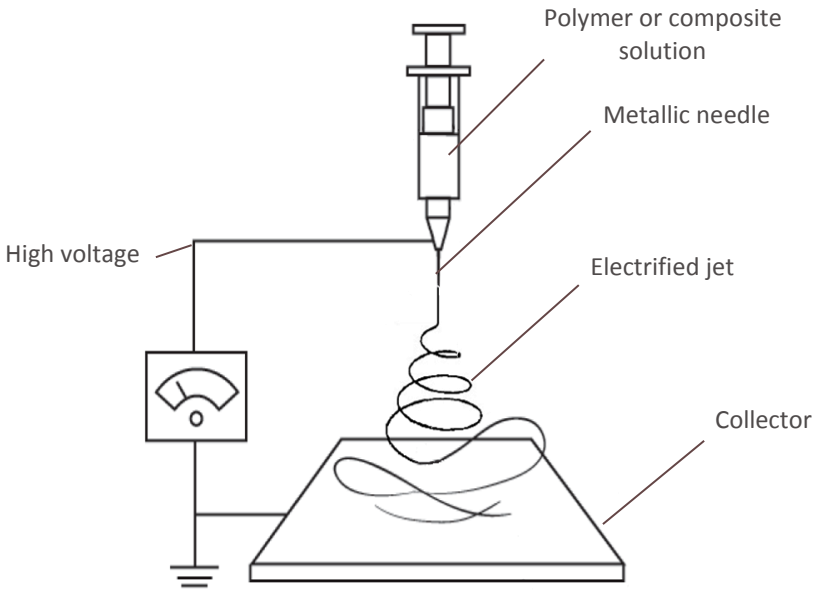

***Figure 2.24** Schematic illustration of the electrospinning technique*[127].

Freeze-drying process to form a porous material consists of two stages: the freezing of the material (solution/dispersion), and the drying of the material by means of solvent sublimation. The freezing process is usually realized by a vertical cooling of the material and the frozen solvent is subsequently removed from the rigid material by sublimation applying a low vacuum and a very slow warming rate. From the voids left by solvent results the porous morphology, so the freezing step is very important in order to produce desirable structures: during the freezing, solvent crystals grow and solute molecules are excluded and solidified between the crystals. Different freezing temperature, freezing rate and solute concentration could have a great impact on the resulting pore structure of the material. For example a fast freezing results in rapid formation of ice nuclei and the growth of small ice crystals which leads to the preparation of materials with small pores and viceversa using slow freezing.

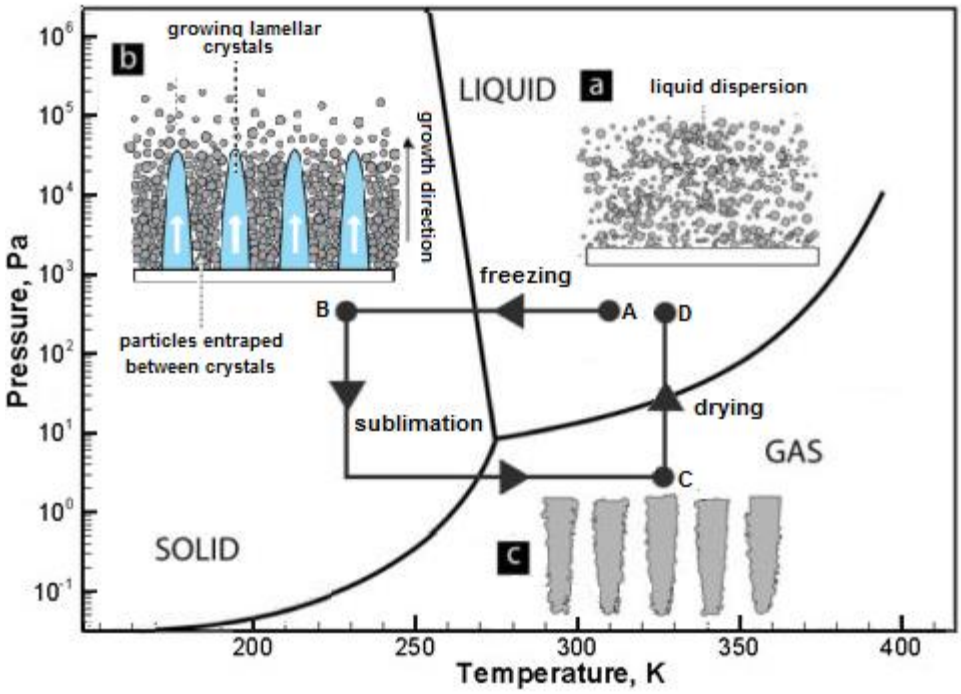

Figure 2.25 *Schematic illustration of the freeze-drying process.*

2.6 References

[1] J. M. Harkness, *A Lifetime of Connections: Otto Herbert Schmitt, 1913-1998*. 2001.

[2] J. F. V Vincent, O. A. Bogatyreva, N. R. Bogatyrev, A. Bowyer, and A.-K. Pahl, "Biomimetics: its practice and theory.," *J. R. Soc. Interface*, vol. 3, no. 9, pp. 471–82, Aug. 2006.

[3] Z. Guo, F. Zhou, J. Hao, and W. Liu, "Stable biomimetic super-hydrophobic engineering materials.," *J. Am. Chem. Soc.*, vol. 127, no. 45, pp. 15670–1, Nov. 2005.

[4] A. Tampieri, S. Sprio, A. Ruffini, G. Celotti, I. G. Lesci, and N. Roveri, "From wood to bone: multi-step process to convert wood hierarchical structures into biomimetic hydroxyapatite scaffolds for bone tissue engineering," *J. Mater. Chem.*, vol. 19, no. 28, p. 4973, Jul. 2009.

[5] J. F. V Vincent and D. L. Mann, "Systematic technology transfer from biology to engineering.," *Philos. Trans. A. Math. Phys. Eng. Sci.*, vol. 360, no. 1791, pp. 159–73, Feb. 2002.

[6] "Biomimetics: Nature-Based Innovation - CRC Press Book." [Online]. Available: https://www.crcpress.com/Biomimetics-Nature-Based-Innovation/BarCohen/9781439834763. [Accessed: 24-Feb-2016].

[7] Y. Bar-Cohen, *Biomimetics: Nature-Based Innovation*. 2011.

[8] Y. Bar-Cohen, "Nature as a Model for Mimicking and Inspiration of New Technologies," *Int. J. Aeronaut. Sp. Sci.*, vol. 13, no. 1, pp. 1–13, Mar. 2012.

[9] R. S. Trask, H. R. Williams, and I. P. Bond, "Self-healing polymer composites: mimicking nature to enhance performance.," *Bioinspir. Biomim.*, vol. 2, no. 1, pp. P1–9, Mar. 2007.

[10] R. Ravichandran, S. Sundarrajan, J. R. Venugopal, S. Mukherjee, and S. Ramakrishna, "Advances in polymeric systems for tissue engineering and biomedical applications.," *Macromol. Biosci.*, vol. 12, no. 3, pp. 286–311, Mar. 2012.

[11] D. W. Green, B. Ben-Nissan, K.-S. Yoon, B. Milthorpe, and H.-S. Jung, "Bioinspired materials for regenerative medicine: going beyond the human archetypes," *J. Mater.*

Chem. B, 2016.

[12] S. Sprio, A. Ruffini, F. Valentini, T. D'Alessandro, M. Sandri, S. Panseri, and A. Tampieri, "Biomimesis and biomorphic transformations: New concepts applied to bone regeneration," *J. Biotechnol.*, vol. 156, no. 4, pp. 347–355, 2011.

[13] O. Schmid, S. Padel, and L. Levidow, "The Bio-Economy Concept and Knowledge Base in a Public Goods and Farmer Perspective," *Bio-based Appl. Econ. J.*, no. 1, 2012.

[14] R. Wool and X. S. Sun, *Bio-Based Polymers and Composites*. 2011.

[15] R. Shukla and M. Cheryan, "Zein: the industrial protein from corn," *Ind. Crops Prod.*, vol. 13, no. 3, pp. 171–192, May 2001.

[16] K. S. Sandhu, N. Singh, and N. S. Malhi, "Some properties of corn grains and their flours I: Physicochemical, functional and chapati-making properties of flours," *Food Chem.*, vol. 101, no. 3, pp. 938–946, Jan. 2007.

[17] X. Liu, Q. Sun, H. Wang, L. Zhang, and J.-Y. J.-Y. Wang, "Microspheres of corn protein, zein, for an ivermectin drug delivery system.," *Biomaterials*, vol. 26, no. 1, pp. 109–15, Jan. 2005.

[18] Y. Xia and R. C. Larock, "Vegetable oil-based polymeric materials: synthesis, properties, and applications," *Green Chem.*, vol. 12, no. 11, p. 1893, Nov. 2010.

[19] E. Cheng, X. Sun, and G. S. Karr, "Adhesive properties of modified soybean flour in wheat straw particleboard," *Compos. Part A Appl. Sci. Manuf.*, vol. 35, no. 3, pp. 297–302, Mar. 2004.

[20] S. Z. Ellouzi, D. Driss, S. Maktouf, M. Neifar, A. Kobbi, H. Kamoun, S. E. Chaabouni, and R. E. Ghorbel, "Isolation and characterization of starch from industrial fresh pasta by-product and its potential use in sugar-snap cookie making.," *J. Food Sci. Technol.*, vol. 52, no. 9, pp. 5754–62, Sep. 2015.

[21] X. Liu, W. Xu, L. Mao, C. Zhang, P. Yan, Z. Xu, and Z. C. Zhang, "Lignocellulosic ethanol production by starch-base industrial yeast under PEG detoxification.," *Sci. Rep.*, vol. 6, p. 20361, Jan. 2016.

[22] P. Liu, P. F. Borrell, M. Božič, V. Kokol, K. Oksman, and A. P. Mathew, “Nanocelluloses and their phosphorylated derivatives for selective adsorption of Ag(+), Cu(2+) and Fe(3+) from industrial effluents.,” *J. Hazard. Mater.*, vol. 294, pp. 177–85, Aug. 2015.

[23] F. Sun, C. Ju, J. Chen, S. Liu, N. Liu, K. Wang, and C. Liu, “Nanoparticles based on hydrophobic alginate derivative as nutraceutical delivery vehicle: vitamin D3 loading.,” *Artif. Cells. Blood Substit. Immobil. Biotechnol.*, vol. 40, no. 1–2, pp. 113–9, Feb. 2012.

[24] B. F. Gibbs, Selim Kermasha, Inteaz Al, “Encapsulation in the food industry: a review,” *Int. J. Food Sci. Nutr.*, vol. 50, no. 3, pp. 213–224, Jul. 2009.

[25] M. Kharaziha, M. Nikkhah, S.-R. Shin, N. Annabi, N. Masoumi, A. K. Gaharwar, G. Camci-Unal, and A. Khademhosseini, “PGS:Gelatin nanofibrous scaffolds with tunable mechanical and structural properties for engineering cardiac tissues.,” *Biomaterials*, vol. 34, no. 27, pp. 6355–66, Sep. 2013.

[26] M. Elnashar, L. Abdel, H. Awad, and S. Mouneir, “Chitosan-benzofuran adduct for potential biomedical applications: Improved antibacterial and antifungal properties,” 2015.

[27] E. Tamimi, D. C. Ardila, D. G. Haskett, T. Doetschman, M. J. Slepian, R. S. Kellar, and J. P. Vande Geest, “Biomechanical Comparison of Glutaraldehyde-Crosslinked Gelatin Fibrinogen Electrospun Scaffolds to Porcine Coronary Arteries.,” *J. Biomech. Eng.*, vol. 138, no. 1, Jan. 2016.

[28] J. Kawadkar, R. Jain, R. Kishore, A. Pathak, and M. K. Chauhan, “Formulation and evaluation of flurbiprofen-loaded genipin cross-linked gelatin microspheres for intra-articular delivery.,” *J. Drug Target.*, vol. 21, no. 2, pp. 200–10, Feb. 2013.

[29] A. Papa, V. Guarino, V. Cirillo, O. Oliviero, and L. Ambrosio, “Optimization of protein cross-linking in bicomponent electrospun scaffolds for therapeutic use,” in *POLYMER PROCESSING WITH RESULTING MORPHOLOGY AND PROPERTIES: Feet in the Present and Eyes at the Future: Proceedings of the GT70 International Conference*, 2015, vol. 1695, p. 020008.

[30] M. G. Patino, M. E. Neiders, S. Andreana, B. Noble, and R. E. Cohen, “Collagen as an

implantable material in medicine and dentistry.," *J. Oral Implantol.*, vol. 28, no. 5, pp. 220–5, Jan. 2002.

[31] B. D. Ratner, A. S. Hoffman, F. J. Schoen, and J. E. Lemons, *Biomaterials Science: An Introduction to Materials in Medicine*. 2004.

[32] A. Tampieri, M. Sandri, E. Landi, D. Pressato, S. Francioli, R. Quarto, and I. Martin, "Design of graded biomimetic osteochondral composite scaffolds," *Biomaterials*, vol. 29, no. 26, pp. 3539–3546, 2008.

[33] C. M. Tierney, M. G. Haugh, J. Liedl, F. Mulcahy, B. Hayes, and F. J. O'Brien, "The effects of collagen concentration and crosslink density on the biological, structural and mechanical properties of collagen-GAG scaffolds for bone tissue engineering.," *J. Mech. Behav. Biomed. Mater.*, vol. 2, no. 2, pp. 202–9, Apr. 2009.

[34] G. Plopper, *Principles of Cell Biology*. Jones & Bartlett Publishers, 2012.

[35] J. Krochta, "Edible and biodegradable polymer films : challenges and opportunities.," 1997.

[36] Y. Ge, J. Wang, Z. Shi, and J. Yin, "Gelatin-assisted fabrication of water-dispersible graphene and its inorganic analogues," *J. Mater. Chem.*, vol. 22, no. 34, p. 17619, Aug. 2012.

[37] S. G. and V. Kokol, *Biomaterials Applications for Nanomedicine*. InTech, 2011.

[38] B. Mohanty and H. B. Bohidar, "Microscopic structure of gelatin coacervates.," *Int. J. Biol. Macromol.*, vol. 36, no. 1–2, pp. 39–46, Jul. 2005.

[39] T. Dai, M. Tanaka, Y.-Y. Huang, and M. R. Hamblin, "Chitosan preparations for wounds and burns: antimicrobial and wound-healing effects.," *Expert Rev. Anti. Infect. Ther.*, vol. 9, no. 7, pp. 857–79, Jul. 2011.

[40] G. Skjåk-Bræk, "Alginates: biosyntheses and some structure-function relationships relevant to biomedical and biotechnological applications," *Biochem. Soc. Trans.*, vol. 20, no. 1, pp. 27–33, Feb. 1992.

[41] *Biomedical Hydrogels: Biochemistry, Manufacture and Medical Applications*. Elsevier,

2011.

[42] J. T. Connelly, A. J. García, and M. E. Levenston, “Inhibition of in vitro chondrogenesis in RGD-modified three-dimensional alginate gels.,” *Biomaterials*, vol. 28, no. 6, pp. 1071–83, Feb. 2007.

[43] P. Sikorski, F. Mo, G. Skjåk-Braek, and B. T. Stokke, “Evidence for egg-box-compatible interactions in calcium-alginate gels from fiber X-ray diffraction.,” *Biomacromolecules*, vol. 8, no. 7, pp. 2098–103, Jul. 2007.

[44] K. K. and Masanao Imai, *Advancing Desalination*. InTech, 2012.

[45] J. Puls, S. A. Wilson, and D. Hölter, “Degradation of Cellulose Acetate-Based Materials: A Review,” *J. Polym. Environ.*, vol. 19, no. 1, pp. 152–165, Nov. 2010.

[46] Y. Dou, S. Xu, X. Liu, J. Han, H. Yan, M. Wei, D. G. Evans, and X. Duan, “Transparent, Flexible Films Based on Layered Double Hydroxide/Cellulose Acetate with Excellent Oxygen Barrier Property,” *Adv. Funct. Mater.*, vol. 24, no. 4, pp. 514–521, Jan. 2014.

[47] Y. Tian, M. Wu, R. Liu, Y. Li, D. Wang, J. Tan, R. Wu, and Y. Huang, “Electrospun membrane of cellulose acetate for heavy metal ion adsorption in water treatment,” *Carbohydr. Polym.*, vol. 83, no. 2, pp. 743–748, Jan. 2011.

[48] Y. Xi-xun, L. Fei, X. Yuan-ting, and W. Chang-xiu, “In vitro study in the endothelial cell compatibility and endothelialization of genipin-crosslinked biological tissues for tissue-engineered vascular scaffolds.,” *J. Mater. Sci. Mater. Med.*, vol. 21, no. 2, pp. 777–85, Feb. 2010.

[49] M. F. Butler, Y.-F. Ng, and P. D. a. Pudney, “Mechanism and kinetics of the crosslinking reaction between biopolymers containing primary amine groups and genipin,” *J. Polym. Sci. Part A Polym. Chem.*, vol. 41, no. 24, pp. 3941–3953, Dec. 2003.

[50] M. R. Hussain and T. K. Maji, “Preparation of genipin cross-linked chitosan-gelatin microcapsules for encapsulation of Zanthoxylum limonella oil (ZLO) using salting-out method,” *J. Microencapsul.*, Oct. 2008.

[51] H. W. Sung, I. L. Liang, C. N. Chen, R. N. Huang, and H. F. Liang, “Stability of a biological

tissue fixed with a naturally occurring crosslinking agent (genipin).," *J. Biomed. Mater. Res.*, vol. 55, no. 4, pp. 538–46, Jun. 2001.

[52] R. TOUYAMA, Y. TAKEDA, K. INOUE, I. KAWAMURA, M. YATSUZUKA, T. IKUMOTO, T. SHINGU, T. YOKOI, and H. INOUYE, "Studies on the blue pigments produced from genipin and methylamine. I: Structures of the brownish-red pigments, intermediates leading to the blue pigments," *Chem. Pharm. Bull.*, vol. 42, no. 3, pp. 668–673.

[53] B. Manickam, R. Sreedharan, and M. Elumalai, "'Genipin' - the natural water soluble cross-linking agent and its importance in the modified drug delivery systems: an overview.," *Curr. Drug Deliv.*, vol. 11, no. 1, pp. 139–45, Jan. 2014.

[54] J.-Y. Lai, "Biocompatibility of genipin and glutaraldehyde cross-linked chitosan materials in the anterior chamber of the eye.," *Int. J. Mol. Sci.*, vol. 13, no. 9, pp. 10970–85, Jan. 2012.

[55] L.-P. Yan, Y.-J. Wang, L. Ren, G. Wu, S. G. Caridade, J.-B. Fan, L.-Y. Wang, P.-H. Ji, J. M. Oliveira, J. T. Oliveira, J. F. Mano, and R. L. Reis, "Genipin-cross-linked collagen/chitosan biomimetic scaffolds for articular cartilage tissue engineering applications.," *J. Biomed. Mater. Res. A*, vol. 95, no. 2, pp. 465–75, Nov. 2010.

[56] K. De Boulle, R. Glogau, T. Kono, M. Nathan, A. Tezel, J.-X. Roca-Martinez, S. Paliwal, and D. Stroumpoulis, "A review of the metabolism of 1,4-butanediol diglycidyl ether-crosslinked hyaluronic acid dermal fillers.," *Dermatol. Surg.*, vol. 39, no. 12, pp. 1758–66, Dec. 2013.

[57] S. C. Choi, M. A. Yoo, S. Y. Lee, H. J. Lee, D. H. Son, J. Jung, I. Noh, and C.-W. Kim, "Modulation of biomechanical properties of hyaluronic acid hydrogels by crosslinking agents.," *J. Biomed. Mater. Res. A*, vol. 103, no. 9, pp. 3072–80, Sep. 2015.

[58] "NIH Research Portfolio Online Reportinf Tools; Regenerative Medicine." [Online]. Available: https://report.nih.gov/nihfactsheets/viewfactsheet.aspx?csid=62. [Accessed: 12-Mar-2016].

[59] M. A. Asnaghi, G. Candiani, S. Farè, G. B. Fiore, P. Petrini, M. T. Raimondi, M. Soncini, and S. Mantero, "Trends in biomedical engineering: focus on Regenerative Medicine.," *J. Appl.*

Biomater. Biomech., vol. 9, no. 2, pp. 73–86, Jan. .

[60] D. F. Williams, *Definitions in Biomaterials, Progress in Biomedical Engineering, Vol. 4.*, Elsevier. Elsevier, 1987.

[61] D. F. Williams, "On the nature of biomaterials.," *Biomaterials*, vol. 30, no. 30, pp. 5897–909, Oct. 2009.

[62] L. L. Hench, "Biomaterials.," *Science*, vol. 208, no. 4446, pp. 826–31, May 1980.

[63] J. Wilson and L. L. Hench, "Surface-active biomaterials.," *Science*, vol. 226, no. 4675, pp. 630–6, Nov. 1984.

[64] L. L. Hench and J. M. Polak, "Third-generation biomedical materials.," *Science*, vol. 295, no. 5557, pp. 1014–7, Feb. 2002.

[65] J. Folkman and A. Moscona, "Role of cell shape in growth control," *Nature*, vol. 273, no. 5661, pp. 345–349, Jun. 1978.

[66] M. Lutolf and J. Hubbell, "Synthetic biomaterials as instructive extracellular microenvironments for morphogenesis in tissue engineering," *Nat. Biotechnol.*, 2005.

[67] *Wheeler's Dental Anatomy, Physiology, and Occlusion*. 2003.

[68] A. Nanci, *Ten Cate's Oral Histology: Development, Structure, and Function*. 2008.

[69] R. W. Brand, D. E. Isselhard, and E. Satin, *Anatomy of Orofacial Structures: A Comprehensive Approach*. Elsevier Health Sciences, 2013.

[70] R. Dastmalchi, A. Polson, O. Bouwsma, and H. Proskin, "Cementum thickness and mesial drift.," *J. Clin. Periodontol.*, vol. 17, no. 10, pp. 709–13, Nov. 1990.

[71] P. D. Marsh and M. V. Martin, "Oral Microbiology," *Butterworth-Heinemann*, 2012. [Online]. Available: http://www.amazon.com/Oral-Microbiology-Evolve-eBooks-Package/dp/0702041483. [Accessed: 10-Mar-2016].

[72] J. Elliott, R. Wilson, and S. Dowker, "Apatite structures," 2002.

[73] M. I. KAY, R. A. YOUNG, and A. S. POSNER, "Crystal Structure of Hydroxyapatite," *Nature*,

vol. 204, no. 4963, pp. 1050–1052, Dec. 1964.

[74] S. Naray-Szabo, “The structure of apatite (CaF) Ca4 (PO4) 3,” *Z. Krist.*, vol. 75, p. 387, 1930.

[75] K. Matsunaga and H. Murata, “Strontium substitution in bioactive calcium phosphates: a first-principles study.,” *J. Phys. Chem. B*, vol. 113, no. 11, pp. 3584–9, Mar. 2009.

[76] J. C. Elliott, *Structure and Chemistry of the Apatites and Other Calcium Orthophosphates*. 2013.

[77] R. LeGeros and M. Tung, “Dissolution properties of C0 3-containing OH and F-apatites,” *J Dent Res*, 1982.

[78] S. A. Redey, M. Nardin, D. Bernache-Assolant, C. Rey, P. Delannoy, L. Sedel, and P. J. Marie, “Behavior of human osteoblastic cells on stoichiometric hydroxyapatite and type A carbonate apatite: role of surface energy.,” *J. Biomed. Mater. Res.*, vol. 50, no. 3, pp. 353–64, Jun. 2000.

[79] S. Onder, F. N. Kok, K. Kazmanli, and M. Urgen, “Magnesium substituted hydroxyapatite formation on (Ti,Mg)N coatings produced by cathodic arc PVD technique.,” *Mater. Sci. Eng. C. Mater. Biol. Appl.*, vol. 33, no. 7, pp. 4337–42, Oct. 2013.

[80] M. J. Olszta, X. Cheng, S. S. Jee, R. Kumar, Y.-Y. Kim, M. J. Kaufman, E. P. Douglas, and L. B. Gower, “Bone structure and formation: A new perspective,” *Mater. Sci. Eng. R Reports*, vol. 58, no. 3–5, pp. 77–116, Nov. 2007.

[81] Z.-Y. Qiu, Y. Cui, C.-S. Tao, Z.-Q. Zhang, P.-F. Tang, K.-Y. Mao, X.-M. Wang, and F.-Z. Cui, “Mineralized Collagen: Rationale, Current Status, and Clinical Applications,” *Materials (Basel).*, vol. 8, no. 8, pp. 4733–4750, Jul. 2015.

[82] T. D. Roy, J. L. Simon, J. L. Ricci, E. D. Rekow, V. P. Thompson, and J. R. Parsons, “Performance of degradable composite bone repair products made via three-dimensional fabrication techniques.,” *J. Biomed. Mater. Res. A*, vol. 66, no. 2, pp. 283–91, Aug. 2003.

[83] P. X. Ma, “Biomimetic materials for tissue engineering.,” *Adv. Drug Deliv. Rev.*, vol. 60, no.

2, pp. 184–98, Jan. 2008.

[84] G. F. Muschler, C. Nakamoto, and L. G. Griffith, “Engineering principles of clinical cell-based tissue engineering.,” *J. Bone Joint Surg. Am.*, vol. 86-A, no. 7, pp. 1541–58, Jul. 2004.

[85] M. Pérez-Sánchez, “Biomaterials for bone regeneration,” *Med Oral Patol Oral …*, 2010.

[86] R. Dimitriou and E. Jones, “Bone regeneration: current concepts and future directions,” *BMC …*, 2011.

[87] N. Bock, A. Riminucci, C. Dionigi, A. Russo, A. Tampieri, E. Landi, V. A. Goranov, M. Marcacci, and V. Dediu, “A novel route in bone tissue engineering: magnetic biomimetic scaffolds.,” *Acta Biomater.*, vol. 6, no. 3, pp. 786–96, Mar. 2010.

[88] A. Tampieri, M. Sandri, E. Landi, and D. Pressato, “Biomimetic Hybrid Composites to Repair Osteochondral Lesions,” *Key Eng. Mater.*, vol. 361–363, pp. 927–930, 2008.

[89] “Hybrid scaffolds for tissue regeneration: chemotaxis and physical confinement as sources of biomimesis,” *J. …*, 2012.

[90] M. Benz, “Superparamagnetism: theory and applications,” *Discussion*, 2012.

[91] J. Chatterjee, Y. Haik, and C.-J. Chen, “Modification and characterization of polystyrene-based magnetic microspheres and comparison with albumin-based magnetic microspheres,” *J. Magn. Magn. Mater.*, vol. 225, no. 1–2, pp. 21–29, Jan. 2001.

[92] W. Andra and H. Nowak, “Magnetism in medicine: a handbook,” 1998.

[93] R. Hergt, S. Dutz, R. Müller, and M. Zeisberger, “Magnetic particle hyperthermia: nanoparticle magnetism and materials development for cancer therapy,” *J. Phys. Condens. Matter*, vol. 18, no. 38, pp. S2919–S2934, Sep. 2006.

[94] D. Bahadur and J. Giri, “Biomaterials and magnetism,” *Sadhana*, vol. 28, no. 3–4, pp. 639–656, Jun. 2003.

[95] M. Iafisco and M. Sandri, “Magnetic bioactive and biodegradable hollow Fe-doped hydroxyapatite coated poly (l-lactic) acid micro-nanospheres,” *Chem. …*, 2013.

[96] S. Panseri, C. Cunha, and T. D'Alessandro, "Magnetic hydroxyapatite bone substitutes to enhance tissue regeneration: evaluation in vitro using osteoblast-like cells and in vivo in a bone defect," *PLoS …*, 2012.

[97] S. Panseri, C. Cunha, T. D'Alessandro, M. Sandri, G. Giavaresi, M. Marcacci, C. T. Hung, and A. Tampieri, "Intrinsically superparamagnetic Fe-hydroxyapatite nanoparticles positively influence osteoblast-like cell behaviour," *J. Nanobiotechnology*, vol. 10, no. 1, p. 32, 2012.

[98] V. Hasirci, E. Vrana, P. Zorlutuna, A. Ndreu, P. Yilgor, F. B. Basmanav, and E. Aydin, "Nanobiomaterials: a review of the existing science and technology, and new approaches," *J. Biomater. Sci. Polym. Ed.*, vol. 17, no. 11, pp. 1241–1268, Jan. 2006.

[99] A. Gupta and S. Wells, "Surface-modified superparamagnetic nanoparticles for drug delivery: preparation, characterization, and cytotoxicity studies," *NanoBioscience, IEEE Trans.*, 2004.

[100] A. Nel, T. Xia, L. Mädler, and N. Li, "Toxic potential of materials at the nanolevel," *Science (80-.).*, 2006.

[101] V. I. Shubayev, T. R. Pisanic, and S. Jin, "Magnetic nanoparticles for theragnostics.," *Adv. Drug Deliv. Rev.*, vol. 61, no. 6, pp. 467–77, Jun. 2009.

[102] A. Tampieri, T. D'Alessandro, M. Sandri, S. Sprio, E. Landi, L. Bertinetti, S. Panseri, G. Pepponi, J. Goettlicher, M. Bañobre-López, and J. Rivas, "Intrinsic magnetism and hyperthermia in bioactive Fe-doped hydroxyapatite.," *Acta Biomater.*, vol. 8, no. 2, pp. 843–51, Feb. 2012.

[103] Y. Jun, Y. Huh, J. Choi, and J. Lee, "Nanoscale size effect of magnetic nanocrystals and their utilization for cancer diagnosis via magnetic resonance imaging," *… Am. Chem. …*, 2005.

[104] H. Wunsch, W. T. Linde-Zwirble, D. C. Angus, M. E. Hartman, E. B. Milbrandt, and J. M. Kahn, "The epidemiology of mechanical ventilation use in the United States.," *Crit. Care Med.*, vol. 38, no. 10, pp. 1947–53, Oct. 2010.

[105] P. Webb, "Air Temperatures in Respiratory Tracts of Resting Subjects in Cold," *J Appl*

Physiol, vol. 4, no. 5, pp. 378–382, Nov. 1951.

[106] J. Walker and R. W. Jr, "Heat and water exchange in the respiratory Tract.," *Surv. …*, 1962.

[107] J. Rathgeber and K. Zuchner, *Foundations of artificial respiration*, Ebelsbach. 1999.

[108] F. J. Hilgers, A. H. Ackerstaff, N. K. Aaronson, P. F. Schouwenburg, and N. Van Zandwijk, "Physical and psychosocial consequences of total laryngectomy.," *Clin. Otolaryngol. Allied Sci.*, vol. 15, no. 5, pp. 421–5, Oct. 1990.

[109] R. J. Scheenstra, "The influence of heat and moisture exchangers on tracheal climate in laryngectomized individuals: toward optimal pulmonary rehabilitation," AMC-UvA, 2011.

[110] ISO, "ISO 9360-2:2001 Anaesthetic and respiratory equipment -- Heat and moisture exchangers (HMEs) for humidifying respired gases in humans -- Part 2: HMEs for use with tracheostomized patients having minimum tidal volumes of 250 ml." 2001.

[111] P. P. Kleemann, "Humidity of anaesthetic gases with respect to low flow anaesthesia.," *Anaesth. Intensive Care*, vol. 22, no. 4, pp. 396–408, Aug. 1994.

[112] K. W. Fritz, A. Osterhaus, and J. Mottner, "The humidification of anesthetic gases during anesthesia using heat and moisture exchangers.," *Anaesthesiol. Reanim.*, vol. 17, no. 3, pp. 133–44, Jan. 1992.

[113] L. Drägerwerk, "Deutsches Patentamt Patentschrift 1 169615."

[114] J. D. Ricard, E. Le Mière, P. Markowicz, S. Lasry, G. Saumon, K. Djedaïni, F. Coste, and D. Dreyfuss, "Efficiency and safety of mechanical ventilation with a heat and moisture exchanger changed only once a week.," *Am. J. Respir. Crit. Care Med.*, vol. 161, no. 1, pp. 104–9, Jan. 2000.

[115] J. Gallagher, J. E. M. Strangeways, and J. Allt-Graham, "Contamination control in long-term ventilation.," *Anaesthesia*, vol. 42, no. 5, pp. 476–481, May 1987.

[116] C. Jackson and A. R. Webb, "An evaluation of the heat and moisture exchange performance of four ventilator circuit filters.," *Intensive Care Med.*, vol. 18, no. 5, pp. 264–8, Jan. 1992.

[117] L. Thomachot, X. Viviand, S. Arnaud, C. Boisson, and C. D. Martin, “Comparing two heat and moisture exchangers, one hydrophobic and one hygroscopic, on humidifying efficacy and the rate of nosocomial pneumonia.,” *Chest*, vol. 114, no. 5, pp. 1383–9, Nov. 1998.

[118] J.-Y. Fagon, J. Chastre, Y. Domart, J.-L. Trouillet, J. Pierre, C. Darne, and C. Gibert, “Nosocomial Pneumonia in Patients Receiving Continuous Mechanical Ventilation.,” *Am. Rev. Respir. Dis.*, Dec. 2012.

[119] M. Fartoukh, B. Maitre, S. Honoré, C. Cerf, J.-R. Zahar, and C. Brun-Buisson, “Diagnosing pneumonia during mechanical ventilation: the clinical pulmonary infection score revisited.,” *Am. J. Respir. Crit. Care Med.*, vol. 168, no. 2, pp. 173–9, Jul. 2003.

[120] J. W. Olds, A. L. Kisch, B. J. Eberle, and J. N. Wilson, “Pseudomonas aeruginosa respiratory tract infection acquired from a contaminated anesthesia machine.,” *Am. Rev. Respir. Dis.*, vol. 105, no. 4, pp. 628–32, Apr. 1972.

[121] A. Kramer, R. Kranabetter, J. Rathgeber, K. Züchner, O. Assadian, G. Daeschlein, N.-O. Hübner, E. Dietlein, M. Exner, M. Gründling, C. Lehmann, M. Wendt, B. M. Graf, D. Holst, L. Jatzwauk, B. Puhlmann, T. Welte, and A. R. Wilkes, “Infection prevention during anaesthesia ventilation by the use of breathing system filters (BSF).,” *GMS Krankenhaushygiene Interdiszip.*, vol. 5, no. 2, Jan. 2010.

[122] A. R. Wilkes, “Heat and moisture exchangers and breathing system filters: their use in anaesthesia and intensive care. Part 2 – practical use, including problems, and their use with paediatric patients,” *Anaesthesia*, vol. 66, no. 1, pp. 40–51, 2011.

[123] “ISO 12500-1:2007 - Filters for compressed air -- Test methods -- Part 1: Oil aerosols.” [Online]. Available: http://www.iso.org/iso/iso_catalogue/catalogue_tc/catalogue_detail.htm?csnumber=41150. [Accessed: 15-Mar-2016].

[124] D. Bartis and J. Pongrácz, *Three dimensional tissue cultures and tissue engineering*. 2011.

[125] N. Z. and X. Chen, *Advances in Biomaterials Science and Biomedical Applications*. InTech, 2013.

[126] J. J. Panda and V. S. Chauhan, “Short peptide based self-assembled nanostructures:

implications in drug delivery and tissue engineering," *Polym. Chem.*, vol. 5, no. 15, p. 4431, Jul. 2014.

[127] A. Zucchelli, M. L. Focarete, C. Gualandi, and S. Ramakrishna, "Electrospun nanofibers for enhancing structural performance of composite materials," *Polym. Adv. Technol.*, vol. 22, no. 3, pp. 339–349, 2011.

MATERIALS AND METHODS

3.1 Raw materials

Several polymeric component were used in the present work as described below. Type I collagen (Coll) extracted from equine tendon, purified and telopeptide-free, and supplied as acetic gel (an aqueous acetic buffer solution with pH = 3.5 containing 1 wt% of pure collagen) was purchased from Opocrin S.p.A., Italy. Type A gelatin from porcine skin, ~280 g Bloom, was purchased from Sigma-Aldrich (S. Louis, MO, USA). Low molecular weight chitosan (degree of deacetylation between 80-85%), medium molecular weight chitosan (degree of deacetylation between 75-85%), high molecular weight chitosan (>75% deacetylated), sodium alginate and cellulose acetate (average M_n ~50,000), were purchased from Sigma-Aldrich.

Calcium hydroxide (≥95.0% pure), sodium hydroxide (≥98% pure), chloridric acid (37% pure), solforic acid (95-98% pure), acetic acid (≥99.7% pure), nitric acid (65% pure), magnesium chloride hexahydrate (≥99% pure), iron(III) chloride hexahydrate (97% pure), iron(II) chloride tetrahydrate (≥99% pure) and calcium chloride (≥97% pure) were all provided by Sigma-Aldrich.

Finally 1,4-butanediol diglycidyl ether (BDDGE, 95 wt.% pure) and 2,4,6-trinitrobenzenesulfonic acid (TNBS, 1 M in H_2O) were purchased from Sigma-Aldrich, genipin (98 wt.% pure) was purchased from Wako Chemicals (USA) and phosphate buffered saline (PBS) was purchased from Gibco (USA).

3.2 Material processing

3.2.1 Freeze-drying process

Porous three-dimensional scaffolds and filters were manufactured by unidirectional freeze-drying technology (se cap. 2.5). Unless differently stated, the freezing ramp was 1 °C/min until -40 °C and heating ramps were performed from -40 °C to -10°C at 5 °C/h and from -10 °C to 15 °C at 1 °C/h under vacuum conditions (at least P = 0.1 mbar). The equipment employed in the present work was a 5Pascal LIO-1000P.

3.2.2 Electrospinning process

Regarding the deposition of thin porous layers electrospinning technique was used. After preparing the electrospinnable dispersion, it was electrospun using a 10 ml syringe, a 21 G nozzle and a needle-collector distance of 15 cm. The fleeces were spun with a feed-rate of 12 mL/h and 7.0 kV of voltage, at 21 °C and a relative humidity of 26%.

Electrospun materials were produced in Friedrich-Schiller-Universität Jena Otto-Schott-Institut für Materialforschung (Jena, Germany) with a home-made instrument.

3.3 Analytical Techniques

3.3.1 Thermogravimetric Analysis (TGA)

Thermogravimetric analysis is a widely used technique where the variation mass of a sample is measured as a function of temperature while the material is heated following a controlled temperature rising in a controlled atmosphere. During this measurement mass loss is often explained by volatile components and/or volatile degradation products which are carried away by the gas flow. The analyzer usually consists of a high-precision balance with a pan loaded with the sample. The sample is placed in a heated oven and the atmosphere may be purged with an inert gas to prevent oxidation or other undesired reactions. Once recorded, the weight loss curve may require digital elaboration: a derivative weight loss curve can be used to define the point at which weight loss

is most apparent. Data regarding mass loss process obtained from TGA is useful to characterize a polymer's thermal stability, composition, and extent of cure.

In this study analysis were carried out on samples weighing 8-10 mg into alumina crucibles, from RT to 800°C for non-mineralized samples and to 1100 °C for mineralized samples at 10°C/min. The equipment employed was a Netzsch Gerätebau Jupiter STA (Simultaneous Thermal Analysis) 449C (Selb, Germany).

3.3.2 Differential Thermal Analysis (DTA)

DTA is a thermoanalytical technique used to study phase transitions of materials. During this analysis a heating rate is setting and the difference in the increasing of temperature of an empty reference pan and a sample is measured.

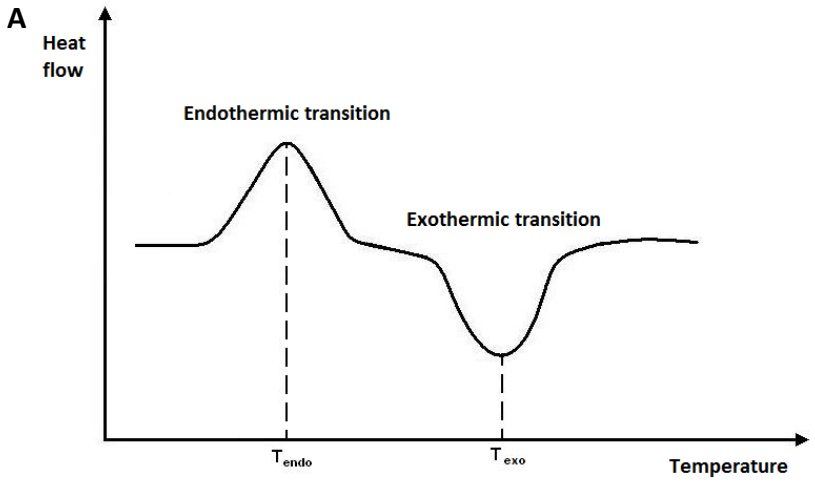

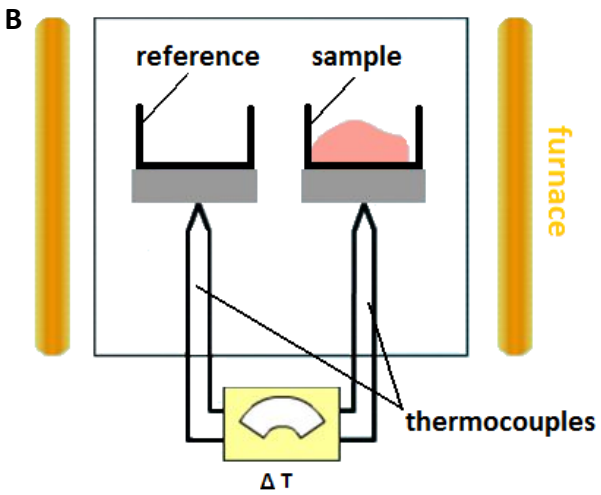

Figure 3.1 *DTA thermogram (A) and scheme of a differential temperature analyzer (B).*

Thus in this way it's possible to study the thermal effects on the material because a difference in temperature is indicative of endothermic or exothermic transformations that have occurred. An example of DTA pattern of heat flux versus temperature is shown in Fig. 3.1A. A DTA apparatus consists of sample and reference holders comprising thermocouples and a furnace (Fig. 3.1B).

In this PhD project about 10 mg of sample were placed in alumina pans and subjected to heating scans at 10 °C/min from room temperature to a 1000°C. DSC measurements were carried out by using a Netzsch Gerätebau Jupiter STA (Simultaneous Thermal Analysis) 449C (Selb, Germany.

3.3.3 X-Ray Diffraction (XRD)

X-ray diffraction is a non-destructive analytical technique which reveals information about the crystallographic structure, crystallite size, and preferred orientation in polycrystalline or powdered solid samples. This technique is based on observing the scattered intensity of an x-ray beam hitting a sample as a function of incident and scattered angle, polarization, and wavelength or energy. X-ray wavelength is comparable with

inter-atomic distances (~150 pm) and thus is an excellent probe for this length scale. Powder diffraction is commonly used to identify unknown substances, by comparing diffraction data against a database of International Center for Diffraction Data (ICDD), or to characterize heterogeneous solid mixtures to determine relative abundance of crystalline compounds. Powder diffraction is also a common method for determining strains in crystalline materials. The great advantages of the technique are the simplicity of sample preparation, the rapidity of measurement and the ability to analyze mixed phases.

Thanks to X-ray wavelength (λ between 10 nm and 1 pm), when this kind of beam hits an atom, the electrons around the atom start to oscillate with the same frequency as the incoming beam. As consequence of the oscillation the electrons will diffuse the incidence radiation in all the directions; this phenomenon is known as the Rayleigh scattering (or elastic scattering). These re-emitted wave fields interfere with each other destructively in the most of the directions, but if some atoms are arranged in a crystalline cell, so in a regular pattern, in a few directions we will have constructive interference (Fig. 3.2). Miller indices (hkl) was usually used to indicate which of the various intersection planes of the mineral's crystal cell refers the constructive interference (d_{hkl}: interplanar distance).

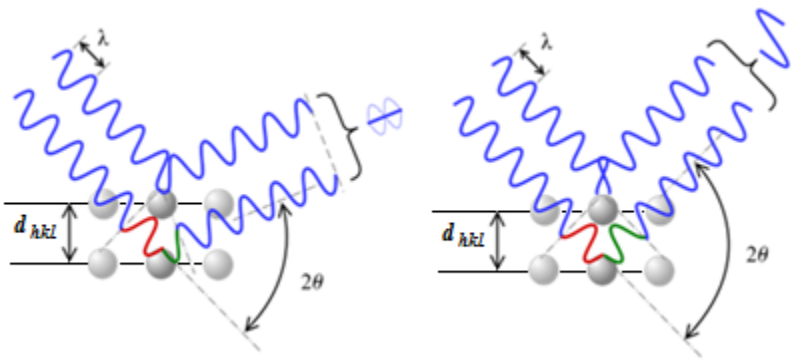

Figure 3.2 *Constructive and destructive interference in Rayleigh scattering of X rays*

The overlapping waves will give rise a well defined scattered X-ray beams leaving the sample at various directions. The resulting wave interference pattern shown as diffracted intensity in function of diffraction angle (2θ) is the basis of diffraction analysis, as

both the positions and the relative intensity of the lines are indicative of a particular phase and material.

In contrast to a crystalline pattern consisting of a series of sharp peaks, amorphous materials produce a broad background signal. Many polymers, organic molecules or inorganic glasses usually exhibit this kind of pattern, but often also inorganic nanostructured crystalline phases can contain also an amorphous fraction.

Most powder diffractometers use the Bragg-Brentano parafocusing geometry. In the parafocusing arrangement (Fig. 3.3), the incident beam produced by the X-ray tube and the detector of the diffracted beam move on a circle that is centered on the sample. Divergent X-rays from the source hit the sample at different points on its surface but during the diffraction process the X-rays are refocused at the detector slit.

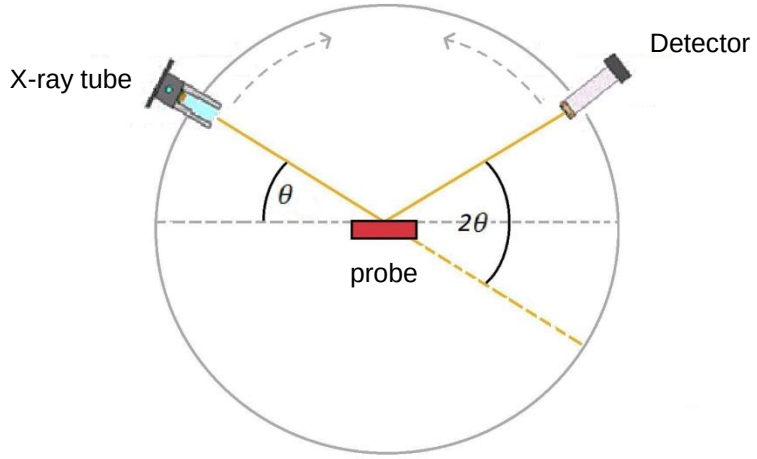

Figure 3.3 *Scheme of a Bragg-Brentano parafocusing difractometer.*

During this work the X-ray diffraction patterns of the samples were recorded in the 2θ range from 10° to 60° with a step size (2θ) of 0.02° and a counting time of 1s. The equipment adopted was a D8 Advance Diffractometer, Bruker (Karlsruhe, Germany) equipped with a Lynx-eye position sensitive detector using CuKa radiation (λ= 1.54178 Å) generated at 40 kV and 40 mA.

3.4.4 Fourier-Transform Infrared Spectroscopy (FTIR)

Infrared spectroscopy is the subset of spectroscopy that deals with the region of the electromagnetic spectrum between 14000 and 10 cm^{-1} (from near to far-IR). The signal is acquired in the time domain, and through the Fourier transform it's possible to obtain the spectrum in function of frequencies.

Infrared spectroscopy exploits the fact that at specific frequencies the interaction with the radiation causes vibrational transitions (Fig. 3.4). The absorption frequencies can be in a first approach related to the strength of the bond and the mass of the atoms at either end of it and around. Thus, the frequencies and the intensity of absorption can be associated with a particular bond type and can be used for the characterization of very complex mixtures.

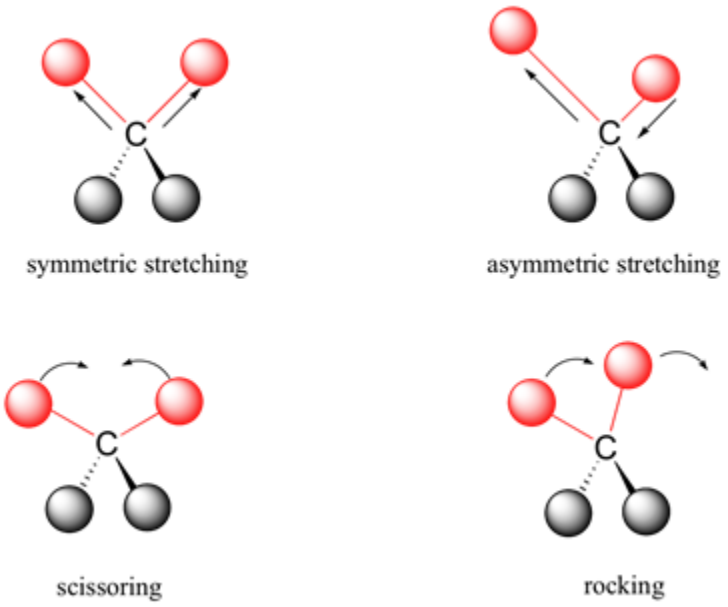

***Figure 3.4** Possible vibrations detected by infrared spectroscopy*

The method employed for sample preparation is to grind finely (to remove scattering effects from large crystals) about 2 mg of the sample with 100 mg of anhydrous potassi-

um bromide, which is used also as a reference. This powder mixture is then pressed at 8000 psi into 7 mm diameter disc to form a translucent pellet through which the beam of the spectrometer can pass through. All the spectra are the average of 64 spectra, acquired at room temperature in the range of 400-4000 cm^{-1} at a resolution of 1 cm^{-1}.

The equipment employed in the present work was a Thermo Nicolet-Avatar 320 FT-IR.

3.3.5 Scanning Electron Microscopy (SEM)

The scanning electron microscope is a microscope which exploits as source radiation a high energy beam of focused electrons that hit the surface of the sample. The primary beam is not fixed, but scan in sequence, recording point by point, a small area of the sample at a time. The type of signals gathered in a SEM vary and can include secondary electrons, characteristic x-rays, and back scattered electrons (Fig. 3.5). In particular, the secondary electrons are generated from anaelastic interactions of the beam with the valence electrons of the atoms of the sample. They emerge from the sample with a very low energy so they can be detected only those products very close to the surface of the sample (from less than 100 nm to around 5 µm into the surface).

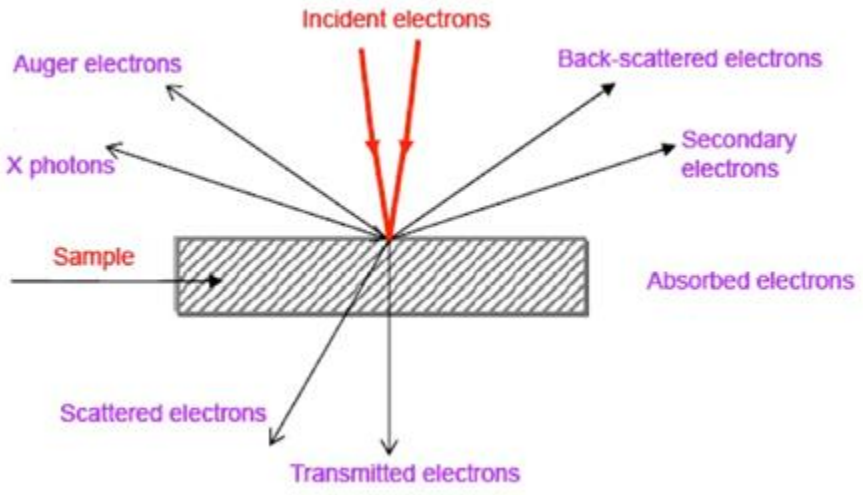

Figure 3.5 *Signals produced by the interaction of the electron beam with the sample*

The intensity of the secondary electron emission is therefore very sensitive to the angle of incidence and to the surface structure of sample. For these reasons the SEM primary use mode, secondary electron imaging, is capable of producing high-resolution images of a sample surface, it has wide range of magnifications and great depth of field yielding a characteristic three-dimensional appearance useful for a material's morphology study.

To carry out a SEM analysis it's necessary a conductive sample, at least at the surface, and electrically grounded. For this reason nonconductive sample, like most of those used in this project, are usually set on a metal stub and coated with a conducting material, like gold, deposited at the top of the sample like an ultrathin coating with a low-vacuum sputter coating. The measure must usually take place under high vacuum ($2 \cdot 10^{-5}$ Torr), to avoid a rapid spread of the electron beam by atmosphere gas, but in ESEM instrument (Environmental Scanning Electron Microscope) low-vacuum (1–50 Torr) with an high relative humidity are possible.

The equipment employed in the present work was a ESEM FEI Quanta 200, Felmi-ZFE (Austria).

3.3.6 Inductively Coupled Plasma Atomic Emission Spectroscopy (ICP-AES)

ICP-AES, is a type of emission spectroscopy that uses a plasma to produce excited atoms that emit electromagnetic radiation at characteristic wavelengths for each element. The intensity of the radiation is proportional to the concentration of the element, which is obtained through a previous calibration obtained with opportune standard solutions. An inductively coupled plasma for spectrometry is sustained in a torch, the end of which is placed inside an induction coil supplied with a radio-frequency electric current. A flow of argon gas is introduced and an electrical spark is applied for a short time to introduce free electrons into the gas stream.

These electrons are then accelerated and sometimes collide with argon atoms, cause the lost by argon of one of its electrons. The process continues until it is obtained an highly ionized gas with a number of electrons and ions of the same so as to be a good electrical conductor, a plasma. The samples to be analyzed are firstly solubilized and then introduced into the hot region through an atomizer. The temperature of the plasma is very high, of the order of 10.000 K, so that the atomization of the sample is nearly complete, improving the accuracy of the analysis. Moreover, the carrier gas is inert (usually argon), so preventing the formation of oxides. As a droplet of atomized sample enters the central channel of the ICP, it evaporates and any substance that were dissolved in the liquid vaporize and then break down into atoms. At the temperatures prevailing in the plasma a significant proportion of the atoms of many chemical elements are ionized, each atom losing its most loosely-bound electron to form a singly charged ion. The emission radiation is then collected by the monochromator and linked to concentration by calibration lines made using standard solutions at concentrations around the expected.

The equipment employed in the present work was a Liberty 200, Varian (Clayton South, Australia)and, prior to the analysis, the amount of samples required to reach 20 mg of inorganic component was dissolved in 2 mL of HNO_3, and the solution volume was increased up to 100 mL with deionized water. Reference solutions were prepared by mixing standard solutions containing the investigated atoms and an equally diluted solution of nitric acid was also analized and the corresponding spectrum subtracted by the experimental one.

3.4 Characterization methods

3.4.1 Magnetic measurements

Magnetic susceptibility

In magnetic materials free unpaired electrons give rise to magnetic forces which are attracted to a strong magnetic field, and the strength of these attractive forces are in direct proportion to the number of free electrons. During the magnetic susceptibility measurement, the interaction between a permanent magnet and the weight being tested is determined as a weight using a high-resolution mass comparator to estimate the magnetization vs magnetic field (M vs H) curve.

After the analysis the recorded curve can be decomposed into the sum of the paramagnetic (linear) contribution and ferromagnetic/super-paramagnetic (S-shaped) contribution (Fig. 3.6).

Magnetization measurements were performed in two different equipment. The fist equipment is a Superconducting Quantum Interference Device (SQUID) magnetometer Quantum Design (San Diego, CA), operating at temperature of 1.8−350 K with a maximum applied magnetic field (H) of 7T. About 20 mg of material were measured in a magnetic field cycle from −2T to +7T at temperature of 310 K (close to the physiological temperature).

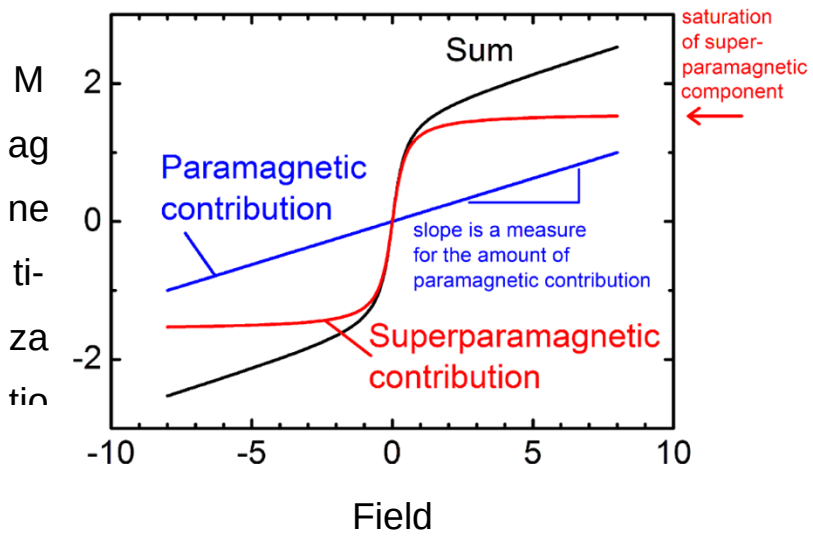

Figure 3.6 *Example decomposition of a superparamagnetic measured curve (black), the paramagnetic contribution (blue) and super-paramagnetic contribution (red)*

The second type of measurements were carried out by vibrating sample magnetometry (VSM) using a magnetometer MICROMAG3900, Princeton Measurements Corp. (Westerville, USA) on about 50 mg of material.

Magnetic susceptibility tests were carried out in collaboration with HZDR (Helmholtz-Zendrum Dresden Rossendorf; Dresden, Germany) and Friedrich-Schiller-Universität Jena Otto-Schott-Institut für Materialforschung (Jena, Germany).

Hyperthermic effect

Measurement of magnetically induced heating were performed by the home-made set-up RLC to generate a variable magnetic field. Because of the small size of the materials and powder tested, a 3-cm-diameter coil was used. The main coil (Fig. 3.7A), where materials are placed in, will be responsible of the alternating magnetic field. With this apparatus, to generate a magnetic field of B=3.90 mT at a frequency of 313 kHz it is necessary to apply a voltage of 24 V.

In order to carry out high precision experimental tests, two concentric tubes which will be positioned inside the main coil to isolate the samples from the outside: an external black one to absorb any possible source of radiation, and another one internal partially closed where the sample will be placed during experimental tests (Fig.3.7B, C, D). The transparent tube include an internal empty space which consists of different passages specifically designed to cool down the internal area with air.

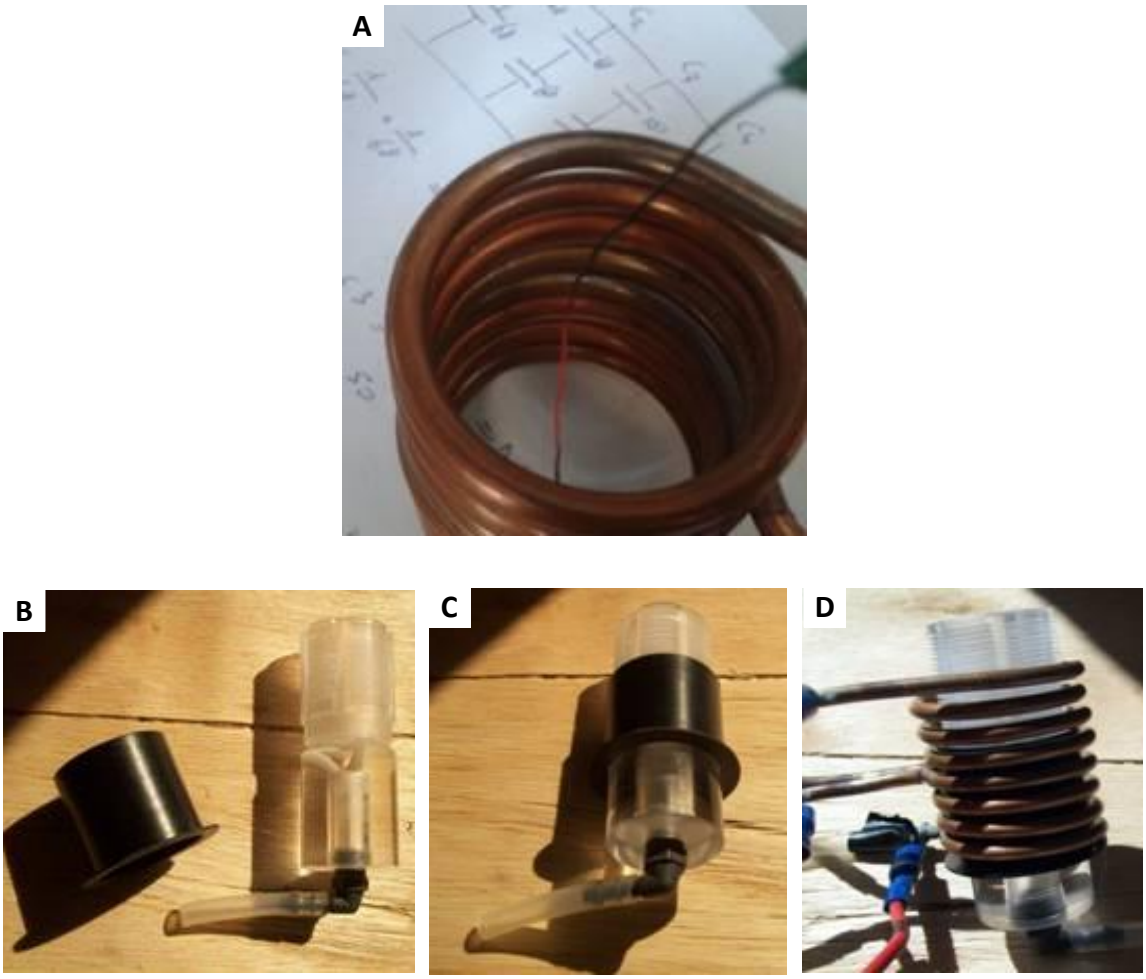

***Figure 3.7** A: Iron wire heated inside the coil after a few seconds as example. B: Transparent and black tubes. C: Tubes assembled. D:Tubes assembled inside the coil.*

Infrared thermometer (RS-1327 Infrared Thermometer, RS Components, United Kingdom) with a field of view 10:1 and temperature range from -20°C to 500°C (Fig. 1.1.6) was used to determine the sample temperature.

Hyperthermic tests were carried out in collaboration with Pollution Srl (Budrio, Italy), with a circuit designed and constructed directly in its R&D laboratory.

3.4.2 Swelling and degradation test

For the evaluation of the swelling degree cylindrical samples (Ø = 2cm, h = 1cm) were weighed, put in phosphate buffered saline at 37° and, at various times, drained superficially by gentle contact with a filter paper and weighed again. The swelling percentage was calculated as:

$$\% \, Sw = \frac{W_s - W_i}{W_i} x \, 100$$

where W_i is the initial weight of dry samples and W_s are the samples weights after swelling.

For the degradation degree, at the same way, the samples were weighed, put in saline solution at 37° and at various times they where removed and weighed again after drying at 37° for 48 h in a vented oven[1]. The degradation degree as percentage of weight remaining was calculated as:

$$\% \, Deg = 100 - \frac{W_i - W_d}{W_i} x \, 100$$

where W_d are weights of dried samples at the end of the degradation test.

Each test consisted of three replicate measurements and result was expressed as an average value.

3.4.3 Wettability measurements

For a good knowledge of the solid–liquid interfacial tensions, so the wetting behavior of water or other solvents on a surface, static contact angle is widely used.

Contact angle measurement is defined geometrically as the angle formed by a liquid at the three-phase boundary where a liquid, gas and solid intersect. It is easily performed by dropping a fixed amount of solvent onto a solid sample and by direct measurement of the tangent angle of a drop standing on the surface of the material. Small contact

angles (θ<90°) correspond to high wettability, while large contact angles (θ>90°) correspond to low wettability (Fig.3 .8).

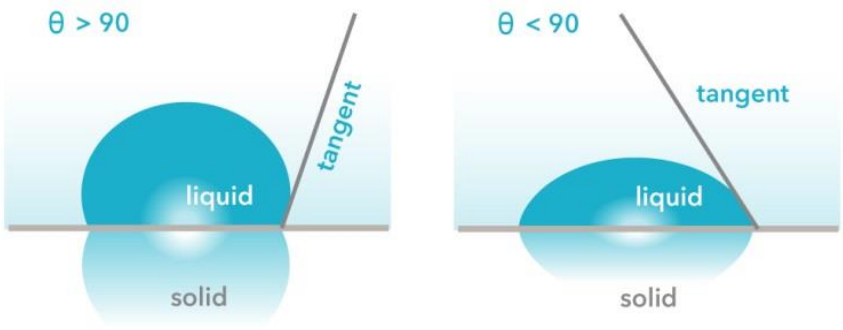

***Figure 3.8** Illustration of contact angles formed by sessile liquid drops on a smooth homogeneous solid surface.*

The water affinity was tested using the static contact angle on the materials in the form of films. In order to produce non porous films suitable for the measurements, wet materials (before cross-linking in the case of gelatin-chitosan mixture) was cast into wells of 24-wells cell-culture multiwell plates and dried at room temperature. Distilled water of approximately 1 µl was dropped onto the surface of the films and the static contact angle of the drops were measured using a tensiometer Video-Based Optical Contact Angle Meter OCA 15+, Innovent (Germany). All data presented were the mean values of five measurements and result was expressed as an average value[2].

3.4.4 Bio-compatibility test

The cells used for the cytotoxicity tests are mouse cells Balb/c 3T3 clone A31 (ATCC, CCL 163) or mouse mesenchymal stem cells (mMSCs; Invitrogen). Some of cell culture experiments illustrated in this Ph.D thesis were carried out in collaboration with LEMI - Laboratoire d'Evaluation des Materiels Implantables (Martillac, France).

Cell viability assay. In order to make an initial assessment of cell viability we used a qualitative test, the Live&Dead viability assay; this is a two-color fluorescence test that permits the simultaneous determination of live and dead cells.

Cylindrical scaffolds, 8.00 mm diameter and 4.00 mm high, were sterilized with ethanol and by UV irradiation. Samples were placed one per well in a 24-well plate and pre-soaked in culture medium. Each scaffold was seeded by carefully dropping 20 µl of cell suspension (5.0 x 10^4 cells) onto the upper scaffold surface, allowing cell attachment for 30 minutes, before addition into each well of cell culture.
At a set time two probes must be added to the cell couture, the calcein acetossimetile-stere (CAM) and the ethidium homodimer (EtD) (Molecular Probes; Live&Dead® Viabil-ity/Cytotoxicity Kit). After the incubation the CAM is converted to the fluorescent form (intense green, $\lambda_{em} \approx$ 520nm) by esterase present in metabolically active, so live, cells; the EtD instead can permeate only damaged plasma membranes of dead cells and bind-ing nucleic acids it becomes fluorescent (bright red, $\lambda_{em} \approx$ 635nm)[3].

Images were acquired by an inverted Ti-E fluorescence microscope (Eclipse, Nikon), us-ing FITC filters (~520nm) for CAM and TRITC filter (~650nm) for the EtD. The qualitative analysis was performed on images with the same fire and overlapping field (FITC/TRITC), at 10x magnification after 7 days of culture.

Cytotoxicity test as direct contact. The first step in biocompatibility evaluation is the study of materials cytotoxicity which was assessed according to the ISO 10993-5 stand-ard[4].

Cells are seeded in multiwell plates (6 wells, 10 cm², Nunc) at the starting density of 35 x 10^3 cells/cm² in culture medium; cultures are incubated for 24 hours. Cylindrical scaf-folds, 18 mm diameter and 5 mm high, were sterilized by γ-ray irradiation and then test material is carefully placed in direct contact with the cells in the center of each replicate wells. Wells are then incubated over a 24 hour period and subsequently for another 2 minutes with Trypan blue (Sigma Aldrich), a blue dye which can penetrate only into the

dead cells' cytoplasm; thereafter dead cells (blue) and living cells (uncoloured) are counted using a hemacytometer.

All cell-handling procedures were performed in a sterile laminar flow hood. All cell-culture incubation steps were performed into an humidity controlled incubator at 37°C with 5% CO_2. Three replicates of the test material are carried out.

3.4.5 Pressure-drop and moisture exchange measurements

The equipment used in this work (Fig. 3.9) is based on the lung model described in ISO 9360[5] and consists of two separate circuits. The first simulates a patient model and includes a 2 liters rubber bag, a heated humidifier (MR428, Fisher & Paykel, Auckland, New Zealand), a precision weighing device and one bidirectional flow control valve and both inspiratory and expiratory air lines. The inspiration and expiration lines inside the simulated patient are separated because in this way it was possible to measure accurately the absolute humidity of both lines with two capacitance-hygrometers (313-S, PCE Instruments, Germany). The secondary circuit basically consists of a mechanical ventilator (Lifecare PLV-100, Philips Respironics, The Netherlands), which generates a bidirectional sinusoidal flow. The flow delivered by the ventilator provokes a continuous low/high pressure effect inside the rigid reservoir which, in turns, simulates the typical patient's respiratory cycle on the primary circuit. The dry air flowing in the inspiratory air line is forced to pass through the filter and through the first psychrometer (where the absolute humidity of the inspired gases is measured) before filling the simulated lung. During the expiratory phase, the air is sent back through the heated humidifier (T=37°C), and the second psychrometer (where the absolute humidity of the expired gases, AH_{exp} is recorded), becoming saturated by the time it reaches the filter. Three tests were made for each sample and each test lasted two hours.

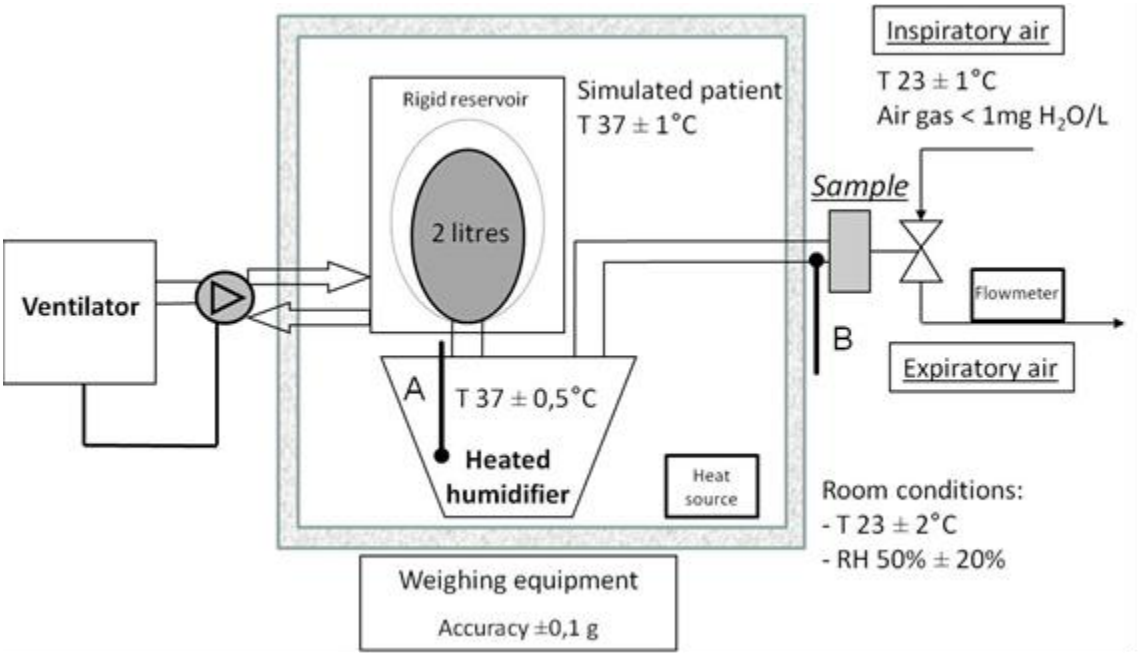

Figure 3.9 *Schematic diagram of the gravimetric method based on ISO 9360 for testing HME devices. A, B: temperature probes.*

The performance of the sample was determined by measuring the mass of water lost from the patient model, assessed with the weight differences of the test apparatus over a given period. Therefore, knowing the value of the absolute humidity of the simulated expired gases (AH_{exp}), it was possible to calculate the moisture output returned to the patient:

$$\text{Moisture output} = AH_{exp} - \text{moisture loss.}$$

Additionally, the humidity efficiency was also calculated with the percentage recovery of absolute humidity (AH_{rec}) proposed by some authors[6]:

$$AH_{rec}\ (\%) = (\text{moisture output} / AH_{exp}) \times 100$$

The pressure drop of each sample was recorded before and after preconditioning the sample in the test apparatus for two hours. A flow-rate of 60 L/min with dry air was used and resistance across the sample holder was measured by an electronic differential manometer (2080P, Digitron, United Kingdom).

Pressure drop and moisture exchange measurement were carried out in collaboration with Pollution s.r.l. (Budrio).

3.4.6 Amine cross-linking degree

In order to evaluate the cross-linking degree which involves polymer primary amine groups, it has been used a method to determine the primary amine residue content of a material[7].

This method is based on the reaction of TNBS (2,4,6-trinitrobenzenesulfonic acid) with primary any primary amine compound, showed in Fig. 3.10.

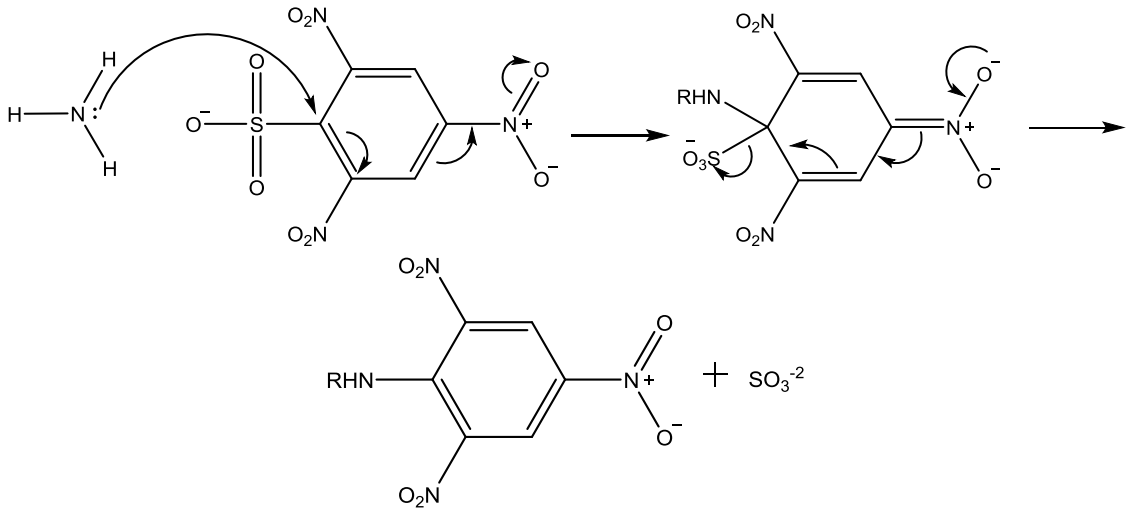

Figure 3.10 *Reaction scheme of TNBS with a generic primary amine group.*

TNBS undergoes a nucleophilic substitution reaction with amine compound replacing the sulphite group. TNBS reacts at alkaline pH with terminal α-amino groups as well as side-chain ε-amino groups and the reaction product strongly absorbs at 345 nm. No re-

action takes place in an acidic medium, this is well suited for a blank. TNBS is added to the primary amine containing target molecule in a large excess, that is respectively 10:1. Unreacted TNBS is masked by adding concentrated hydrochloric acid.

Specifically, using 50 mL Greiner test tubes, 10.0 mg of materials was added into each of the 4 used tubes. At 3 of these tubes (used as replicate) 1 mL of $NaHCO_3$ 4 wt% and then 2 mL of TNBS 1 wt% each were added, while in the last tube 1 mL of $NaHCO_3$ 4 wt%, 3 mL of and then 2 mL of hydrochloridric acid 37 wt% and then TNBS 1 wt% each were added. All the test tubes was shacked in a waterbath at 37°C for 3 hours and then at the first 3 tubes 10 mL of hydrochloridric acid 37 wt% and 5 mL of milli-Q water were added, while in the last tube 3 mL of hydrochloridric acid 37 wt% and 5 mL of milli-Q water were added. All the test tubes was shacked in a waterbath at 37°C for 20 hours and then cooled down to room temperature. The yellow solution was diluted 20 times before UV-Vis spectrometry analysis. The instrument used during this work was a Lambda 35 UV/VIS Spectrometer, Perkin Elmer Instrument (USA) and the spectra was collect from 200 to 800 nm at 240 nm/min.

Through an absorbance vs concentration calibration curve it was possible to quantify the free primary amines present in the samples. The non-crosslinked material was used as the 100% free amine standard, while for each sample was chemically simulated a fully cross-linked material (the forth tube where acidic medium was created before the TNBS added) as 0% free amine standard.

3.4.7 Determination of bactericidal and/or bacteriostatic capability

The evaluation of the ability of materials to counter the growth of bacteria and molds was conducted as quantitative surface test carried out in according with the UNI EN 13697:2001 standard method procedure[8] for the evaluation of bactericidal properties for a filter.

The *in vitro* test was conducted using strains of Escherichia coli (gram-negative), Pseudomonas aeruginosa, Staphylococcuus aureus (gram-positive, bacteria belonging to the human-derived genus), Staphylococcus epidermidis, Candida albicans (yeast) and Aspergillus niger (mold) as microorganisms tested. The tests were conducted at 20±1 °C, with reagents and culture media specific for each strain and with a contact time of 1, 4, 24 and 72 hours.

Each sample surface under study (upper and inner surface) has separately been contaminated with an inoculum of 1 mL of each microbial suspension (microbial title of 10^6 cfu/mL for bacteria and 10^5 cfu/mL for fungi). Specifically the chosen surface was artificially contaminated with the test organisms in the presence of a specific culture media; alongside these test, control plates without any testing material are also prepared. After the prescribed contact time, the test product is neutralized for ensuring that the specified contact time is adhered to and surviving bacteria were counted after 72 hours incubation at 37 °C. The performance of the product is determined by calculating a $\log_{10}$ reduction factor using the number of organisms recovered from the test materials and the number recovered from the control plates.

3.5 References

[1] V. Chiono, E. Pulieri, G. Vozzi, G. Ciardelli, A. Ahluwalia, and P. Giusti, "Genipin-crosslinked chitosan/gelatin blends for biomedical applications.," *J. Mater. Sci. Mater. Med.*, vol. 19, no. 2, pp. 889–98, Feb. 2008.

[2] M. Cheng, J. Deng, F. Yang, Y. Gong, N. Zhao, and X. Zhang, "Study on physical properties and nerve cell affinity of composite films from chitosan and gelatin solutions," *Biomaterials*, vol. 24, no. 17, pp. 2871–2880, Aug. 2003.

[3] P. Decherchi, P. Cochard, and P. Gauthier, "Dual staining assessment of Schwann cell viability within whole peripheral nerves using calcein-AM and ethidium homodimer," *J. Neurosci. Methods*, vol. 71, no. 2, pp. 205–213, Feb. 1997.

[4] "ISO 10993-5:2009. Biological evaluation of medical devices - Part 5: Tests for in vitro cytotoxicity."

[5] "ISO 9360-1:2000. Anaesthetic and respiratory equipment. Heat and moisture exchangers (HMEs) for humidifying respired gases in humans - Part 1: HMEs for use with minimum tidal volumes of 250 ml."

[6] J. J. J. Lucato, A. B. Adams, R. Souza, J. A. Torquato, C. R. R. Carvalho, and J. J. Marini, "Evaluating humidity recovery efficiency of currently available heat and moisture exchangers: a respiratory system model study.," *Clin. (São Paulo, Brazil)*, vol. 64, no. 6, pp. 585–90, Jan. 2009.

[7] R. B. Sashidhar, A. K. Capoor, and D. Ramana, "Quantitation of ϵ-amino group using amino acids as reference standards by trinitrobenzene sulfonic acid," *J. Immunol. Methods*, vol. 167, no. 1–2, pp. 121–127, Jan. 1994.

[8] "UNI EN 13697-2001. Chemical disinfectants and antiseptics - quantitative non-porous surface test for the evaluation of bactericidal and/or fungicidal activity of chemical disinfectants used in food, industrial, domestic and institutional areas - test meth."

DENTAL REGENERATION

The contemporary mineralization of organic matrix and self-organization of the mineralized products are processes which naturally occurs in the human body during formation of hard tissues. Bio-inspired mineralization and self-assembling processes are the leading thread for the development of scaffolds for dental repair and regeneration which should exhibit physical-chemical-microstructural features mimicking different human tissues, in order to create a tissue conductive system.

Natural polymers like collagen and gelatin, at state of solution or suspensions in presence of ions involved in the biomineralization process, are induced to assemble into fibers by pH variation. In such conditions, the self-assembly of the polymer fibrils/molecules as well as the heterogeneous nucleation of hydroxyapatite were simultaneously induced. Chemically and morphologically graded constructs were designed thus mimicking the multi-tissutal complexus.

In this chapter, the developed materials was explained through two main sections:

I. Dentin-like scaffold
II. Try-layer periodontium-like scaffold, which, in turn, is divided in:
    i. Alveolar bone-like layer
    ii. Periodontium-like layer
    iii. Cementum-like layer

4.1 Dentin

Dentin is an high mineralized tissue (it is composed of about 70% of inorganic components), with a channel like structure traversing its entire thickness from the inner part to

the external. The mineral phase is a non stoichiometric and low crystalline apatite, while the organic component is represented mainly by collagen.

In this work gelatin was used as a promising organic template for the biomineralization process and low-cost material to develop scaffolds for hard tissue regeneration. During my thesis I synthetized dentin-like scaffolds using gelatin biomineralized with magnesium-doped hydroxyapatite (MgHA/Gel) and blending it with alginate (MgHA/Gel+Alg). With a controlled freeze-drying process and alginate cross-linking was possible to develop scaffolds with microscopic channels comparable to dentin tubules appropriate for cell penetration and matrix deposition.

The mineral phase, represented by magnesium-hydroxyapatite (MgHA), was directly nucleated on the gelatin molecules at room temperature during their simultaneous self-assembling; in this way the low crystallinity of the inorganic phase is assured. Magnesium ions were introduced to increase the physio-chemical, structural and morphological affinities of the composite with newly formed natural bone[1]. An high degree of mineralization of gelatin has been sought, in order to mimic the natural chemical composition of the dentin but the material resulted too brittle. After several tests, alginate was chosen as an organic and biocompatible supporting material for the previous described mineralized phase[2] since it makes possible to create a scaffold with a stable 3D morphology without decreasing the overall mineralization degree. The channel-like pores was reached exploiting the freeze-drying technique[3,4] and cross-linking of the alginate with Ca^{2+} ions, which also makes possible to reduce the degradation rate of the scaffold in physiological conditions.

4.1.1 Synthesis processes

The direct nucleation of the inorganic phase on the gelatin molecules was performed following a biologically inspired biomineralization process based on an acid-base neutralization reaction[5]. So firstly 5 g of gelatin powder was dissolved in 100 mL of demin-

eralized water at temperature of 40°C under magnetic stirring for 1 hour. The solution was then cooled at room temperature and 100 mL of H_3PO_4 0.7 M solution were added. After a complete homogenization this solution was dropped in a $Ca(OH)_2$ suspension (9,04 g in 500 mL of distilled water) previously enriched with $MgCl_2 \cdot 6H_2O$ (1.19 g in 25 mL of distilled water) to yield a MgHA/Gel composite material in the ratio 80:20 wt%. The amount of $MgCl_2 \cdot 6H_2O$ was calculated to obtain a Mg/Ca ratio equal to 5 mol%. The drop-wise addition procedure was performed under vigorous magnetic stirring, assuring a slow decrease of pH up to neutrality. At the end of the dripping, the precipitate was left to ripen in the mother liquor for 2 hours. The product was then centrifuged and cross-linked for 24 h at 25 °C adding a 1% w/w BDDGE aqueous solution, setting up a BDDGE/Gelatin ratio equal to 1 wt%. The final product was then washed three times in 1 L of distilled water, freeze-dried and sieved under 300 μm.

The mineralized gelatin-alginate composite was then produced preparing an aqueous dispersion of the previously described MgHA/Gel with a concentration of 20% w/w and an alginate solution 8% w/w produced dissolving the sodium alginate in demineralized water at room temperature and completing the dissolution with 1 hour of sonication. The alginate solution was then mixed with the MgHA/Gel dispersion in a ratio of 1:1, in order to obtain a (MgHA/Gel)/Alginate ratio of 5:2. This mixing was poured into 48-wells cell-culture multiwell plates and freeze-dried obtaining a strong and porous material. Without removing these materials from their molds, to cross-link the alginate and stabilize the porous structure it was added 1 mL of 1M calcium chloride solution for each; at this concentration the calcium/alginate complexation takes place before the alginate-in-water dissolution so that the interconnected 3D porous microstructure of the scaffolds obtained by the previous freeze-drying could be retained. The materials was then washed from the excess of $CaCl_2$ by placing them 10 times in fresh deionized water, and freeze-dried again to preserve the cylindrical shape and the well aligned porous structure (Fig. 4.1).

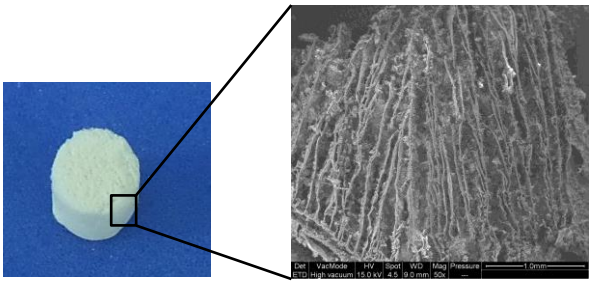

***Figure 4.1** MgHA/Gel+Alg dentin-like scaffold*

Other kind of materials were developed by changing the ration between the components:

a) MgHA(½)/Gel+Alg(½) was made at the same conditions of MgHA/Gel+Alg but mixing, during the blending phase, a MgHA/Gel dispersion with a concentration of 10% w/w and a 4% w/w alginate solution.

b) MgHA/Gel+Gel, was made mixing a 20% w/w dispersion of MgHA/Gel with a 8% w/w gelatin solution; this mixing was cross-linked with BDDGE for 48h at RT before freeze-drying.

c) MgHA/Alg+Alg, was made using the same conditions of bio-mineralization but on alginate matrix; a 20% w/w dispersion of MgHA/Alg was then mixed with a 8% w/w alginate solution; the cross-linking and the freeze-drying processes were the same to those used for MgHA/Gel+Alg.

The material MgHA/Gel+Alg was finally chosen as the most promising for in vitro evaluations because of its structure very close to the dentin one and its high stability in physiological environment. As reference material for biological tests not-mineralized samples (Gel/Alg), were made with the same protocol of the mineralized one, but during the blending phase a 10% w/w gelatin solution was mixed with a 4% w/w alginate solution.

4.1.2 Chemical-physical characterization

4.1.2.1 Thermogravimetric Analysis

The overall loss of weight (TG) and its derivative (DTG) undergone by freeze-dried mineralized gelatin and final composite are shown in Fig. 4.2. Thermal decomposition profile of MgHA/Gel alone shows two distinct weight losses; the first, in the rage temperature of 30-150 °C was due to loss of absorbed water, while the second weight loss, occurred between 250 and 550 °C, was attributed to decomposition of gelatin molecules.

The thermogravimetric analysis of the final material, MgHA/Gel+Alg, shows instead three weight losses: the losses due to water evaporation and gelatin molecules decomposition can be overlaid to those of the first thermal profile, while the new weight loss between 200 and supposedly 350°C, may be attributed to the decomposition of alginate[6].

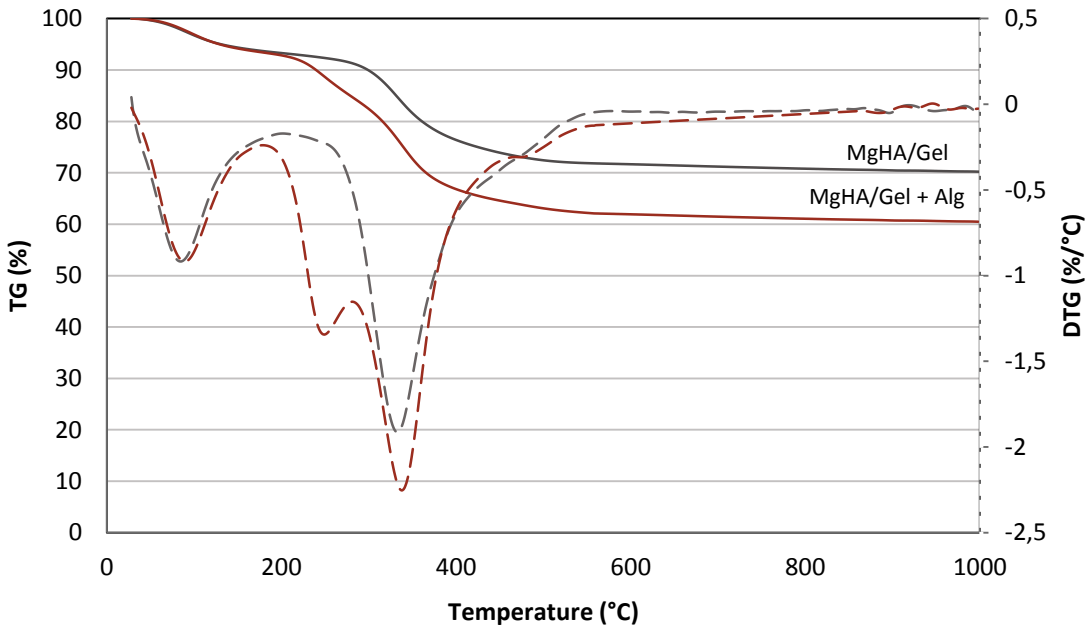

***Figure 4.2** Thermal decomposition profile (TG) and its derivative (DTG) of MgHA/Gel and MgHA/Gel+Alg.*

The thermal decomposition is completed around 600°C, with an overall decrease of organic components of about 35% of the total weight. The final weight ratio between for inorganic/organic composition was so fixed to 60/35 wt.

4.1.2.2 X-Ray Diffraction

XRD diffraction was used to characterize the mineral phase present into the composite, its crystallinity degree and ensure the absence of secondary phases.

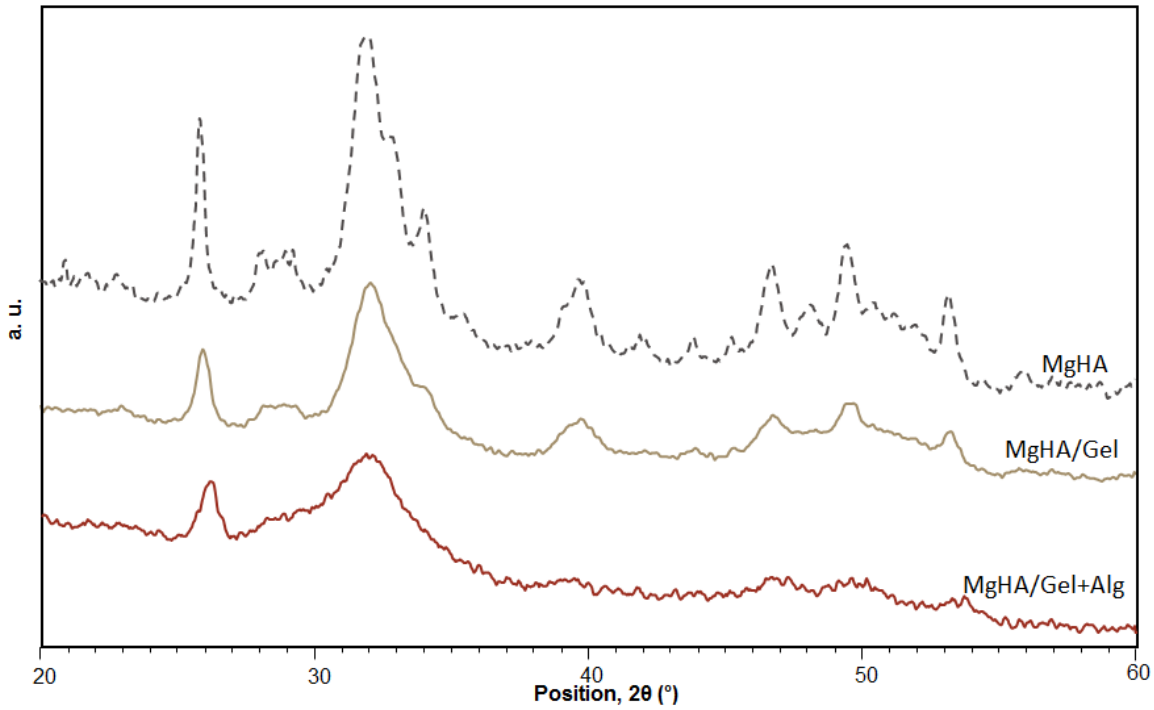

***Figure 4.3** XRD spectra of MgHA/Gel+Alg, MgHA/Gel compared with synthetic MgHA.*

XRD spectra of MgHA/Gel and MgHA/Gel+Alg dried materials are shown in Fig. 4.3 and in both of diffraction patterns hydroxyapatite was identified as a main phase (ICDD card n. 09-0432) and it can be stated that no secondary phases are appreciated (XRD spectra of MgHA prepared with the same neutralization process was shown as example in broken line; the main (hkl) indices for nanometer sized apatite are (002), (102), (210), (211), (112), (300), (202), (130), (222), (213) and (004), which occur at 2θ = 25.9°, 28,2°, 29,1°, 32,0°, 33,1°, 34,1°, 35,7°, 39,9°, 46,7°, 49,5°, 53,2°[4;5]).

About the crystal study, it's easy to see a large broadening of reflections, caused partially by the presence of organic compounds, but also typical for a very low crystalline mineral phase.

4.1.2.3 Fourier-Transform Infrared Spectroscopy

Infrared spectroscopy analysis was used to determine the bands relative to functional groups typically present in the composite components (apatite, gelatin and alginate) and also to study the probable interaction between organic and inorganic phases. Fig. 4.4A shows MgHA/Gel+Alg spectra and compares MgHA/Gel spectrum with the one relative to not mineralized gelatin.

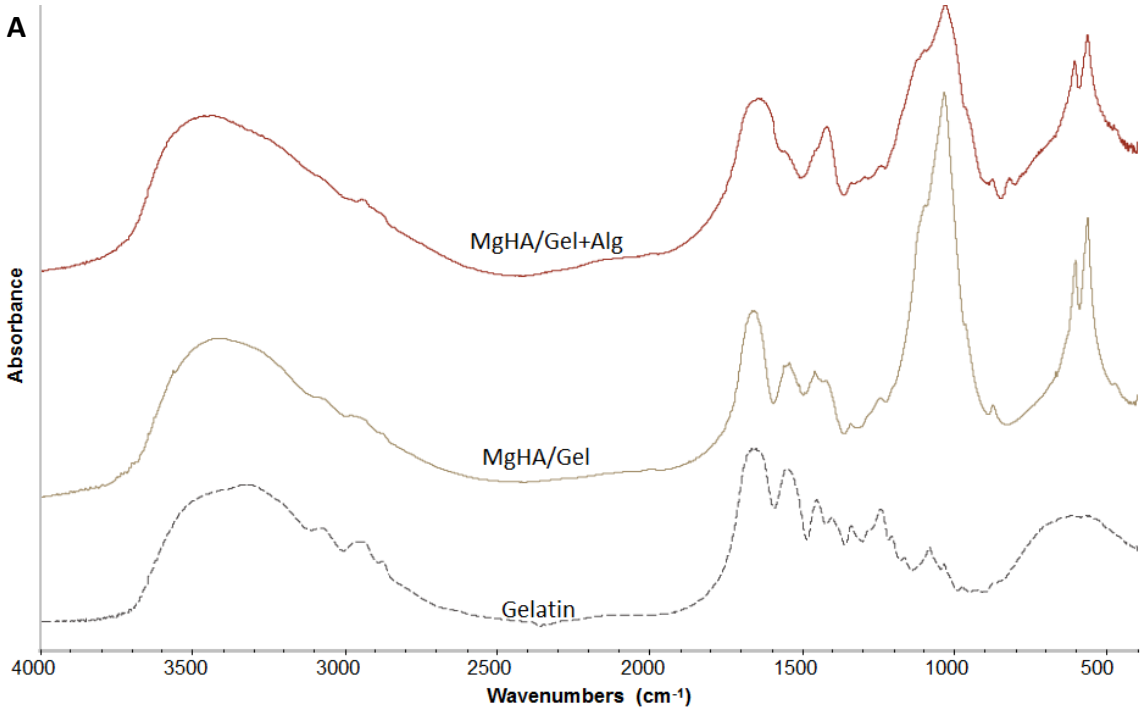

***Figure 4.4** A: FTIR analysis of MgHA/Gel+Alg anf MgHA/Gel compared with pure gelatin.*

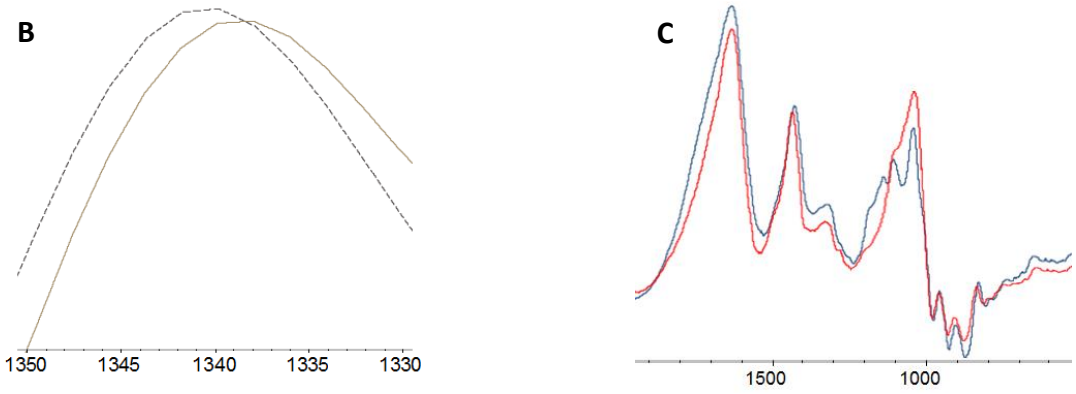

***Figure 4.4** B: Detail of the pure (broked line) and mineralized gelatin (solid line) spectra from 1350 to 1330 cm^{-1}. C: Detail of the starting sodium alginate (blue line) and complexed calcium alginate (red line) spectra from 2000 to 500 cm^{-1}.*

Gelatin exhibited significant broad band at 3330 cm^{-1} typical for O–H stretching, an almost hidden band at 3082 cm^{-1} related to N–H stretching and bands around 2955 cm^{-1} and 2880 cm^{-1} could be attributed to CH_2 asymmetrical and symmetrical stretching respectively. It's possible to see the band at 1659 cm^{-1}, related to C=O stretching, a band at 1550 cm^{-1} which refers to N–C stretching of a secondary amine and a band at 1452 cm^{-1}, typical for CH_2 bending. Other significand bands are the one at 1340 cm^{-1}, corresponding to the stretching of –COO group, the band at 1240 cm^{-1}, reconducible to N–H bending and the band at 1082 cm^{-1}, characteristic of C=O stretching[8].

The main absorption bands characteristic of hydroxyapatite appear at 1110 and 1035 cm^{-1}, related with the triply degenerated asymmetric stretching of the O–P–O bonds of the HA phosphate groups, at 604 cm^{-1} and 566 cm^{-1}, assignable to O–H and O–P–O bending respectively. The peak at 1415 cm^{-1} assignable to the stretching modes of carbonate groups implies carbonation of the inorganic phase during the nucleation process[9]. Concerning the natural incorporation of carbonate ions in the apatite lattice during its *in-situ* synthesis, two cases can be distinguished: when carbonate ions replace tetrahedral PO_4 sites (leading to the so-called B-type carbonation) and when carbonate groups occupy OH positions (A-type carbonation). In this case we are in the presence of B-Type carbonation, proved by the bending of the carbonate group at 873 cm^{-1} instead

of 880 cm^{-1}, typical for the A-type carbonation[10]. A proof of the chemical interaction between MgHA and gelatin molecules into the MgHA/Gel composite comes from the shift of the band corresponding to the stretching of –COO group of gelatin from 1340 cm^{-1} to 1338 cm^{-1} [11](Fig. 4.4B).

Finally typical alginate absorption bands which can be detected into the composite are at 1417 cm^{-1} (which added to the gelatin band results in an single broader band at 1421 cm^{-1}), 1097 cm^{-1} and 819 cm^{-1}, related to –COO stretching, C=O stretching and mannuronic acid residues respectively, while the peak related to guluronic acid residues are covered by hydroxyapatite stronger bands[12]. The coordination of the Ca^{2+} into the alginate structure is proved by the shift from 1127 cm^{-1} to 1028 cm^{-1} of the frequency regarding the C–O stretching of both alcoholic and ether groups[13] and by the shift of the band due to –COO stretching symmetric motion from 1411 to 1417 cm^{-1} [12] (Fig. 4.4C).

4.1.2.4 Scanning Electron Microscopy Analysis

Scaffold morphology determination was carried out by scanning electron microscope. SEM images at low magnification (Fig. 4.5A, B) show a channel-like structure as it's easy to see from the cross and longitudinal section of the scaffold. At medium magnification (Fig. 5C, D) it's possible to see the dimensions of channels which results between 70 and 130 µm. The SEM image at high magnification (Fig. 4.5E) shows, instead, the structural interaction between the MgHA/Gel composite and the alginate: the mineralized powder (showed in detail in Fig. 4.5F) result completely incorporated into the alginate structure, and this well integration permits the good stability of the scaffold which does not crumble even ones putted in water. In comparison with the final dentin-like scaffold, in Fig. 4.5G and Fig. 4.5H it's shown the cross and longitudinal section of the not mineralized scaffold Gel/Alg. The pores result not arranged in longitudinal channels and the surfaces of the material are much more smooth compared to those of the mineralized material.

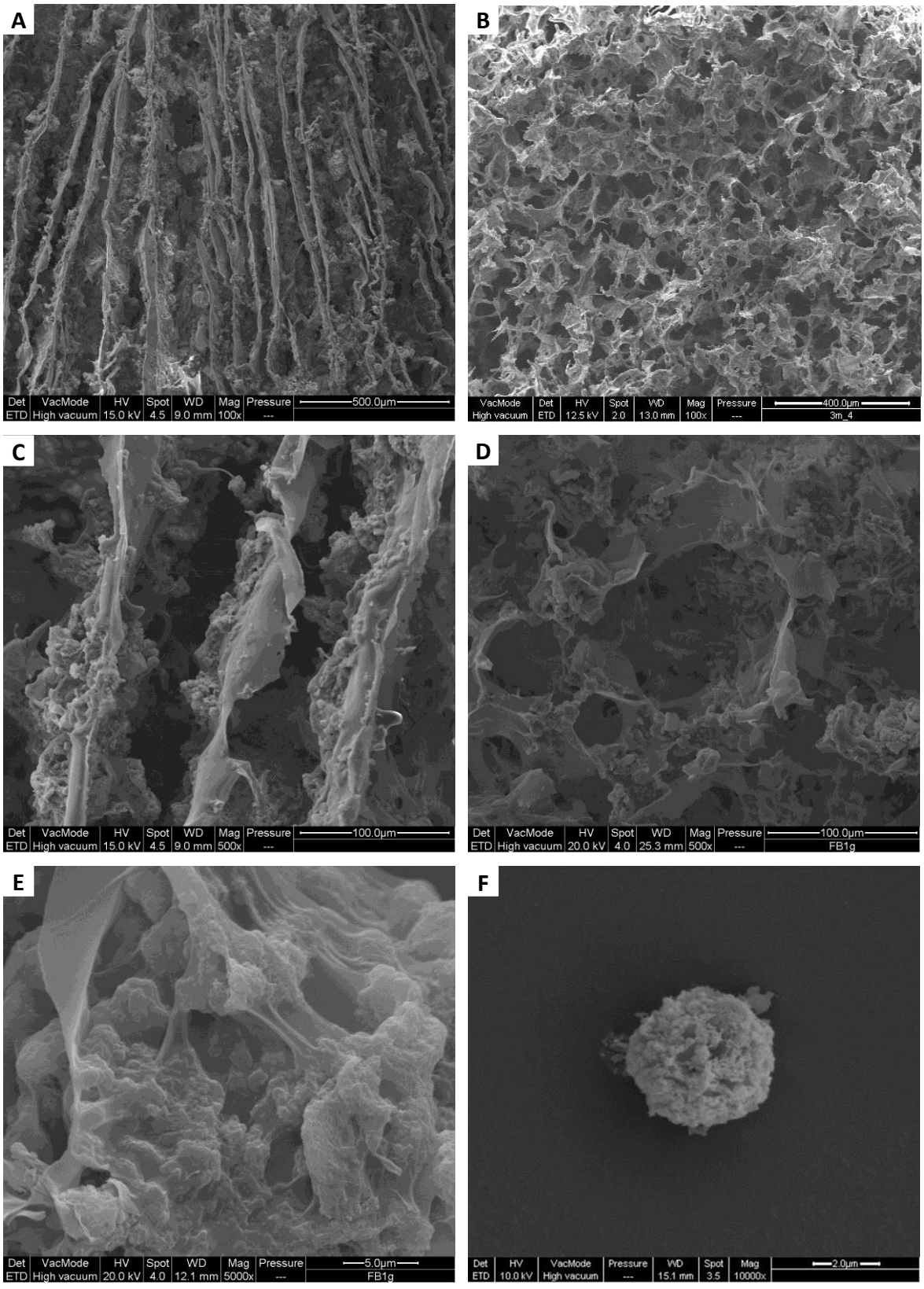
A
Det ETD
VacMode High vacuum
HV 15.0 kV
Spot 4.5
WD 9.0 mm
Mag 100x
Pressure ---
500.0µm
B
VacMode High vacuum
Det ETD
HV 12.5 kV
Spot 2.0
WD 13.0 mm
Mag 100x
Pressure ---
400.0µm
3m_4
C
Det ETD
VacMode High vacuum
HV 15.0 kV
Spot 4.5
WD 9.0 mm
Mag 500x
Pressure ---
100.0µm
D
Det ETD
VacMode High vacuum
HV 20.0 kV
Spot 4.0
WD 25.3 mm
Mag 500x
Pressure ---
100.0µm
FB1g
E
Det ETD
VacMode High vacuum
HV 20.0 kV
Spot 4.0
WD 12.1 mm
Mag 5000x
Pressure ---
5.0µm
FB1g
F
Det ETD
HV 10.0 kV
VacMode High vacuum
Pressure ---
WD 15.1 mm
Spot 3.5
Mag 10000x
2.0µm

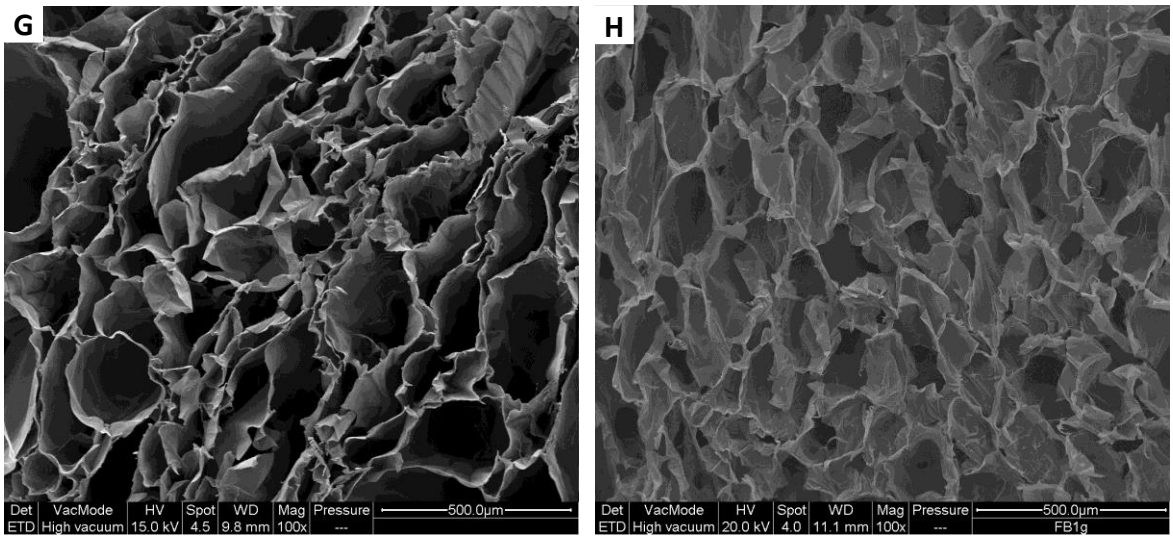

***Figure 4.5** SEM images of MgHA/Gel+Alg longitudinal (A,C) and cross section (B, D) at 100x (A, B) and 500x magnification (C, D). Detail of the morphological feature of MgHA/Gel+Alg (E) and MgHA/Gel particle (F). Comparison with longitudinal (G) and cross section (H) of not mineralized Gel/Alg scaffold as reference material for biological evaluations.*

4.1.2.5 Inductively Coupled Plasma Atomic Emission Spectroscopy

Quantitative ICP was applied to determine the overall content of Ca, P and Mg constructing the mineral phase of hybrid materials. In Tab. 4.1 are shown the most significant data from the results of this analysis. For the intermediate material MgHA/Gel and for the final material MgHA/Gel+Alg.

Materials	(Mg+Ca)/P (mol)	Ca/P (mol)	Mg/Ca (mol)	P (wt%)	Ca (wt%)	Mg (wt%)
MgHA/Gel	1,69 ± 0,02	1,64 ± 0,03	3,5 ± 0,3	14,4 ± 0,3	30,4 ± 0,4	0,60 ± 0,02
MgHA/Gel+Alg	1,92 ± 0,02	1,87 ± 0,05	3,0 ± 0,2	14,6 ± 0,3	34,7 ± 0,5	0,59 ± 0,03

***Table 4.1** ICP features of MgHA/Gel and MgHA/Gel+Alg composites.*

About MgHA/Gel composite the (Ca+Fe)/P molar ratio is very close to the hydroxyapatite theoretical one (Ca/P = 1,68 mol), confirming the effective replacement of calcium

ions with magnesium ions. Besides it's possible to see that the amount of magnesium ions detected by ICP is quite lower than the nominal one fixed for the synthesis (Ca/Mg = 5% mol) but according to the composition of natural dentin. So we can conclude that the mineralization of gelatin with magnesium-substituted hydroxyapatite was conducted effectively.

Comparing the results for MgHA/Gel and MgHA/Gel+Alg was observed an increase of calcium because of that reacted with the alginate matrix during the cross-linking process. However, considering the unchanged amount of magnesium and phosphorous it's possible to deduce that the amount of hydroxyapatite in MgHA/Gel+Alg is no different compared to MgHA/Gel so the methodology can be considered preservatives towards the mineral phase.

4.1.2.6 Swelling and degradation test

Degradation test was conducted simulating physical condition. This test was crucial for the material selecting because it's fundamental in regenerative medicine avoid that the scaffold degrades before the complete tissue rebuilding.

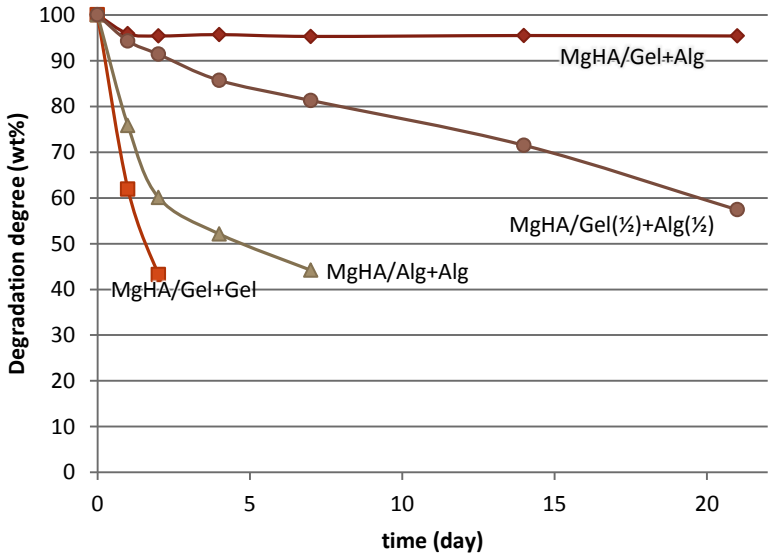

***Figure 4.6** Degradation weight loss for different dentin-like scaffolds*

Fig. 4.6 shows the degradation weight loss for four of the best materials developed as dentin-like scaffold: MgHA/Gel+Alg, MgHA/Gel(½)+Alg(½), MgHA/Gel+Gel and MgHA/Alg+Alg. It's easy to see that only the MgHA/Gel+Alg composite shows suitable properties to be implanted and to constitute a valid support for cells proliferation because MgHA/Gel+Gel and MgHA/Alg+Alg, which had seemed promising, degraded in less than a week in PBS at 37° C and MgHA/Gel(½)+Alg(½) shows an abundant and steady degradation. Instead, after an initial loss of 5%wt, MgHA/Gel+Alg is stable for more than three weeks.

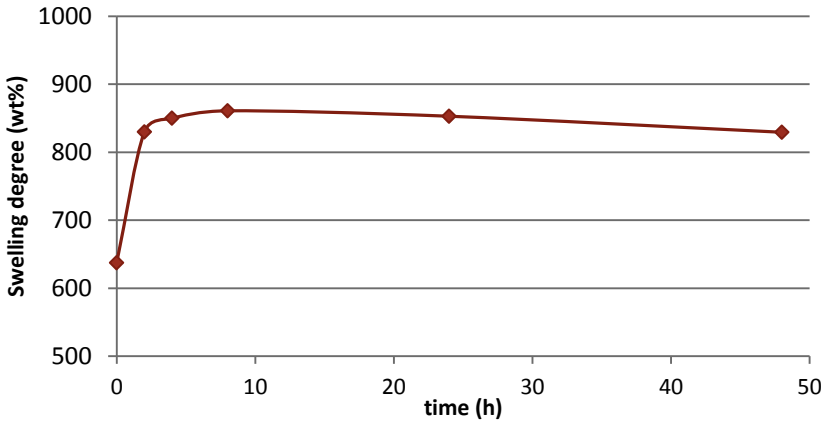

***Figure 4.7** Swelling degree for MgHA/Gel+Alg scaffold*

Swelling and water uptake properties are fundamental for the regenerative process because the penetration of body fluids into the scaffold allows the proliferation and survival of the cells. Fig. 4.7 shows the swelling degree of the MgHA/Gel+Alg composite in physical conditions. Thanks to its high porosity, after 10 hours in PBS at 37° C the scaffold is able to uptake close to 900% of its weight of fluid.

4.1.3 Biological characterization

4.1.3.1 Cell viability assay

Qualitative cell viability test with Live&Dead assay was conducted on MgHA/Gel+Alg samples and not mineralized samples (Gel+Alg) was used as comparison test. As show in Fig. 4.8, live cell ratio was very higher respect dead cells in all the samples, but it was notable that the cell morphology was completely different: into the mineralized samples it's possible to see that cells are well-spread, sign that there is a good cell adhesion, contrariwise into the not-mineralized scaffold cells had round shape. Cell spreading is an essential function of a cell which has adhered to a surface and precedes the function of cell proliferation; in fact it is well known that the size and shape of cell spreading area is decisive for further migratory, proliferative and differentiation behavior of anchorage-dependent cells. If this extent is very small (i.e. attachment of round cells without formation of focal contacts and spreading), the cells usually do not survive[14]. The chemical composition and the aligned porosity of the mineralized scaffold resulted suitable for a nice cell/material interactions, as it's possible to see also in the Fig. 4.9A, which shows a well-spread cell covered surfaces. Negative results were showed by Gel+Alg (Fig. 4.9B) confirming the mineralized component is very important in 3D MSCs adhesion.

Another important aspect is the scaffold colonization: even in Fig. 4.8 it's possible to see that the HA/Gel+Alg scaffold structure permits to the cells to adhere to the surfaces, and cell density increase from day 1 up to day 21. The non-mineralized Gel+Alg scaffold, instead, showed few cells compared to its mineralized counterpart.

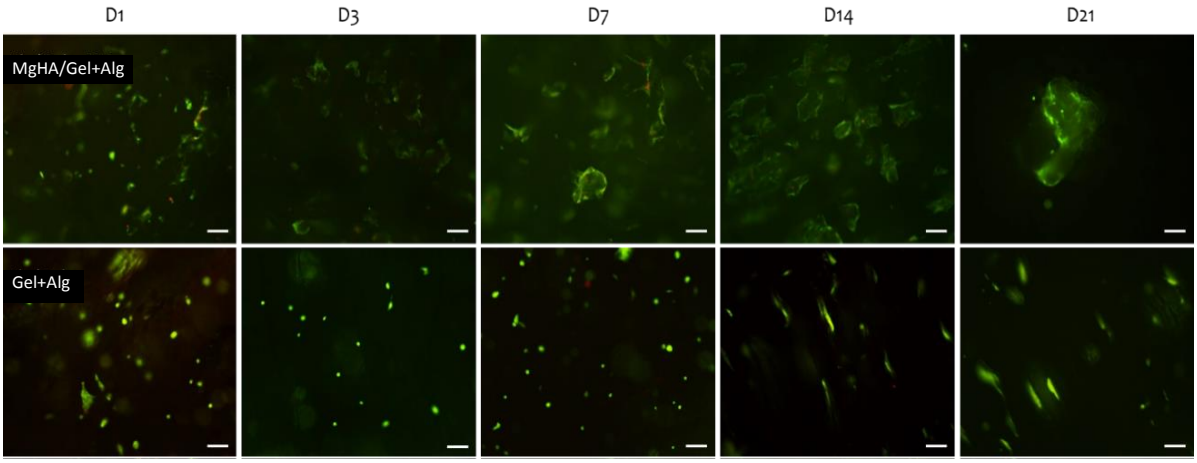

***Figure 4.8** Cell viability of cell-seed MgHA/Gel+alg and Gel+Alg scaffols analyzed by the Live/Dead assay. The scale bar is 100µm.*

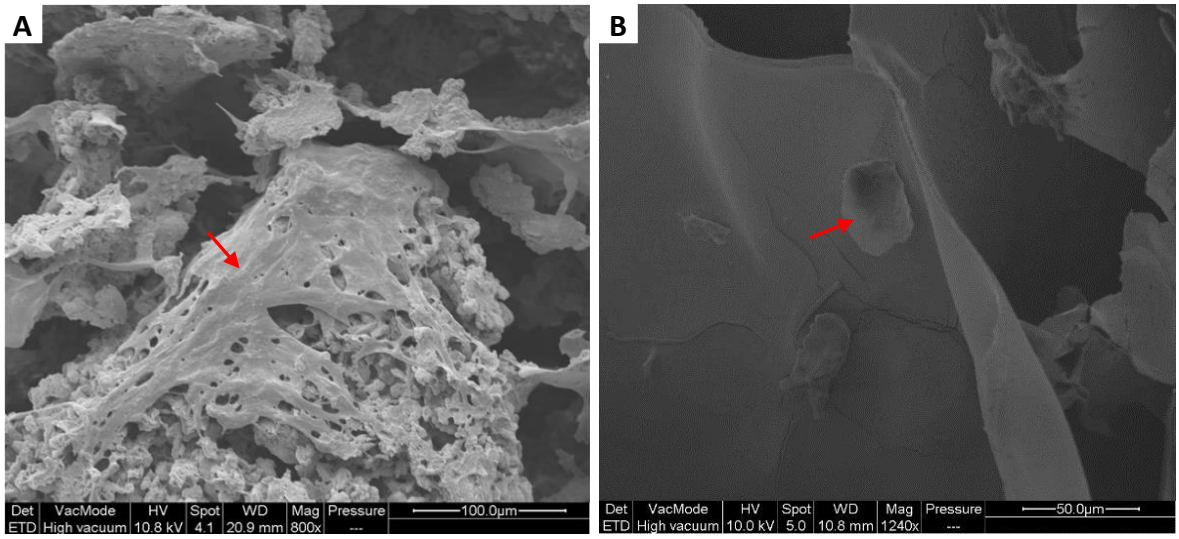

***Figure 4.9** SEM images of mMSC grown on MgHA/Gel+Alg (left) and Gel/Alg (right) samples after 21 days from seeding. Cell are marked by the arrows.*

The 3D cell culture with mMSC showed the promising properties of the new scaffolds in term of cell adhesion and colonization.

4.1.3.2 Cytotoxicity test by direct contact

Also quantitative tests regarding the biological evaluation of medical devices were conducted; according to ISO 10993-5[15] a material results not cytotoxic when cell growth inhibition of Balb/c 3T3 should not be higher than 30%.

Materials	% of viability	Results
MgHA/Gel	84	Non cytotoxic
Alginate	98	Non cytotoxic
MgHA/Gel+Alg	91	Non cytotoxic

***Table 4.2** Biological evaluation of cytotoxicity of intermediate and final materials for dentin-like scaffold.*

As indicated in Tab. 4.2, starting, intermediate and final materials result not cytotoxic during *in vitro* tests. These data confirm the results previously obtained by the qualitative Live&Dead test so MgHA/Gel+Alg results suitable for medical applications.

4.1.4 Conclusion

MgHA/Gel composite was prepared through a biologically inspired mineralization process, with the purpose of create a low coast hybrid material with the chemical features as close as possible to the composition of mineralized human tissue. Alginate hydrogel was then added in order to get, after a freeze-drying process, a channel like structure, obtaining a morphological high mimicry of the natural dentin.

The results obtained by the TGA, XRD and ICP show that the material has proper chemical features and by SEM images it was possible to know that a correct morphology was reached. By swelling and degradation test, simulating the body environment, MgHA/Gel+Alg material was chosen as the most promising for the regeneration of dentin tissue because of its good resistance.. Its bio-compatibility and cells proliferation were established through *in vitro* investigations.

These positive results constitute the necessary prerequisites for further biological *in vivo* investigations into the potential application to remineralisation process in the dentin cavities left by caries.

4.2 Periodontal apparatus: alveolar bone

In this section highly porous and magnetic collagen-based scaffold was used as replacing material for alveolar bone. The process was directed to heterogeneously nucleate superparamagnetic iron-substituted hydroxyapatite (FeHA) particles on collagen molecules, so to obtain hybrid magnetic composites. For this purpose both ferrous and ferric ions were introduced in form of soluble iron salts during the bio-mineralization process; in this way the of specific calcium crystallographic sites with a specific coordination[16] by iron ions generates in the HA lattice two different sub-lattices whose interaction induces a magnetic behavior into the mineral phase[17].

As previously explained, a bio-mimetic mineralization requires that the apatite phase is directly nucleated into and onto collagen fibrils during their self-assembling exploiting their pH-dependent fibration[18]. Guidance of chemical features and spatially confinement imposed by polymeric matrix leads a wide nucleation sites but a limited growth of inorganic nuclei achieving amorphous and nano-sized crystals.

The obtained constructs was stabilized by cross-linking procedures, in order either to make the hybrid composite more resistant towards physiological fluids and bio-erosion and thus mechanical properties. Finally, by means of freeze-drying process, an organization of composite fibers into three-dimensional networks occurs, obtaining a material with pore size and distribution suitable for cells colonization.

4.2.1 Synthesis process

The magnetic composite was synthesized following a biologically inspired approach[19]. In order to obtain scaffold mimicking the chemical composition of bone, the weight ratio between mineral and organic phases was fixed to 70:30 wt%.

The nucleation of a magnetic FeHA on collagen molecules requires the preservation of both iron species so that they can enter the HA structure in two different coordination

position and induce the superparamagnetism: actually the acetic acid present in the collagen gel suspension would have oxidize Fe^{2+} to Fe^{3+}. In order to avoid the oxidation a NaOH 0.1M solution was dropped on 150 g of 1%wt of collagen gel up to pH 5.5 were the collagen fibers precipitate. The assembled collagen was washed three times with distilled water and mixed with 250 mL of H_3PO_4 0.083M solution, which allows the collagen disassembly. This dispersion was then dropped in a $Ca(OH)_2$ suspension (2.71 g in 500 mL of distilled water) previously enriched with $FeCl_2 \cdot 4H_2O$ (0.689 g in 25 mL of distilled water) and $FeCl_3 \cdot 6H_2O$ (0.956 g in 25 mL of distilled water) to yield a FeHA/Coll composite material in the ratio 70:30 wt%. The total amount of iron chloride salts was calculated to obtain a molar ratio Fe/Ca equal to 20% mol in the mineral phase and the ratio Fe^{2+}/Fe^{3+} equal to 1:1[20]. In such conditions, self-assembly and self-organization of the polymer fibrils as well as the heterogeneous nucleation of HA nano-crystals will be simultaneously induced. The drop-wise addition procedure was performed under manual stirring, assuring a slow decrease of pH from 12 to 8 and at the end of the addiction the composite was left to ripen in the mother liquor for 2 hours.

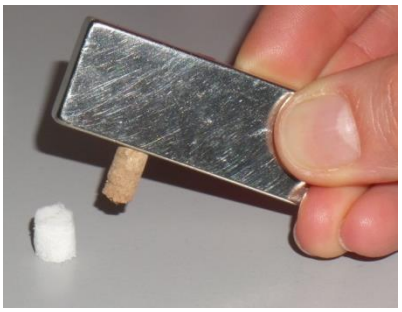

Figure 4.10 *FeHA/Coll alveolar bone-like scaffold (brownish scaffold attached to the magnet) compared with a not magnetic HA/Coll scaffold (the white one)*

After the synthesis the mineralized collagen was washed placing it 3 times in fresh deionized water and filtered by a metallic sieve (50 µm). In this way we could separate the bigger mineralized fibrous fraction from hydroxyapatite not attached to the organic matrix and the denaturated fibers which could be created due to warming, both of which can pass through the sieve. The latter part of the material was cross-linked for 48 h at

25 °C adding a 1% w/w genipin aqueous solution, setting up a genipin/collagen ratio equal to 2 wt%, so washed with deionized water from the residual unreacted cross-linker. The material was finally poured into 24-wells cell-culture multiwell plates and freeze-dried.

The synthesis temperature during the bio-mineralization process which leads to the material with the best performance, called FeHA/Coll, was found to be 40 °C, but others two different temperatures, as comparing, were investigated (25 and 50 °C) and the respective synthesis products were called FeHA/Coll_25 and FeHA/Coll_50.

For the stabilization of magnetic biohybrid FeHA/Coll scaffolds five others cross-linking methods was tested: a genipin/collagen ratio equal to 1 wt% for 48 h at 25 °C, a BDDGE/collagen ratio equal to 1 wt% for 48 h at 25 °C[21], a BDDGE/collagen ratio equal to 2 wt% for 48 h at 25 °C, a ribose/collagen ratio equal to 1 wt% for 24 h at 25 °C[22] and a ribose/collagen ratio equal to 2 wt% for 24 h at 25 °C. Respective synthesis products were called FeHA/Coll_gen1, FeHA/Coll_BDD1, FeHA/Coll_BDD2, FeHA/Coll_rib1, FeHA/Coll_rib2.

4.2.2 Chemio-physical characterization

4.2.2.1 Thermal Analysis

Thermogravimetric investigations were carried out on the FeHA/Coll samples synthetized at the three different temperatures (25, 40 and 50°C). The result curve (TG) and its derivative (DTG) are shown in Fig. 4.11 and show three distinct weight loss. The first weight loss, of about 5-8%, is observed in the range of 50-160 °C and related to the loss of water of hydration of collagen; the second and the most plentiful loss of weight is between 210 and 430 °C, due to the thermal degradation of collagen[23]. The process of thermal decomposition is completed between 600-700°C with the final combustion of organic residues and with an overall decrease of about 41, 45 and 53% of weight respec-

tively for FeHA/Coll_25, FeHA/Coll and FeHA/Coll_50. About the mineralization extent in the scaffolds, the inorganic phase was found to be in the range of 51−62 wt% instead of the nominal hydroxyapatite/collagen ratio of 70/30 wt%. The discrepancy between the nominal and the real composition of the materials can be assigned to the reaction yield, which does not reach 100%. Moreover the amount of mineral phase into the three differ materials are slightly different and decrease with the increasing of the temperature of the synthesis (62%, 60% and 51%). This effect is probably due to the partial denaturation of the polymer at higher temperature as well as the increase in its nano-assembly, trigger to a reduction in the calcium and iron ions binding[21,22], whereas at low temperatures the availability of the nucleation sites on collagen is higher. It is well known that the temperature of thermal denaturation of the collagen strongly depends on its degree of cross-linking between the chains[25,26].

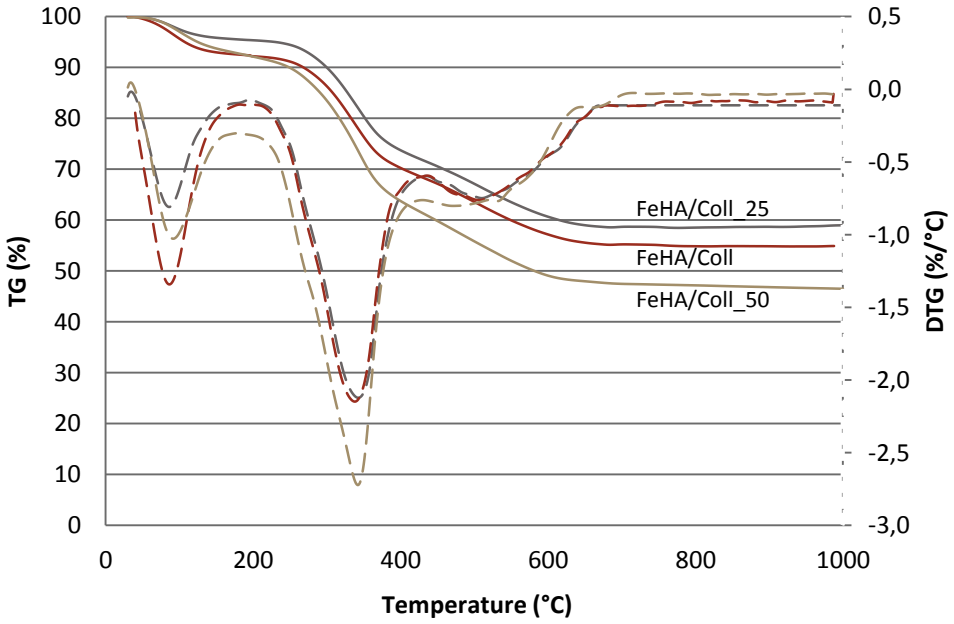

***Figure 4.11** Thermal decomposition profile (TG) and its derivative (DTG) of FeHA/Coll_25, FeHA/Coll and FeHA/Coll_50.*

DTA plots relative to the composite FeHA/Coll, FeHA/Coll-gen1 and the not cross-linked one (FeHA/Coll_NCL) are shown in Fig. 4.12. Within the temperature range from 30 to

about 130 °C a broad endothermal peak appears in each sample; this peak is known to be associated with the denaturation of collagen structure, with a simultaneous transformation from triple helical to random coil of collagen[23], and is connected with mass decrement, as is seen in TG curves, whereas the breakage of inter- and intra-molecular hydrogen bonds allow the release of bound water[28].

The maximum of the peak for cross-linked composites compared to the one of not cross-linked are significantly shifted to the region of higher temperatures (91,2 °C, 93,0 °C and 98,4 °C respectively for FeHA/Coll_NCL, FeHA/Coll_gen1 and FeHA/Coll). Thereby, the obtained results indicate that cross-linking process induced partial changes in the structure of collagen fibers, because of the thermal stability of secondary structure of reticulated samples increased. We could conclude that the cross-linking processes has been successful and that the reticulation between chains occurred to a greater extent with increasing of cross-linker amount.

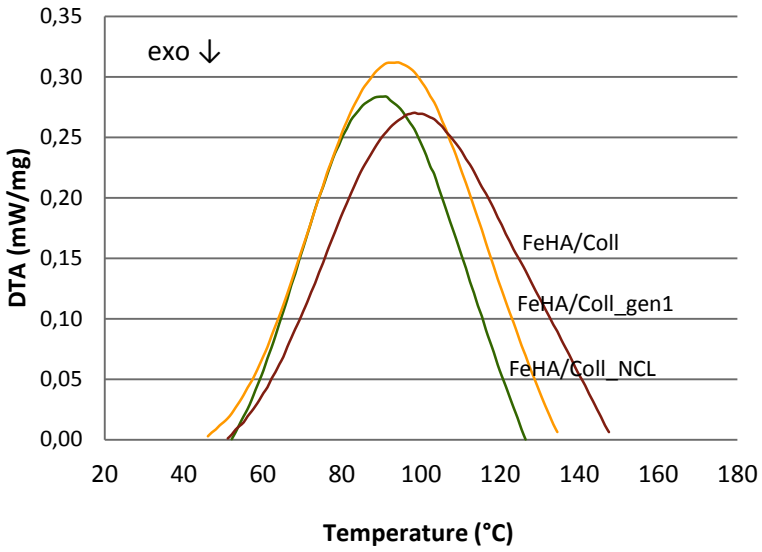

***Figure 4.12** Differential Scanning Calorimetry of FeHA/Coll_NCL, FeHA/Coll_gen1 and FeHA/Coll.*

4.2.2.2 X-Ray Diffraction

XRD diffractogram of the FeHA/Coll_25, FeHA/Coll and FeHA/Coll_50, shown in Fig. 4.13, display the typical shape ascribable to a calcium phosphate phase with the characteristic broad peaks of nano-crystalline apatite with very low coherent length[10], since the interaction with the organic template confined the mineral nuclei growth at the nano-scale[11]. The presence of ionic substitutions in the apatite structure, which is accomplished by the increase of the number of structural defects, is a further reason of broad weak peaks. The decreasing of the resolution of the spectra indicate ad increasing in the amorphous character of the apatite, resembling that of newly formed bone.

None of the three spectra display the peak at 2θ≈36° attributed to the presence of magnetite or maghemite, even at synthesis temperatures of 50°C, where the magnetite and maghemite formation is favored[20]. This progress has been achieved slowing down the biomineralization reaction thanks to the slow addiction of collagen and iron ions during the reaction.

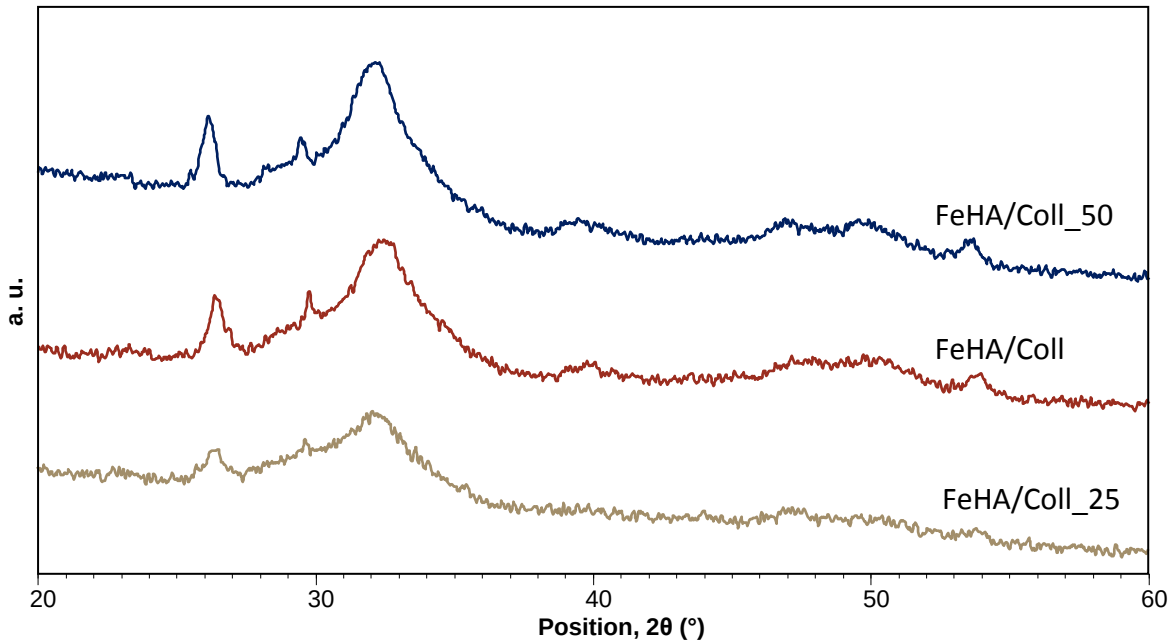

***Figure 4.13** XRD spectra of FeHA/Coll scaffolds synthetized at 25°C (FeHA/Coll_25), 40°C (FeHA/Coll) and 50°C (FeHA/Coll_50).*

4.2.2.3 Fourier-Transform Infrared Spectroscopy

Fourier transform infrared spectrum of the FeHA/Coll composite, compared with the pure collagen and FeHA spectra, is shown in Fig. 4.14A. The typical bands relative to hydroxyapatite[9] are clearly visible in FeHA/Coll spectrum, in particular the bands at 1032, 565, and 601 cm^{-1}.

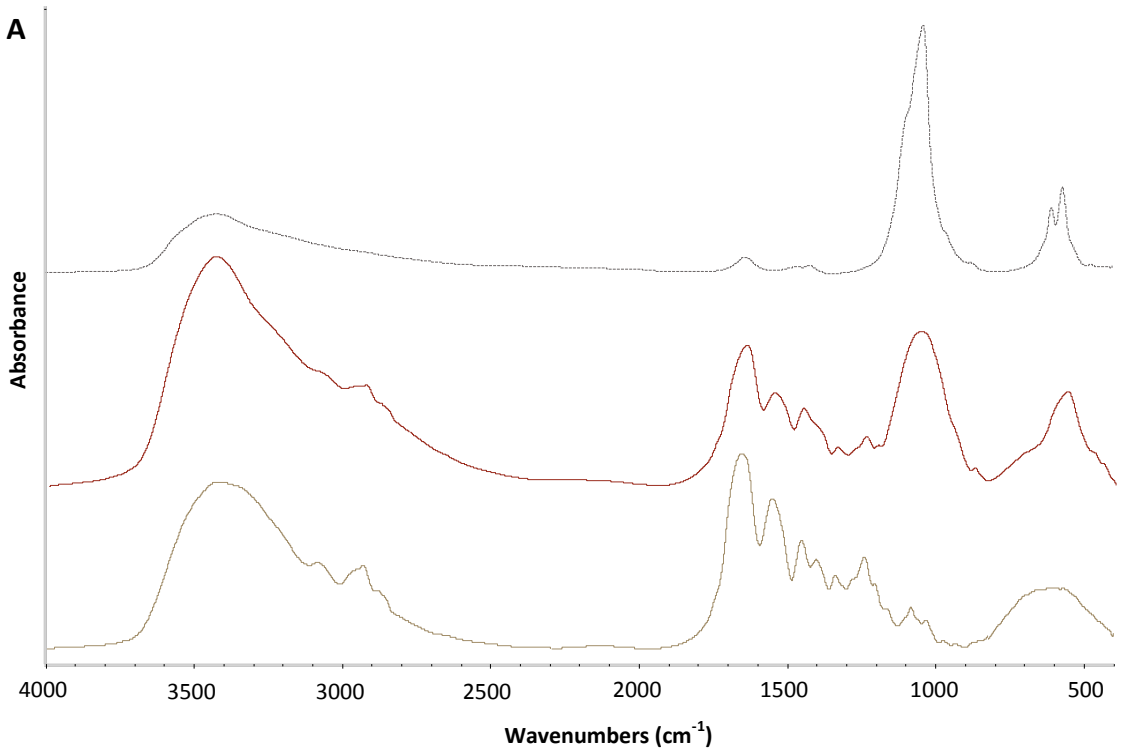

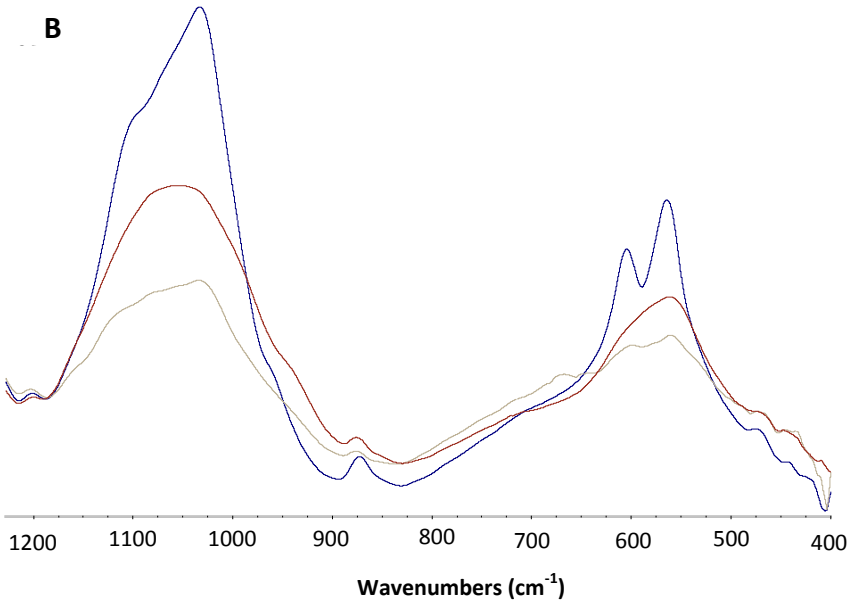

Figure 4.14 *A: FTIR analysis of FeHA/Coll compared with pure collagen and FeHA.*

B: Detail of FeHA/Coll_25, FeHA and FeHA_50 spectra from 1200 to 400 cm^{-1}.

The resolution of the bands relative to hydroxyapatite is low and decreases as a function of the temperature of the bio-mineralization. These effects indicate that the mineral phase nucleated on collagen fibers is non-stoichiometric and its crystallinity degree decrease with the synthesis temperature[20].

4.2.2.4 Scanning Electron Microscopy

SEM images of freeze-dried FeHA/Coll composite (A, B, C) and a comparison with not mineralized collagen (D) are shown in Fig. 4.15. The morphology of the hybrid composite appears very similar to that natural bone: it's possible to see that nano-globular and quite amorphous apatite crystals cover completely the collagen fibers (Fig. 4.15B, C). The freeze-drying process, instead, allows to achieve a porous material characterized by an architecture with a 3D network of macro- and micro-porosity (Fig. 4.15A, B), to favor cells adhesion and proliferation. Comparing the mineralized scaffold (Fig. 4.15B) and the

not mineralized one (Fig. 4.15D) it's easy to see that the mineralization, which occurs during the self-assembling of collagen, allow a nucleation and growth of hydroxyapatite crystals not only inside the fibers[29], but also externally, obtaining rough surfaces.

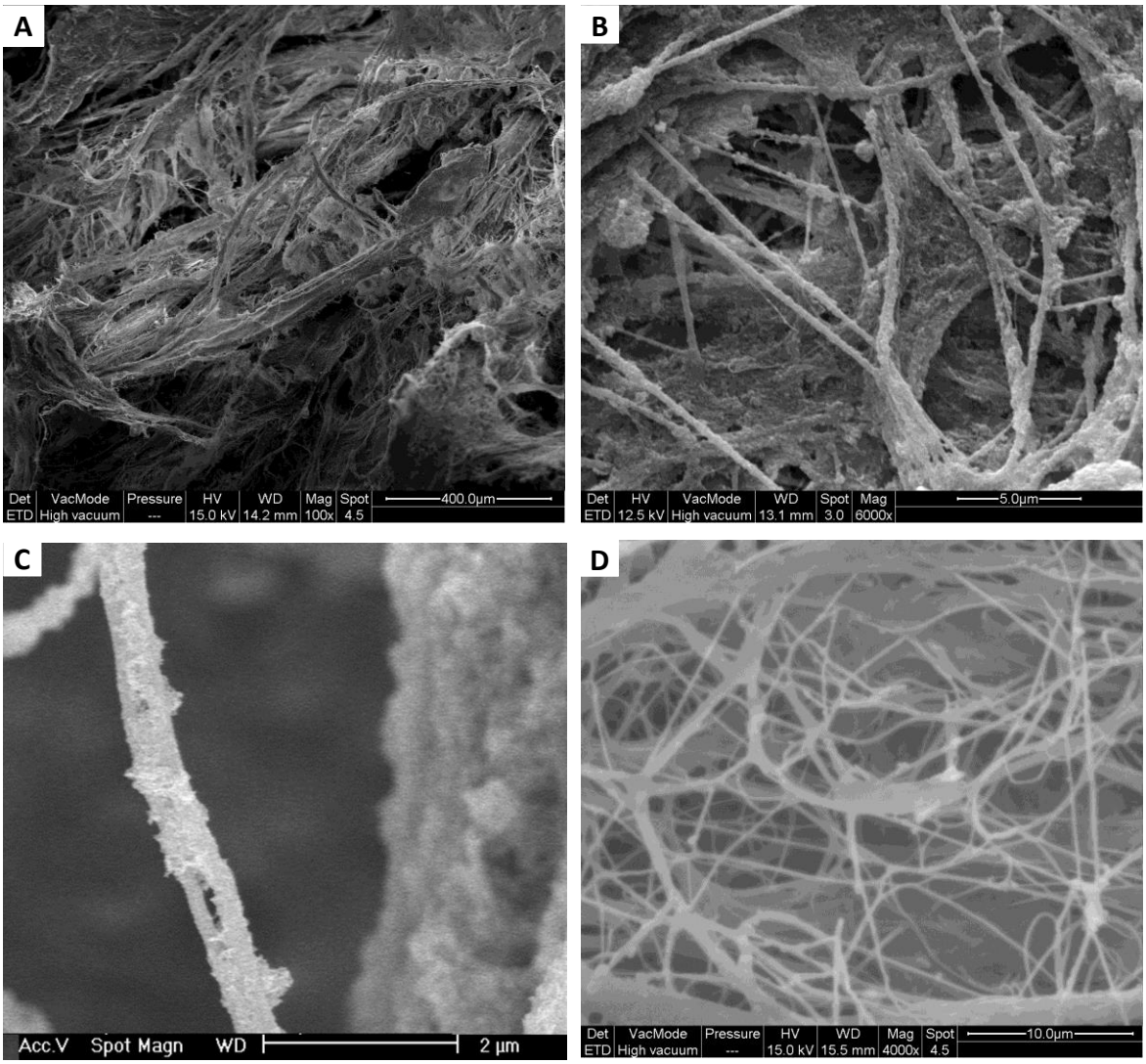

***Figure 4.15** SEM images of FeHA/Coll at 100x (A) and 6000x magnification (B). Detail of morphological feature of mineralized FeHA/Coll fiber at 30000x magnification (C) and comparison with pure freeze-dried collagen at 4000x magnification (D).*

4.2.2.5 Inductively Coupled Plasma Atomic Emission Spectroscopy

A chemical composition analysis of the mineral phase of the composites FeHA/Coll_25, FeHA/Coll and FeHA/Coll_50 was conducted by ICP. In Tab. 4.3 are shown the most significant data from the results of this analysis.

Materials	Ca/P (mol)	(Fe+Ca)/P (mol)	Fe/Ca (mol%)	Fe/(Fe+Ca) (mol%)
FeHA/Coll_25	1,40 ± 0,03	1,65 ± 0,02	18,0 ± 0,5	15,25 ± 0,01
FeHA/Coll	1,38 ± 0,04	1,68 ± 0,02	21,5 ± 0,6	17,66 ± 0,03
FeHA/Coll_50	1,37 ± 0,07	1,69 ± 0,08	22,84 ± 0,3	18,59 ± 0,01

***Table 4.3** ICP features of FeHA/Coll_25, FeHA and FeHA_50 composites.*

The (Ca+Fe)/P molar ratio results very close to the hydroxyapatite theoretical one for all the three composites, confirming the effective replacement of calcium ions with iron ions at all the synthesis temperature tested. The amount of iron ions respect to the sum of all cations present in the mineral phase is quite lower respect to the nominal one fixed for the synthesis (Fe/Ca = 20 mol%) but it's possible to conclude that the reaction of iron-doping has taken place efficiently. The increasing of the amount of iron with the increasing of the temperature indicate that the higher temperature favors the replacement of iron ions instead of calcium.

4.2.2.6 Swelling and degradation test

The degradation test for several hybrid scaffolds is shown in Fig.16. During this test the FeHA/Coll_25, FeHA/Coll and FeHA/Coll_50 was tested (Fig. 4.16A), but also FeHA/Coll not cross-linked (FeHA/Coll_NCL), FeHA/Coll_gen4, FeHA/Coll_BDD2, FeHA/Coll_BDD4, FeHA/Coll_rib2 and FeHA/Coll_rib4 (Fig. 4.16B), in order to establish whether the cross-linking was effective. From the degradation behavior test as a function of the synthesis temperature (Fig. 4.16A) it's possible to see that there is an increasing of the weight loss during the testing time with the increasing of the reaction temperature. This result im-

plies that a bio-mineralization at temperatures higher than the physiological one could denature and degrade the collagen fibrils[30] which have more difficulties to assembly into stable and strong fibers.

About the degradation test regarding the not cross-linked material (FeHA/Coll_NCL) and the same material with different kind and amount of cross-linking agents (Fig. 4.16B), 2% wt of genipin compared to collagen (FeHA/Coll) results the best cross-linking condition for mineralized collagen. In fact after three weeks into simulated body condition the scaffold weight loss is stable and less than 15%. This effect is probably due to the properties of the genipin as cross-linker: unlike the BDDGE, genipin dimerization subsequent to collagen binding can lead to an intermolecular and intramolecular crosslinking network thanks to its cyclic structure within collagen fibers[31].

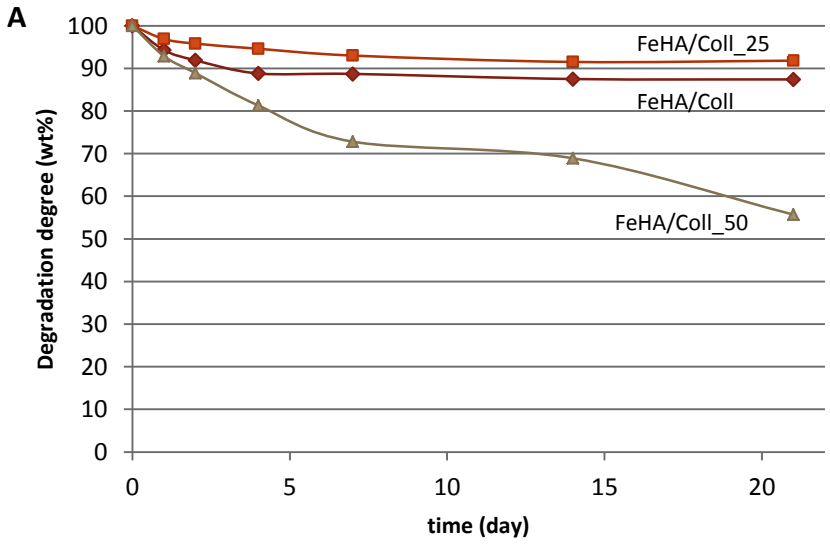

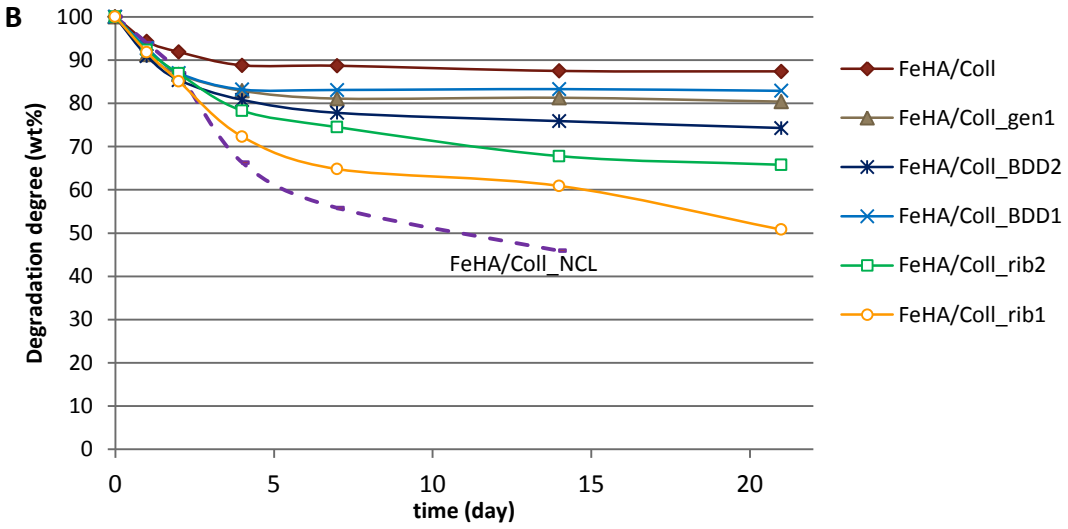

***Figure 4.16** Degradation weight loss for alveolar bone-like scaffolds (FeHA/Coll) synthetized at various temperatures (A) and stabilized with various kind and amount of cross-linkers (B).*

Swelling properties was tested for the samples deemed suitable after the biodegradability test: FeHA/Coll_25 and FeHA/Coll (Fig.17A) in order to observe the swelling difference according to the synthesis temperature, but also FeHA/Coll not cross-linked (FeHA/Coll_NCL), FeHA/Coll_gen4, FeHA/Coll_BDD2, FeHA/Coll_BDD4, FeHA/Coll_rib2 and FeHA/Coll_rib4 (Fig. 4.17B), for establish the best cross-linking condition for emphasize the hybrid composites water uptake properties. It's possible to see that the synthesis temperature affects the hydration time, but after 24 hours in PBS at 37° C the two samples show about the same swelling degree (485% for FeHA/Coll and 477% for FeHA/Coll_25).

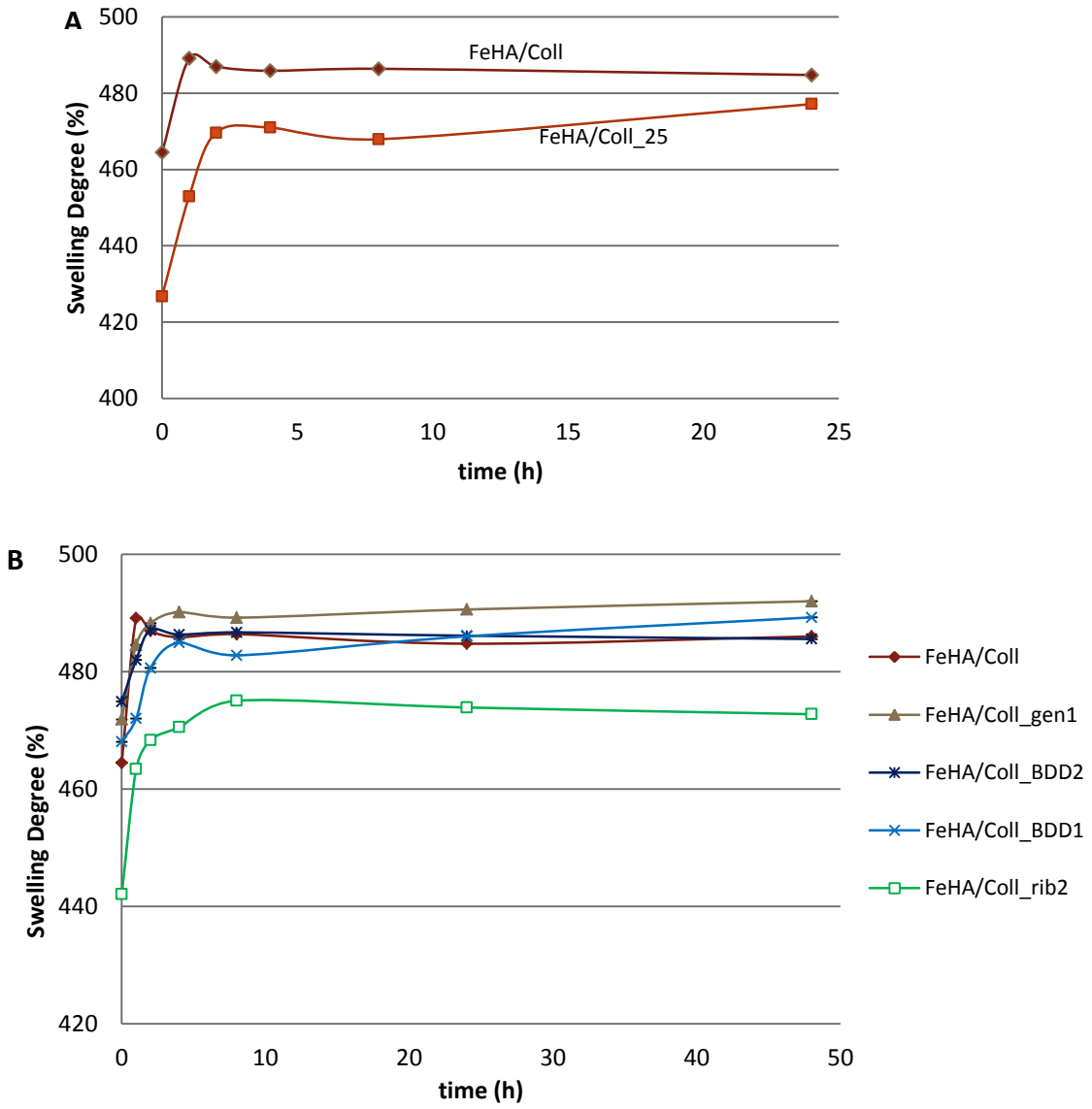

Figure 4.17 *Swelling degree for alveolar bone-like scaffolds synthetized at various temperatures (A) and stabilized with various kind and amount of cross-linkers (B).*

About changes regarding the different cross-linking methods, it's possible to see that all samples have a very close swelling degree after 24 hours, between 495 and 485%, except for the material cross-linked with ribose with a collagen/ribose ratio of 2% w/w which show a lower swelling degree, 473%.

4.2.2.7 Magnetic susceptibility

The magnetization curves of FeHA/Coll_25, FeHA/Coll and FeHA/Coll_50 are shown in Fig. 4.18A, 4.18B and 4.18C respectively, and the results resumed in Tab. 4.4. The measured black curves can be decomposed into two principal components, explained in the FeHA/Coll curve: a linear part which represents the susceptibility and a S-shaped component, a sign of ferromagnetism or superparamagnetism[32].

Materials	Susceptibility [emu/(g·T)]	Superparamagnetic saturated moment [emu/g]
FeHA/Coll_25	0.134	≈ 0
FeHA/Coll	0.125	0.5
FeHA/Coll_50	0.091	0.3

***Table 4.4** Magnetic features of FeHA/Coll_25, FeHA/Coll and FeHA/Coll_50 composites.*

It is apparent that the paramagnetic contribution is almost identical for all three samples and all the materials show almost no hysteresis at zero field, which is an indicator for absence of ferromagnetism. This can be interpreted so that the content of the paramagnetic material is the same in all materials, so that such paramagnetism could be an intrinsic property of FeHA whatever its synthesis temperature. The superparamagnetism behavior, instead, is broader with respect to FeHA/Coll (0.51 emu/g at 7T), lesser for FeHA/Coll_50 (0.33 emu/g at 7T) and practically nonexistent for FeHA/Coll_25 since such a linear curve shape is typical for materials without superparamagnetic content.

For the FeHA/Coll_25 sample (Fig. 4.18A), the low crystallinity and poor organization of hydroxyapatite lattice cause a scarce coordination level of the iron ions, reflecting in a low magnetization of the scaffold. For the FeHA/Coll and FeHA/Coll_50 samples (Fig. 4.18B, C), the different magnetization values are caused probably by a different mineral amount into the hybrid scaffold, confirmed also by the TGA analysis and by the susceptibility values (Tab. 4.4), which decrease at higher temperature.

In the field of magnetic implants a smaller magnetic field is applied, about 0.1T [33], and so low applied magnetic field would not magnetize the FeHA/Coll_25 and FeHA/Coll_50 scaffolds very strongly. Therefore, in order to have the more apparent effect of magnetization FeHA/Coll is the most performing material.

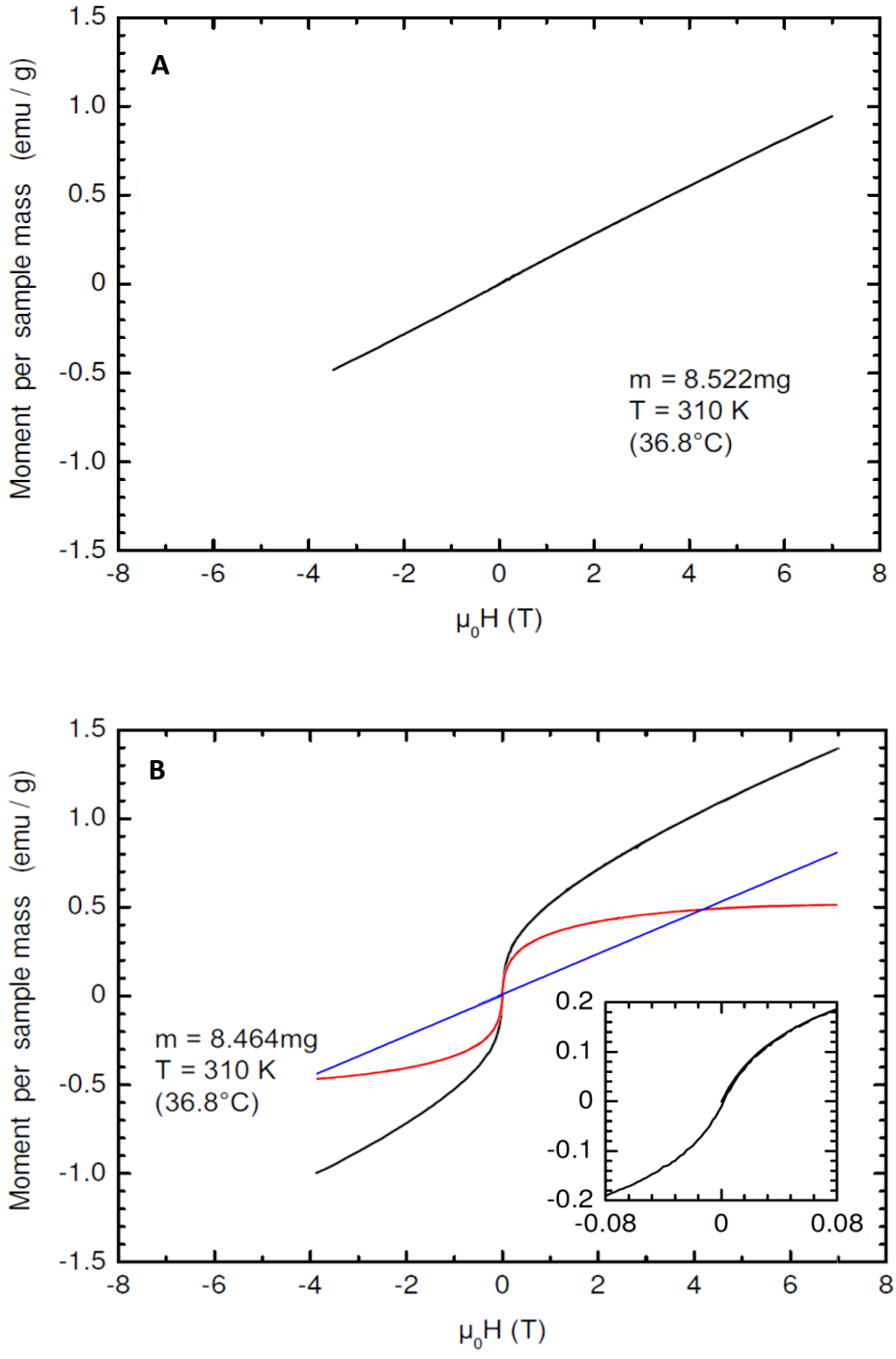

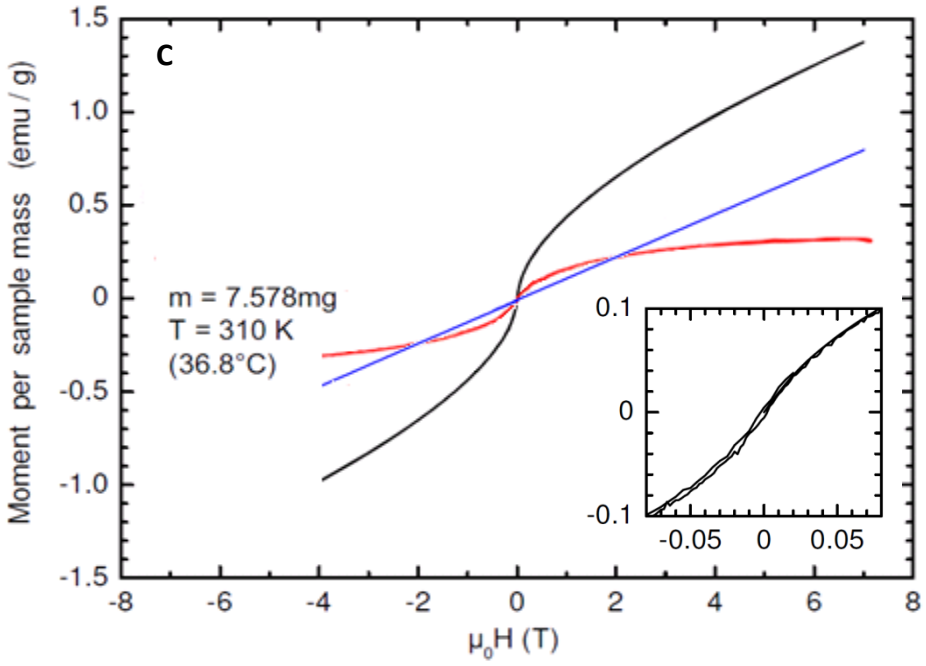

Figure 4.18 *Magnetization curve of FeHA/Coll_25 (A), FeHA/Coll (B) and FeHA/Coll_50 (C). Black line: measured curves; blue line: paramagnetic (non-saturating) contribution; red line: superparamagnetic (saturating) contributions.*

4.3 Periodontal apparatus: periodontal ligament

This part of PhD project deals with collagen-based scaffold used as replacing material for periodontal ligament, the central portion of the tri-layer scaffold mimicking the periodontal apparatus. The purpose has been to develop a very highly porous membrane in order to allow an extensive vascularization of the tissue because the cement depends metabolically by nutrients that diffuse from the periodontal ligament.

The chemical bio-mimicry of the natural tissue was important as the morphological features so we selected the type I collagen as base material for this scaffold section and the main factor on which we focused has covered the cross-linking of the collagen, since the scaffold must withstand in physiological environment enough to allow the cells engraftment and the deposition of new cellular matrix.

Freeze-drying was finally used to obtain the desired structure, with wide and interconnected pores.

4.3.1 Synthesis process

The non-mineralized section of the tri-layered scaffold was produced firstly increasing the pH of the initial acid suspension of collagen up to 5.5 dropping NaOH 0,5 M; this pH value causes the spontaneous fiber formation and precipitation of collagen. The so created collagen fibers was collected with the aid of a sieve, washed placing 3 times with fresh deionized water and then treated with BDDGE as cross-linking agent through immersion for 24 hours in a cross-linker aqueous solution of 1% w/w setting up a BDDGE/Collagen ratio equal to 1 wt%[34]. The resulting material was washed from the unreacted cross-linker residues, poured into 24-wells cell-culture multiwell plates and freeze-dried. The obtained material was namely “Coll” (Fig. 4.19).

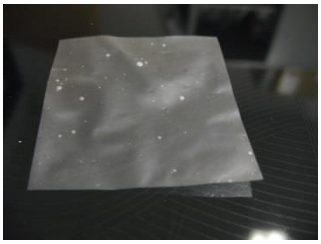

***Figure 4.19** Coll periodontal ligament-like membrane*

About the cross-linking process, five others cross-linking methods was tested: a genipin/collagen ratio equal to 2 wt% for 48 h at 25 °C, a genipin/collagen ratio equal to 1 wt% for 48 h at 25 °C, a BDDGE/collagen ratio equal to 2 wt% for 24 h at 25 °C, a ribose/collagen ratio equal to 1 wt% for 24 h at 25 °C and a ribose/collagen ratio equal to 2 wt% for 24 h at 25 °C. Respective synthesis products were called Coll_gen2, Coll_gen1, Coll_BDD2, Coll_rib1 and Coll_rib2.

4.3.2 Chemical-physical characterization

4.3.2.1 Thermal Analysis

The thermal degradation analysis was conducted on freeze-dried Coll sample and also no the not cross-linked collagen (Coll_NCL) and Coll_BDD2 as comparison. From the TGA curves and them derivative you can see three main weight loses: in the range of 50-160 °C there is a reduction in weight by about 10%, due to the breakage of inter- and intra-molecular hydrogen bonds accompanied by gradual loss of water; at about 200 °C starts the subsequent weight loss, as a degradation and decomposition of the polymer with a decrease of 50% in weight, followed by the third final weight loss in the range of 400-660°C, due to the combustion of the organic residues.

From the second and the third weight losses it's possible to note the cross-linking effect on collagen: the crosslinking treatment shifts both of degradation temperatures at high-

er values showing the thermal denaturation and degradation is hindered by increasing BDDGE cross-linking[23].

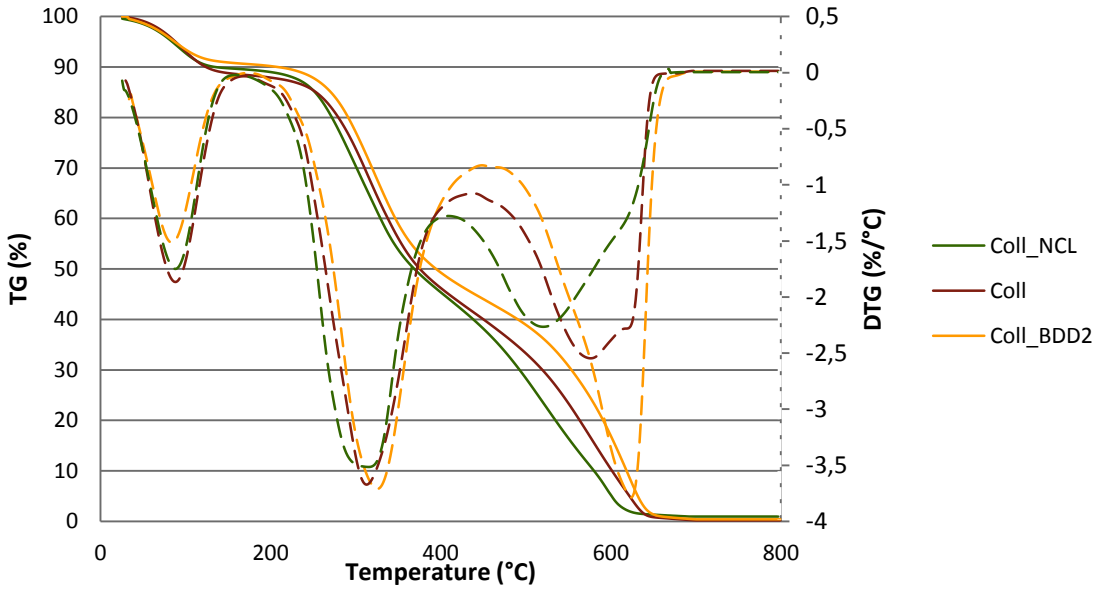

***Figure 4.20** Thermal decomposition profile (TG) and its derivative (DTG) of not cross-linked collagen (Coll_NCL), collagen cross-linked with 1% w/w of BDDGE (Coll) and collagen cross-linked with 2% w/w of BDDGE (Coll_BDD2).*

The same result can be inferred by the DTA plots relative to Coll_NCL, Coll and Coll_BDD2 shown in Fig. 4.21. From 30 to about 170 °C the exothermal peak related to the denaturation of collagen structure appears in all the three samples.

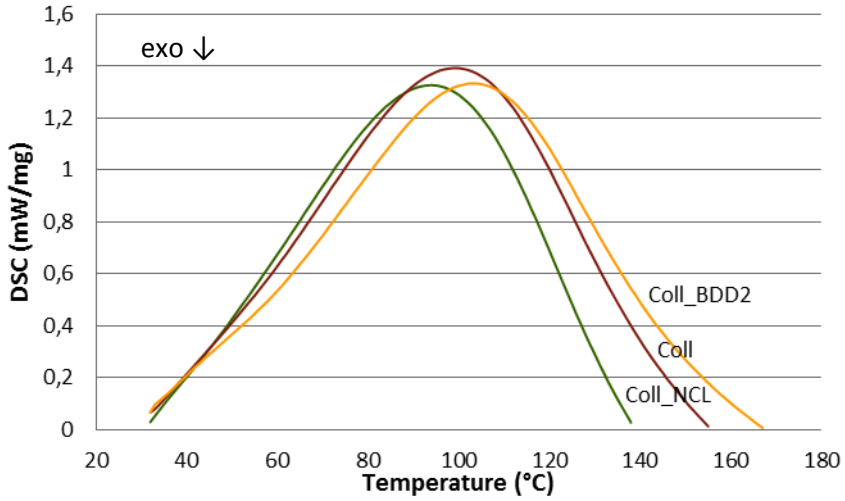

***Figure 4.21** Differential Thermal Calorimetry of not cross-linked collagen (Coll_NCL), collagen cross-linked with 1% w/w of BDDGE (Coll) and collagen cross-linked with 2% w/w of BDDGE (Coll_BDD2).*

With the increasing of the cross-linker agent the maximum of the peaks is shifted to higher temperatures (94 °C, 97 °C and 102 °C) respectively for Coll_NCL, Coll and Coll_BDD2, so also in this case, the cross-linking has taken place, improving the thermal stability of the collagen structure.

4.3.2.2 Fourier-Transform Infrared Spectroscopy

Figure 4.22A shows the FT-IR spectra of collagen before and after the crosslinking. The natural collagen spectra is characterized by a broad band at 3454 cm^{-1} assigned to the O–H stretching, and a peaks at 1452 cm^{-1} and 1242 cm^{-1}, related respectively to CH_2 and NH_2 bending[35]. Peptide group arise in addiction four bands at 3353, 2929, 1651, and 1542 cm^{-1} which are commonly known as amide A, B, I and II, respectively. The amide A and B bands are mainly associated with the stretching of N–H groups, the amide I band is originated from C=O stretching vibrations coupled to N–H bending vibrations and he amide II band arises from the N–H bending vibrations coupled to C–N stretching vibrations[36].

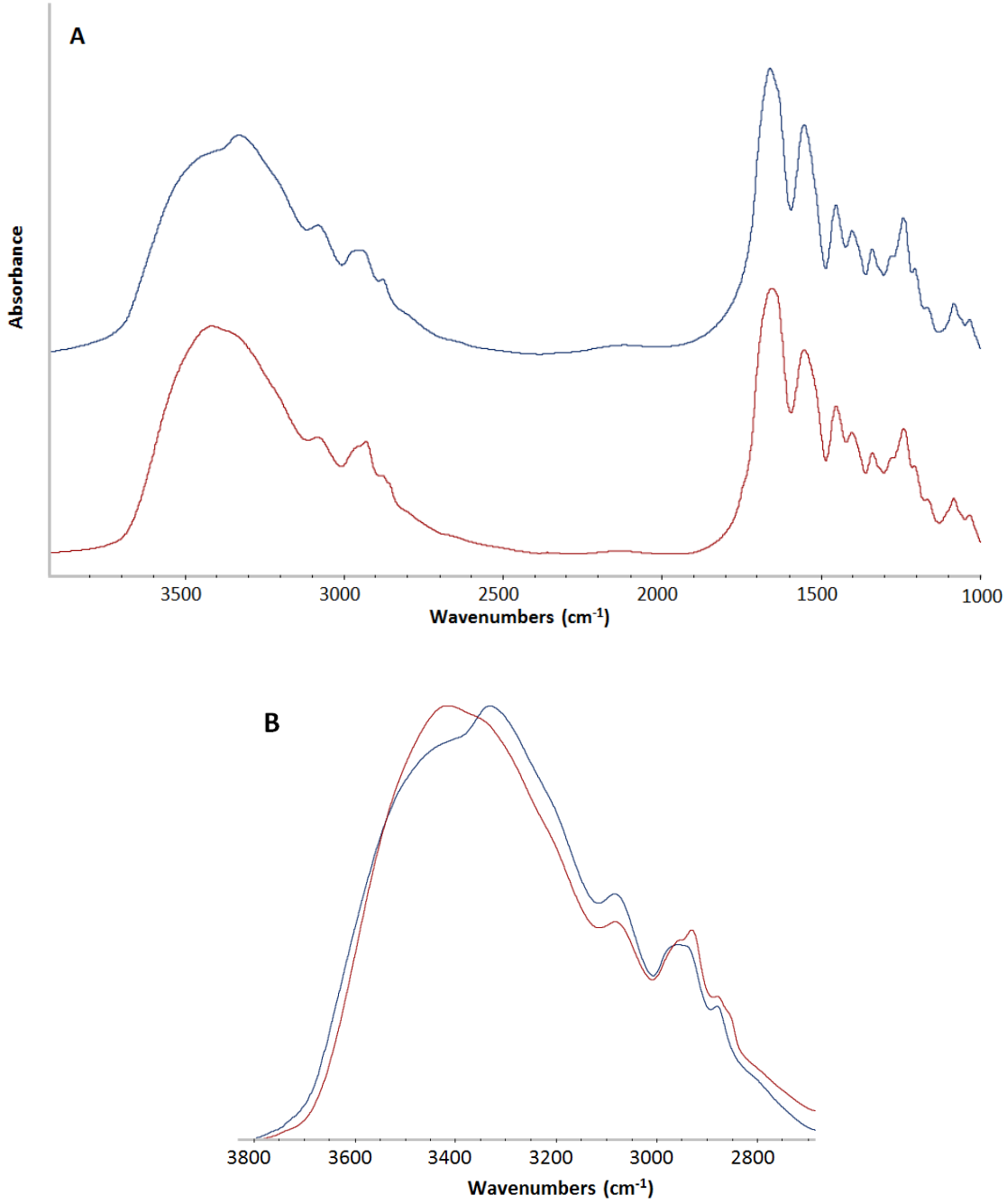

Figure 4.22 *A: FTIR analysis of Coll compared with Coll_NCL.*

B: Detail of Coll and Coll_NCL spectra from 3800 to 2700 cm^{-1}.

The intensity of amide A (Fig. 4.22B) decrease in the spectra of cross-linked collagen, indicating that the amount of $-NH_2$ group decreases. Also the spectral feature of the

amide B (Fig. 4.22B) was considerably influenced by the cross-linking, indicating a conformational change of the secondary structure of collagen matrix[37].

4.3.2.3 Scanning Electron Microscope

The cross-section morphology of freeze-dried Coll sample at various magnification is shown by SEM images in Fig. 4.23; Coll_NCL, Coll_BDD2, Coll_gen1, Coll_gen2, Coll_rib1 and Coll_rib2 are shown as comparison.

The final Coll scaffold owns a homogeneously structure (Fig. 4.23A), with wide and open porosity (Fig. 4.23B). It's possible to see onto the structure collagen fibers condensed in sheets (Fig. 4.23C) and also single fibers with the typical alternating light and dark bands correspond to the 40-nm gaps between pairs of aligned collagen triple helices.

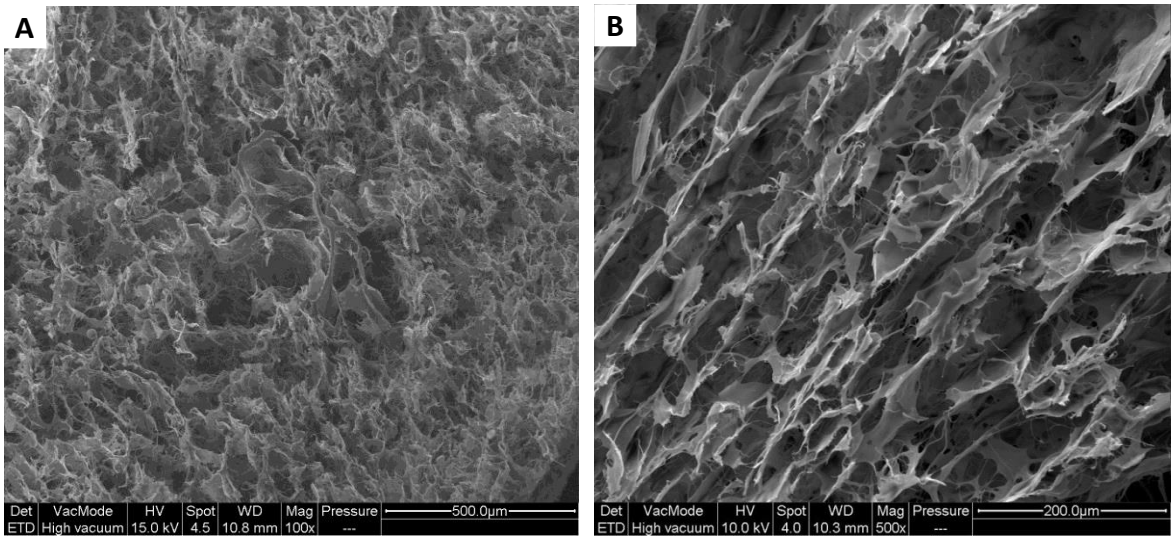

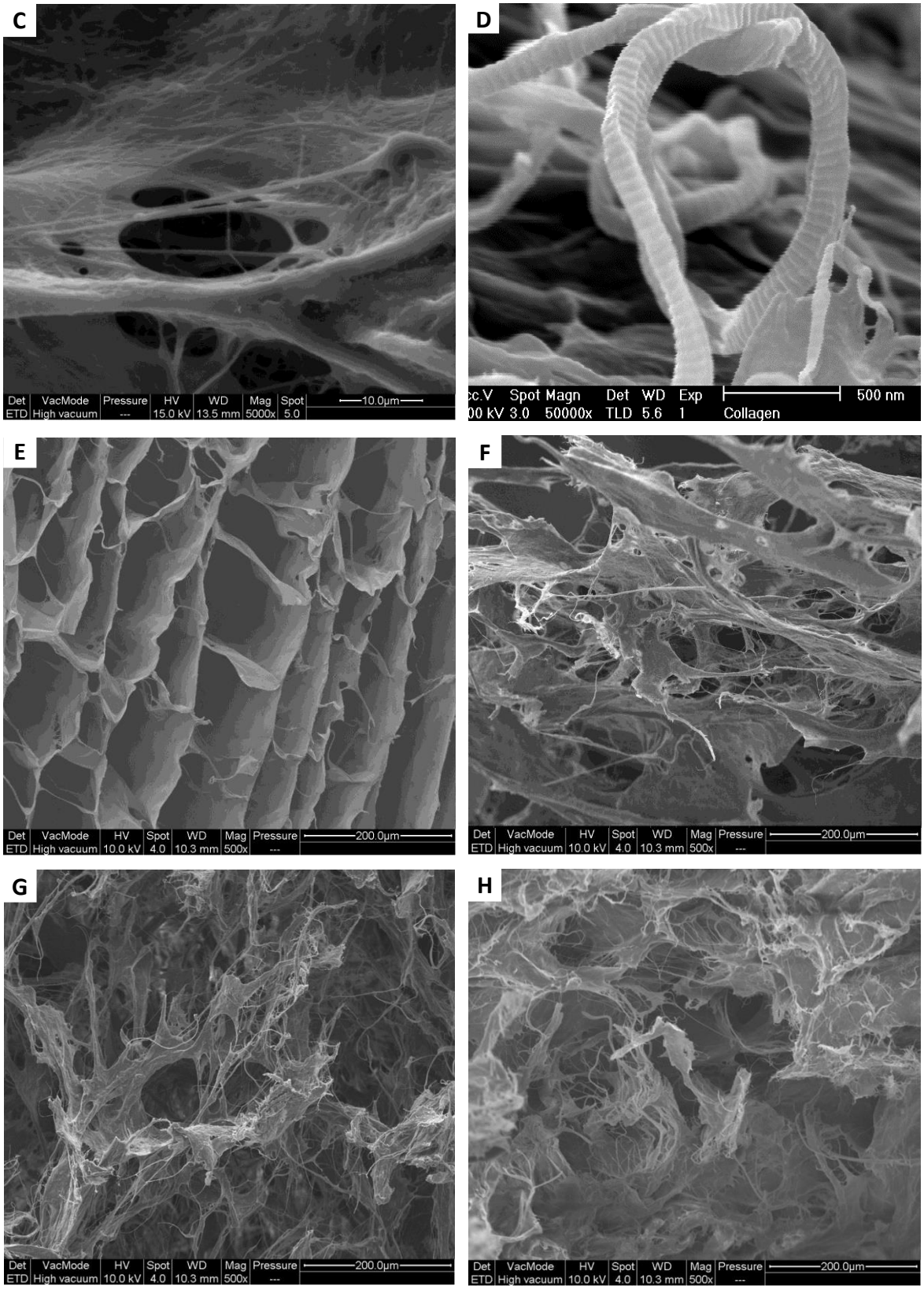
C
Det VacMode Pressure HV WD Mag Spot
ETD High vacuum --- 15.0 kV 13.5 mm 5000x 5.0
10.0µm
D
cc.V Spot Magn Det WD Exp
00 kV 3.0 50000x TLD 5.6 1
500 nm
Collagen
E
Det VacMode HV Spot WD Mag Pressure
ETD High vacuum 10.0 kV 4.0 10.3 mm 500x ---
200.0µm
F
Det VacMode HV Spot WD Mag Pressure
ETD High vacuum 10.0 kV 4.0 10.3 mm 500x ---
200.0µm
G
Det VacMode HV Spot WD Mag Pressure
ETD High vacuum 10.0 kV 4.0 10.3 mm 500x ---
200.0µm
H
Det VacMode HV Spot WD Mag Pressure
ETD High vacuum 10.0 kV 4.0 10.3 mm 500x ---
200.0µm

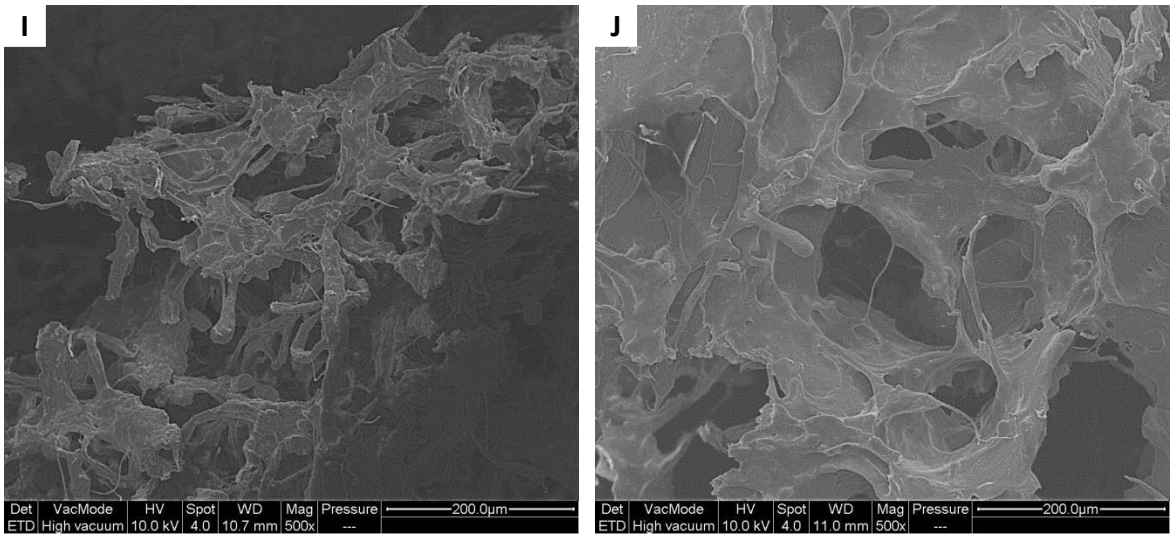

Figure 4.23 *SEM images of Coll at 100x (A) and 500x (B) magnification. Detail of morphological feature of collagen sheet at 5000x (C) collagen fiber at 50000x (D) and comparison with Coll_NCL (E), Coll_BDD2 (F), Coll_gen1 (G), Coll_gen2 (H), Coll_rib1 (I) and Coll_rib2 (J).*

The collagen scaffold before cross-linking treatments (Fig. 4.23E) show an orderly and regular 3D morphology; this effect occurs because during the freezing of freeze-drying process, the collagen fibers are not incorporated into the solid–liquid interface but rejected from it[38]. This high mobility of the fibers comes from the low assembling of the material and what emerges is that the collagen is highly concentrated in the non-crystallized channels between the ice crystals and the pore structure is built up from parallel collagen layers connected by collagen walls.

Regardingthe cross-linked collagen (Fig.4.23B, E, F, G, H, I, J), SEM images show, for the entirety, structures with pores less organized and tighter. It is clear that the cross-link reduced polymer mobility during the freeze-drying process, so the 3D geometry arises fewer and fewer from the morphology imposed by the ice growing during freeze-drying, while increases the component of the molecule packing resulting from the cross-linking process. Coll and Coll_rib1 still show less regular but open porosity, with an interconnected network of fibrils; Coll_BDD2, Coll_rib2, Coll_gen1 and Coll_gen2 show instead random and less porous structure. This effect is probably caused both by the lower water content of the dispersions before freeze-drying, but also by the high density of links

between fibers which induce them to be combined to form sheets, leading to the fusion of smaller pores[39]. Thus the cross-linked collagen fibers result too stiff to be displaced by the growing of ice-crystals and they get encapsulated into the solid–liquid structure. The resulting scaffolds, ones dried, show more sheet-like structures with wide but few pores.

4.3.2.4 Swelling and degradation test

As previous mentioned, a low degradation degree and high swelling properties are crucial in the view of scaffold implantation, because for a successful tissue regeneration the scaffold has to preserve its structure until cell colonization and must be readily permeable by body fluids for nutrient diffusion and waste removal. In order to test them resistance to degradation and them swelling properties, Coll, Coll_NCL, Coll_BDD2, Coll_gen1, Coll_gen2, Coll_rib1 and Coll_rib2 was tested in physiological.

The degradation test (Fig. 4.24) shows that the rate of weight loss is higher for not cross-linked collagen, which after 21 days lost about the 8% of its weight, and for collagen cross-linked with 1% w/w ratio of ribose (4,1% after 21 days). About the others materials, after an initial and limited weight loss, the scaffolds remain stable until the end of the test, with a final weight loss between 0.7% and 3%.

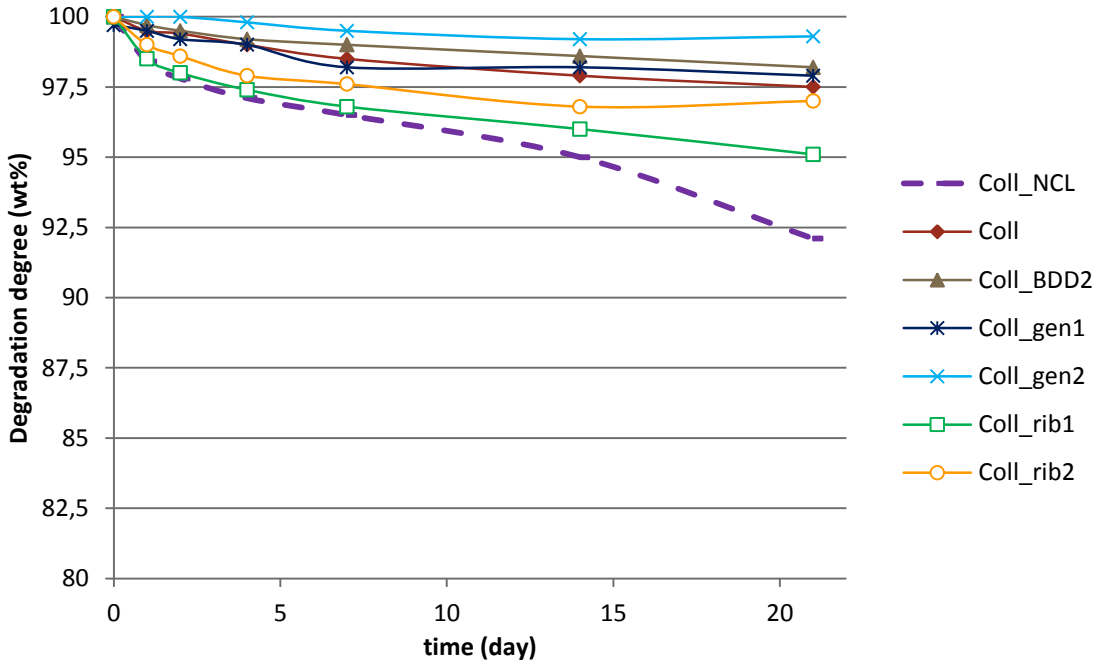

***Figure 4.24** Degradation weight loss for collagen not cross-linked and cross-linked in different ways.*

The swelling degree of the various collagen scaffolds change a lot at varying of cross-linking conditions, from about 950 to 600% of them starting weight (regarding the not cross-linked scaffold and the scaffold cross-linked with 2% w ratio of genipin respectively). The water uptake ability could be attributed to both of the hydrophilicity of the material and the three-dimensional structure of the scaffold. Indeed, the swelling ratio decreases as the cross-linking degree is increases because of the decrease of the hydrophilic groups[40], and because the melting of the 3D ordered structure will cause the reduction of the porosity, hence, the volume for water storage, leading to the decrease of the swelling capacity[41].

All the scaffold however show a fast hydration, since after 4-8 hours reach the plateau.

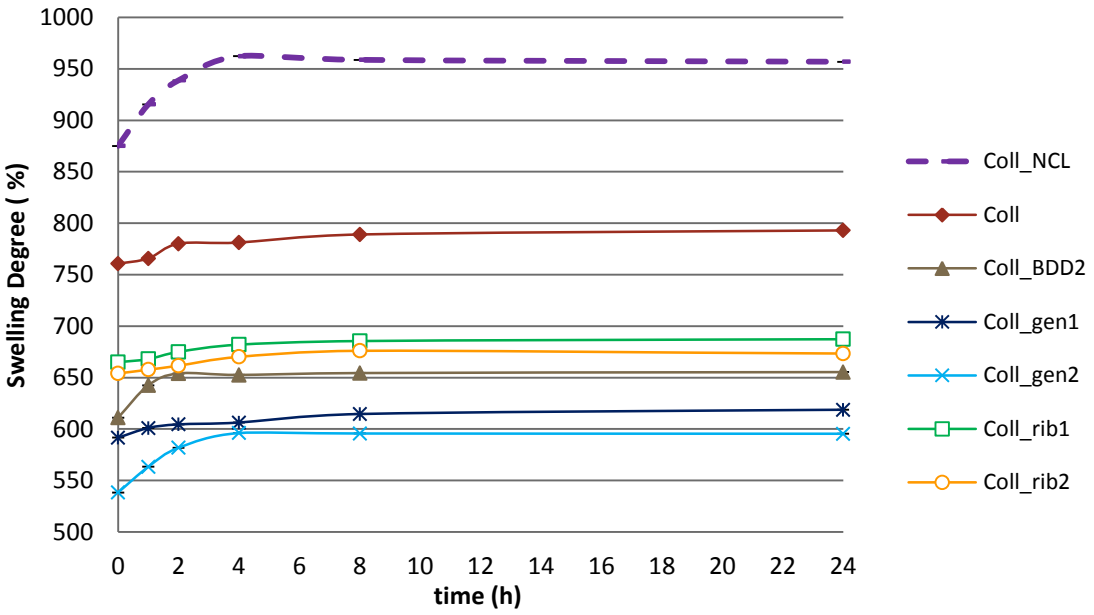

Figure 4.25 *Swelling degree for alveolar bone-like scaffolds synthetized at various temperatures (A) and stabilized with various kind and amount of cross-linkers (B).*

4.4 Periodontal apparatus: cementum

The third layer belonging to the scaffold mimicking the periodontal apparatus is represented by the cementum, similar in structure to bone but is less hard since its mineralization degree is about 50%. Within the periodontal apparatus, this section has the task of binding to the periodontal ligament ensuring a strong adhesion between the tooth and its anatomic site.

In this part of the PhD project we wanted to create a very thin layer morphologically and chemically close to the natural cementum and to do so we exploited a bio-inspired synthesis of hydroxyapatite, in order to create a non-stoichiometric nanostructured apatitic phase, and the electrospinning of a bio-erodible polymer, which enables the production of mats composed by non-woven micrometric fibers. In this way it's possible to produce a porous and very thin layer of fibers added with an high amount of the mineral component.

In order to rise higher bio-activity and bio-reabsorbability, iron ions was introduced into the hydroxyapatite cell structure prompting magnetic features.

4.4.1 Synthesis process

The first step in the preparation of the cementum-like scaffold consist in the synthesis of the magnetic inorganic component. The synthesis of FeHA powder was carried out by adding thr iron(III) chloride hexahydrate solution (17.86 g of $FeCl_3 \cdot 6H_2O$ in 75 mL of water) and the iron(II) chloride tetrahydrate solution (12.74 g of $FeCl_2 \cdot 4H_2O$ in 75 mL of water), as sources of Fe^{3+} and Fe^{2+} ions respectively, into a suspension of calcium hydroxide (50 g of $Ca(OH)_2$ in 400 mL of H_2O) at 40°C. A phosphoric acid solution (44.40 g of H_3PO_4 in 300 mL of H_2O) was then added dropwise into the basic suspension over a period of 2 h, under constant heating and stirring thanks to a heating mantle and me-

chanical stirring (Fig. 4.26). During this neutralization process into the reaction flask pH decreases from 12 to 5.

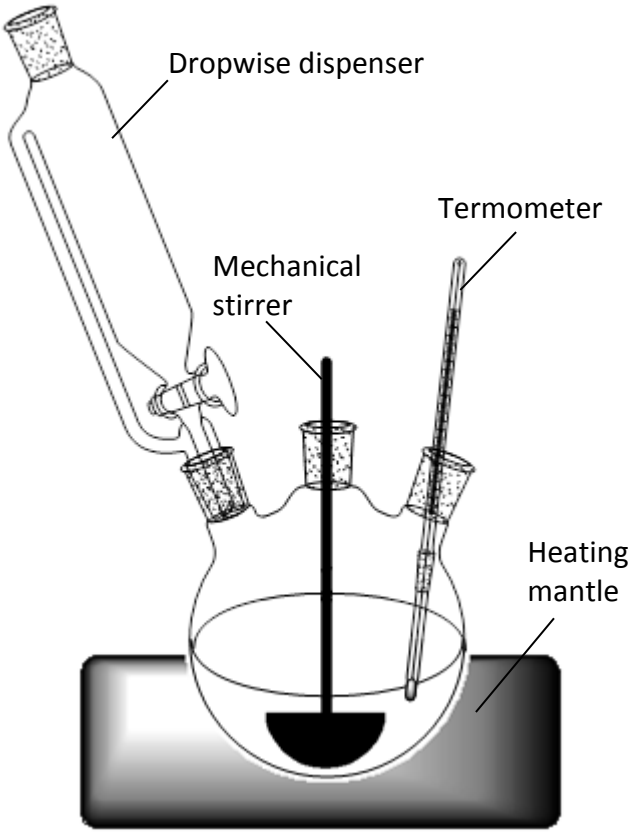

***Figure 4.26** Equipment for the synthesis of FeHA powder*

The amount of reactants was set up in order to keep the calcium/phosphorus ratio equal to 1.667, so that a competition between Ca^{2+} and the substituting ions (Fe^{3+} and Fe^{2+}) could be established with PO_4^{3-}; the total amounts of iron ions with respect to calcium ions were adjusted so as to obtain Fe/Ca=20 mol%. During synthesis, a brownish precipitate formed; when the dripping of the phosphate solution was completed, the precipitate was left to ripen in the mother liquor for 24 hours, then the supernatant was eliminated and the product was washed three times in 1 L of distilled water and centrifuged. The product, identified as “FeHA” was stored at 4°C into a solution of 100 mg/L to avoid the particles aggregation and, if necessary, freeze-dried and sieved under 150 µm

(Fig. 4.27A, B). Other two different temperature were investigated for FeHA synthesis, 25°C and 50°C, and the respective products were called FeHA_25 and FeHA_50.

About the production of the final FeHA+CA fleeces, firstly the dry FeHA, synthetized as previously described, was added to the solvent (composed of 80:20 wt. butanone/butanol) under constant magnetic stirring, followed by sonication for 30 minutes and further shaking with vortex mixer. After this dispersion step, cellulose acetate (CA) was added in order to obtain a 35% w/w. solution of CA respect to the solvent and CA/FeHA ratio of 1; the mixture was shaken again until the CA dissolved completely. The fleeces were spun for four consecutive times on a water soluble PVA-foil (SOLVY, Gunold; thickness of 20 µm) and was treated at 70°C and 200 mbar in a desiccator to remove residual solvents, especially butanol which cannot evaporates completely during the spinning process because of its high boiling point. The final scaffold (Fig. 4.27) was called FeHA+CA.

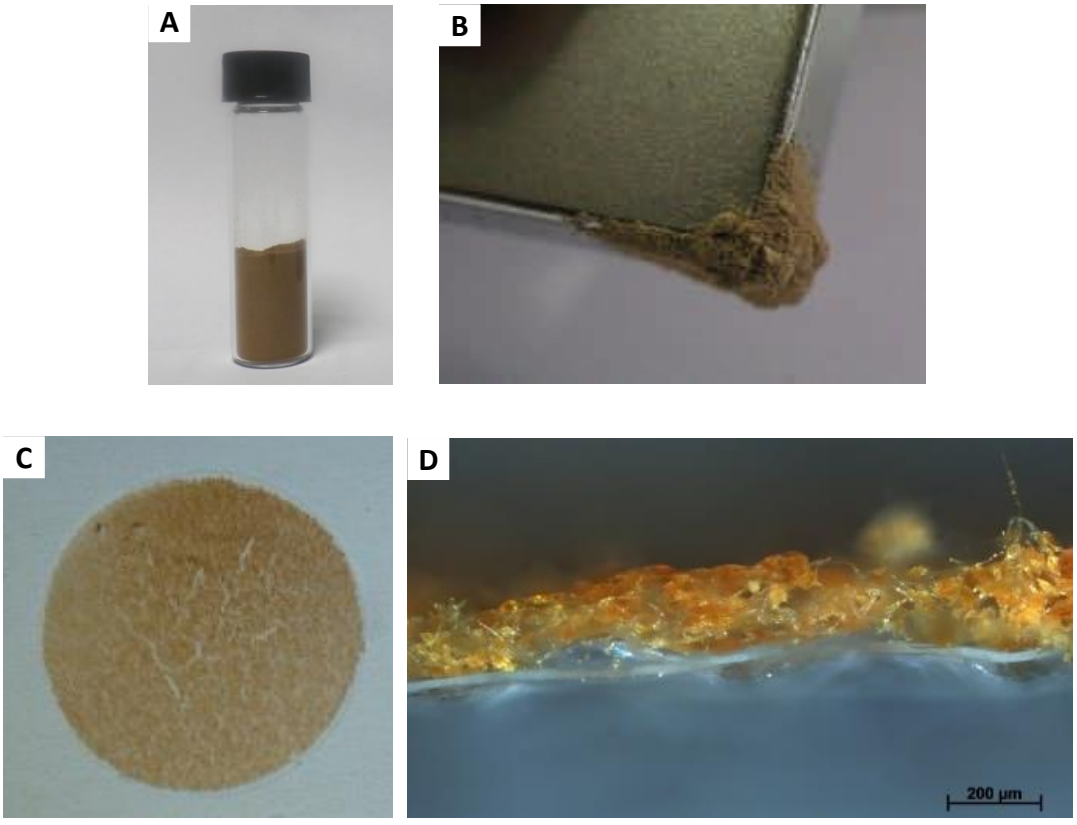

Figure 4.27 *FeHA powder (A) and FeHA powder attracted by a magnet (B), and (C, D) FeHA+CA cementum-like scaffold*

4.4.2 Chemical-physical characterization

4.4.2.1 Thermogravimetric Analysis

The TG-DTG curves relative to the FeHA+CA composite are shown in Fig. 4.28. The thermogravimetric profile shows the degradation of the organic component, with a first weak but steady weight loss from 60 to 240 °C, due to the evaporation of residual absorbed water, but also to the degradation of some possibly additives or contaminants in the sample. The main weight loss, the second, has the a maximum degradation rate at 314°C, and regars the principal thermal degradation of the cellulose acetate chains. The third and final weight loss, with the maximum rate at 358 °C, corresponds to carbonization of degraded products to ash; at the end of the analysis the overall weight loss is about 50%[24]. The total residues are about 50% wt, which regard the apatite component of the composite.

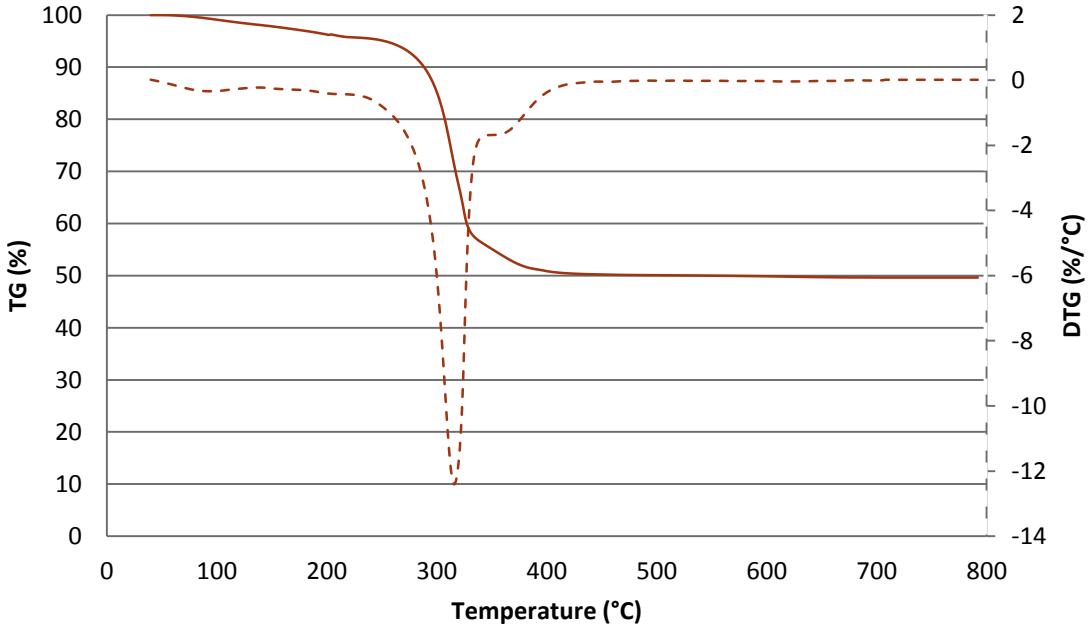

Figure 4.28 *Thermal decomposition profile (TG) and its derivative (DTG) of FeHA+CA scaffold.*

Thermal analysis performed on FeHA+CA showed an extend of mineral component of about 50%, very close to the one nominally set up and the biological cementum one.

4.4.2.3 X-Ray Diffraction

The X-ray diffraction patterns of FeHA_25, FeHA and FeHA_50 are shown in Fig. 4.29A and reveal a low-crystalline apatite[4,5], with a crystallinity extend which decreases with decreasing of the synthesis temperature.

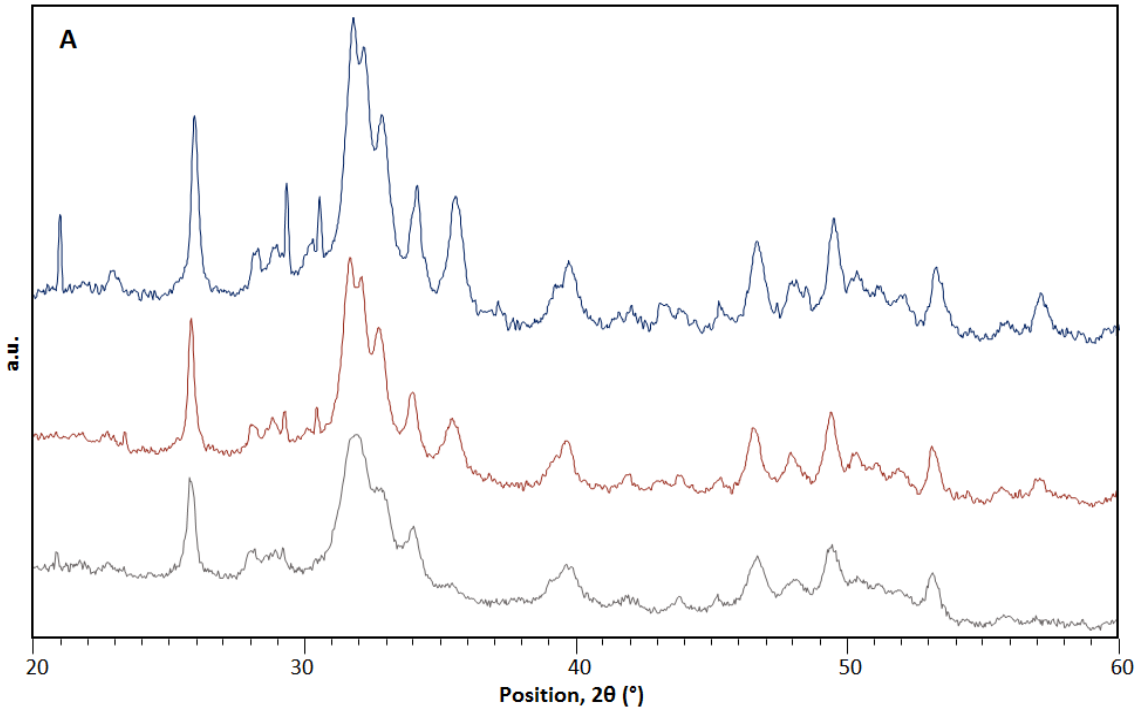

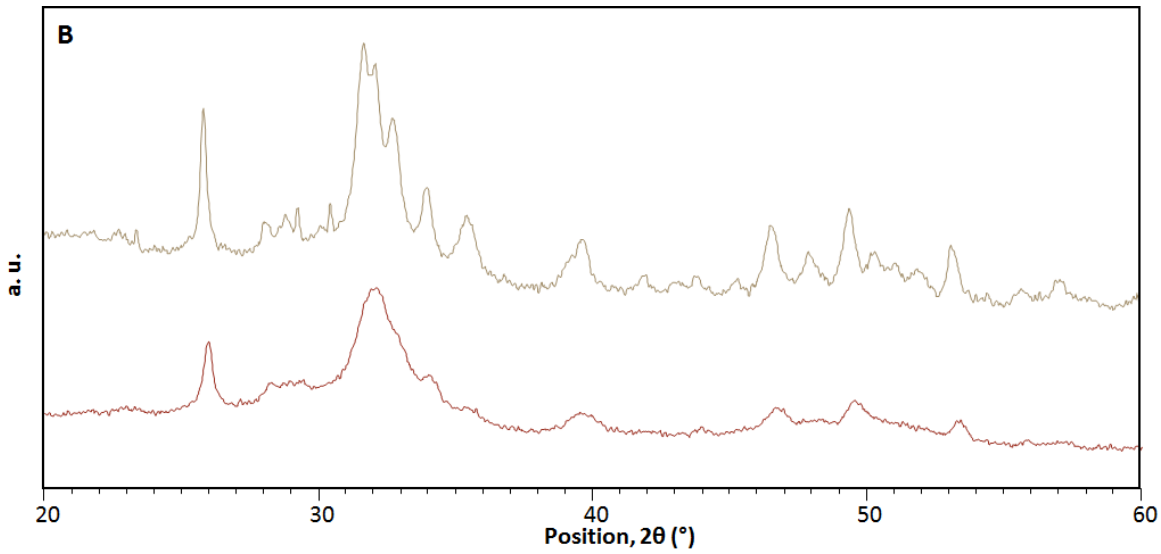

***Figure 4.29** A: XRD spectra of FeHA powder synthetized at 25°C (FeHA_25), 40°C (FeHA) and 50°C (FeHA_50). B: XRD spectra of FeHA powder and FeHA+AC scaffold.*

In FeHA_50 spectra it's also possible to see other secondary phase like brushite (ICDD card n. 09-0077), the main peak of which occurs at 2θ=21.0°, and magnetite (ICDD card n. 025-1376), with the main peaks at 2θ=35,4° and 57,3°. Even if in smaller amounts, also in FeHA it's possible to see the presence of magnetite, while there isn't in FeHA_25 sample. It's clear that the temperature increasing causes the increasing of both magnetite formation and apatite crystallization[42]. From the XRD analysis it's also possible to confirm the substitution of iron ions into the hydroxyapatite lattice at Ca-substituting position and not at cell interstitial position: the replacement of the calcium ion by an iron ion has little effect on the XRD pattern, contrariwise the introduction of an iron ion into one of the possible interstitial positions heavily modifies the relative intensities of the peaks[43]. In all of the samples the presence of iron hampers the crystalline organization, making peaks broad and lowering the resolution in XRD spectra (the crystallinity degree is lower than the non-substituted hydroxyapatite prepared at the same temperature[44]), but doesn't modify the structure of the apatitic phase and the XRD main profile.

Finally FeHA and FeHA+CA spectra was compared (Fig. 4.29B) and it's possible to see that despite the high content of amorphous cellulose acetate, the X-Ray diffraction profile of FeHA+CA the presence of hydroxyapatite was identified with its main peak at 25,7° and 32,0°.

4.4.2.4 Fourier-Transform Infrared Spectroscopy

The FTIR spectra of FeHA+CA (Fig. 4.30) shows the typical bands of the CA at 3472 cm^{-1} (attributed to the O–H stretching), 2954 and 2891 cm^{-1} (stretching of C–H in CH_3 and CH_2 groups), 1745 and 1651 cm^{-1} (symmetric and asymmetric stretching of C=O), 1441 cm^{-1} (bending of CH_2) and 1375 cm^{-1} (bending of CH)[45;46]. Additionally, bands of FeHA becomes visible around 1032 cm^{-1}, 604 cm^{-1} and 562 cm^{-1}[9].

Also by the FTIR spectrum of the FeHA+CA it's clear that the incorporation of the FeHA into the fibrous CA structure was successful.

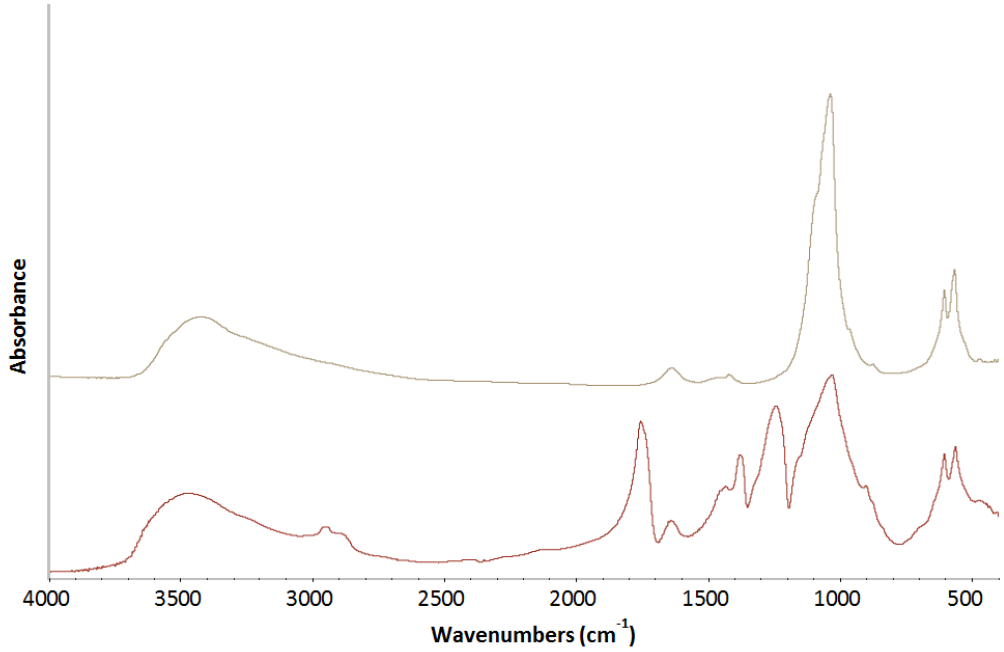

***Figure 4.30** FTIR analysis of FeHA+CA compared with FeHA.*

4.4.2.5 Scanning Electron Microscopy

SEM images of FeHA powder and FeHA+CA scaffold at various magnification are shown in Fig. 4.31.

Paying attention to the FeHA images, it's possible to note that the powder is composed by micrometric particle (Fig. 4.31A), which are agglomerate of smaller nanoparticle (Fig. 4.31B); from these images it's possible to confirm the nanostructural nature of this magnetic powder.

From the FeHA+CA (Fig. 4.31C, D) images, instead, it can be inferred that the final scaffold is formed by several layers of micrometric bead-on string fibers. The fiber surfaces are rough, a sign that FeHA is embedded into the CA fibers. The mat show a very high density of very tight pores, exactly how we want to achieve, since the cement is a dense and avascularized tissue without cells inside. The mean fiber thickness results 4±3 with an average porosity of 44±7% of the area, while the average mats thickness is 200±100 µm.

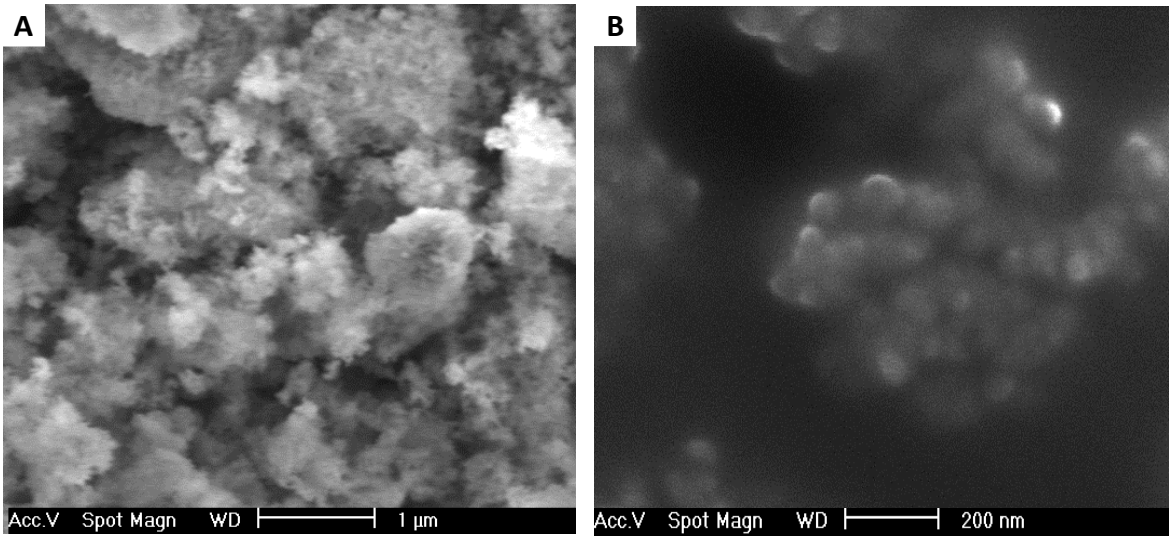

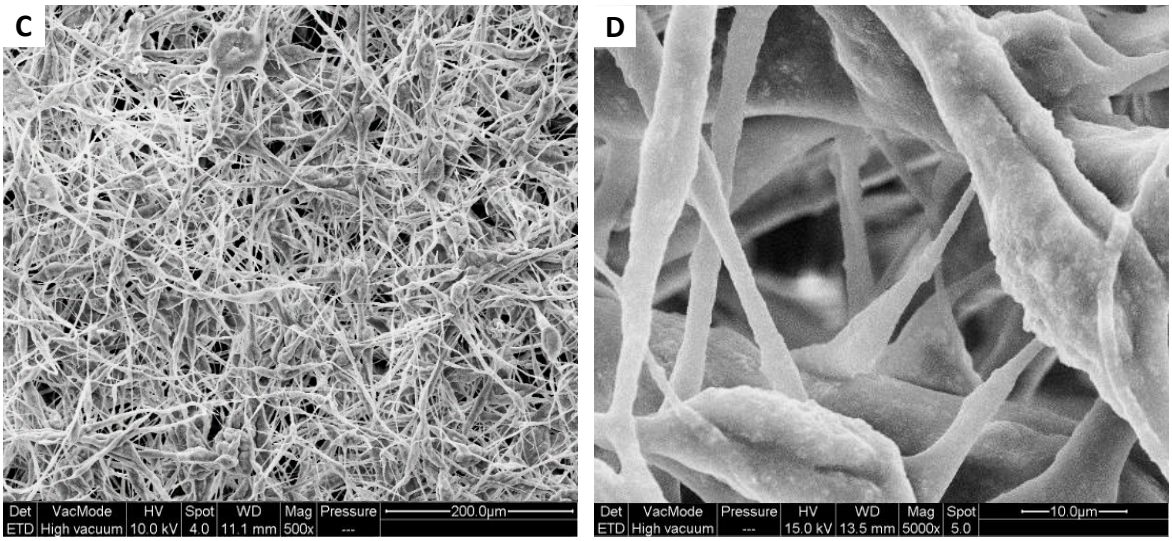

Figure 4.31 *SEM images of FeHA at 20000x (A) and 75000x (B) magnification. Images of FeHA+CA at 500x (A) and 5000x (B) magnification.*

4.4.2.6 Inductively Coupled Plasma Atomic Emission Spectroscopy

ICP analysis was conducted on FeHA to define the overall content of Ca, P and Fe constructing the mineral phase of FeHA+CA composite; Tab. 4.5 shows the results of the analysis.

Materials	(Fe+Ca)/P (mol)	Ca/P (mol)	Fe/Ca (mol)	Fe/(Ca+Fe) (mol)
FeHA_25	1,67 ± 0,02	1,37 ± 0,03	21,6 ± 0,3	17,8 ± 0,02
FeHA	1,69 ± 0,05	1,37 ± 0,07	22,7 ± 0,5	19,0 ± 0,01
FeHA_50	1,70 ± 0,03	1,38 ± 0,03	23,9 ± 0,4	19,27 ± 0,03

Table 4.5. *ICP features of FeHA synthetized at 25 °C (FeHA_25), 40 °C (FeHA) and 50 °C (FeHA_50).*

The ICP analysis confirm the presence of iron into the apatitic powders and that the replacement of the iron has taken place efficiently, because the 96,3%, 90,0% and 89,0% of the iron nominally introduced as reagent was introduced into the hydroxyapatite lat-

tice respectively for FeHA_50, FeHA and FeHA_25. Furthermore, for all the sample the Ca/P molar ratio is lower than the one of the stoichiometric hydroxyapatite (1,68), but the (Fe+Ca)/P molar ratio is very close to the theoretical value, confirming the replacement of calcium with iron. As already seen in the composite analysis, also in mineral phase synthetized alone, the highest inclusion of iron ions into hydroxyapatite lattice is reached with the increasing of the synthesis temperature.

4.4.2.7 Swelling and degradation test

Swelling and degradation test in physical condition was conducted for FeHA+CA mat and the results are shown in Fig. 4.31 and 4.32 respectively.

Regarding the degradation behavior it's easy to see that the material shows suitable properties to be used as implanting material, as in 21 days in PBS at 37° C it's fully stable, with a final weigh loss of about 1%.

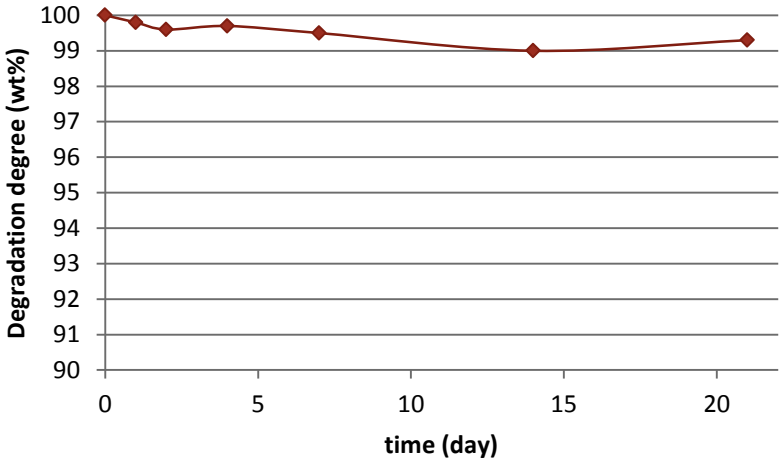

***Figure 4.31** Degradation weight loss for the FeHA+CA cementum-like layer.*

This material shows a poor swelling properties as it uptake water only up to 93% of its dry weight, probably due to the low porosity, but since it has to be assembled to other materials with high swelling, cells growth should not be affected.

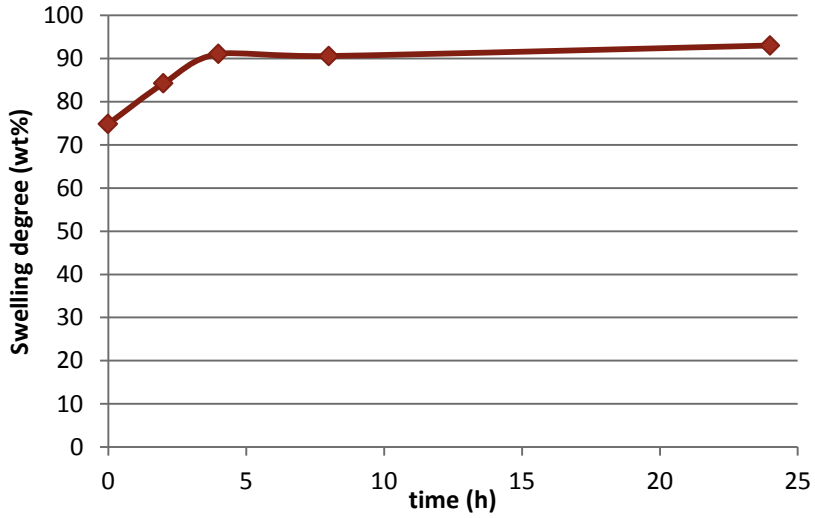

Figure 4.32 *Swelling degree for the FeHA+CA cementum-like layer.*

4.4.2.9 Magnetic susceptibility

The magnetization curves, as saturated moment in function of applied magnetic field for FeHA, CA and FeHA+CA are shown in Fig. 4.33, and the results resumed in Tab. 4.6.

The curves show no magnetic features for the organic component and the typical superparamagnec behavior for FeHA and its composite, since the M_S/M_R value, which indicates the amplitude of hysteresis at zero-field, is around 0. Thanks to the quite high synthesis temperature FeHA sample shows a high magnetic value and the mixing with CA and the electrospinning process doesn't affect this property, since also the composite show a high value of magnetization, considering an overall mineral amount of 49%.

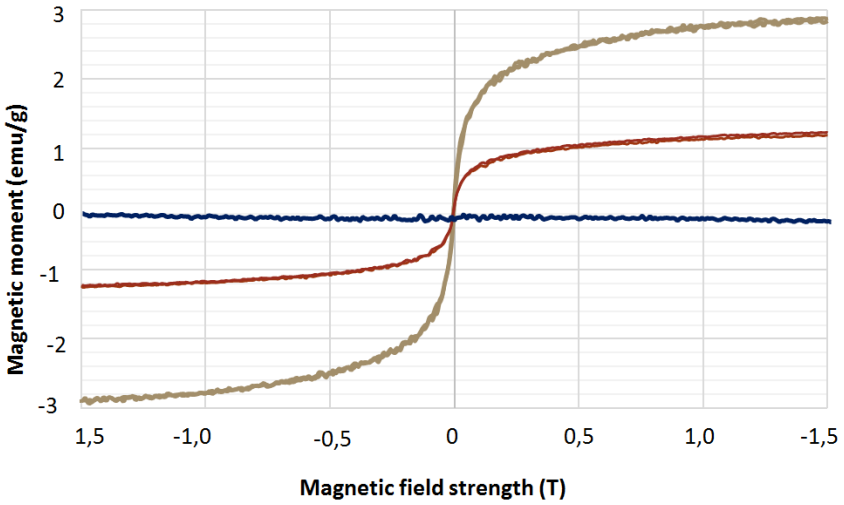

Figure 4.33 *Superparamagnetic contribution of FeHA+CA and comparison with FeHA and CA alone.*

Materials	Superparamagnetic saturated moment [emu/g]	M_s/M_R
FeHA	2.85	0.03
CA	-0.06	≈ 0
FeHA+CA	1.09	≈ 0

Table 4.6 *Magnetic features of FeHA/Coll_25, FeHA and FeHA_50 composites.*

In this way we obtained a fleece with more than double superparamagnetic value compared to the bone-like scaffold with a low amount of mineral phase. An higher magnetization is necessary because of the thickness of the layer: in order to replace the natural size of the various components of periodontal apparatus, cementum provides a lesser amount of material, so a higher magnetic power to reach a suitable signal is required.

4.5 Periodontal apparatus: assembling process

After the development of all the three single components of the periodontal-like scaffold, the assembling process is crucial in order to create a stable scaffold with strictly linked layers which don't delaminate.

In this view the FeHA/Coll was prepared and spread on a metal plate tailored for the freeze-dryer, with a thickness of about 5 mm; the wet Coll was also spread on a mylar sheet, tipped and then piled up the first layer making sure that the two interfaces adhere perfectly before removing the sheet. Finally the FeHA+CA fleece was put into deionized water in order to dissolve the PVA foil on which it was electrospun, and the residual PVA was then removed by purging the composite with pure water. Then it was lying on a mylar sheet tipped and piled up on the top of the structure, making it adhere well to the previous layer. This material was then freeze-dried leaving the mylar sheet on its top. The obtained material is shown in Fig. 4.34.

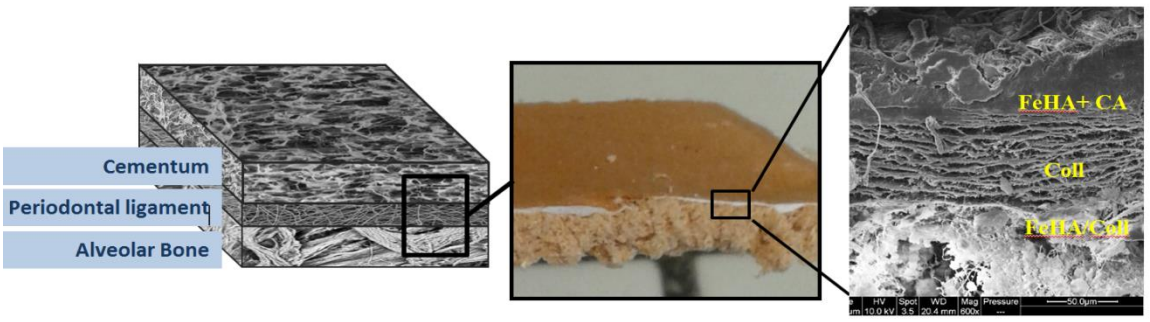

Figure 4.34 *FeHA/Coll – Coll – FeHA+CA tri-layer scaffold mimicking the periodontal apparatus*

4.5.1 Chemical-physical characterization

4.5.1.1 Scanning Electron Microscope

The cross-section morphology of the tri-layer scaffold at various magnification is shown by SEM images in Fig. 4.35A, B; details of the two interface of the scaffold was also shown in Fig. 4.35 C, D.

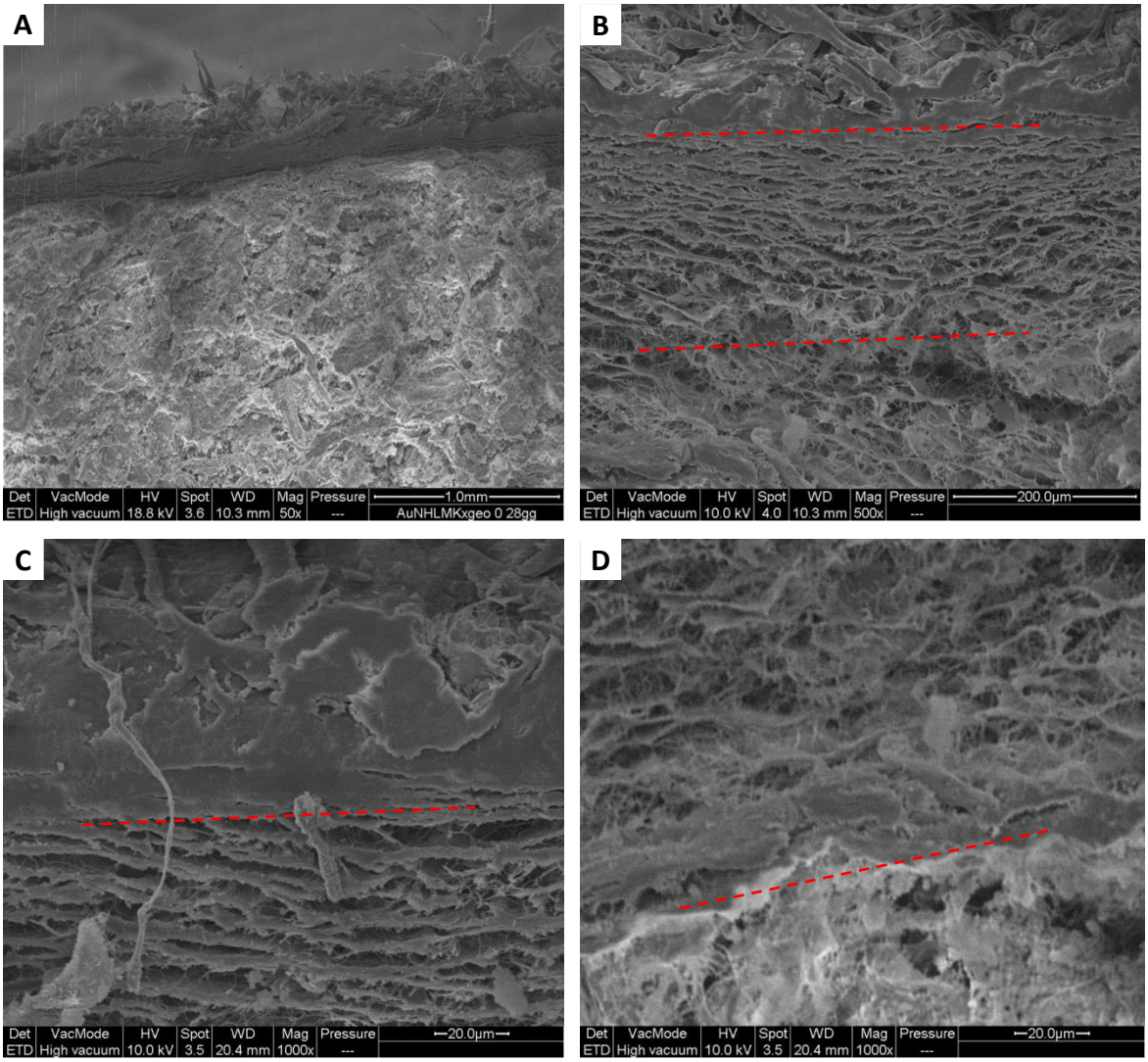

***Figure 4.35** SEM images of the tri-layer scaffold at 50x (A) and 500x magnification (B); the broken line indicates the separation between the layers. Detail of FeHA+CA – Coll interface (C), and detail of Coll – FeHA/Coll interface (D) at 2000x magnetization.*

These images show a very compact scaffold, with layers well adherent one to another. The cementum-like layer preserved its compact morphology, whereas the ligament-like

and bone-like layers retained them porous structure. So we can conclude that the final scaffold was efficiently generated.

4.5.2 Biological characterization

4.5.2.1 Cell viability assay

Qualitative cell viability test was conducted on FeHA/Coll, Coll and FeHA+CA samples with Live&Dead assay. Fig. 4.36 show that the totality of the cell seed on all three scaffold are alive because once observed with a fluorescence microscope, the intracellular esterase activity of the live cells allow an intense green fluorescence, while is not present red fluorescence relative to nuclei of dead cells. In Fig. 4.36B, relative to the ligament-like scaffold, the cells are more spread compared to those of the other materials, however there is the absence of dead cells.

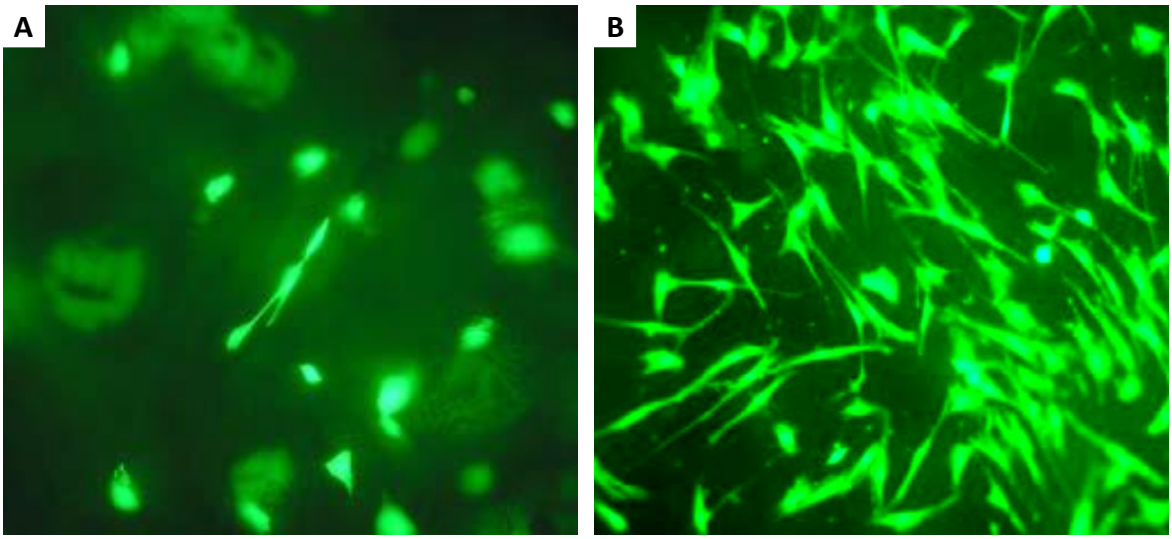

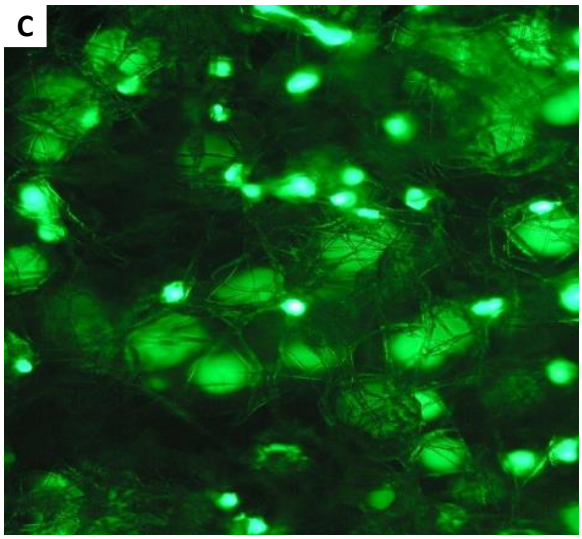

Figure 4.36 *Cell viability of cell-seed FeHA/Coll (A), Coll (B) and FeHA+CA (C) scaffolds analyzed by the Live/Dead assay at magnetization of 20x.*

We can deduce that the chemical composition and the morphology of the scaffolds resulted suitable for a cell survival and colonization.

4.5.2.2 Cytotoxicity test by direct contact

Quantitative biocompatibility tests were conducted according to ISO 10993-5[15] and resulted data are shown in Tab. 4.7. All the three material show no cytotoxicity since cell growth inhibition isn't higher than 30% for none of materials.

Materials	% of viability	Results
FeHA/Coll	71	Non cytotoxic
Coll	88	Non cytotoxic
FeHA+CA	73	Non cytotoxic

Table 4.7 *Biological evaluation of cytotoxicity of the material composing the tri-layer scaffold.*

FeHA/Coll and FeHA+CA exhibit some cell growth inhibition which level is close but still lower to the level permitted in the ISO standard. One can assume that the weakly cyto-

toxic effect observed can disappear mimicking in vivo conditions. In facts, implantation sites are open environments that can rapidly eliminate the slightly compounds; this is not the case for an *in vitro* test, where the environment is closed[47].

These tests confirms the results previously obtained by the qualitative test so the tri-layer scaffold composed by FeHA/Coll – Coll – FeHA+CA results suitable for medical applications.

4.5.3 Conclusion

A magnetic collagen-based hybrid scaffold was developed using a bio-mimetic approach, exploiting the natural pH-depend assembling of collagen molecules and inducing, at the same time, the heterogeneous nucleation of the apatitic phase. In order to produce a magnetic scaffold, ferrous and ferric ions was introduced during the bio-mineralization process and the temperature synthesis was adjusted for obtain a material as magnetic as possible. The TGA, XRD and ICP analysis proved that the mineralization occurred and the substitution of calcium ions with iron ions was reached. Magnetic measurement has confirmed the presence of a superparamagnetic phase and with swelling and degradation test we proved that the scaffold is suitable for implantation.

Non-mineralized scaffold was developed exploiting the properties that a suitable cross-linking process confers to the material. By DSC, FTIR and SEM images we proved that the cross-linking occurs and from swelling and degradation process was chosen the most appropriate material for cell infiltration and attachment.

Finally was developed an highly magnetic apatitic powder, optimizing the synthesis condition to minimize the formation of magnetite as secondary phase and introduced into an electrospun fleece, obtaining a thin and porous layer with an high amount of mineral phase. TGA, XRD and ICP analyses shown that the material has the required chemical properties to mime the cementum tissue and by SEM images it was possible to observe

that a porous but compact morphology was reached. Degradation test showed in adding a very high strength in physiological environment.

Assembling of the try-layer was optimized in order to preserve the desired morphology for all the layers and prevent the delamination. For these reason the layers was assembled still damp and all the material was subjected to an unique process of freeze-dying.

At the end all the developed materials were subjected to *in vitro* test in order to ensure about their biocompatibility with good results for each layer.

The material so produced has all of the chemical and morphological characteristics to be compatible for depth analysis with “in vivo” implantation.

4.6 References

[1] C. M. Serre, M. Papillard, P. Chavassieux, J. C. Voegel, and G. Boivin, “Influence of magnesium substitution on a collagen-apatite biomaterial on the production of a calcifying matrix by human osteoblasts.,” *J. Biomed. Mater. Res.*, vol. 42, no. 4, pp. 626–33, Dec. 1998.

[2] C.-Y. Chen, C.-J. Ke, K.-C. Yen, H.-C. Hsieh, J.-S. Sun, and F.-H. Lin, “3D porous calcium-alginate scaffolds cell culture system improved human osteoblast cell clusters for cell therapy.,” *Theranostics*, vol. 5, no. 6, pp. 643–55, Jan. 2015.

[3] S. Zmora, R. Glicklis, and S. Cohen, “Tailoring the pore architecture in 3-D alginate scaffolds by controlling the freezing regime during fabrication,” *Biomaterials*, vol. 23, no. 20, pp. 4087–4094, Oct. 2002.

[4] E. Landi, F. Valentini, and A. Tampieri, “Porous hydroxyapatite/gelatine scaffolds with ice-designed channel-like porosity for biomedical applications,” *Acta Biomater.*, vol. 4, no. 6, pp. 1620–1626, 2008.

[5] V. M. Rusu, C.-H. Ng, M. Wilke, B. Tiersch, P. Fratzl, and M. G. Peter, “Size-controlled hydroxyapatite nanoparticles as self-organized organic-inorganic composite materials.,” *Biomaterials*, vol. 26, no. 26, pp. 5414–26, Sep. 2005.

[6] L. Fan, Y. Du, R. Huang, Q. Wang, X. Wang, and L. Zhang, “Preparation and characterization of alginate/gelatin blend fibers,” *J. Appl. Polym. Sci.*, vol. 96, no. 5, pp. 1625–1629, Jun. 2005.

[7] R. K. Brundavanam, G. E. J. Poinern, and D. Fawcett, “Modelling the Crystal Structure of a 30 nm Sized Particle based Hydroxyapatite Powder Synthesised under the Influence of Ultrasound Irradiation from X-ray powder Diffraction Data,” *American Journal of Materials Science*, vol. 3, no. 4. Scientific & Academic Publishing, pp. 84–90, 2013.

[8] J. . Muyonga, C. G. . Cole, and K. . Duodu, “Fourier transform infrared (FTIR) spectroscopic study of acid soluble collagen and gelatin from skins and bones of young and adult Nile perch (Lates niloticus),” *Food Chem.*, vol. 86, no. 3, pp. 325–332, Jul. 2004.

[9] J. Reyes-Gasga, E. L. Martínez-Piñeiro, G. Rodríguez-Álvarez, G. E. Tiznado-Orozco, R. García-García, and E. F. Brès, "XRD and FTIR crystallinity indices in sound human tooth enamel and synthetic hydroxyapatite.," *Mater. Sci. Eng. C. Mater. Biol. Appl.*, vol. 33, no. 8, pp. 4568–74, Dec. 2013.

[10] J. Gómez-Morales, M. Iafisco, J. M. Delgado-López, S. Sarda, and C. Drouet, "Progress on the preparation of nanocrystalline apatites and surface characterization: Overview of fundamental and applied aspects," *Prog. Cryst. Growth Charact. Mater.*, vol. 59, no. 1, pp. 1–46, 2013.

[11] N. Roveri, G. Falini, M. . Sidoti, A. Tampieri, E. Landi, M. Sandri, and B. Parma, "Biologically inspired growth of hydroxyapatite nanocrystals inside self-assembled collagen fibers," *Mater. Sci. Eng. C*, vol. 23, no. 3, pp. 441–446, Mar. 2003.

[12] S. K. Papageorgiou, E. P. Kouvelos, E. P. Favvas, A. A. Sapalidis, G. E. Romanos, and F. K. Katsaros, "Metal–carboxylate interactions in metal–alginate complexes studied with FTIR spectroscopy," *Carbohydr. Res.*, vol. 345, no. 4, pp. 469–473, Feb. 2010.

[13] J. P. Chen, L. Hong, S. Wu, and L. Wang, "Elucidation of Interactions between Metal Ions and Ca Alginate-Based Ion-Exchange Resin by Spectroscopic Analysis and Modeling Simulation," *Langmuir*, vol. 18, no. 24, pp. 9413–9421, Nov. 2002.

[14] L. Bacáková, E. Filová, F. Rypácek, V. Svorcík, and V. Starý, "Cell adhesion on artificial materials for tissue engineering.," *Physiol. Res.*, vol. 53 Suppl 1, pp. S35–45, Jan. 2004.

[15] "ISO 10993-5:2009. Biological evaluation of medical devices - Part 5: Tests for in vitro cytotoxicity." [Online]. Available: http://www.iso.org/iso/catalogue_detail.htm?csnumber=36406. [Accessed: 09-Jan-2016].

[16] M. Jiang, J. Terra, A. M. Rossi, M. A. Morales, E. M. Baggio Saitovitch, and D. E. Ellis, "Fe 2 + / F e 3 + substitution in hydroxyapatite: Theory and experiment," *Phys. Rev. B*, vol. 66, no. 22, p. 224107, Dec. 2002.

[17] S. Panseri, C. Cunha, T. D'Alessandro, M. Sandri, G. Giavaresi, M. Marcacci, C. T. Hung, and A. Tampieri, "Intrinsically superparamagnetic Fe-hydroxyapatite nanoparticles

positively influence osteoblast-like cell behaviour," *J. Nanobiotechnology*, vol. 10, no. 1, p. 32, 2012.

[18] L. C. Palmer, C. J. Newcomb, S. R. Kaltz, E. D. Spoerke, and S. I. Stupp, "Biomimetic systems for hydroxyapatite mineralization inspired by bone and enamel.," *Chem. Rev.*, vol. 108, no. 11, pp. 4754–83, Nov. 2008.

[19] A. Tampieri, G. Celotti, E. Landi, M. Sandri, N. Roveri, and G. Falini, "Biologically inspired synthesis of bone-like composite: Self-assembled collagen fibers/hydroxyapatite nanocrystals," *J. Biomed. Mater. Res. Part A*, vol. 67A, no. 2, pp. 618–625, 2003.

[20] A. Tampieri, M. Iafisco, M. Sandri, S. Panseri, C. Cunha, S. Sprio, E. Savini, M. Uhlarz, and T. Herrmannsdörfer, "Magnetic bioinspired hybrid nanostructured collagen-hydroxyapatite scaffolds supporting cell proliferation and tuning regenerative process.," *ACS Appl. Mater. Interfaces*, vol. 6, no. 18, pp. 15697–707, Sep. 2014.

[21] A. Tampieri, M. Sandri, E. Landi, D. Pressato, S. Francioli, R. Quarto, and I. Martin, "Design of graded biomimetic osteochondral composite scaffolds," *Biomaterials*, vol. 29, no. 26, pp. 3539–3546, 2008.

[22] D. I. Zeugolis, G. R. Paul, and G. Attenburrow, "Cross-linking of extruded collagen fibers--a biomimetic three-dimensional scaffold for tissue engineering applications.," *J. Biomed. Mater. Res. A*, vol. 89, no. 4, pp. 895–908, Jun. 2009.

[23] L. He, C. Mu, J. Shi, Q. Zhang, B. Shi, and W. Lin, "Modification of collagen with a natural cross-linker, procyanidin.," *Int. J. Biol. Macromol.*, vol. 48, no. 2, pp. 354–9, Mar. 2011.

[24] S. Leikin, D. C. Rau, and V. A. Parsegian, "Temperature-favoured assembly of collagen is driven by hydrophilic not hydrophobic interactions," *Nat. Struct. Biol.*, vol. 2, no. 3, pp. 205–210, Mar. 1995.

[25] C. Mu, D. Li, W. Lin, Y. Ding, and G. Zhang, "Temperature induced denaturation of collagen in acidic solution.," *Biopolymers*, vol. 86, no. 4, pp. 282–7, Jul. 2007.

[26] G. I. Tsereteli, T. V. Belopol'skaya, and T. N. Mel'nik, "Thermal properties of the collagen-water system -- II. Conformation and conformational mobility of macromolecules in the

native and denatured states," *G. I. Tsereteli, T. V. Belopol'skaya, T. N. Mel'nik. 1997. Therm. Prop. collagen-water Syst. -- II. Conform. Conform. Mobil. Macromol. Nativ. denatured states. Biophys. 42 575-581.*, vol. 3, no. 42, pp. 575–581, 1997.

[27] A. Sionkowska, J. Skopinska-Wisniewska, M. Gawron, J. Kozlowska, and A. Planecka, "Chemical and thermal cross-linking of collagen and elastin hydrolysates.," *Int. J. Biol. Macromol.*, vol. 47, no. 4, pp. 570–7, Nov. 2010.

[28] K. Pietrucha, "Changes in denaturation and rheological properties of collagen-hyaluronic acid scaffolds as a result of temperature dependencies.," *Int. J. Biol. Macromol.*, vol. 36, no. 5, pp. 299–304, Sep. 2005.

[29] A. Tampieri, S. Sprio, M. Sandri, and F. Valentini, "Mimicking natural bio-mineralization processes: A new tool for osteochondral scaffold development," *Trends Biotechnol.*, vol. 29, no. 10, pp. 526–535, 2011.

[30] Y. Sun, W.-L. Chen, S.-J. Lin, S.-H. Jee, Y.-F. Chen, L.-C. Lin, P. T. C. So, and C.-Y. Dong, "Investigating mechanisms of collagen thermal denaturation by high resolution second-harmonic generation imaging.," *Biophys. J.*, vol. 91, no. 7, pp. 2620–5, Oct. 2006.

[31] A. Bigi, G. Cojazzi, S. Panzavolta, N. Roveri, and K. Rubini, "Stabilization of gelatin films by crosslinking with genipin.," *Biomaterials*, vol. 23, no. 24, pp. 4827–32, Dec. 2002.

[32] B. Issa, I. M. Obaidat, B. A. Albiss, and Y. Haik, "Magnetic nanoparticles: surface effects and properties related to biomedicine applications.," *Int. J. Mol. Sci.*, vol. 14, no. 11, pp. 21266–305, Jan. 2013.

[33] B. B. Yellen, Z. G. Forbes, D. S. Halverson, G. Fridman, K. A. Barbee, M. Chorny, R. Levy, and G. Friedman, "Targeted drug delivery to magnetic implants for therapeutic applications," *J. Magn. Magn. Mater.*, vol. 293, no. 1, pp. 647–654, May 2005.

[34] A. Nicoletti, M. Fiorini, J. Paolillo, L. Dolcini, M. Sandri, and D. Pressato, "Effects of different crosslinking conditions on the chemical–physical properties of a novel bio-inspired composite scaffold stabilised with 1,4-butanediol diglycidyl ether (BDDGE)," *J. Mater. Sci. Mater. Med.*, vol. 24, no. 1, pp. 17–35, 2013.

[35] H.-U. Gremlich and B. Yan, *Infrared and Raman Spectroscopy of Biological Materials*. CRC Press, 2000.

[36] C. Mu, F. Liu, Q. Cheng, H. Li, B. Wu, G. Zhang, and W. Lin, "Collagen Cryogel Cross-Linked by Dialdehyde Starch," *Macromol. Mater. Eng.*, p. NA–NA, Jan. 2010.

[37] M. C. Chang and J. Tanaka, "FT-IR study for hydroxyapatite/collagen nanocomposite cross-linked by glutaraldehyde," *Biomaterials*, vol. 23, no. 24, pp. 4811–4818, Dec. 2002.

[38] H. Schoof, J. Apel, I. Heschel, and G. Rau, "Control of pore structure and size in freeze-dried collagen sponges," *J. Biomed. Mater. Res.*, vol. 58, no. 4, pp. 352–357, 2001.

[39] Z. Xia, X. Calderon-Colon, M. Trexler, J. Elisseeff, and Q. Guo, "Thermal denaturation of type I collagen vitrified gels," *Thermochim. Acta*, vol. 527, pp. 172–179, Jan. 2012.

[40] M. Reháková, D. Bakos, K. Vizárová, M. Soldán, and M. Jurícková, "Properties of collagen and hyaluronic acid composite materials and their modification by chemical crosslinking.," *J. Biomed. Mater. Res.*, vol. 30, no. 3, pp. 369–72, Mar. 1996.

[41] L. Ma, C. Gao, Z. Mao, J. Zhou, J. Shen, X. Hu, and C. Han, "Collagen/chitosan porous scaffolds with improved biostability for skin tissue engineering.," *Biomaterials*, vol. 24, no. 26, pp. 4833–41, Nov. 2003.

[42] O. Perales Perez, Y. Umetsu, and H. Sasaki, "Precipitation and densification of magnetic iron compounds from aqueous solutions at room temperature," *Hydrometallurgy*, vol. 50, no. 3, pp. 223–242, 1998.

[43] A. Tampieri, T. D'Alessandro, M. Sandri, S. Sprio, E. Landi, L. Bertinetti, S. Panseri, G. Pepponi, J. Goettlicher, M. Bañobre-López, and J. Rivas, "Intrinsic magnetism and hyperthermia in bioactive Fe-doped hydroxyapatite.," *Acta Biomater.*, vol. 8, no. 2, pp. 843–51, Feb. 2012.

[44] I. R. Gibson and W. Bonfield, "Preparation and characterization of magnesium/carbonate co-substituted hydroxyapatites," *J. Mater. Sci. Mater. Med.*, vol. 13, no. 7, pp. 685–693.

[45] W. K. Son, J. H. Youk, T. S. Lee, and W. H. Park, "Electrospinning of ultrafine cellulose

acetate fibers: Studies of a new solvent system and deacetylation of ultrafine cellulose acetate fibers," *J. Polym. Sci. Part B Polym. Phys.*, vol. 42, no. 1, pp. 5–11, Jan. 2004.

[46] M. da C. C. Lucena, A. E. V. de Alencar, S. E. Mazzeto, and S. de A. Soares, "The effect of additives on the thermal degradation of cellulose acetate," *Polym. Degrad. Stab.*, vol. 80, no. 1, pp. 149–155, Jan. 2003.

[47] C. M. Sayes, K. L. Reed, and D. B. Warheit, "Assessing toxicity of fine and nanoparticles: comparing in vitro measurements to in vivo pulmonary toxicity profiles.," *Toxicol. Sci.*, vol. 97, no. 1, pp. 163–80, May 2007.

HEAT AND MOISTURE EXCHANGE FILTERS

In this section of my PhD research project the goal was to create a filter for gaseous systems capable of heat and moisture exchange, therefore able to humidify and warm the cold and dry gases from the pulmonary ventilator. Such filters accumulate the moisture that arises from the patient breath and afterwards transfer it to the synthetic gases flowing through the filter during inspiration. At the same time the filter must warm the cold synthetic air before it reaches the patient, ensuring a bactericidal action on microbes eventually contained in the air from the patient. The device was conceived to ensure chemical stability and adequate stiffness in dry and wet environments, so to preserve the shape during functioning.

The developed bio-inspired device exploits chemical properties of low cost natural polymers; blending processes to combine a hydrophilic component allowing the accumulation of the water vapor delivered from expired air and a less hydrophilic and reinforcing component controlling the moisture capture and release and avoiding the collapse of the porous structure. Moreover a paramagnetic hybrid component is included to heat the cold air passing through the filter by hyperthermia effect activated under a magnetic field.

All the components of this filter are from renewable sources and have a high availability and low processing expense, to ensure a low cost of the final device to be applied in a large scale production with a competitive price.

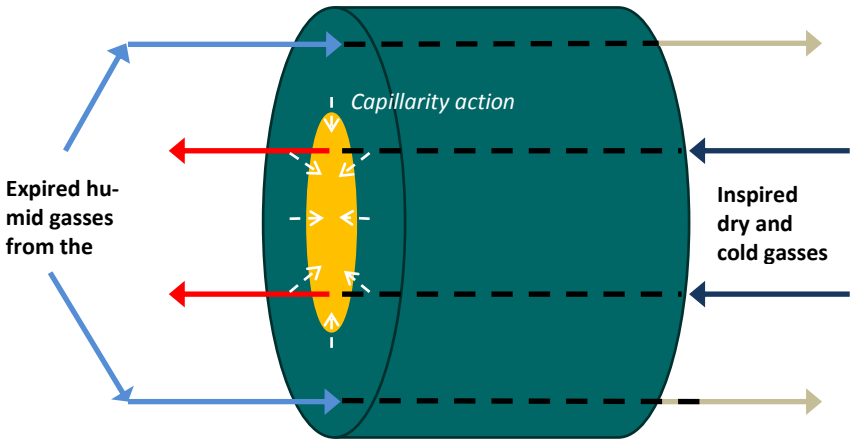

***Figure 5.1**. Schematic design of an HME filter*

In addition, the building of a HME new device may consist in the combination of two different sections in close collaboration, with the following structure: an external area with hydrophilic features where the expired gases will flow, and an internal one with warming characteristics for the inspired gases of the patient and where the moisture accumulated in the external area might be guided via capillary action. Fig.1 shows a possible schematic design of this device.

In order to have different strictly ways for air inlet and outlet, a two ways biodegradable filter holder specifically developed for this project from a consortium partner, Pollution, as shown in Fig.5.2).

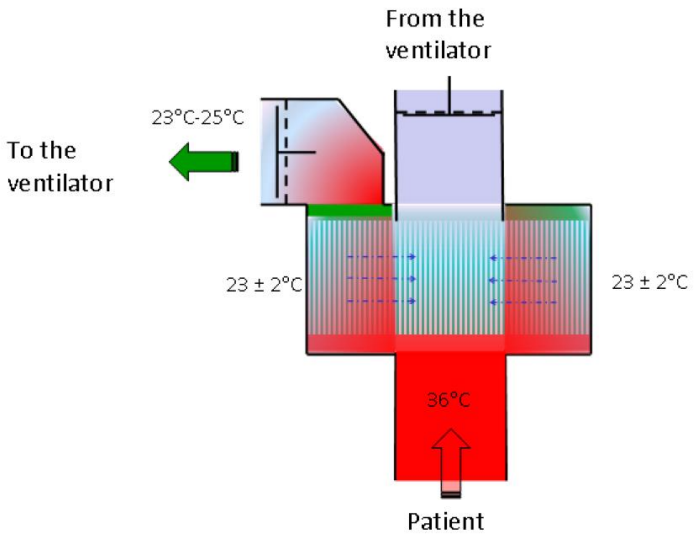

***Figure 5.2** Schematic design of an HME filter holder*

For the evaluation of moisture supply a dummy circuit was implemented, which is based on a pulmonary model where breathing and humidity condition are simulated.

5.1 Moisture exchange section

Gelatin and chitosan were chosen as high available natural polymers thanks to their different behavior in water: gelatin is an hydrophilic and water soluble protein polymer[1], while chitosan is a polysaccharide, less hydrophilic than gelatin soluble only in acidic condition[2] and with high structural properties as it's possible to see in crustacean shells, the source from which it is extracted. Polysaccharide-protein conjugates are common in nature and often this conjugation confers peculiar mechanical properties[3]; gelatin (or collagen) and chitosan (or chitin) do not exist blended together in nature, but the specific properties of each can be used to produce stable artificial hybrid materials which give the unique structural and chemical properties[4]. Genipin was then used as natural cross-linker able to create irreversible covalent bonds both with gelatin and chitosan, leading to an increase of chemical and mechanical properties of the blend and assuring the stability of the filter in water[5].

A strictly controlled freeze-drying process was used to obtain tubular porous structure in order to facilitate the passage of the air through the filter, but also to maximize the contact surface between the gas and the materials to increasing the moisture exchange.

5.1.1 Synthesis processes

The dissolution of gelatin was performed heating 66 mL of distilled water at 40 °C and adding slowly 1,4 g of gelatin powder under magnetic stirring; the heating and stirring was maintained until the complete dissolution, about 1h. The dissolution of chitosan was performed adding 0,6 g of chitosan powder to 30 mL of 1 wt% solution of acetic acid in bidistilled water under vigorous stirring and using ultrasound until a clear solution was reached (about 30 minutes). The two solutions were then combined under quite slow magnetic stirring to avoid foaming and 4 mL of a 1% w/w of genipin solution was added: the final solution was composed by gelatin/chitosan ratio of 70:30, polymer concentration of 2% and genipin/polymer ratio of 2%. The stirring was maintained at room temperature until a complete homogenization of the system (about 15 min). The mixture was casted into a 100 mL mold with metal bottom of 5 cm of diameter and plastic walls covered with a lid in order to prevent the water evaporation. This particular mold was homemade by a partner of the European Project, Pollution, and was built in order to optimize the vertical freezing of the hydrogel during the lyophilization process: the metal bottom promote the temperature transmission at the upper material, while the plastic wall disadvantage the horizontal cooling. After two days at room temperature the light yellow solution has become a dark green-blue gel thanks to the polymer/genipin cross-linking; this hydrogel was freeze-dried with a freezing temperature of -40 °C and a heating ramp of 5 °C/h up to -10 ° C and 1 °C/h up to 15 °C. After the lyophilization, the upper and the lower surfaces was cut off about 2 mm of thickness. The produced material was coded Gel/Chit (Fig. 5.3)

***Figure 5.3** Gel/Chit filter*

The freeze-drying process was optimized after a study on the effect of different freezing temperatures (-20, -40 a -80 °C) and heating ramps (1, 5, 10 °C/h) on the final material.

Several blend compositions obtained by varying the polymers ratio (50:50, 70:30, 80:20), the final hydrogel concentration (1, 2, 3%) and the ratio between cross-linker and polymers (1, 2, 4%) were experimented in order to optimize the parameters related to the specific functions that lead the device to be suitable as HME filter,. The composition are resumed in Tab. 5.1.

Materials	Gelatin/chitosan ratio (%)	Hydrogel concentration (%wt)	Cross-liker/polymers ratio (%)
Gel/Chit	70:30	2	2
Gel/Chit_NCL	70:30	2	0
Gel/Chit1	70:30	2	1
Gel/Chit2	70:30	2	4
Gel/Chit3	70:30	1	2
Gel/Chit4	70:30	3	2
Gel/Chit5	80:20	2	2
Gel/Chit6	50:50	2	2

***Table 5.1** Resume of compositions and codes of the several gelatin/chitosan based materials.*

5.1.2 Chemic-physical characterizations

5.1.2.1 Thermal Analysis

Thermogravimetric profile of uncrosslinked and differently cross-linked samples are shown in Fig. 5.4.

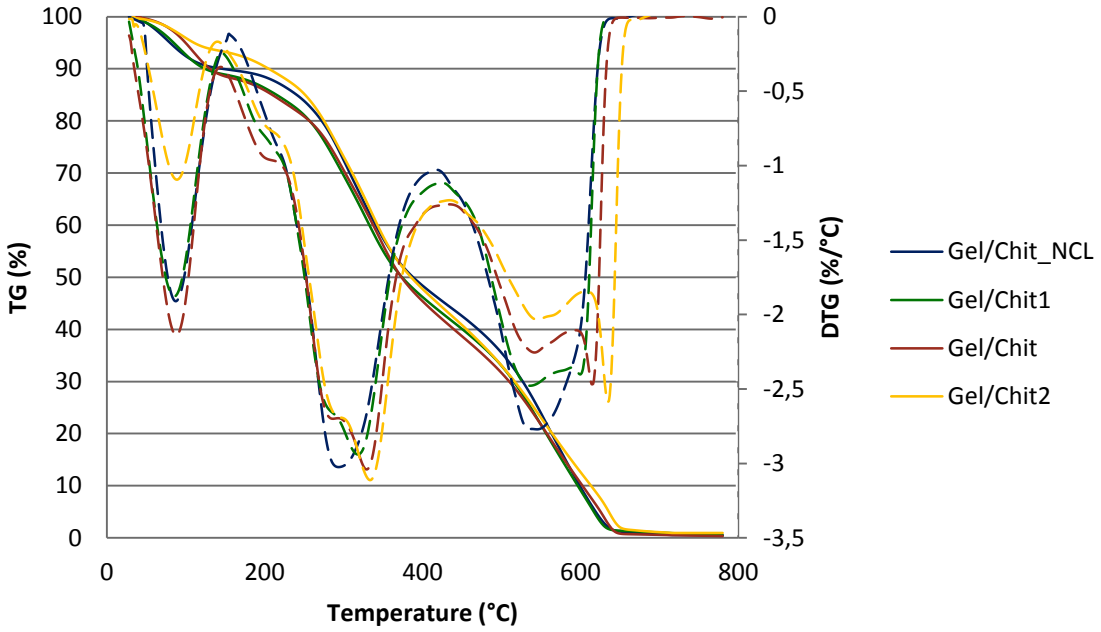

***Figure 5.4** Thermal decomposition profile (TG) and its derivative (DTG) of uncross-linked sample (Gel/Chit_NCL), and samples cross-liked with 1% (Gel/Chit1), 2% (Gel/Chit) and 4% (Gel/Chit2) of genipin/polymers ratio*

Decomposition traces display three main weight loss phenomena: a water desorption between 30 and 150 °C, a second weight loss regarding the partial gelatin decomposition and the chitosan molecular rearrangement and subsequent detachment of volatile species[6]. The final chitosan pyrolysis appears in the 450-650 °C temperature range[7].

It's possible to observe that in the not cross-linked sample (Gel/Chit_NCL) the decompositions take place in a single stage, while in the cross-linked samples decomposition processes are doubled. In addition, in each of the decomposition step, the second stage prevails on the first, leading the blend decompositions at higher temperatures, with the increasing of the cross-linking degree.

The two degradation temperatures at which weight loss rate is the maximum are usually used as a measure of thermal stability[8], so as a conclusion the use of genipin affect significantly the heat resistance of gelatin/chitosan based material.

Moreover, DTA was conducted on gelatin/chitosan blend non cross-linked and cross-linked in the several ways (Fig. 5.5).

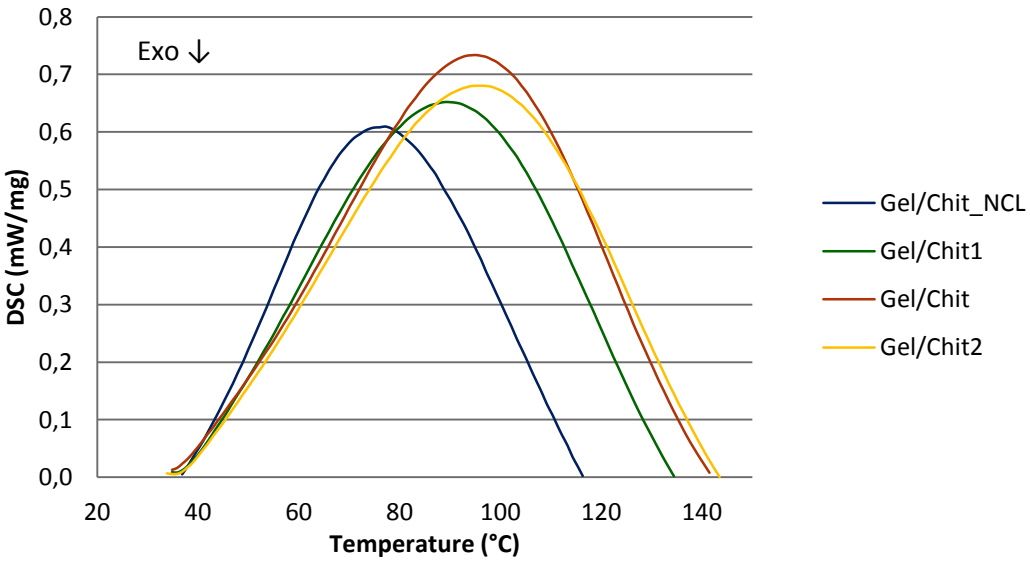

Figure 5.5 *Differential Thermal Calorimetry of uncross-linked sample (Gel/Chit_NCL), and samples cross-liked with 1% (Gel/Chit1), 2% (Gel/Chit) and 4% (Gel/Chit2) of genipin/polymers ratio.*

The Fig. 5.3 show an endothermic peak from 30 °C to 120-145 °C, due to denaturation transitions which result in the loss of moisture of the composite[9]. The DSC results indicate that the temperature at which the denaturation occurs increases with increasing of the cross-linker/polymers ratio. This systematic increase in denaturation temperature (78.5, 89.4, 92.8 and 94.8 °C respectively for Gel/Chit_NCL, Gel/Chit1, Gel/Chit and Gel/Chit2), reveals that the cross-linking enhances the thermal stability in the material.

5.1.2.2 Fourier-Transform Infrared Spectroscopy

Infrared spectroscopy analysis, show in Fig. 5.6 was used to determine the bands relative to functional groups typical of each blend component also to determine the occurred cross-linking.

The not cross-linked blend shows the first main peak at 3436 cm^{-1}, the typical of N–H stretching band both for chitosan and gelatin, which almost hides that related to O–H stretching at around 3330 cm^{-1}. The bands attributed specifically to gelatin (indicated in Fig.5.5 with G) appears at 1641, 1548 and at 1254 cm^{-1}, regarding the amide I, II and III vibration respectively[10], 1461 and 1354 cm^{-1}, for CH_2 and C–H bending and finally at 1414 cm^{-1} about the symmetric stretching of COO^- group[11]. The bands attributed specifically to chitosan (indicated in Fig.5.5 with C) not covered by gelatin peaks appear, instead, at 1163 and 1092 cm^{-1} and are assigned to saccharine structure, in particular to asymmetric stretching of C-O-C and stretching of skeletal C–O respectively; the amine bands, around 1668 and 1571 cm^{-1} are overlapped by gelatin peaks[12].

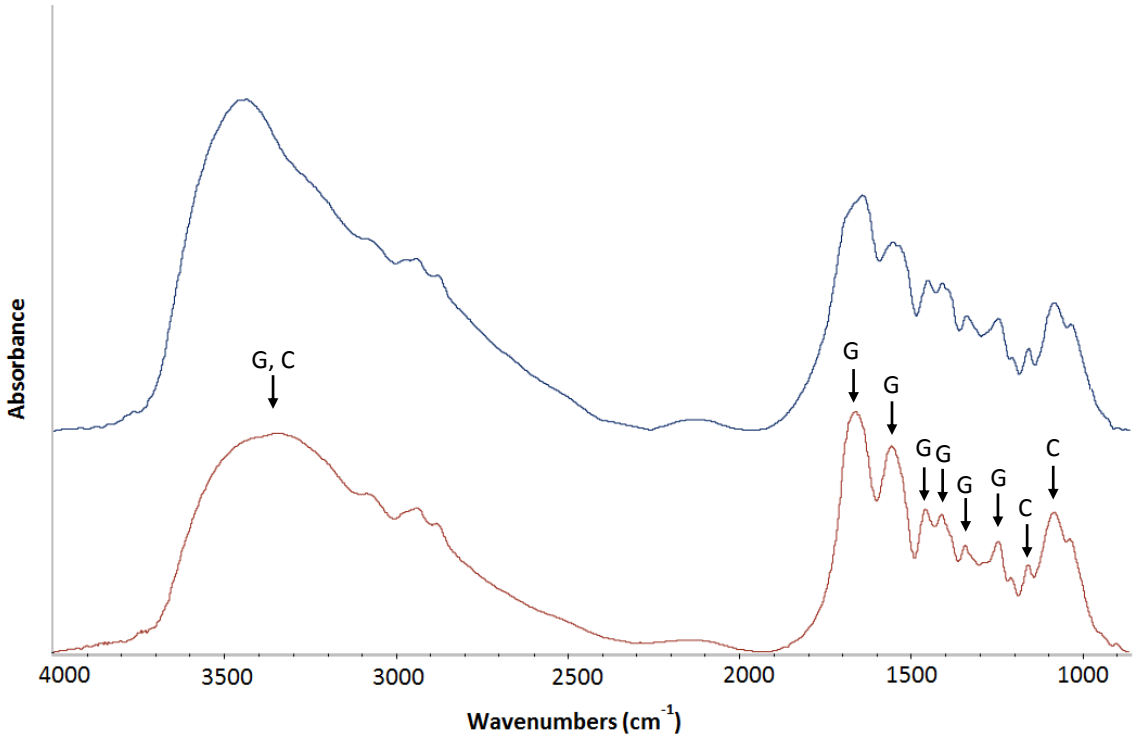

Figure 5.6 *FTIR analysis of Gel/Chit (red) compared with Gel/Chit_NCL (blue).*

From the comparison between the cross-linked and not cross-linked blend it's clear that the N–H stretching band is decreased as a result of cross-linking and the amide I and amide II bands of gelatin/chitosan composite increased in intensity and moved to higher

wave numbers, from 1641 to 1655 cm^{-1} and from 1548 to 1551 cm^{-1} respectively. These spectral changes confirmed that the cross-linking was occurred[11,13].

5.1.2.3 Scanning Electron Microscopy Analysis

From SEM images it was possible to study the variables which affect the gelatin/chitosan based material morphology.

Freezing temperature and cooling rates has a crucial influence on the pore size. As shown in Fig. 5.7 D and E, a too low cooling rate (1°C/min) and a relative high freezing temperature (-20°C) lead to obtain heterogeneous porous structure with a large variation in average pore diameter. A material freeze-dried with a too low freezing temperature, instead, is characterized by smaller and more randomly oriented pores (Fig. 5.7F). It's well known that the disposition of the material during the freeze-drying process is influenced by both the rate of nucleation of ice crystals, which defines the number of ice crystals that form, and the rate of heat diffusion, which defines the size of ice crystals[14]. An high difference between the temperature of freezing and the actual temperature of the material during the freezing process lead to an increased rate of nuclei of ice crystallization with a decreased heat diffusion rate away from the point of nucleation[15]. Therefore, with a too low freezing temperature, small crystals are formed and a tiny ice growth is allowed, leading to a material with a smaller average pore diameter following sublimation[16]. In addition, the direction and the speed of heat transfer influence the shape of growing ice crystals: a massive predominant direction of heat transfer leads to the formation of columnar ice crystals[17]. On the other hand, with a low cooling rate and/or a to high freezing temperature the vertical temperature gradient during cooling is lower, thus could lead to an even horizontal growth of some ice crystals nuclei[18].

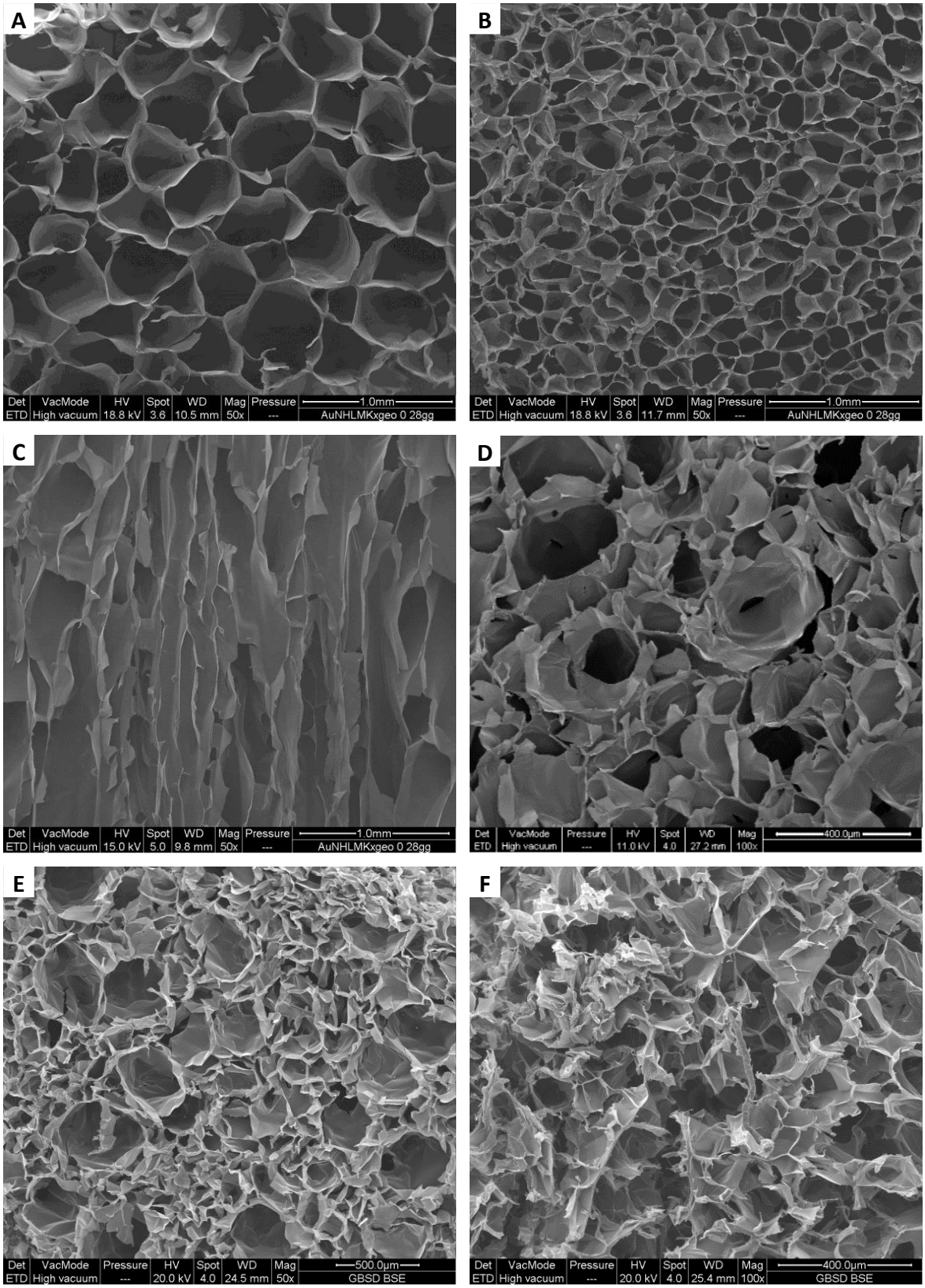
A
Det | VacMode | HV | Spot | WD | Mag | Pressure | 1.0mm
ETD | High vacuum | 18.8 kV | 3.6 | 10.5 mm | 50x | --- | AuNHLMKxgeo 0 28gg
B
Det | VacMode | HV | Spot | WD | Mag | Pressure | 1.0mm
ETD | High vacuum | 18.8 kV | 3.6 | 11.7 mm | 50x | --- | AuNHLMKxgeo 0 28gg
C
Det | VacMode | HV | Spot | WD | Mag | Pressure | 1.0mm
ETD | High vacuum | 15.0 kV | 5.0 | 9.8 mm | 50x | --- | AuNHLMKxgeo 0 28gg
D
Det | VacMode | Pressure | HV | Spot | WD | Mag | 400.0µm
ETD | High vacuum | --- | 11.0 kV | 4.0 | 27.2 mm | 100x
E
Det | VacMode | Pressure | HV | Spot | WD | Mag | 500.0µm
ETD | High vacuum | --- | 20.0 kV | 4.0 | 24.5 mm | 50x | GBSD BSE
F
Det | VacMode | Pressure | HV | Spot | WD | Mag | 400.0µm
ETD | High vacuum | --- | 20.0 kV | 4.0 | 25.4 mm | 100x | GBSD BSE

Figure 5.7 *SEM images of Gel/Chit upper (A) and lower (B) transversal sections and longitudinal section (C). Upper transversal section of Gel/Chit lyophilized with a cooling ramp of 1°C/min (D) and with a freezing temperature of -20 (E), and -80°C (F).*

Paying attention to the cross-linking degree (in ascending order of reticulation Fig. 5.7G, A, I), it's possible to see that no significant changes occurred with respect to pore size, but there are some changing in pores morphology: the pore walls are more brittle for the less reticulated sample (Fig. 5.7G), so that it's possible to see some network breaks, while they are much thicker for the more cross-linked sample (Fig. 5.7I); it's clear that an increasing of linkage between polymer chains lead an hardy material. In adding, unidirectionality of the channel decreasing with the cross-linking degree increases; this effect could be explained by the increasing of the viscosity of the hydrogel with increasing of cross-linking degree, which is unfavorable to the water and the molecular chains moving in the solution. Therefore the ice crystals grow more difficultly in the solution with high viscosity than in that with a low one. It means that the filters with higher cross-linking are much closer in structure than that with lower reticulation[18].

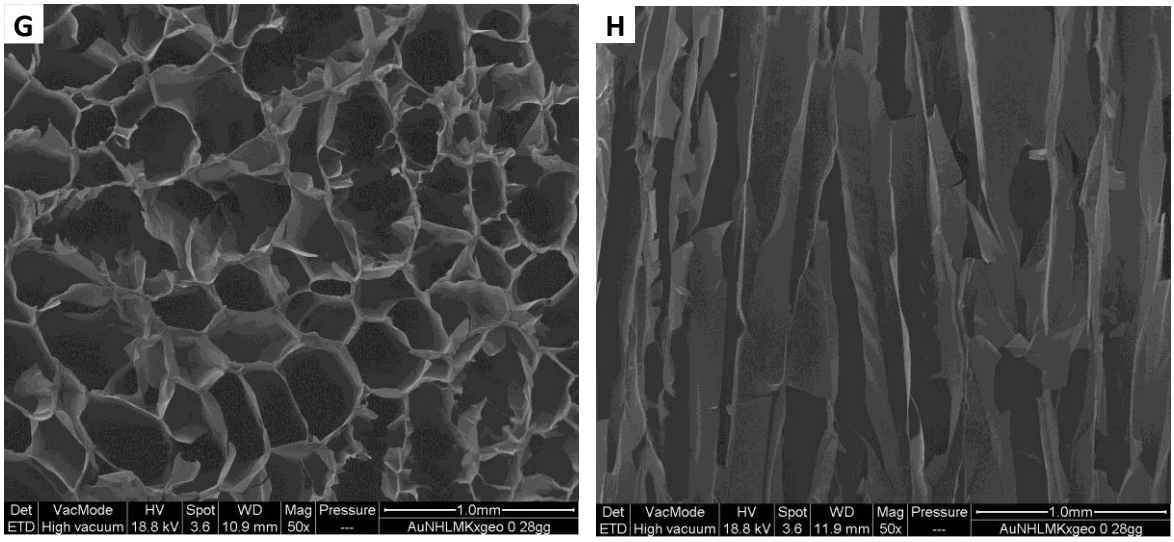

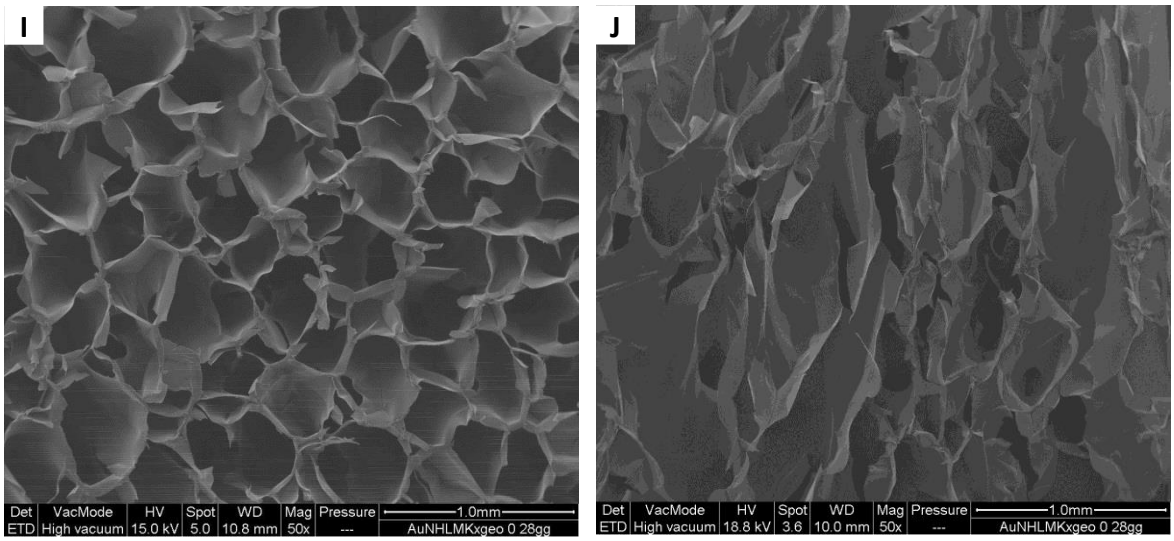

Figure 5.7 *SEM images of Gel/Chit upper transversal section and longitudinal section of Gel/Chit1 (G, H) and Gel/Chit2 (I, J), respectively the samples with 1% and 4% of cross-linker/polymers ratio.*

The concentration of gelatin/chitosan hydrogel is another important parameter whit a strong effect on the vapor uptake from the material and thus on mean pore size. For the same volume of gelatin/chitosan solution and freeze-dried to porous scaffold, the lower concentration of the solution (Fig. 5.7M, A, K), the thinner pore walls and the smaller pore size. This occurs because the number of ice nuclei in the solution with high concentration is smaller[18] and more difficult to grow than those of the low concentration one: if the molecules are subjected to small resistance when moving, ice crystals can grow quickly and straighter.

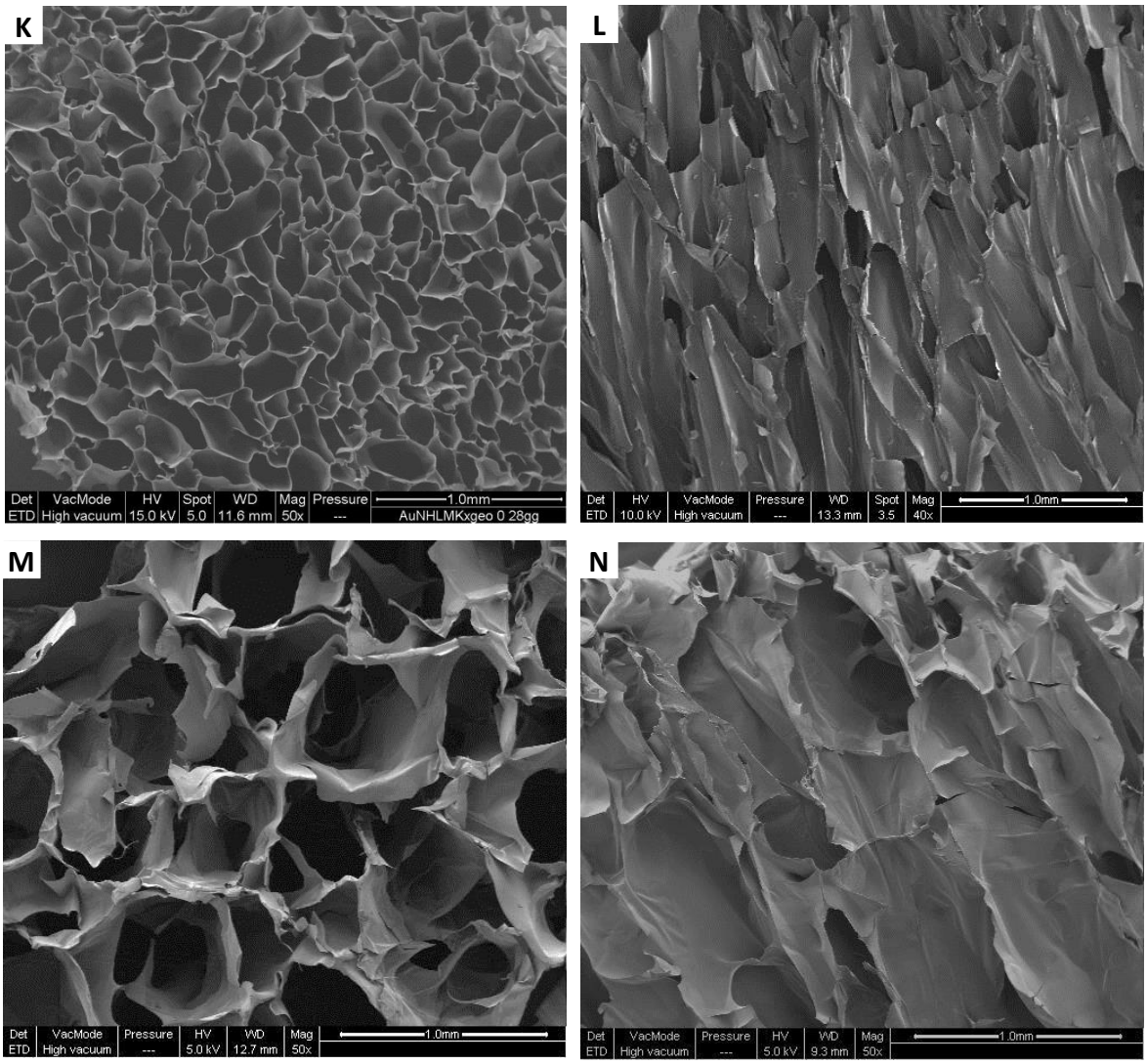

Figure 5.7 *SEM images of Gel/Chit upper transversal section and longitudinal section of Gel/Chit3 (K,L) and Gel/Chit4 (M, N), respectively the samples at 1% and 3% of hydrogel concentration.*

Some other significant changes occurred with respect to pore size and morphology with changing the polymer ratio. A greater amount of gelatin leads a more disordered morphology in the final material (Fig. 5.7O, P), while a greater contribution of chitosan carry out a more tailoring structure(Fig. 5.7Q, R); this is because the gelatin tends to freeze-dry with globular and randomly disposed pores, while the chitosan tends to freeze-dry arranging packaging in layers.

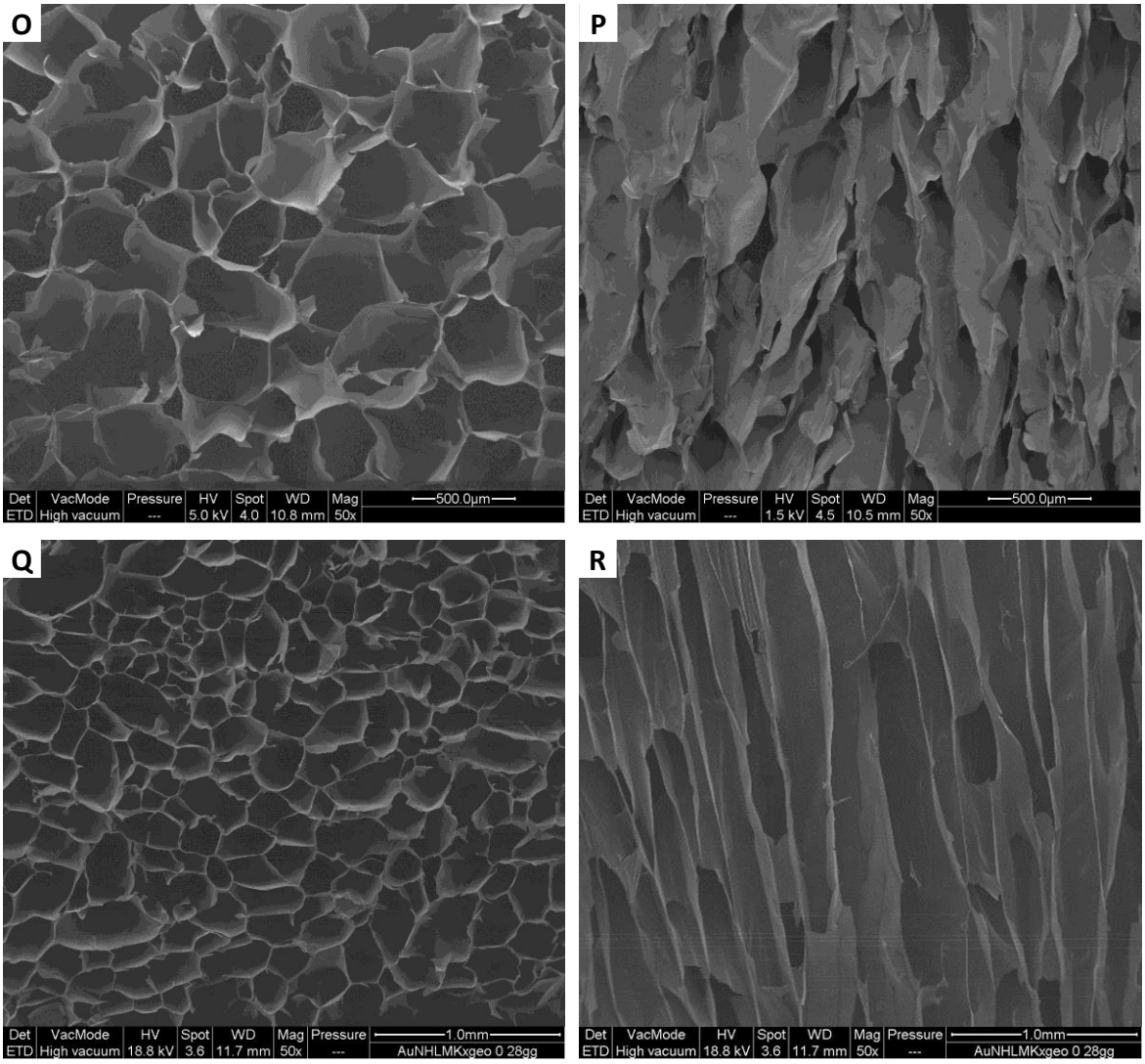

Figure 5.7 *SEM images of Gel/Chit upper transversal section and longitudinal section of Gel/Chit5 (O, P) and Gel/Chit6 (Q, R), respectively the samples with 80:20 and 50:50 of gelatin/chitosan ratio.*

5.1.2.4 Contact angle test

The wettability of the gelatin/chitosan surfaces was measured using a static water contact angle on films and the results are shown in Fig. 5.8.

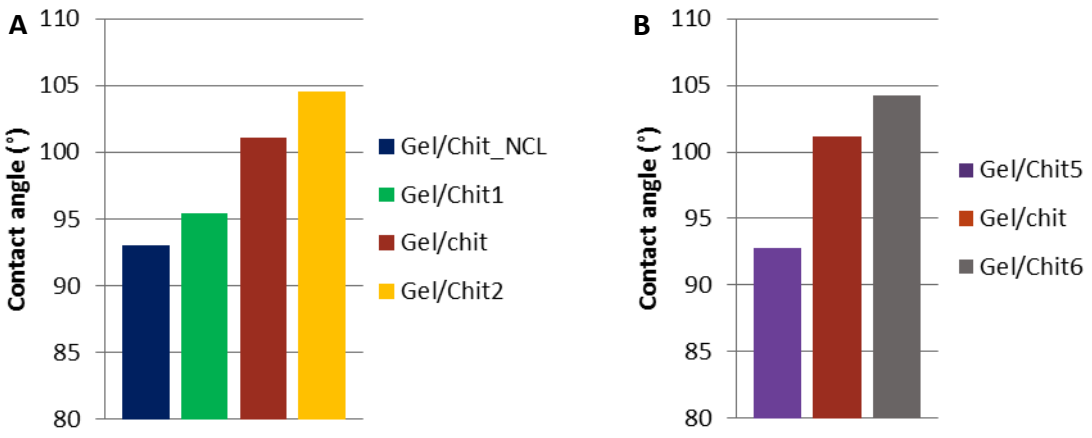

***Figure 5.8** A: Static contact angle of gelatin/chitosan based material not cross-linked (Gel/Chit_NCL), cross-linked with 1% (Gel/Chit1), 2% (Gel/Chit) and 4% (Gel/Chit2) of genipin/polymers ratio. B: Static contact angle of gelatin/chitosan based material with gelatin/chitosan ratio of 80:20 (Gel/Chit5), 70:30 (Gel/Chit) and 50:50 (Gel/Chit6).*

All the materials showed high contact angles, more than 70, indicating that all these materials had poor hydrophilicity. Nevertheless, the cross-linking process and the different content of chitosan induce little changes. The not-cross-linked blend (Fig. 5.8A) shows a higher hydrophilicity, and after a cross-linking process, so a formation of a molecular network trough covalent bonds implying free amino groups, the water contact angle increases with increasing genipin content, which that the water affinity depend on the number of hydrophilic free amino groups present into the blend[20].

It's also possible to see that the increasing into the blend of chitosan amount leads an increasing of contact angle; this finding is attributed to the higher hydrophilicity of gelatin compared to chitosan[21]: increasing the hydrophilic component there is an overall increase of the hydrophilicity of the material.

5.1.2.5 Determination of amine cross-linking degree

In order to evaluate the cross-linking degree of the gelatin/chitosan blend with genipin, the TNBS method[7] has been used to evaluate the amount of free primary amine groups, so not cross-linked. The results are shown in Tab. 5.2

Materials	Genipin/polymers ratio (%)	Cross-linking degree (%)
Gel/Chit	2	78
Gel/Chit1	1	56
Gel/Chit2	4	81

***Table 5.2** Experimental values of cross-linking degree of the chitosan/gelatin based hydrogels cross-linked with different amount of genipin.*

It's clear that a genipin/polymers ratio of 1% w/w is not enough for an efficient reticulation; between 2 and 4%, instead there is only a little difference in the degree of cross-linking. These findings suggest that cross-linking of the blend with higher genipin amounts than 2% w/w did not affect significantly its crosslinking degree, so a genipin amount equals to 2% w/w was identified as the optimal content for the crosslinking process.

5.1.2.6 Degradation test

Degradation test was conducted simulating the physical condition of the breath, so the measurement were carried out in distilled water at pH 7,4[22] at 37°C. Typical disposable HME filter have a time of use of about one week, but the test was conducted up to three weeks on not cross-linked sample (Gel/Chit_NCL), cross-linked with 1% (Gel/Chit1), 2% (Gel/Chit) and 4% (Gel/Chit2) of genipin/polymers ratio, with an hydrogel concentration of 1% (Gel/Chit3) and 3% (Gel/Chit4) and with a gelatin/chitosan ratio of 80:20 (Gel/Chit5) and 50:50 (Gel/Chit6). The results were shown in Fig. 5.9.

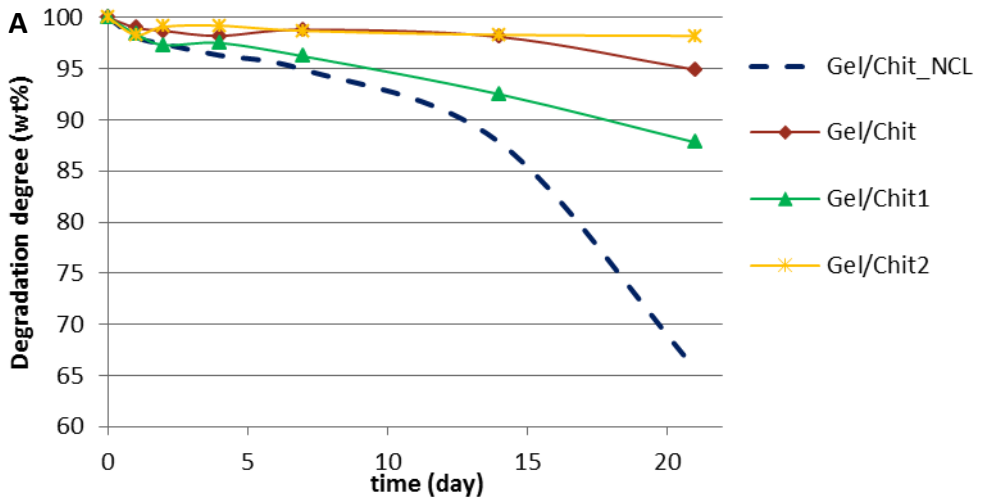

Figure 5.9 *Degradation weight loss for the different gelatin/chitosan based materials. A: degradation as a function of genipin amount (respectively 0%, 1%, 2% and 4% for Gel/Chit_NCL, Gel/Chit1, Gel/Chit and Gel/Cht2).*

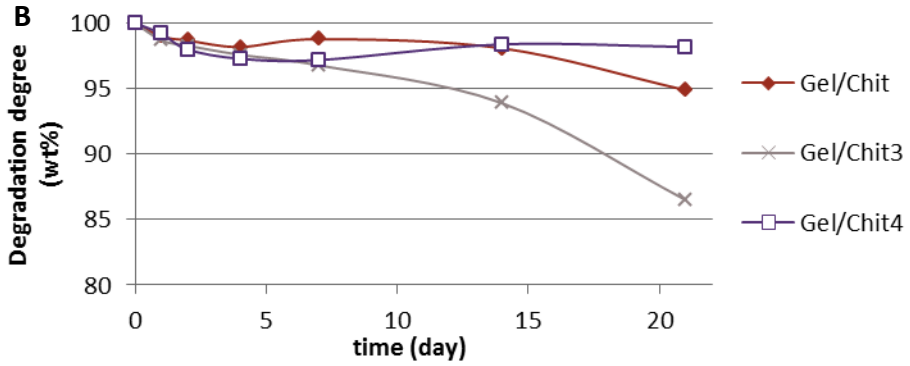

Figure 5.9 *B: degradation as a function of hydrogel concentration (respectively 1%, 2% and 3% for Gel/Chit3, Gel/Chit and Gel/Chit4).*

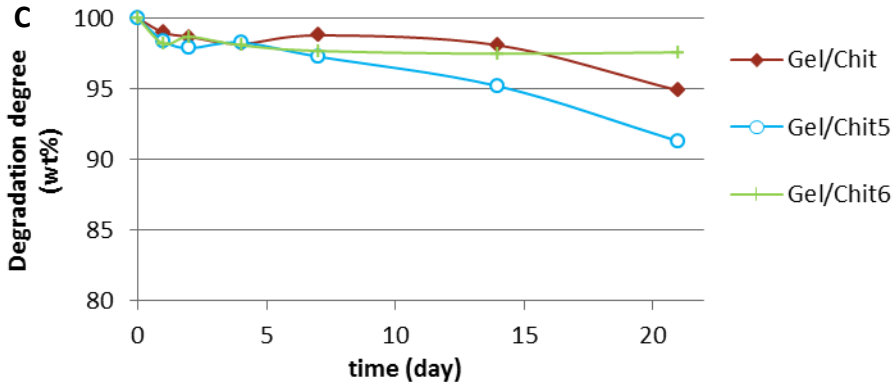

***Figure 5.9** C: degradation as a function of gelatin/chitosan ratio (respectively 80:20, 70:20 and 50:50 for Gel/Chit5, Gel/Chit and Gel/Chit6).*

All the samples considered show a degradation within 5% in one week, but proceeding with the test it's possible to see that the uncross-linked sample degrades quickly and also Gel/Chit1, Gel/Chit3 and Gel/Chit5 show a greater degradation compared with the other materials. The stability of the materials in aqueous media increases with the increase of the genipin amount, sign that the cross-linking process leads to a direct increasing of the stability of the blend. Another parameter that influences the filter degradation is the hydrogel concentration before freeze-drying, because a smaller hydrogel concentration lead to a faster degradation. After two weeks the filter containing less material starts to dissolve, a sign that it was not compromised the biodegradability of the material, but the cross-linking extends the material resistance. Finally the dissolution degree decrease with increasing the chitosan amount, due to the natural insolubility of the polymer at pH higher than 6.5.

5.1.2.7 Determination of the bacteriostatic/bactericidal activity

In filtering devices for hospital using, bactericide/bacteriostatic properties are required to avoid the proliferation of bacteria inside and over the filter. Specific tests, following the UNI-EN 13697:2001 standard[23] were conducted on the surface and internal section of the filters, the percentage of growing inhibition of several tested microbes are explained in Tab. 5.3 and 5.4.

Microbes	Contact time			
	1 hours	4 hours	24 hours	72 hours
E.coli	7%	7%	14%	14%
P.aeruginosa	0%	0%	0%	17%
S.aureus	8%	54%	95%	>99%

S.epidermidis	14%	80%	95%	>99%
C.albicans	17%	17%	50%	93%
Asp. Niger	0%	0%	17%	17%

***Table 5.3** Inhibition of microbial growing for surface of Gel/Chit.*

Microbes	Contact time			
	1 hours	4 hours	24 hours	72 hours
E.coli	29%	29%	30%	31%
P.aeruginosa	0%	17%	17%	17%
S.aureus	23%	75%	95%	>99%
S.epidermidis	14%	79%	96%	>99%
C.albicans	17%	25%	67%	97%
Asp. Niger	0%	0%	17%	17%

***Table 5.4** Inhibition of microbial growing for internal section of Gel/Chit.*

The results obtained during the *in vitro* test demonstrated the effective inhibition of microbial growth in the tested sample. Through a quantitative test by the direct contact with different microbial strains, the material showed a bactericidal or bacteriostatic activity against the majority of micro-organisms in time.

It was estimated a bacteriostatic activity against gram-negative bacteria, such as Pseudomonas, and coliforms, eg. Escherichia coli, and it was detected lievicid activity against pathogens yeast such as Candida albicans.

The sample showed, in addiction, a funghistatic effect against molds belonging to the Aspergillus genus, while it was detected a very good bactericidal activity against gram-positive bacteria, like Staphylococcus, with a reduction of 95% after 24 hours of contact.

5.1.2.8 Moisture exchange and pressure drop evaluation

The previous tests allowed to choose the most suitable samples in terms of stability and morphology; successively the samples chosen, were evaluated in terms of moisture exchange and pressure drop. This test was crucial for the materials selecting because following the ISO 9360 standards[24], the minimum moisture output accepted values is around 30 mgH_2O/L, (80% of recovery of absolute humidity in our condition) and for the pressure drop the higher accepted value is 5 mbar.

In Fig. 5.10 are shown below the pressure drop results for all the materials and Fig. 5.11 are shown the moisture exchange behaviors.

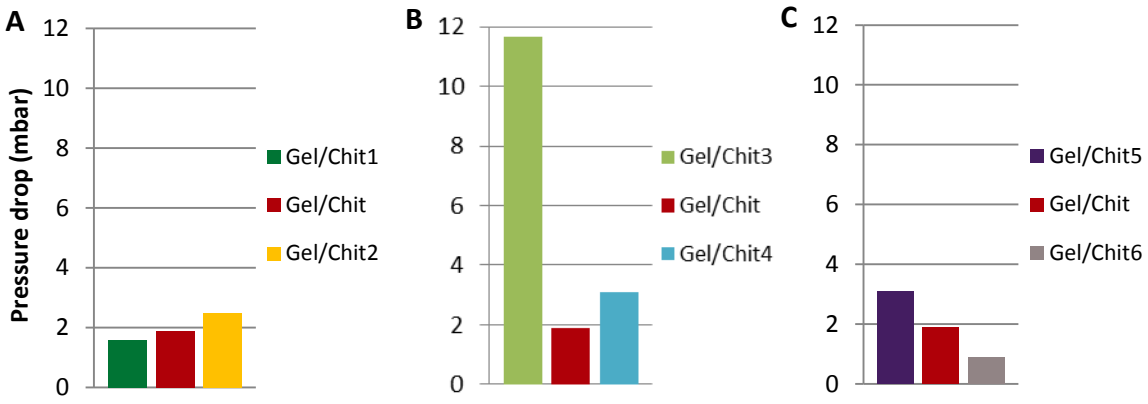

Figure 5.10 *Pressure drop of gelatin/chitosan based filters as a function of genipin amount (A), hydrogel concentration (B) and gelatin/chitosan ratio (C) for samples cross-linked with 1% (Gel/Chit1), 2% (Gel/Chit) and 4% (Gel/Chit2) of genipin/polymers ratio, with nominal hydrogel concentration of 1% (Gel/Chit3) and 3% (Gel/Chit4) and with gelatin/chitosan ratio of 80:20 (Gel/Chit5) and 50:50 (Gel/Chit6).*

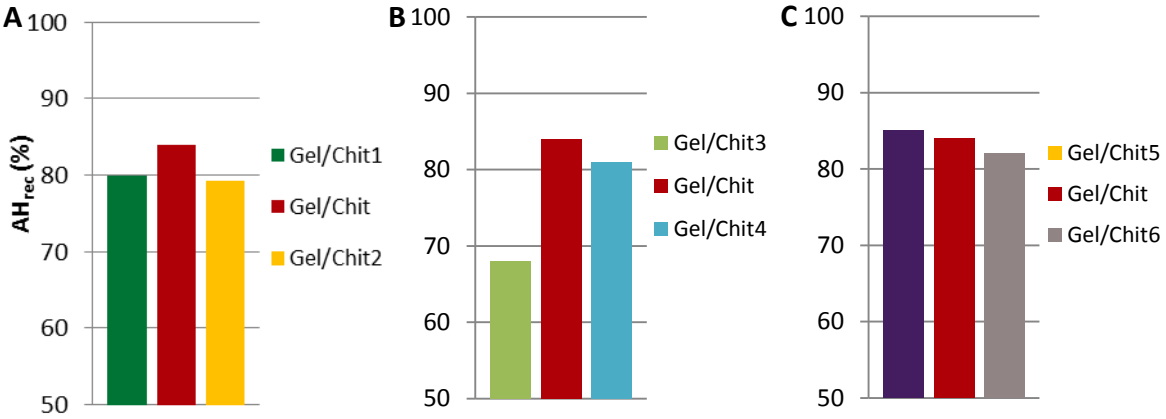

***Figure 5.11** Percentage recovery of absolute humidity of gelatin/chitosan based filters as a function of genipin amount (A), hydrogel concentration (B) and gelatin/chitosan ratio (C) for samples cross-linked with 1% (Gel/Chit1), 2% (Gel/Chit) and 4% (Gel/Chit2) of genipin/polymers ratio, with nominal hydrogel concentration of 1% (Gel/Chit5) and 3% (Gel/Chit6).*

Pressure drop of the filters does not vary in a clear manner as function of genipin amount, from 1,6 to 2,5 mbar; this finding could be attributed to the morphological similarity of the samples. Also by SEM images it was possible to see that all three filters show channel-like morphology even if Gel/Chit2 showed a structure a little less orderly that the other two materials. About the pressure drop changing as function of hydrogel concentration instead we could note some evident changings: Chit/Gel3 show a very high hurdle to the airflow, in fact has a pressure drop of about 11,5 mbar in relation to the 1,9 mar of Gel/Chit. This phenomena could be explained by the very closed morphology of this material: by SEM images it was possible understand that the pores are smaller respect to Gel/Chit, and the vertical path of the little pores are often interrupted by channel mergers. This irregular morphology probably obstructs the passage of air through the filter. Finally the polymers ratio affects the pressure drop only a little: the most tailored structure of the Gel/Chit6 show obviously less pressure drop compared with the two other samples; the difference are, however, slight.

Also moisture exchange behavior shows only little changes varying the different parameters. In function of cross-linking process, A medium value of cross-link is the optimal condition for the hydrophobic/hydrophilic balancing, so as the percentage of moisture

exchanged is 84 compared to Gel/Chit1, 80, and Gel/Chit2, 79. By changing, instead, hydrogel concentration a minimal difference was observed between Gel/Chit and Gel/Chit4, while the value is very low for Gel/Chit3. This result was valid taking into account that moisture exchange is affected by the material nature but also by the pressure drop, therefore the air outlet is a smaller quantity, also the final exchange of moisture will be smaller. Regarding the polymer ratio, the moisture exchange decreased with the increasing of chitosan amount, sign that the hydrophobic component affects negatively the final property of the device. The difference are, however, small enough to be not very significant.

After these test Gel/Chit was chosen as the most promising material, with a pressure drop and moisture exchange values in line with ISO standards, high resistance during test simulations and good bacteriostatic/bactericidal behaviour.

5.2 Heater section

The second important characteristic of the device to develop is the presence of magnetic hydroxyapatite in addition to the polymeric fibrous matrix which should allow to induce magnetic forces inside the devices under the action of an external variable magnetic field. In this way it is expected hyperthermia properties inside the filters, which should make them suitable to warm the cold gases deriving from the pulmonary ventilator. The aim of this part of the project was to create a self-consisting material, since then it must be integrated into the previously developed matrix, containing the greatest possible amount of a superparamagnetic mineral phase trapped into a polymeric matrix to ensure that it can't detach during using of the filter.

5.2.1 Synthesis process

The magnetic part of the filter was created starting with the synthesis of an high magnetic hydroxyapatite powder which was prepared as explained in 4.4.1 paragraph, namely with a neutralization process where a solution of phosphoric acid was dropwise added to a basic suspension containing calcium hydroxide plus iron(III) chloride hexahydrate and iron(II) chloride tetrahydrate as sources of Fe^{3+} and Fe^{2+} ions.

Unlike the previous explained synthesis, the amount of reactants was set up in order to keep the total amounts of iron ions so that Fe/Ca=40 mol%, with a synthesis temperature of 50°C, in order to maximize the magnetic power of the material. This product, stored at 4°C into a solution of 100 mg/L, was coded Fe40HA.

The dispersion of Fe40HA was mixed with a 10% w/w alginate aqueous solution at room temperature and completing the dissolution with sonication. The amount of reactants was set up in order to keep the apatite/alginate = 80:20. This mixing was poured into metal bottomed molds with 2 cm of diameter and freeze-dried obtaining a porous and

brittle material. Without removing these materials from theirs molds, a 1M calcium chloride solution was added in the mould to crosslink the composite and the sample was freeze-dried again. The final material, coded Fe40HA+Alg is shown in Fig. 5.12.

***Figure 5.12** Freeze-dried Fe40HA+Alg composite*

In adding to a mixing process, also a mineralization process of FeHA40HA was tried on alginate matrix as comparison for magnetic power. An alginate solution was produced at concentration of 5% w/v in water and a diluted phosphoric acid was added to this solution. Ones created this acid solution, the biomineralization processes was conducted as previously described in 4.4.1 paragraph for the mineralization of gelatin, with the adding of Fe^{2+} and Fe^{3+} ions into the basic dispersion. After the washing process and a first liophylization above the material was poured a 1M calcium chloride solution and freeze-dried again. The final material, coded Fe40HA/Alg.

5.2.2 Chemic-physical characterizations

5.2.2.1 Thermal Analysis

Thermogravimetric investigations were carried out on Fe40HA+Alg freeze-dried sample and the result curve (TG) and its derivative (DTG) are shown in Fig. 5.13.

The first weight loss, in the rage of 30-170 °C is due to loss of absorpted water, while the second weight loss, between 200 and supposedly 500°C, could be attributed to the decomposition of alginate[25].

The decomposition is completed around 600°C, with an overall decrease of the organic component of about 22% of the total weight. The final weight ratio between for inorganic/organic composition was so fixed to 77:23 wt., very close to the theoretical one.

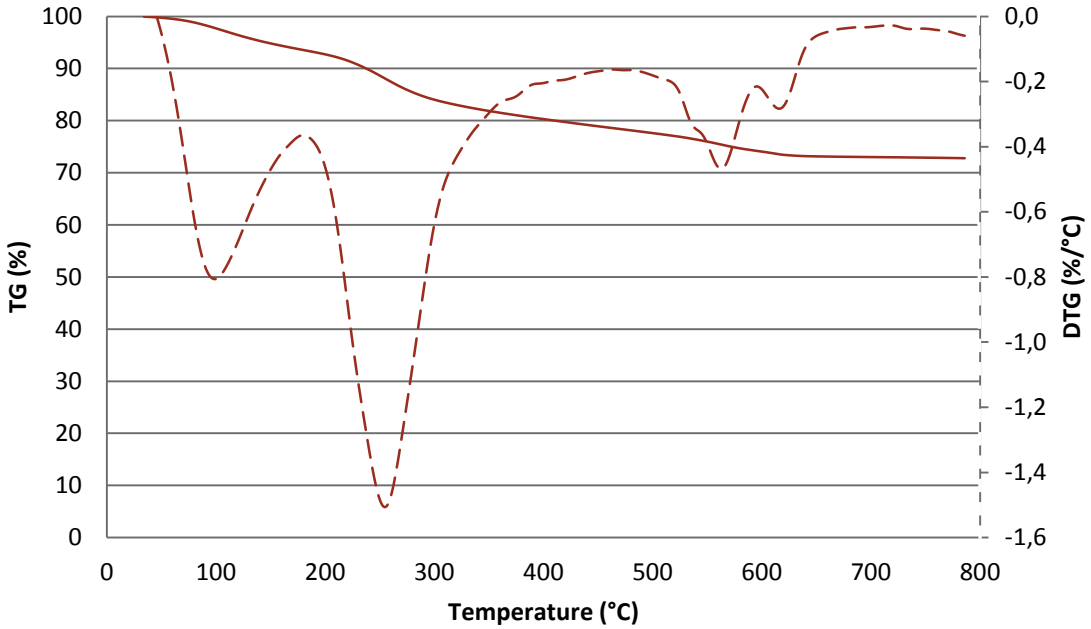

***Figure 5.13** Thermal decomposition profile (TG) and its derivative (DTG) of FeHA40HA+Alg.*

5.2.2.2 X-Ray Diffraction

The X-ray diffraction patterns of Fe40HA+Alg is shown in Fig. 5.14 and Fe40HA pattern is shown as comparison. From the XRD spectra of the mineral phase we could deduce the presence of apatite, with its typical peaks at 2θ=26.5, 32.0 and 34.0°, and magnetite as secondary product, with the main peak at 2θ=35,4°, while the spectra of the composite shows the same peaks but with a low resolution, sign of the adding of an amorphous polymer.

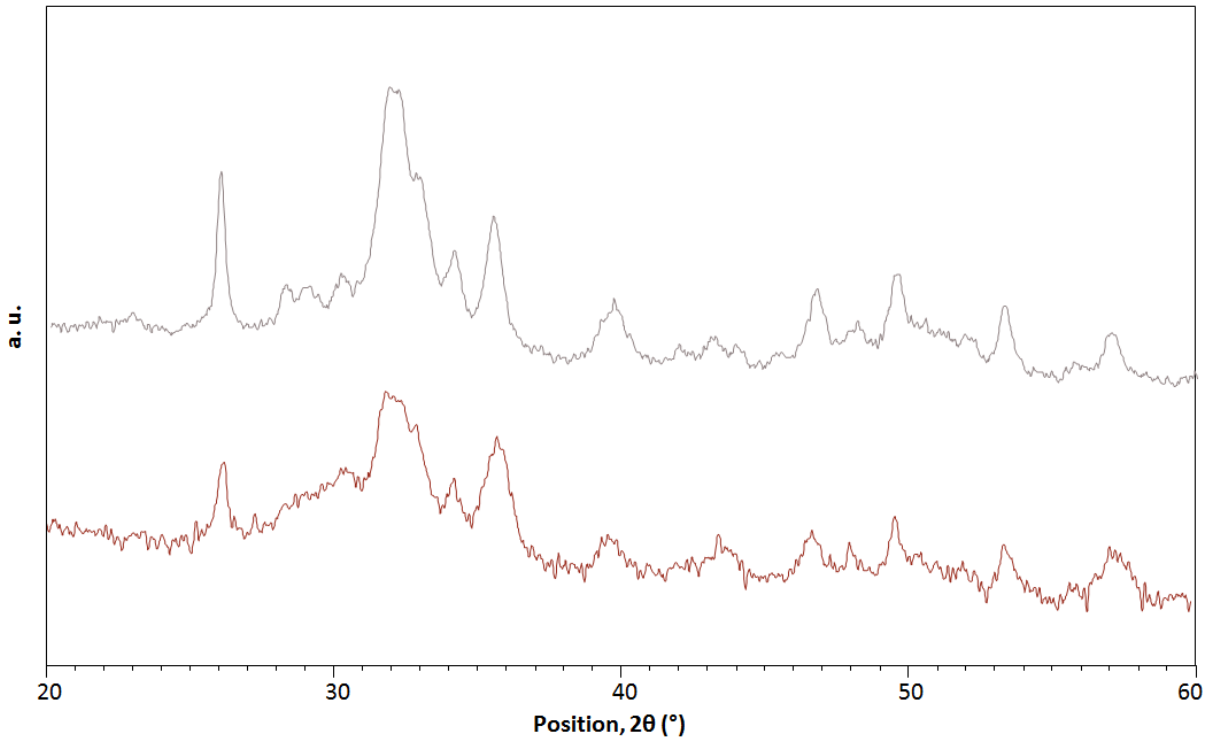

***Figure 5.14** XRD spectra of Fe40HA+Alg (red) and Fe40HA (grey).*

4.1.2.3 Fourier-Transform Infrared Spectroscopy

Infrared spectra of Fe40HA+Alg is shown in Fig. 5.15 and it's possible to recognize the bands relative to functional groups typically present in the composite components (apatite and alginate).

The main absorption bands characteristic of hydroxyapatite appear at 3429 cm^{-1}, attributed to O-H stretching and at 1034, 606 and 565 cm^{-1}, related to phosphate stretching and bending motions, while the typical alginate absorption bands can be detected at 1624 and 1419 cm^{-1}, related to COO group stretching.

***Figure 5.15** FTIR analysis of Fe40HA+Alg.*

5.2.2.4 Scanning Electron Microscopy

SEM images of Fe40HA+Alg are shown in Fig. 5.16; it's clear that the composite has a very porous morphology, with rough surfaces due to the high presence of mineral phase. The Fe40HA is easily visible in the high magnification image, and we could deduce that it's disposed into the composite in small aggregates from 10 to 2 µm sized.

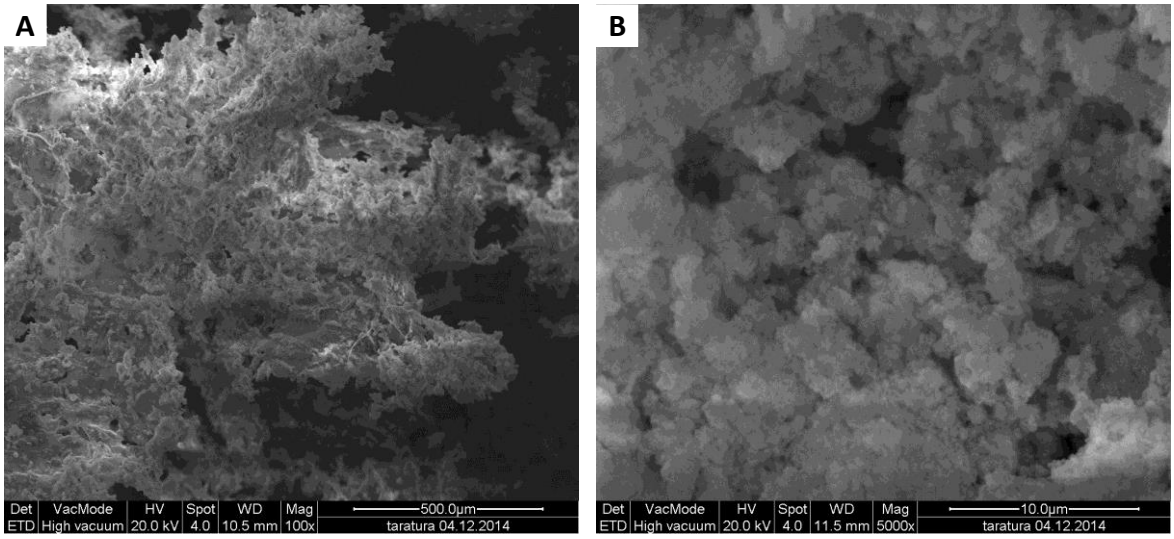

***Figure 5.16** SEM images of Fe40HA+Alg at 100x (A) and 5000x magnification (B).*

5.2.2.5 Inductively Coupled Plasma Atomic Emission Spectroscopy

The overall composition analysis of the mineral phase and the composite was evaluated by ICP analysis and the results are shown in Tab. 5.4.

Materials	Ca/P (mol)	(Fe+Ca)/P (mol)	Fe/Ca (mol%)	Fe/(Fe+Ca) (mol%)
Fe40HA	1,38 ± 0,05	1,98 ± 0,03	43,46 ± 0,2	30,81 ± 0,04
Fe40HA+Alg	1,41 ± 0,04	1,99 ± 0,03	41,82 ± 0,2	30,37 ± 0,03

***Table 5.4** ICP features of Fe40HA and Fe40Ha+Alg composite.*

About the Fe40HA, the (Ca+Fe)/P molar ratio results higher compared to the hydroxyapatite theoretical one (Ca/P = 1,68 mol), sign that the mineral phase isn't composed entirely of apatite and confirming the presence of an additional iron-based component. In the Fe40HA+Alg analysis, the calcium amount results slightly more than that of the mineral phase alone due to the calcium chloride used for the crosslinking reaction of the alginate.

5.2.2.6 Hyperthermic effect

Hyperthermia effect of Fe40HA powder was measured trough a variable magnetic field of 2.6, 3.9 and 4.9 mT intensity and with a frequency of 442, 313 and 221 kHz. The Fig. 5.17A, B, C show the result respectively for 2.6, 3.9 and 4.9 mT intensity of magnetic field, while Fig. 5.18 shows the comparison between hyperthermia effect of Fe40HA. Fe40HA+Alg and Fe40HA/Alg composites.

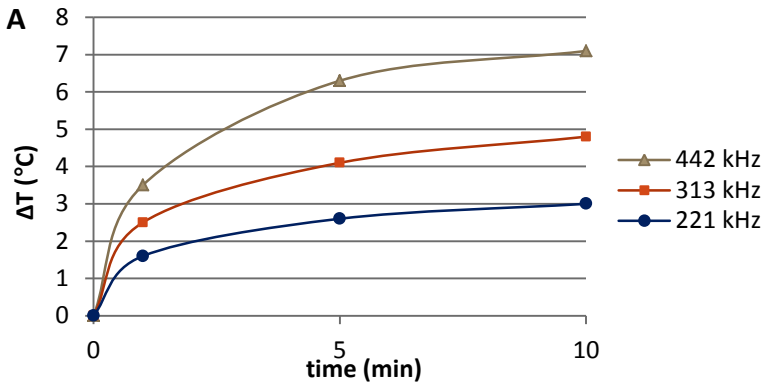

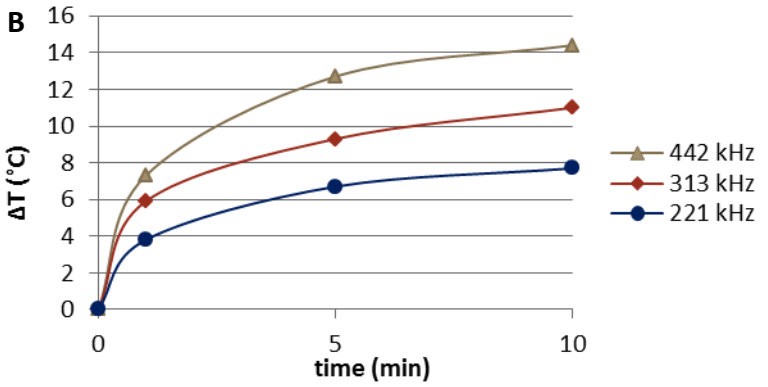

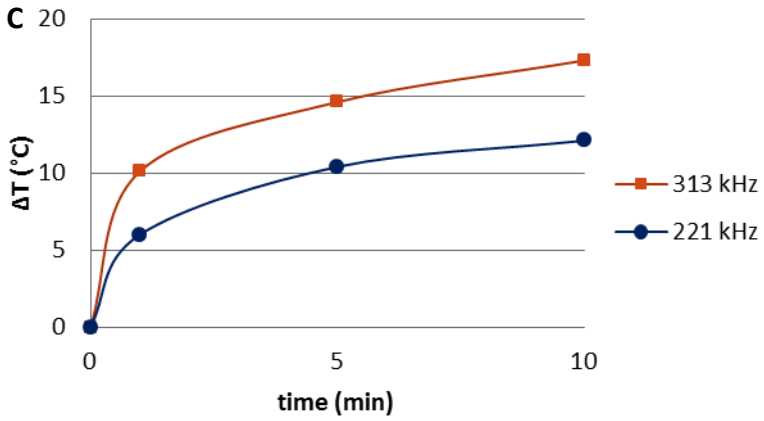

***Figure 5.17** Warming curve of Fe40HA subjected to a magnetic field at various intensity (A: 2.6; B: 3.9; C: 4.9 mT) and frequencies.*

Obviously, higher warming effect was obtained from the powder and lower effect with Fe40HA+Alg composite due to the presence of polymer and particle aggregation into the organic matrix that obstruct the magnetization and reduce the effective amount of the magnetic phase[26]. No hyperthermic effect has been noticed for Fe40HA/Alg (Fig. 5.18).

The tests carried out varying the intensity and frequency of the magnetic field, showing that the temperature raise is influenced mainly by the intensity. A proof of that, powders under a magnetic field field of 4.9 mT at 221 kHz increase temperature of around 12,1°C, whereas under a magnetic field of 2.6 mT (half) at 442 kHz (double) the rise is only of 7,1°C.

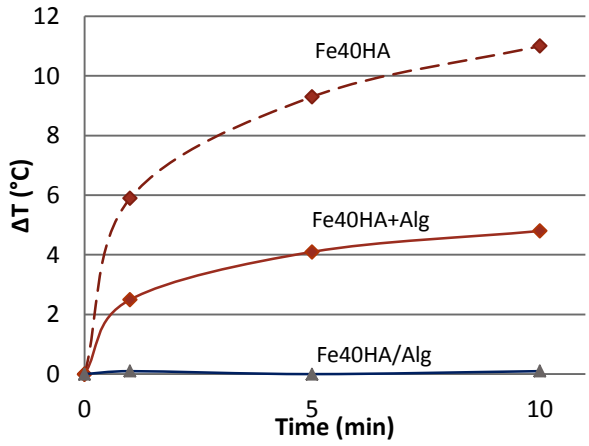

Figure 5.18 *Warming curve of Fe40HA, Fe40HA+Alg and Fe40HA/Alg subjected to a magnetic field at 3.9 mT and 313 kHz.*

5.3 HME filters: assembling process

After the development of the magnetic core of the filter an effective assembling method was implemented in order to obtaining the final Heat and Moisture Exchange air filter.

The obtained magnetic material was placed, once lyophilized, in the middle of the 5 cm filter mold and the solution of gelatin, chitosan and genipin previously optimized was added before the cross-linking occurs. After 48 hours, when the cross-liking took place the magnetic core is integrated in the middle of the hydrogel and after the last freeze-drying it's possible to obtain a single well-integrated material. This final device was made by Gel/Chit as the shell part, destined to the exhaled air, interpenetrated into the Fe40HA+Alg as the core. The final HME filter was shown in Fig. 5.19.

***Figure 5.19** Fe40HA+Alg – Gel/Chit core-shell filter.*

5.3.1 Chemic-physical characterizations

5.3.1.1 Scanning Electron Microscope

The cross-section morphology of the core-shell filter interface is shown by SEM images in Fig. 5.20A, B; details of the two sections of the filter was also shown in Fig. 5.20C (core), D (shell).

These images prove the well adhesion of the two section of the filter; the internal core, the more rugged material in Fig.5.20B, results in fact to loss its primary structure during

the assembling process, in order to deposit on the interior surfaces of the pores formed during the lyophilization of the gelatin/chitosan based hydrogel (the smooth material in Fig.5.20B). In this way the magnetic material could be directly in contact with the air passing through the filter, and the mineral phase results recovered by the polymeric phase to prevent its detachment during use of the device. The channel-like structure of the original Gel/Chit material has not been altered so as to maintain low the pressure drop and a perfect interpenetration was reached, in order in order to ensure an efficient capillary transport of the humidity.

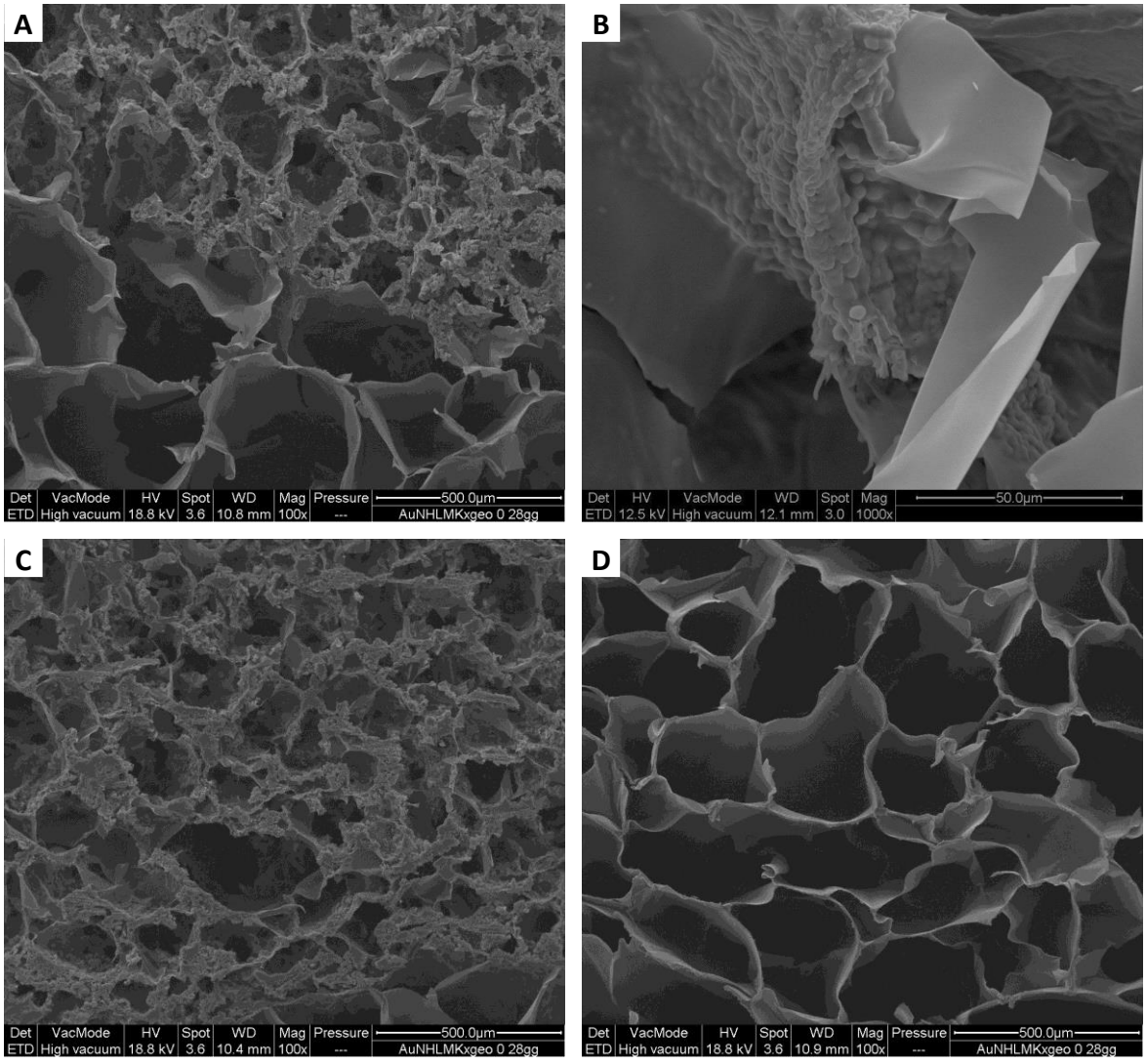

***Figure 5.20** SEM images of the core-shell filter at 100x (A, B, C) and 1000x magnification (B); A, B show the detail of the macroscopic and microscopic interfaces of the two materials.*

5.3.2 Conclusion

A homogeneous blend composed by gelatin, chitosan and cross-linked with genipin was optimized in order to create an hydrogel capable to become a 3D device with an organized porous structure by means of the lyophilization technique. The ratio between the polymers and the amount of cross-linking agent were setup to obtain a highest moisture exchange efficacy and to avoid the collapse of the filter during the utilization. The hydrogel concentration and the freeze-drying variables have been fixed to be able to get the lowest possible pressure drop of the device. The final data of moisture exchange and pressure drop are perfectly aligned with the fixed ISO standards.

A neutralization process has been employed to synthetize hydroxyapatite powder in which the addiction of ferric and ferrous ions leads to a partial substitution of calcium and the formation of a small percentage of magnetite as secondary product. This powder results highly hypertermic once subjected to an alternate magnetic field. A little cylindrical material composed by calcium alginate endowed with an high amount of this hyperthermic powder was created; just a low intensity of magnetic field is sufficient to start hyperthermia effects in this composite.

The blend composed by gelatin and chitosan crosslinked with genipin and the alginate added with magnetic hydroxyapatite were successfully assembled to obtain the final Heat and Moisture Exchange air filter presenting a well adherent core-shell structure where the external section is suitable for catching the moisture from the humid exhaled air, while the internal part is dedicated to the warming and humidification of dry and cold air from the artificial ventilation.

The actual efficacy of the final device to warm the inspired air as well as the effectiveness of moisten the dry inspired gases, will be tested with the filter holder with two different ways for air inlet and outlet.

5.4 References

[1] H. Takahashi, T. Miyoshi, and K. Boki, “Study on hydrophilic properties of gelatin as a clinical wound dressing. I. Hydrophilic properties of gelatin as a wound dressing.,” *Tokushima J. Exp. Med.*, vol. 40, no. 3–4, pp. 159–67, Dec. 1993.

[2] H. Yang, S. Zhou, and X. Deng, “Preparation and properties of hydrophilic-hydrophobic chitosan derivatives,” *J. Appl. Polym. Sci.*, vol. 92, no. 3, pp. 1625–1632, May 2004.

[3] T. Chen, H. D. Embree, L.-Q. Wu, and G. F. Payne, “In vitro protein-polysaccharide conjugation: tyrosinase-catalyzed conjugation of gelatin and chitosan.,” *Biopolymers*, vol. 64, no. 6, pp. 292–302, Sep. 2002.

[4] A. Sionkowska, M. Wisniewski, J. Skopinska, C. J. Kennedy, and T. J. Wess, “Molecular interactions in collagen and chitosan blends,” *Biomaterials*, vol. 25, no. 5, pp. 795–801, 2004.

[5] L.-S. Wang, C. Du, J. E. Chung, and M. Kurisawa, “Enzymatically cross-linked gelatin-phenol hydrogels with a broader stiffness range for osteogenic differentiation of human mesenchymal stem cells.,” *Acta Biomater.*, vol. 8, no. 5, pp. 1826–37, May 2012.

[6] S. Fakirov, M. E. Cagiao, F. J. Baltá Calleja, D. Sapundjieva, and E. Vassileva, “Melting of Gelatin Crystals below Glass Transition Temperature: A Direct Crystal-Glass Transition as Revealed by Microhardness,” *Int. J. Polym. Mater.*, vol. 43, no. 3–4, pp. 195–206, May 1999.

[7] C. Casado-Coterillo, M. Del Mar López-Guerrero, and A. Irabien, “Synthesis and Characterisation of ETS-10/Acetate-based Ionic Liquid/Chitosan Mixed Matrix Membranes for CO2/N2 Permeation.,” *Membranes (Basel).*, vol. 4, no. 2, pp. 287–301, Jan. 2014.

[8] M. M. Rahman, S. Pervez, B. Nesa, and M. A. Khan, “Preparation and characterization of porous scaffold composite films by blending chitosan and gelatin solutions for skin tissue engineering,” *Polym. Int.*, vol. 62, no. 1, pp. 79–86, Jan. 2013.

[9] K. Ganguly, T. M. Aminabhavi, and A. R. Kulkarni, “Colon Targeting of 5-Fluorouracil Using Polyethylene Glycol Cross-linked Chitosan Microspheres Enteric Coated with Cellulose Acetate Phthalate,” *Ind. Eng. Chem. Res.*, vol. 50, no. 21, pp. 11797–11807, Nov. 2011.

[10] C. Mu, F. Liu, Q. Cheng, H. Li, B. Wu, G. Zhang, and W. Lin, “Collagen Cryogel Cross-Linked by Dialdehyde Starch,” *Macromol. Mater. Eng.*, p. NA–NA, Jan. 2010.

[11] J. . Muyonga, C. G. . Cole, and K. . Duodu, “Fourier transform infrared (FTIR) spectroscopic study of acid soluble collagen and gelatin from skins and bones of young and adult Nile perch (Lates niloticus),” *Food Chem.*, vol. 86, no. 3, pp. 325–332, Jul. 2004.

[12] F.-L. Mi, “Synthesis and characterization of a novel chitosan-gelatin bioconjugate with fluorescence emission.,” *Biomacromolecules*, vol. 6, no. 2, pp. 975–87, Jan. .

[13] S. Gorgieva and V. Kokol, “Preparation, characterization, and in vitro enzymatic degradation of chitosan-gelatine hydrogel scaffolds as potential biomaterials.,” *J. Biomed. Mater. Res. A*, vol. 100, no. 7, pp. 1655–67, Jul. 2012.

[14] F. O’Brien, “Influence of freezing rate on pore structure in freeze-dried collagen-GAG scaffolds,” *Biomaterials*, vol. 25, no. 6, pp. 1077–1086, Mar. 2004.

[15] W. Kurz and D. J. Fisher, *Fundamentals of solidification, Volume 1*. 1986.

[16] C. G. Gebelein and R. L. Dunn, Eds., *Progress in Biomedical Polymers*. Boston, MA: Springer US, 1990.

[17] H. Schoof, J. Apel, I. Heschel, and G. Rau, “Control of pore structure and size in freeze-dried collagen sponges,” *J. Biomed. Mater. Res.*, vol. 58, no. 4, pp. 352–357, 2001.

[18] J. S. Mao, L. G. Zhao, Y. J. Yin, and K. De Yao, “Structure and properties of bilayer chitosan–gelatin scaffolds,” *Biomaterials*, vol. 24, no. 6, pp. 1067–1074, Mar. 2003.

[19] J. Jin, M. Song, and D. J. Hourston, “Novel chitosan-based films cross-linked by genipin with improved physical properties.,” *Biomacromolecules*, vol. 5, no. 1, pp. 162–8, Jan. 2004.

[20] V. Chiono, E. Pulieri, G. Vozzi, G. Ciardelli, A. Ahluwalia, and P. Giusti, “Genipin-crosslinked chitosan/gelatin blends for biomedical applications.,” *J. Mater. Sci. Mater. Med.*, vol. 19, no. 2, pp. 889–98, Feb. 2008.

[21] T. Yasuda, T. Okuno, and H. Yasuda, “Contact Angle of Water on Polymer Surfaces,” *Langmuir*, vol. 10, no. 7, pp. 2435–2439, Jul. 1994.

[22] A. O. Paget-Brown, L. Ngamtrakulpanit, A. Smith, D. Bunyan, S. Hom, A. Nguyen, and J. F. Hunt, “Normative data for pH of exhaled breath condensate.,” *Chest*, vol. 129, no. 2, pp. 426–30, Feb. 2006.

[23] “UNI EN 13697-2001. Chemical disinfectants and antiseptics - quantitative non-porous surface test for the evaluation of bactericidal and/or fungicidal activity of chemical disinfectants used in food, industrial, domestic and institutional areas - test meth.” [Online]. Available: http://www.freestd.us/soft2/785998.htm. [Accessed: 20-Jan-2016].

[24] ISO, “ISO 9360-2:2001 Anaesthetic and respiratory equipment -- Heat and moisture exchangers (HMEs) for humidifying respired gases in humans -- Part 2: HMEs for use with tracheostomized patients having minimum tidal volumes of 250 ml.” 2001.

[25] L. Fan, Y. Du, R. Huang, Q. Wang, X. Wang, and L. Zhang, “Preparation and characterization of alginate/gelatin blend fibers,” *J. Appl. Polym. Sci.*, vol. 96, no. 5, pp. 1625–1629, Jun. 2005.

[26] J. M. Vargas, L. M. Socolovsky, M. Knobel, and D. Zanchet, “Dipolar interaction and size effects in powder samples of colloidal iron oxide nanoparticles,” *Nanotechnology*, vol. 16, no. 5, pp. S285–S290, May 2005.

CONCLUSIONS AND FUTURE PERSPECTIVES

Petroleum-based materials has become an increasingly problem for both the economy and the nature, since petroleum resources are finite, their prices are likely to rise in the future and polluting and global warming, caused in part by fossil resources extraction, are worsening the environment. The aim of this work was to produce newly conceived bio-inspired solutions towards the local treatment of dental diseases and the air filtration in hospital mechanical ventilation.

Following concept of hierarchical organization combining microfabricated elementary building blocks that could be assembled into more complex structures, a scaffold chemically and morphologically mimicking the dentin was developed. A biomineralization process was applied to nucleate magnesium-doped hydroxyapatite nanoparticles (MgHA) on gelatin molecules and obtain a biomimetic hybrid composite with an high content of mineral phase. Moreover, by blending the mineralized composite with alginate was possible to impart to the material the desired channel-like structure. My means of cross-linking and freeze-drying processes, it was possible to fabricate a 3D scaffold stable in physiological environment and mimicking the chemical and morphological features of dentin.

Chemically and morphologically graded construct was designed and developed thus mimicking the whole periodontium (cementum, periodontal ligament, alveolar bone). Hybrid composites endowed with superparamagnetic properties were synthetized to mimicry the hard tissues and further improve the regenerative potnetial, moreover a collagen-based porous layer was developed with analogous characteristic of the periodontal ligament.

Alveolar bone-like layer (FeHA/Coll) was realized through the biomineralization approach, with a simultaneous nucleation of iron-doped hydroxyapatite (FeHA) and a pH-

dependent assembling of collagen fibers. The synthesis temperature and the introduction of ferrous and ferric ions into the apatitic lattice during the stage of hydroxyapatite nucleation induces in the final composite chemic-physical, structural and morphological features close to those of bone along with superparamagnetic properties.

The cementum-like layer, was successfully obtained by processing a blend of cellulose acetate with FeHA nano-powder with electrospinning technique suitable to fabricate thin and dense but porous layers. . At this purpose, a synthetic procedure to obtain a magnetic (Fe^{2+}/Fe^{3+})-lattice substituted hydroxyapatite have been optimized in order to induce superparamagnetic behavior and minimize the formation of magnetite as secondary phase, potentially toxic once metabolized.

Finally the middle layer, the periodontal ligament-like one, was obtained by processing type I collagen properly cross-linked to control its durability in physiological conditions.

Peculiar structural features, as open and interconnected pores were achieved through the applications of freeze-drying technique.

The three layer were than stacked together obtaining a 3D scaffold reproducing the chemical and morphological feature of the whole periodontium.

In vitro investigations performed on these biomimetic scaffolds demonstrate their biocompatibility, underlining their good ability to support cell adhesion and proliferation.

Therefore, the biohybrid scaffolds developed in this work are promising candidates for the regeneration of dentin and periodontal region, since they have not only the potential to provide a tissue-conductive system that mimics the tree-dimensional environment of the tissues, but also thanks to their magnetic properties, they can furnish osteoconductive stimuli necessary for a faster and effective tissue regeneration.

Employing biomimetic principles, also a Heat and Moisture Exchange air filter based on natural components was developed. A moisture exchange device was firstly optimized using the freeze-drying process on a cross-linked hydrogel based on a gelatin and chitosan blend. This filter section, which will represent the shell of the final device, was developed in order to minimize the air pressure drop and maximize the hygrometric exchange.

Separately, the synthetic procedure to obtain a magnetic (Fe2+/Fe3+)-substituted hydroxyapatite was optimizing in order to maximize the magnetic behavior and therefore the hyperthermic effect. The achieved powder was then added into an alginate solution and thanks to cross-link and freeze-drying processes a magnetic core for the air filter was realized.

In this way it was realized an HME core-shell filter which offer the possibility of warming cold air from the artificial ventilator once subjected to an external magnetic field and high efficient in condensate vapor from the patient exhaled breath and release it into the inhaled air. A further function of this HME filters concerns the antibacterial and antiviral filtering capabilities.This filter is completely made from renewable sources, that guarantee affordable prices, so it might find a new large and interesting market.

This work has thus led the development of scaffolds mimicking dentin which could be used to fill the cavities left by caries lesions and induce regeneration process, so that to be a solution in the case of superficial or deep and penetrating caries and prevent endodontic treatments and prolong the vitality of natural teeth.

While in patients with missing teeth, such innovative solutions could be beneficial in the primary stabilization of the titanium dental implants. Indeed, the amount of regenerated bone is crucial for the implant stability over time.

A significant advantage of the collagen scaffold is that it is natural polymer and therefore bioactive, allowing osteoblasts to maintain high metabolic rates that increase overtime.

Magnetic property of FeHA phase together with its biocompatibility open the door of the regenerative medicine to a conceptually newly family of biomimetic composites able to be manipulated or activated in situ by means of an external magnetic field.

The control mechanisms inherent in the whole process of self-assembling and mineralization, scaled at pilot plant, could allow to establish a technological platform based on

highly repeatable, scalable and cost-effective technology for the manufacturing of multi-functional devices with huge economic, environmental and social impact. In this respect, roadmaps addressing wider industrial exploitation could be prepared, basing on the knowledge gained in this PhD project.

These results can also represent a proof of concept for further development of smart devices obtained by biologically-inspired self-assembling processes.

List of publications

B. Vazquez, A. Nicosia, F. Belosi, G. Santachiara, P. Monticelli, M. Sandri, E. Savini, and A. Tampieri; “Natural Polymers as Heat and Moisture Exchange Devices for Medical Applications” Adv. Sci. Technol., vol. 96, pp. 39–44, Oct. 2014.

A. Tampieri, M. Iafisco, M. Sandri, S. Panseri, C. Cunha, S. Sprio, E. Savini, M. Uhlarz, and T. Herrmannsdörfer; “Magnetic bioinspired hybrid nanostructured collagen-hydroxyapatite scaffolds supporting cell proliferation and tuning regenerative process” ACS Appl. Mater. Interfaces, vol. 6, no. 18, pp. 15697–707, Sep. 2014

M. Sandri, G. Filardo, E. Kon, S. Panseri, M. Montesi, M. Iafisco, E. Savini, S. Sprio, C. Cunha, G. Giavaresi, F. Veronesi, M. Fini, L. Salvatore, A. Sannino, M. Marcacci, A. Tampieri; “Engineering of a collagen-BDDGE-elastin core-shell scaffold for tendon regeneration”. (Accepted from Frontiers in Bioengineering and Biotechnology)

S. Panseri, M. Montesi, S. M. Dozio, E. Savini, A. Tampieri and M. Sandri; “3D Cell Culture in Porous Scaffolds with Oriented Microtubules Designed for Dentinal al Regeneration”. (Accepted from Frontiers in Bioengineering and Biotechnology)

Scientific contributions to international congresses and schools

E. Savini, M. Sandri, A. Tampieri "Synthesis of biomineralized multilayer scaffold for dental repair and regeneration". Book of Abstracts of the European Calcified Tissue Society PhD Training (2013)

M. Sandri, M. Iafisco, S. Panseri, E. Savini, and A. Tampieri, "Fully Biodegradable Magnetic Micro-Nanoparticles: A New Platform for Tissue Regeneration and Theranostic" ASME 2013 2nd Global Congress on NanoEngineering for Medicine and Biology (2013)

E. Savini, S. Panseri, M. Montesi, M. Sandri, A. Tampieri "Biomineralized multilayer scaffold for dental repair and regeneration". Book of Abstracts of the MiMe – Material in Medicine (2013)

K. Chatzipanagis, R. Wallace, C. Baumann, E. Savini, M. Sandri, A. Tampieri, R. Kröger "Mechanical and microstructural properties of mineralized collagen studied by in situ micro Raman spectroscopy and electron microscopy" Book of Abstracts of the Microscience Microscopy congress (2014)

E. Savini, M. Sandri, P. Monticelli, F. Belosi, B. Vazquez, A. Nicosia, A. Tampieri "Gelatin/chitosan blends for smart air filters with moisture exchange capabilities". Book

of Abstracts of the Bio-based Polymers and Composites Congress (2014)

B. Vazquez, P. Monticelli, A. Nicosia, F. Belosi, G. Santachiara, M. Sandri, E. Savini, A. Tampieri "Environmental and medical applications of natural polymers" Book of Abstracts of the Leading Enabling Technologies for Societal Challenges - LET'S (2014)

S. Panseri, M. Montesi, E. Savini, S.M. Dozio, M. Sandri, A. Tampieri "3D Cell Cultures in Porous Scaffolds with Oriented Microtubules Designed for Dental Regeneration" Book of Abstracts of the Tissue Engineering & Regenerative Medicine International Society congress (2015)

A.Nicosia, F.Belosi, B.Vazquez, G.Santachiara, D.Wesołek, W.Gieparda, M.L.Focarete, E.Savini, M.Sandri, A.Tampieri "Experimental and theoretical description of electrospun biopolymer nanofibrous membranes for filtration applications" Book of Abstracts of the Aerosol Technology (2015)

S. Panseri, M. Montesi, E. Savini, S.M. Dozio, M. Sandri, A. Tampieri "Oriented Microtubules designed scaffolds for bone and dental regeneration" Book of Abstracts of the World Conference on Regenerative Medicine (2015)

Scientific contributions to national congresses

E. Savini, A. Ruffini, M. Sandri, A. Tampieri "Novel pH-sensitive bio-hybrid systems for drug controlled release" Book of Abstracts of the SIB (Società italiana Biomateriali) congress (2013)

E. Savini, M. Sandri, S. Panseri, M. Montesi, A. Tampieri "Bio-inspired scaffolds for dental repair and regeneration" Book of Abstracts of the SIB (Società italiana Biomateriali) congress (2014)

Acknowledgments

I would like to thank Pollution s.r.l. (Budrio) for the pressure drop, moisture exchange and hyperthermia measurement.

I would like to thank also HZDR (Helmholtz-Zendrum Dresden Rossendorf; Dresden, Germany) for the magnetic measurements and Friedrich-Schiller-Universität Jena Otto-Schott-Institut für Materialforschung (Jena, Germany) for the magnetic measurements too and for the electrospun materials.

Finally, thanks to my tutors Maria Letizia Focarete and Monica Sandri, and to all the CNR-ISTEC for all the technical support.

This work was supported by the EU project “SMILEY” NMP-2012-SMALL-6-310637.